JARA|FIT

Fundamentals of Future
Information Technology

Annual Report 2014

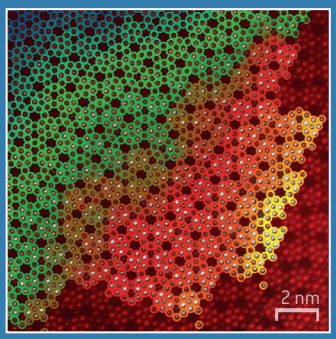

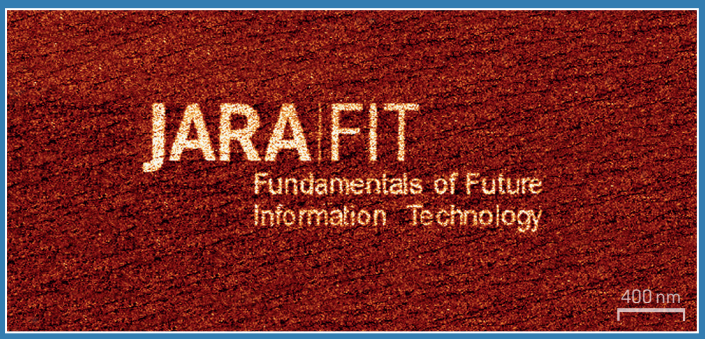

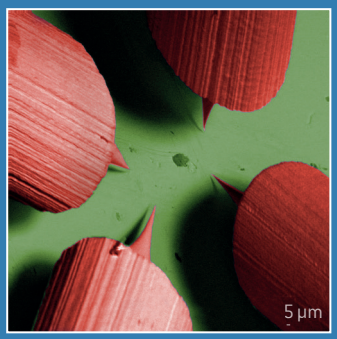

AN INITIATIVE OF

RWTH AACHEN UNIVERSITY

JÜLICH FORSCHUNGSZENTRUM

Publication Details

JARA-FIT
Jülich Aachen Research Alliance
for Fundamentals of Future Information Technology
Annual Report 2014

Published by:
Forschungszentrum Jülich GmbH, 52425 Jülich
RWTH Aachen University, 52062 Aachen

Editors:
Dr. Wolfgang Speier
Managing Director JARA-FIT
Forschungszentrum Jülich GmbH
52425 Jülich
Germany
Phone: ++49-2461-61-3107

Prof. Dr. Stefan Tautz
Scientific Director JARA-FIT
Peter Grünberg Institute –
Functional Nanostructures at Surfaces
Forschungszentrum Jülich GmbH
52425 Jülich
Germany
Phone: ++49-2461-61-4561

Prof. Dr. Matthias Wuttig
Scientific Director JARA-FIT
I. Institute of Physics A
RWTH Aachen University
52074 Aachen
Germany
Phone: ++49-241-8027155

Contact:
Dr. Wolfgang Speier
w.speier@fz-juelich.de

Layout:
Ulrike Adomeit
Silke Schilling

Year of publication:
2015

2015

JARA-FIT

Jülich Aachen Research Alliance for

Fundamentals of Future Information Technology

Annual Report 2014

Forschungszentrum Jülich

RWTH Aachen University

Dear Reader,

The remarkable success of electronics in the past forty years has been based on a continuous decrease of the feature size ("Moore's law") and an accompanying reduction in energy consumption. However, this concept is approaching its physical limits. Traditional semiconductor-based electronics is based on charge storage. Within JARA-FIT we are striving to develop alternatives to charge-based storage and follow two rather complimentary approaches. In striking contrast to charge-based storage, a set of resistive switching phenomena exists in oxides and higher chalcogenides in which the change of atomic configurations including atomic and ionic defects represents the essential functionality. It is the goal of our Collaborative Research Centre (SFB 917) to understand and explore the potential of advanced nanoswitches based on such configuration changes. Since the SFB 917 was established on July 1, 2011, this field has witnessed rapid growth and spectacular findings. These advances can be divided into three categories; a dramatically improved understanding of materials, the increased significance of data for modern societies, and the desire to develop concepts that go beyond the classical von Neumann architecture. We are very pleased that the German Science Foundation (DFG) has decided to extend the funding of SFB 917 for a second period, which will last until June 2019.

A second research initiative focusses on the use of entanglement and the quantum superposition principle, which promises an exponential speed-up of certain computational tasks. Several possibilities to implement quantum bits (qubits), the basic building blocks of a quantum computer leveraging this potential, have been experimentally demonstrated. For practical use, current few-qubit devices have to be scaled up to millions of qubits. The goal of this initiative applying for a Collaborative Research Centre is to address some of the scientific and technological challenges that need to be overcome to demonstrate such scalability. We envision that a quantum processor will also require integrated classical control electronics. Our focus is thus on semiconductor-based qubits, which are well matched to current information technology. A set of projects pursue the development of a particular type of qubit using electron spins in GaAs quantum dots and study open questions regarding the underlying physics that are relevant for realizing an integrated processor using these devices. We will also investigate important alternatives (e.g. Si- or graphene-based spin qubits) that are currently less advanced, but offer advantages that could eventually lead to better overall performance.

Successful activity in these two different research fields will pave the road to novel memories and alternative computer architectures. We strongly believe that with these concepts studied within JARA-FIT we can realize novel electronic functionalities, which can inspire and shape the next digital revolution. Yet, pursuing such ambitious goals also requires excellent infrastructures and teams being able to handle scientific challenges of increasing complexity. We are grateful that the opening of the Helmholtz Nanoelectronic Facility has provided an excellent platform for our research. Furthermore, in recent years we have witnessed a steady improvement in the ability to tackle complex challenges, discuss across the borders of the different disciplines involved and to harvest substantial synergy gains. These developments provide a healthy basis for exciting discoveries in the years to come. The present report summaries some of the most interesting findings we have achieved within JARA-FIT in the last year and should serve as an overview of the wide range of successful activities undertaken in 2014.

Matthias Wuttig
Scientific Director JARA-FIT

Stefan Tautz
Scientific Director JARA-FIT

Contents

JARA-FIT Highlights

Nanoelectronic Days 2015: Insights into the world of Green IT

JARA-FIT organized the Nanoelectronic Days 2015, which were held from 27. to 30. April 2015 in Jülich. The Nanoelectronic Days, jointly initiated by Forschungszentrum Jülich and RWTH Aachen University, were held for the third time and were devoted to green information technology. International experts from science and industry exchanged views on the latest achievements and new approaches that can be used to reduce the amount of energy consumed by information technology. The digital revolution has led to rapid growth in data acquisition, traffic and processing and has led to increasing demands placed on energy consumption. In fact, products already consume more than 10% of the total electric power produced in the western world, making energy-efficient computing a key technology for the sustainable scaling of information technology performance.

The opening session featured presentations by world-class scientists from industry on the general issue of energy efficiency as the driver for future information technology. Heike Riel from IBM Research Rueschlikon in Switzerland, at the same time member of the supervisory board of the Forschungszentrum Jülich, gave an overview over “Semiconducting Nanowires – What are they good for in future Nanoelectronics” and Myron Flickner from IBM Research Almaden in the US gave insights into “TrueNorth: A Brain Inspired Supercomputer on a Chip”.

The Nanoelectronic Days covered a wide set of fields in the following sessions:

- Nanoswitches
- Nanowires
- Steep Slope Devices
- Hybrid Structures and New Materials
- Towards Zero Power Systems.

Invited talks

Klaus Kern (MPI Stuttgart)
Quantum Engineering of Metal-Organic Contacts

Lars Samuelson (Lund University, Sweden)
NANOWIRES - basic materials science creating real-world applications

Matthias Wuttig (RWTH Aachen University)
Unravelling the transformation kinetics in Phase Change Memories

Christoph Stampfer (RWTH Aachen University)
Road to large-scale high-mobility graphene

Alexander Zaslavsky (Brown Univ., USA)
CMOS-compatible alternative transistors: from tunneling to feedback

Henning Riechert (PDI Berlin)
New epitaxial rules for the growth of two-dimensionally bonded materials

Adrian M. Ionescu (Nanolab, Ecole Polytechnique Fédérale de Lausanne, CH)
Energy efficient devices and technologies for functional diversification in future Cyber-Physical Systems

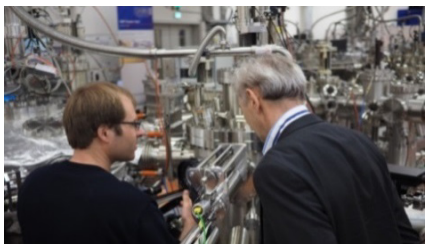

Each session started with invited talks followed by a set of short presentations accompanied by a poster session. Lab tours were offered, in particular to the Helmholtz Nanoelectronic Facility and the newly established Nanocluster complemented the conference.

The Nanoelectronic Days attracted up to 200 scientists and found support by the German Research Foundation (DFG).

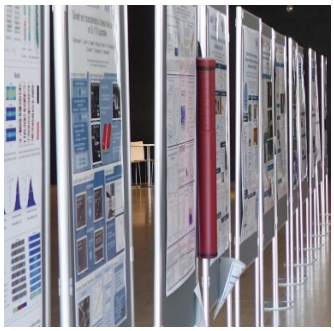

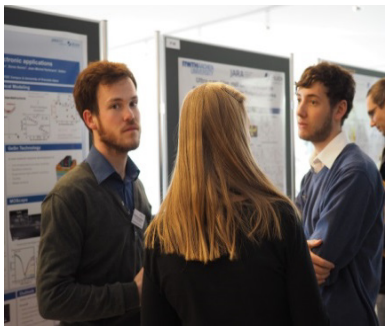

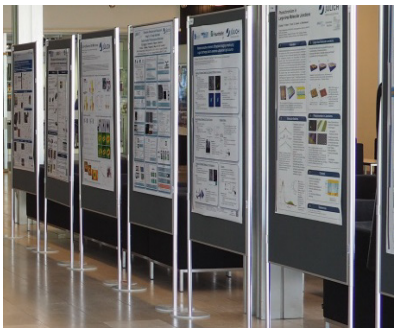

Installation of the nanocluster completed

The installation of the nanocluster, a ultra-high vacuum tool combining eight deposition chambers, has been completed. The nanocluster is operated jointly by the Peter Grünberg Institute und the RWTH Aachen University and is located in the Helmholtz Nanoelectronic Facility (HNF).
The nanocluster, developed and build by Omicron®, consists of:

- a group III-As MBE
- a group III-As/Sb MBE
- an ALD
- a metal-MBE
- a phase change MBE
- an oxide sputter chamber
- a metal sputter chamber
- a metal oxide MBE.

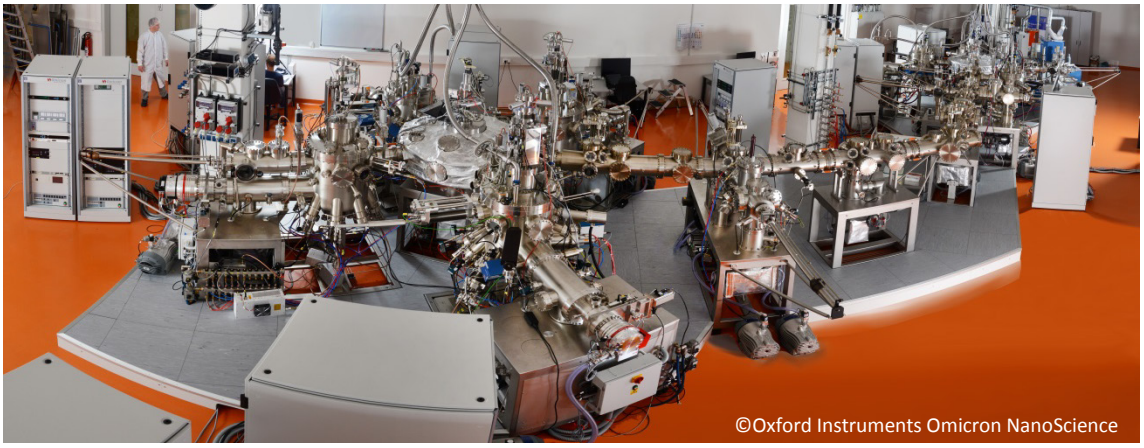

The nanocluster is designed for substrates up to 4'' and enables the growth of in-situ passivated high quality nanostructures as well as complex heterostructures. In combination with the HNF this allows fabricating and investigating new devices within the JARA-FIT and "GreenIT" framework.

SFB 917 "Nanoswitches" extended

In May 2015, the German Research Foundation approved the extension of the Collaborative Research Centre: Resistively Switching Chalcogenides for Future Electronics - Structure, Kinetics and Device Scalability ("Nanoswitches", SFB 917) for an additional, the second funding period. The Collaborative Research Centre is anchored in JARA-FIT as a joint endeavour of RWTH Aachen University and the Forschungszentrum Jülich and has been successfully running since 2011.

JARA-FIT Researchers received ERC Starting Grants

JARA-FIT scientists Martin Salinga and Norbert Schuch have been awarded prestigious European Research Council Starting Grants. The researchers succeeded in a competitive two-stage selection process and have received project funding in the amount of approximately 1.5 million Euros each over a period of five years.

Martin Salinga teaches and conducts research as a senior researcher at the Institute of Physics of New Materials at RWTH Aachen and is subproject team leader in the Collaborative Research Center "Nanoswitches" initiated by the JARA-FIT collaboration. He receives the grant for his project "Dynamics of Amorphous Semiconductors: Intrinsic Nature and Application in Neuromorphic Hardware". After decades of progress in computer technology it is safe to say that traditional computer architectures are not able to achieve the efficiency of biological neural networks. For this reason, an increasing number of researchers is working on biomimetic approaches in information processing. A neural network consists of interconnected neurons which as part of the nervous system form a functional entity. The NEURAMORPH

project aims at developing compact components that regulate the strength of synaptic connections between artificial neurons. To this purpose, due to the natural dynamics of their electric excitability, amorphous seminconductor materials are to be used – a completely novel approach. Adequate control of the properties of these synaptic elements requires a thorough understanding of the relaxation processes in such amorphous materials. The project seeks to offer new insights into the relationships between material composition, structural dynamics, and the changing electric excitability with the help of physics experiments and computer simulations.

Norbert Schuch is Junior Professor in Theoretical Physics with a focus on Condensed Matter at the RWTH Aachen Institute of Quantum Information, which is anchored in JARA-FIT. He receives the grant for his project “Wavefunctions for strongly correlated systems“. Complex systems of interacting quantum-mechanical particles show a wide range of diverse unconventional effects. These may serve as a basis for future technologies such as high-precision measuring devices, high-performance storage media, or novel quantum computers.The diversity of the involved physics phenomena is due to the quantum-mechanical entanglement of these systems. Parts of such a system cannot be described in isolation, which makes it highly difficult to understand its underlying physical mechanisms. The project “Wavefunctions for strongly correlated systems“ (WASCOSYS) uses methods from quantum information theory, in particular from entanglement theory, in order to develop new approaches for the modeling of complex quantum many body systems. These methods are expected to contribute to a fundamental, comprehensive understanding of the structure of complex quantum systems and thus, in the long term, to the development of novel quantum materials.

JARA-FIT member Rainer Waser receiced Taiwan’s highest scientific accolade

Rainer Waser has been awarded the Tsungming-Tu Prize by the National Science Council in Taiwan. Endowed with prize money of US$ 75,000, the award is the highest academic distinction which can be bestowed on non-Taiwanese citizens. Since 2007, the prize has been used to honour outstanding accomplishments in all areas of science and also serves to initiate further joint research projects. The award ceremony took place on 17 April 2015 in Taipei.

JARA-FIT member Rainer Waser received honorary doctorate from the University of Silesia

JARA-FIT member Rainer Waser received an honorary doctorate from the University of Silesia. According to Andrzej Ślebarski from the August Chełkowski Institute of Physics, University of Silesia, the award was given in recognition of his outstanding scientific achievements and merits in setting new directions of research in physics and materials science as well as his extensive cooperation with the Institute of Physics in Katowice. The laudatory emphasized: "Thanks to the personal involvement of Rainer Waser, the Institute of Physics has equipped its laboratories with professional and expensive equipment for scientific research".

End-of-year keynote lecture of the Forschungszentrum Jülich 2014 on “Ion Migration in the Nanoworld – From Electronic Phenomenon to Technology of the Future”

The Jülich end-of-year keynote lecture 2014 in the Rhineland Regional Museum (LVR-LandesMuseum), focused on data storage devices of the future and areas where they might be applied. JARA-FIT member Rainer Waser gave approximately 350 guests from politics, science, and industry as well as from Forschungszentrum Jülich insights into his research about electronic phenomena that could be used for novel information storage systems, logic devices, or energy conversion, such as ReRAM storage.

Distinguished Professorships of the RWTH Aachen University given to members of JARA-FIT

As part of the Excellence Initiative, the RWTH Aachen University aims to further develop and restructure the natural sciences as one of the core competencies of RWTH Aachen to secure a leading position both nationally and internationally and to ensure a sustainable exchange with the engineering fields. For this, projects to strengthen the natural sciences are selected and funded through a "Distinguished Professorship." The funds may be used for new research equipment, the recruitment of research staff, research visits, and the hosting of visiting scholars. Funding for the second round has been awarded to two JARA-FIT members: Richard Dronskowski, Chair of Solid-State and Quantum Chemistry and Institute of Inorganic Chemistry, for his project “Crystal Structure of Carbonic Acid” and Matthias Wuttig, Chair of Experimental Physics I A and Physics Institute I, for his project “Devising Treasure Maps for Thermoelectrics and Topological Insulators”.

Helmholtz International Fellow Award given to ER-C visitor David Smith

The Helmholtz Association has granted a Helmholtz International Fellow Award to the physicist David J. Smith from Arizona State University (USA). Forschungszentrum Jülich nominated the expert in electron microscopy for the accolade. The award honours excellent research and supports establishing new cooperation structures with international research institutions. In addition to a prize money, David J. Smith has the ability to conduct flexible research stays at the Ernst Ruska-Centre (ER-C) for Microscopy and Spectroscopy with Electrons in order to carry out research in the field of basic and applied electron optics.

European Microscopy Society’s “Outstanding Paper Award” winners from ER-C

Scientists from the Ernst Ruska-Centre (ER-C) have won two of three prizes awarded annually by the European Microscopy Society (EMS) for outstanding papers. Rafal E. Dunin-Borkowski, Director at the Peter Grünberg Institute and the ER-C, together with Martina Luysberg and Lothar Houben received, as co-authors of the winning publications in the category “Materials Sciences”, an Outstanding Paper Award 2014 for the paper “Polarity-Driven Polytypic Branching in Cu-Based Quaternary Chalcogenide Nanostructures” by R. R. Zamani, M. Ibanez, M. Luysberg, N. Garcia-Castello, L. Houben, J. D. Prades, V. Grillo, R. E. Dunin-Borkowski, J. Ramon Morante, A. Cabot, und J. Arbiol (ACS Nano 8 (2014) 2290–2301 (2014)) The panel gave the following reason for their decision: “Zamani and co-workers have employed a sophisticated combination of aberration corrected STEM imaging, image simulation and ab-initio modelling to understand the role of polarity in the growth mechanism of Cu-based chalcogenide nano structures.”

In the category “Life Sciences”, the winning paper was entitled “Cryo-scanning transmission electron tomography of vitrified cells” by S Grayer Wolf, L Houben and M Elbaum (Nature Methods 11 (2014) 423-429 (2014)). The panel based their decision on the following: “Wolf and co-workers have convincingly demonstrated that STEM has the potential to produce tomograms from unstained relatively thick cryo-sectional samples. These tomograms are shown to be less hampered by multiple scattering effects and chromatic aberration than tomograms recorded using TEM.”

The publications were a result of the scientists´ expertise and the use of the electron microscopes at the ER-C. The first authors will each receive prize money of €1000. The award ceremony took place during the Microscience Microscopy Congress 2015 in Manchester.

Awards for young scientists from JARA-FIT

Nils von den Driesch, Ph.D. student at the Peter Grünberg Institute-9: Semiconductor Nanoelectronics has won the “Best Student Paper Award” at the 9th International Conference on Silicon Epitaxy and Heterostructures (ICSI-9), held in Montréal (Canada) between 18-22 May 2015. He received the ICSI-9 Award for his presentation “Thick GeSn alloys for mid IR lasing applications”, discussing the epitaxial growth and characterization of direct bandgap GeSn alloys, which offer the possibility of creating efficient Group IV light emitters. The ICSI, held in biennial succession, brings together scientists and engineers from both academia and industry to discuss about latest developments in physics, device technologies and instrumentation of Si-based epitaxy, heterostructures, nanostructures, and quantum systems.

Gia Vinh Luong, doctoral student from the same institute, has won the "Best Paper Award" for his contribution at the international conference "Ultimate Integration of Silicon 2014" (ULIS 2014) in Stockholm. In his conference paper "High On-currents with Highly Strained Si Nanowire MOSFETs" he presented the improved current level in silicon nanowire MOSFETs by using high tensile strain in the

nanowires. The research was partially supported by the EU-Project E2SWITCH and the BMBF Project “UltraLowPow”. The ULIS conference provides a public forum for the presentation and discussion of current research topics in the field of semiconductor technology. The topics encompass silicon CMOS technology, new transistor concepts and new materials, sensors, circuit design, simulation and characterization methods..

Bernd Zimmermann, working at the division for Quantum Theory of Materials at the Peter Grünberg Institute and the Institute for Advanced Simulation, was the recipient of the "ThyssenKrupp Electrical Steel Dissertation Prize 2015". The prize, endowed with €1000, is awarded by the Magnetism Work Group (AGM) of the German Physical Society (DPG) for outstanding scientific research undertaken within the framework of a doctoral thesis as well as for its excellent written and oral presentation. He received the award for his PhD thesis entitled "Ab initio description of transverse transport due to impurity scattering in transition metals". The award ceremony took place on 16 March 2015 at the spring meeting of the DPG in Berlin.

PICO 2015: Third Conference on Frontiers of Aberration Corrected Electron Microscopy

PICO 2015, the third Conference on Frontiers of Aberration Corrected Electron Microscopy, took place at Kasteel Vaalsbroek between the 19. and 23. April 2015. The meeting was attended by more than 150 delegates including company representatives and a good number of international colleagues. Organisers put together an oral programme of 44 scientific keynote lectures. About the same number of contributions were scheduled for poster presentations. The event, which was organised by the Ernst Ruska-Centre, was supported by the German Research Foundation, FEI Company, JEOL Ltd, CEOS GmbH, Nion Inc, DENSsolutions, Hitachi Inc, Gatan GmbH, EA Fischione Instruments, and HREM Research Inc. The scientific programme of PICO 2015 contained a wide range of oral and poster presentations focusing on recent advances in methods and applications for the study of structural and electronic properties of solids by the application of advanced electron microscopy techniques. Topical issues of aberration corrected electron microscopy research were highlighted in keynote presentations given by leading invited experts. One of the highlights of the meeting was a symposium held to honour the scientific careers of Harald Rose, a close collaborator of JARA-Senior Professor Knut Urban and the ER-C, on the occasion of his 80th birthday in 2015. Conference proceedings have been published in a special issue of Ultramicroscopy (Volume 151, 2015).

VITI Spinograph School in Aachen

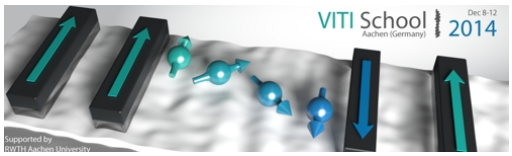

The Virtual Institute for Topological Insulators is a joint endeavour of the Forschungszentrum Jülich and the RWTH Aachen University together with Würzburg University and the Chinese Academy of Sciences, Shanghai (SIMIT). In collaboration with the EU network "Spinograph" a VITI School on spin transport in 2-dimensional systems was held on 12th of December 2014 in Aachen. During the school different subjects related to tranport in topological insulators and graphene were addressed. Beside speakers from VITI and the Spinograph network a number of external lecturers were invited.

Autumn School on Correlated Electrons: DMFT at 25: Infinite Dimensions

The year 2014 marks the 25. anniversary of the discovery that the many-body problem drastically simplifies in the limit of infinite dimensionality. This forms the basis of the dynamical mean-field theory, which nowadays is the state of the art for treating systems with strong electronic correlations. To celebrate this breakthrough, the 2014 Autumn School on Correlated Electrons brought the protagonists of this development to Jülich, some of the pioneers of the field for the first time. In the week from 15 to 19 September 2014, they lectured on the past, present, and future of the realistic modeling of materials with strong correlations. 100 young researchers from all over the world were excited to learn first-hand about the modern methods, their development, use, and extensions. The school was organised by by JARA-FIT member Eva Pavarini together with Erik Koch from the German Research School for Simulation Sciences (GRS), Dieter Vollhardt from the University of Augsburg, and Alexander Lichtenstein from the University of Hamburg. Participants came from 25 countries, which, in addition to Germany and countries in the EU, included the USA, Canada, Colombia, Brazil, Argentina, Russia, Japan, China, India, Morocco, Algeria, Ethiopia, and Nigeria. Ten of the international participants received Travel Awards from the Institute for Complex Adaptive Matter (ICAM). The speakers and many European students were supported by the DFG Research Unit 1346 "Dynamical Mean-Field Approach with Predictive Power for Strongly Correlated Materials". Comprehensive lecture notes were printed as a book and is distributed through the Verlag des Forschungszentrum Jülich (ISBN 978-3-89336-953-9). Moreover, in order to be as widely accessible as possible, the book has been made available via open access.

JARA-FIT Lab Course Nanoelectronics

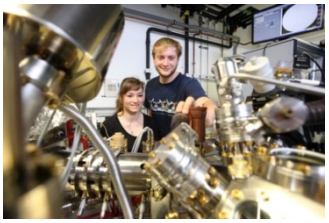

This year, 38 students participated in our one week 10th JARA-FIT Lab Course Nanoelectronics. Addressees were master students of physics, electrical engineering, chemistry, and materials science. The idea of the Nanoelectronics lab course is to bring students into contact as early as possible with real top-level research equipment used by Jülich JARA-FIT scientists. The Lab Course introduced the students also to current research topics of JARA-FIT. The students received introductory lectures, performed one experiment per day in small groups, and were able to discuss scientific issues as well as carrier issues with their JARA-FIT supervisors. The students came from Aachen as part of their master courses, and additionally several students came from all over Germany.

JARA-FIT Science Days 2014

The JARA-FIT Science Days serve the purpose of providing a forum for intense scientific exchange among JARA-FIT scientists and initiation of new interdisciplinary projects. Participants are PhD students, PostDocs and scientists from RWTH Aachen University and Forschungszentrum Jülich. The Science Days in 2014 brought 100 scientists together for two days, on 7. and 8. November 2014, in a retreat in Schleiden, a small town in the Eifel mountains close to Aachen and Jülich. The two days were filled with tutorial lectures, presentations and a poster session.

During the Science Days the participants elected poster prizes to:

- Rebecca Liffmann for her work on "Nanoelectronic Devices based upon stable Janus-Gold-Nanoparticles (JARA FIT Seed Fund)"
- Tymofiy Khodkov for his work „Low temperature compatible electrostatic comb-drive actuators with integrated graphene"
- Christian Rodenbücher for his work "Resistive switching in Nb:$SrTiO_3$ single crystals", and
- Christian Schulte-Braucks for his work on „Towards Energy Efficient Nanoelectronics with Nanowire Tunnel FETs".

Outreach publication of RWTH Aachen University highlighting JARA

The RWTH Aachen University highlights the JARA-cooperation in its latest outreach publication, the "RWTH THEMEN" (2/2014). The publication addresses the general public and is widely distributed. It includes topical contributions from each JARA-section. In the case of JARA-FIT the publication focusses on Nanoswitches and Graphene.

We congratulate …

…the former JARA-FIT member Alexander Böker, Chairman of the Department for Macromolecular Materials and Surfaces at RWTH Aachen University and Deputy Scientific Director of the DWI-Leibnitz Institute for Interactive Materials, on his new position as head of a Fraunhofer institute. He left Aachen beginning 2015 to take over this position at the Fraunhofer-Institute for Applied Polymer Research IAP in Potsdam-Golm.

JARA-FIT Seed Fund projects

Within the Excellence Initiative JARA provides Seed Funds with the incentive to have new ideas developed to the point where they can attract subsequent third-party funding. As a measure to further strengthen the scientific collaborations between Aachen and Jülich within JARA-FIT, calls for Seed Fund projects have been launched for the period 2013/2014/2015. The topics of the projects should be new, creative and can be of high risk. They should not already be addressed by national or international publicly funding programs. The following projects have been selected as a result of the evaluation process within JARA-FIT.

Call 2013/1014

1. **Stabile Janus-Gold-Nanopartikel basierte Bauelemente für die Nanoelektronik**
   Melanie Homberger, Institut für Anorganische Chemie, RWTH Aachen University
   Silvia Karthäuser, Peter Grünberg Institut-7, Forschungszentrum Jülich
2. **Large-scale density functional theory study of localization of donor electrons in phosphorus-doped silicon**
   Riccardo Mazzarello, Institut für Theoretische Festkörperphysik, RWTH Aachen University
3. **Adiabatic demagnetization cooling with (and of) molecular magnets**
   Ruslan Temirov, Peter Grünberg Institut-3, Forschungszentrum Jülich
   Paul Kögerler, Institut für Anorganische Chemie, RWTH Aachen University
   Raphael Herrmann, Peter Grünberg Institut-4 / Jülich Center of Neutron Science, Forschungszentrum Jülich
4. **Zweidimensionale Gradienten von Nanopartikel assoziierten Zelladhäsionsliganden für den in-vitro Aufbau von gerichteten Neuronennetzwerke**
   Ulrich Simon, Institut für Anorganische Chemie, RWTH Aachen University
   Dirk Mayer, Peter Grünberg Institut-8, Forschungszentrum Jülich
5. **Carbon-based conductors as readout for qubits made of spin-crossover allogon complexes**
   Claire Besson, Institut für Anorganische Chemie, RWTH Aachen University
   Carola Meyer, Peter Grünberg Institut-6, Forschungszentrum Jülich
   Christoph Stampfer, II. Physikalisches Institut B, RWTH Aachen University
6. **Magneto-Optical Nanoscale Laboratory Imaging for Spintronic Applications**
   Larissa Juschkin, Lehr- und Forschungsgebiet Experimentalphysik des Extrem-Ultravioletts der RWTH Aachen University
   Roman Adam, Peter Grünberg Institut-6, Forschungszentrum Jülich
7. **Toward III-V Heterostructure Band-to-Band Tunnel FETs**
   Joachim Knoch, Institut für Halbleitertechnik, RWTH Aachen University
   Detlev Grützmacher und Dr. Mihail Ion Lepsa, Peter Grünberg Institut-9, Forschungszentrum Jülich

Call 2014/1015

8. **Self-assembled QDs for optical read out of spin qubits**
   Beata Kardynal, Peter Grünberg Institut-9, Forschungszentrum Jülich
   Hendrik Bluhm, II. Institut für Physik, RWTH Aachen University
9. **Topological solitons in chiral magnetism**
   Christof Melcher, Lehrstuhl I für Mathematik, RWTH Aachen University
   Yuriy Mokrousov and Stefan Blügel, Peter Grünberg Institut-1/Institute for Advanced Simulation-1, Forschungszentrum Jülich
10. **Laboratory-based element-selective photoemission spectro-microscopy with a new plasma-based light source in the extreme ultraviolet**
    Larissa Juschkin, Experimentalphysik des Extrem-Ultravioletts, RWTH Aachen University
    Carsten Wiemann, Peter Grünberg Institut-6, Forschungszentrum Jülich
    F. Stefan Tautz, Peter Grünberg Institut-3, Forschungszentrum Jülich
11. **Studying the Influence of surface passivation on the charge carrier distribution of electrically contacted InAs-Nanowires with Infrared SNOM**
    Thomas Taubner, I. Physikalisches Institut, RWTH Aachen University
    Hilde Hardtdegen and Thomas Schäpers, Peter Grünberg Institut-9, Forschungszentrum Jülich
12. **Defects in graphene quantum dots**
    Riccardo Mazzarello, Manuel J. Schmidt, and Carsten Honerkamp, Institut für Theoretische Festkörperphysik, RWTH Aachen University
    Christoph Stampfer, II. Physikalisches Institut B, RWTH Aachen University/Peter Grünberg Institut-9, Forschungszentrum Jülich
13. **Electronic Modification of Polyoxovanadate Single Molecules from the Perspective of Future Redox-Based Memory Devices**
    Kirill Monakhov, Institut für Anorganische Chemie, RWTH Aachen University
    Marco Moors, Peter Grünberg Institut-7, Forschungszentrum Jülich

General Information

JARA-FIT Members

Prof. Dr. St. Appelt, Lehrstuhl für Technische und Makromolekulare Chemie,
Lehr- und Forschungsgebiet Niederfeld-NMR (Methoden der NMR),
RWTH Aachen University
Zentralinstitut für Engineering, Elektronik und Analytik - Systeme der Elektronik,
Forschungszentrum Jülich

Prof. Dr. H. Bluhm, II. Physikalisches Institut – Quantum Technology Group, RWTH Aachen University

Prof. Dr. S. Blügel, Peter Grünberg Institut/Institute for Advanced Simulation – Quanten-Theorie der Materialien, Forschungszentrum Jülich

Prof. Dr. T. Brückel, Peter Grünberg Institut/Jülich Centre for Neutron Science – Streumethoden, Forschungszentrum Jülich

Prof. Dr. A. Böker, Makromolekulare Materialien und Oberflächen, DWI – Leibniz Institute for Interactive Materials, Aachen *(till end of 2014)*

Prof. Dr. D. P. DiVincenzo, Institut für Quanteninformation, RWTH Aachen University
Peter Grünberg Institut/Institute for Advanced Simulation – Theoretische Nanoelektronik, Forschungszentrum Jülich

Prof. Dr. R. Dronskowski, Lehrstuhl für Festkörper- und Quantenchemie und Institut für Anorganische Chemie, RWTH Aachen University

Prof. Dr. R. Dunin-Borkowski, Peter Grünberg Institut – Microstrukturforschung, Forschungszentrum Jülich
Ernst Ruska-Centre für Mikroskopie und Spektroskopie mit Elektronen

Prof. Dr. D. Grützmacher, Peter Grünberg Institut – Halbleiter-Nanoelektronik, Forschungszentrum Jülich

Prof. Dr. S. Grün, Institut für Neurowissenschaften und Medizin, Computational and Systems Neuroscience Forschungszentrum Jülich

Prof. Dr. C. Honerkamp, Institut für Theoretische Festkörperphysik, RWTH Aachen University

Prof. Dr. L. Juschkin, Lehr- und Forschungsgebiet Experimentalphysik des Extrem-Ultraviolett, RWTH Aachen University

Prof. Dr. P. Kögerler, Institut für Anorganische Chemie (Molekularer Magnetismus), RWTH Aachen University
Peter Grünberg Institut – Elektronische Eigenschaften, Forschungszentrum Jülich

Prof. Dr. U. Klemradt, II. Physikalisches Institut B, RWTH Aachen University

Prof. Dr. J. Knoch, Institut für Halbleitertechnik, RWTH Aachen University

Prof. Dr. P. Loosen, Lehrstuhl für Technologie Optischer Systeme, RWTH Aachen University
Fraunhofer-Institut für Lasertechnik, Aachen

Prof. Dr. S. Mantl, Peter Grünberg Institut – Halbleiter-Nanoelektronik, Forschungszentrum Jülich

Prof. Dr. M. Martin, Institut für Physikalische Chemie, RWTH Aachen University

Prof. Dr. J. Mayer, Gemeinschaftslabor für Elektronenmikroskopie, RWTH Aachen University
Ernst Ruska-Centre für Mikroskopie und Spektroskopie mit Elektronen

Prof. Dr. R. Mazzarello, Institut für Theoretische Festkörperphysik, RWTH Aachen University

Prof. Dr. V. Meden, Institut für Theorie der Statistischen Physik, RWTH Aachen University

Prof. Dr. Chr. Melcher, Lehrstuhl I für Mathematik, RWTH Aachen University

Prof. Dr. W. Mokwa, Institut für Werkstoffe der Elektrotechnik 1 – Mikrostrukturintegration, RWTH Aachen University

Prof. Dr. M. Morgenstern, II. Physikalisches Institut B, RWTH Aachen University

Prof. Dr. T. Noll, Lehrstuhl für Allgemeine Elektrotechnik und Datenverarbeitungssysteme, RWTH Aachen University

Prof. Dr. A. Offenhäusser, Peter Grünberg Institut/Institute of Complex Systems – Bioelektronik, Forschungszentrum Jülich

Prof. Dr. E. Pavarini, Peter Grünberg Institut/Institut for Advanced Simulation, Forschungszentrum Jülich

Prof. Dr. R. Poprawe Fraunhofer-Institut für Lasertechnik, Aachen

Prof. Dr. G. Roth, Institut für Kristallographie, RWTH Aachen University

Prof. Dr. H. Schoeller, Institut für Theorie der Statistischen Physik, RWTH Aachen University

Prof. Dr. U. Simon, Institut für Anorganische Chemie, RWTH Aachen University

Prof. Dr. C. Stampfer, II. Physikalisches Institut A, RWTH Aachen University
Peter Grünberg Institut – Halbleiter-Nanoelektronik, Forschungszentrum Jülich

Prof. Dr. C. M. Schneider, Peter Grünberg Institut – Elektronische Eigenschaften, Forschungszentrum Jülich

Prof. Dr. T. Taubner, I. Physikalisches Institut A, RWTH Aachen University

Prof. Dr. S. Tautz, Peter Grünberg Institut – Funktionale Nanostrukturen an Oberflächen, Forschungszentrum Jülich

Prof. Dr. B.M. Terhal, Institut für Quanteninformation, RWTH Aachen University

Prof. Dr. A. Vescan, Lehr- und Forschungsgebiet GaN-Bauelementtechnologie, RWTH Aachen University

Prof. Dr. R. Waser, Institut für Werkstoffe der Elektrotechnik 2, RWTH Aachen University
Peter Grünberg Institut – Elektronische Materialien, Forschungszentrum Jülich

Prof. Dr. M. Wegewijs, Peter Grünberg Institut – Theoretische Nanoelektronik, Forschungszentrum Jülich

Prof. Dr. S. Wessel, Institut für Theoretische Festkörperphysik, RWTH Aachen University

Prof. Dr. J. Witzens, Institut für Integrierte Photonik, RWTH Aachen University

Prof. Dr. M. Wuttig, I. Physikalisches Institut A, RWTH Aachen University

JARA-FIT Institutes

Zentralinstitut für Engineering, Elektronik und Analytik: Systeme der Elektronik (ZEA-2), Forschungszentrum Jülich & Institut für Technische und Makromolekulare Chemie (ITMC), RWTH Aachen University

St. Appelt

Our research revolves around spin order generation, the manipulation, measurement and transfer of spin order by combining Hyperpolarization technology with Nuclear Magnetic Resonance (NMR) spectroscopy. Starting from states with high spin orders, like nuclear singlet states or highly premagnetized (hyperpolarized) spin systems, we investigate the field dependancy of the complexity, and thus information content, of corresponding NMR spectra in very low magnetic fields. Our research includes chemical synthesis as a means for substrate generation and optimization of spin order transfer, the development and construction of new hardware for mobile NMR spectroscopy as well as the investigation of the underlying quantum mechanical principles of coupled spins in low magnetic fields.

Peter Grünberg Institut / Institute for Advanced Simulation – Quantum Theory of Materials, Forschungszentrum Jülich

S. Blügel

The analysis and computation of electronic properties of solid-state systems relevant for basic science and practical applications in collaboration with experimentalists are the hallmark of our research. An important asset of our institute is the competence in developing conceptual and computational methods (density functional theory, many-body perturbation theory and beyond, topology). Emphasis is on the investigation of complex magnetism, magnetism in reduced dimensions, oxide interfaces and heterostructures, oxides with large defects, topological matter, graphene, organic molecules in contact with metallic and insulating substrates, spin- and spin-orbit-dependent electronic transport phenomena, collective excitations and quasi-particles, and high-performance computing. A second research theme is nano-scale tribology, friction, adhesion, plastic deformation. Computational materials science research is established by combining first-principles results with macroscopic methods (molecular and spin-dynamics, Monte Carlo).

II. Physikalisches Institut, Quantum Technology Group, RWTH Aachen University

H. Bluhm

The research group is aiming to realize highly coherent two-level quantum systems in semiconductor quantum dots for quantum information processing. The group studies the physics governing these devices and pushes forward their technological development. Key topics include high fidelity control, decoherence measurements and multi-qubit circuits. In addition, the group is pursuing scanning SQUID microscopy at ultra-low temperatures for magnetic imaging and ultra-sensitive magnetic measurements on mesoscopic structures.

Lehrstuhl für Makromolekulare Materialien und Oberflächen (Physikalische Chemie) & DWI – Leibniz Institute for Interactive Materials

A. Böker

The chair of Macromolecular Materials and Surfaces is part of the DWI – Leibniz Institute for Interactive Materials. The DWI is associated with RWTH Aachen University via a cooperation agreement focusing on polymer / soft matter materials development with the mission of novel and active properties. Under the heading “Science for Innovation” we aim at a tailor-made surface functionality of soft materials, especially fibers, films, membranes, textiles, and biomaterials. Beyond knowledge-oriented, basic approaches, work at DWI is dedicated to the translation and implementation of this knowledge into application-oriented concepts for functional films and surfaces, antimicrobial polymers and surfaces, encapsulation and release, functional membranes, and biomedical devices. The major research topics at the chair of Macromolecular Materials and Surfaces include bioconjugate polymer materials, nanoparticle composites and guided self-assembly.

Peter Grünberg Institut / Jülich Centre for Neutron Science - Streumethoden, Forschungszentrum Jülich

Th. Brückel

At the Institute of Scattering Methods, we focus on the investigation of structural and magnetic order, fluctuations and excitations in complex or nanostructured magnetic systems and highly correlated electron systems. Our research is directed at obtaining a microscopic atomic understanding based on fundamental interaction mechanisms. The aim is to relate this microscopic information to macroscopic physical properties. To achieve this ambitious goal, we employ the most advanced synchrotron X-ray and neutron scattering methods and place great emphasis on the complementary use of these two probes. Some of our efforts are devoted to dedicated sample preparation and characterization from thin films and multilayers via nano-patterned structures to single crystals for a wide range of materials from metals to oxides.

Peter Grünberg Institut / Institut for Advanced Simulation – Theoretische Nanoelektronik, Forschungszentrum Jülich

D. P. DiVincenzo, group leaders G. Catelani, T. Costi, E. Pavarini, M. Wegewijs

The behavior of interacting electrons in nano-scale structures is a primarly focus. The Kondo effect, involving the interaction of an isolated spin impurity with conduction electrons, or the formation and transport of high-spin complexes forming spin quadripoles, are particular areas of expertise. Novel computational techniques permit accurate calculations with thousands of atoms, and in complex multi-functional perovskites. Correlated electrons also form the basis of the physical creation of qubits, and the coherence and dynamics of such qubits, and mutiqubit systems, is being investigated.

Institute for Quantum Information, RWTH Aachen University

D. P. DiVincenzo, group leaders B. M. Terhal, F. Hassler, and N. Schuch

The institute has a broad agenda of topics in the theory of quantum information. New principles for the implementation of quantum computation in noisy systems, particularly Fermionic many-body systems. This includes particularly the investigation of Majorana qubits realized in semiconductor nanowires. Protocols for fault tolerance in quantum computation are investigated. New applications of the theory of quantum entanglement for efficient classical simulations are developed. Detailed modeling of hardware for superconducting qubits and circuit-quantum electrodynamic structures is underway, in close collaboration with experiment.

Lehrstuhl für Festkörper- und Quantenchemie und Institut für Anorganische Chemie, RWTH Aachen University

R. Dronskowski

The institute is specialized in the fields of synthetic and quantum-theoretical solid-state chemistry, bordering with materials science, solid-state and theoretical physics, crystallography, as well as quantum and computational chemistry. In detail, we synthesize novel, sometimes extremely sensitive, compounds and elucidate their compositions and crystal structures by means of X-ray and neutron diffractional techniques. The characterization of their physical properties, that is electronic transport and magnetism, also plays a very important role.
We regularly perform solid-state quantum-chemical calculations from first principles to yield the electronic (band) structures and, in particular, to extract the important chemical bonding information needed to thoroughly understand the interplay between chemistry and physics. Syntheses are theory-driven and experiments challenge theories.

Peter Grünberg Institut – Mikrostrukturforschung, Forschungszentrum Jülich & Ernst Ruska-Centre for Microscopy and Spectroscopy with Electrons

R. E. Dunin-Borkowski

The institute works on topical fields in solid state physics. Strategically, two directions are followed: first, to make key contributions to the development and application of ultra-high-resolution transmission electron microscopy, in particular to aberration-corrected electron optics for sub-Ångstrom structural and spectroscopic resolution and, second, to produce a number of selected material systems and to study their physical properties. Examples of materials systems that are studied are high temperature

superconductors and novel complex metallic alloys. The high temperature superconductors provide the basis for the institute's work on SQuID sensors and Hilbert spectroscopy. The head of the institute is co-director of the Ernst Ruska-Centre for Microscopy and Spectroscopy with Electrons.

Institute of Neuroscience and Medicine - Computational and Systems Neuroscience (INM-6) and Institute for Advanced Simulation – Theoretical Neuroscience (IAS-6)

S. Grün together with M. Diesmann, A. Morrison and M. Helias

The institute is specialized in the integration of experimental data on the structure and the dynamics of the brain into mathematical models and in overcoming bottlenecks in simulation technology and workflows. The group “Statistical Neuroscience” led by Sonja Grün focuses on the development and application of methods to analyze multi-channel activity data in close contact to experimental groups. A focus is the connection between neural data recorded on different temporal and spatial scales and on the structure of correlations of spiking activity. The group “Computational Neurophysics” headed by Markus Diesmann focuses on bottom-up approaches in order to integrate physiological and anatomical data into models, in particular model development, theory of neuronal networks, and correlation dynamics. This also requires the development of simulation technology for neural networks. The group “Functional Neural Circuits” led by Abigail Morrison investigates mechanisms underlying neural computation through the development of models on the level of networks of spiking neurons. It applies a predominantly top-down approach to discover functional constraints on structure, plasticity and dynamics, particularly with respect to learning and memory. The secondary focus is on simulation technology for high-performance computers. Moritz Helias’ group “Theory of multi-scale neuronal networks” focuses on the investigation of mechanisms shaping the correlated and oscillatory activity in neuronal networks with structured connectivity on several spatial scales. This requires the development of quantitative theoretical descriptions, adapted from statistical physics, combined with direct simulations of neuronal networks at cellular resolution.

Peter Grünberg Institut – Halbleiter-Nanoelektronik, Forschungszentrum Jülich

D. Grützmacher

The institute’s research activities are based on its competence in semiconductor heterostructure and nanostructure research, both in fundamental and device physics as well as in material and process development. They address three major fields. (1) Si-CMOS technology: novel materials and new device concepts are used to drive CMOS to its limits. (2) III-V and III-nitride semiconductors: high frequency devices are developed up to and into the terahertz range. (3) Nanostructures for quantum electronics: devices based on the tunneling effect and ferromagnetic/semiconductor hybrid structures are investigated, the latter particularly in view of spintronic applications.

Institut für Theoretische Festkörperphysik, RWTH Aachen University

C. Honerkamp, R. Mazzarello, M. Schmidt, S. Wessel

The research groups in this institute study many-particle interactions in solids, ranging from quantum effects in magnetic systems over electron correlation effects leading to unconventional superconductivity and magnetism to the dynamics of structural phase transitions. Recent work has focused on interaction effects in graphene systems, topological insulators, pnictide high-temperature superconductors and chalcogenide phase-change materials. The powerful theoretical methods employed and developed here comprise quantum Monte Carlo techniques, the functional renormalization group, density-functional theory and molecular dynamics.

Lehr- und Forschungsgebiet Experimentalphysik des Extrem-Ultravioletts, RWTH Aachen University

L. Juschkin

The research in the field of extreme ultraviolet (EUV) radiation is a major contribution for nanoelectronics and future developments in information technology. At the Chair for Experimental Physics of EUV different aspects related to the EUV radiation are investigated ranging from generation and characterization of EUV, to wave propagation and light-matter interaction as well as developing new methods and applications. In combination of EUV interference lithography and the self-organized growth of nanostructures novel materials are prepared, and their properties are analyzed. Moreover, in cooperation with the Fraunhofer Institute for Laser Technology in Aachen different concepts of EUV sources are investigated. On the application side, a series of measurement procedures for which the specific features of EUV radiation can be used, for example, the EUV microscopy and spectroscopic reflectometry, are investigated.

II. Physikalisches Institut (IIB) – Röntgenstreuung und Phasenumwandlungen, RWTH Aachen University

U. Klemradt

Our research is centered at the investigation of nanoscale structures and fluctuations, with focus on nanoparticles, polymer-based nanocomposites and ferroic materials. Of particular interest are phase transitions in smart materials like shape memory alloys. The main experimental tools are X-ray scattering and acoustic emission spectroscopy. We use both laboratory tubes and international synchrotron facilities for X-ray experiments. Core techniques are small angle X-ray scattering (SAXS), grazing incidence scattering (GISAXS and reflectometry), and photon correlation spectroscopy using coherent X-rays (XPCS).

Institut für Halbleitertechnik, RWTH Aachen University

J. Knoch

The institute carries out research on semiconductor technology and device with a special focus on low power and energy harvesting technologies with the long-term vision of energy autonomous systems. To be specific, we work on nanoelectronics transistor devices based on Si- and III-V nanowires as well as on carbon nanotubes and graphene particularly aiming at a realization of so-called steep slope switches that enable a significant reduction of the power consumption of highly integrated circuits. In addition, the institute has broad experience in the science and engineering of Si wafer-based solar cells and also performs research on Si-based third generation photovoltaic cells. A combination of our know-how in micro- and nanotechnology with the solar cell technology is used to investigate and realize novel concepts for energy harvesting and storage based e.g. on efficient direct solar water splitting.

Institut für Anorganische Chemie – Molekularer Magnetismus, RWTH Aachen & Peter Grünberg Institut – Elektronische Eigenschaften (Molekularer Magnetismus), Forschungszentrum Jülich

P. Kögerler

The Molecular Magnetism Group focuses on the chemistry and fundamental physics of discrete and networked magnetically functionalized inorganic molecules. Based on its experience with the control and understanding of magnetic characteristics of purely molecular origin, the group synthesizes magnetic materials based on transition metal clusters that exhibit a complex interplay of charge transport and static/ dynamic magnetic properties such as phase transitions, hysteresis, or quantum tunneling. To functionally combine magnetic state switching and charge transport in systems for FIT spintronic devices, the molecule-surface interface is addressed, in particular employing surface structure-directed coupling reactions to molecular aggregates, single-stranded molecular conductors, or 2D networks.

Lehrstuhl für Technologie Optischer Systeme, RWTH Aachen (RWTH-TOS) & Fraunhofer-Institut für Lasertechnik, Aachen

P. Loosen

Extreme ultraviolet radiation (XUV, 1-50 nm, or EUV at 13.5 nm) enables new optical, analytical and manufacturing technologies because of its characteristic interaction with matter, its short wavelength and recent progress on light sources and optical components (e.g. EUV lithography). XUV tools are already deployed by the semiconductor industry, which significantly pushes the further development of XUV technology. Future applications which will support scientific progress in a variety of fields such as nanoelectronics or biotechnology are also within the scope of our research. Activities include structuring on a nanometer scale using interference lithography, XUV microscopy for imaging of dynamic processes or at-wavelength inspection of multilayer mask-blanks for hidden defects, and characterization of thin film coated surfaces using grazing-incidence reflectometry.

Institut für Physikalische Chemie (IPC), RWTH Aachen University

M. Martin

The institute's research activities are based on its competence in the physical chemistry of solids with a special emphasis on defects and diffusion in inorganic solids, in particular oxides. Within JARA-FIT two major fields are addressed. (1) Ionic transport: transport of oxygen ions in the bulk, across and along grain

boundaries and in space charge zones is investigated by means of secondary ion mass spectrometry (SIMS), density functional theory and Monte Carlo simulations. (2) Electronic transport: amorphous and highly non-stoichiometric oxides are investigated concerning correlations between structure, electrical conductivity, and electronic structure with a view to applications in resistive switching.

GFE – Gemeinschaftslabor für Elektronenmikroskopie & Ernst Ruska-Centre for Microscopy and Spectroscopy with Electrons

J. Mayer

GFE is a central facility of RWTH Aachen University and has state-of-the-art equipment in the fields of transmission electron microscopy, scanning electron microscopy, electron microprobe analysis, focused ion beam instruments and atomic force microscopy. GFE provides services for a large number of institutes from RWTH Aachen University and a broad range of industrial companies. In the field of information technology, GFE participates in research projects on nonvolatile memories and on nanoscale CMOS devices. The head of the GFE is co-director of the Ernst Ruska-Centre for Microscopy and Spectroscopy with Electrons and coordinates the RWTH user activities and contribution to the Centre.

Institut für Theorie der Statistischen Physik, RWTH Aachen University

V. Meden, H. Schoeller, M. Wegewijs

The members of the institute are investigating the spectral and transport properties of low-dimensional quantum systems in contact with heat and particle reservoirs. The research focuses on the development of many-body methods for strongly correlated mesoscopic systems in nonequilibrium (quantum field theory and renormalization group in nonequilibrium) as well as on the application to experimentally realizable physical systems like semiconductor quantum dots, quantum wires (e.g. carbon nanotubes), and molecular systems.

Lehrstuhl I für Mathematik, RWTH Aachen University

Ch. Melcher

The research at our institute has a focus on nonlinear partial differential equations from mathematical physics and materials science. We are particularly interested in the emergence and dynamics of patterns and topological solitons in models from micromagnetics and Ginzburg-Landau theory. Using tools from functional and multiscale analysis, our aim is to capture the qualitative behavior of solutions to such complex theories and, if possible, to identify simpler models, whose behavior is easier to understand or simulate.

Institute of Materials in Electrical Engineering I, RWTH Aachen University

W. Mokwa

The institute´s research activities are focused on the development of micro systems for medical and life science applications. Main activities lie on coupling of biological systems to technical systems, development of "intelligent" implants and prostheses and micro fluidic systems for biotechnology and medical diagnostics. For the development of these systems silicon and thin film technologies, silicon micromechanics, micro electroplating, soft lithography as well as sophisticated packaging technologies are used in a clean room of about 600 m^2.

II. Physikalisches Institut (IIB) – Rastersondenmethoden, RWTH Aachen University

M. Morgenstern

The research group develops scanning probe methods working in particular at low temperatures down to 0.3 K and in high magnetic fields up to 14 T in order to investigate the electronic structure of interacting electron systems and systems relevant for nanoelectronic applications. Thereby, we exploit the advantage of mapping the electronic structure down to the atomic scale at an energy resolution down to 0.1 meV, but also use the scanning probes for the excitement of the systems under study, which is probed with ps time resolution. Current topics of interest are topological insulators and Majorana fermions, electronic and mechanic properties of graphene, quantum Hall physics in graphene and III-V-materials, confined wave functions in quantum dots, nanomagnetic systems, and phase change materials.

Chair of Electrical Engineering and Computer Systems, RWTH Aachen University

T. Noll

The group is conducting research on architectural strategies, circuit concepts and design methodologies for highly integrated circuits in nano-scale CMOS as well as potential post-CMOS technologies. The focus is on circuits for applications of high-throughput digital signal processing and special emphasis is placed on the issues of reliability and energy-efficiency.

Peter Grünberg Institut / Institute of Complex Systems – Bioelektronik, Forschungszentrum Jülich

A. Offenhäusser

Our research aims for the application of micro- and nanoelectronics to brain and life sciences. Research activities focus on two main topics: electromagnetic sensing and bioelectronic hybrid systems. This requires a better understanding of the interactions between biological systems and electronic substrates and the development of new technologies, resulting in new concepts of the interconnection of biological matter to electronic probes, and novel approaches to study cellular functions at the micro- and nanoscale. Here, we aim at a better understanding of the physiological behavior and mechanisms of neuronal information processing and new tools for diagnostics and imaging.

Institute of Crystallography, RWTH Aachen University

G. Roth

The institute's research profile covers the topics synthesis, structure and properties of novel materials. The synthetic activities include the preparation of new or crystal-chemically modified compounds with interesting properties in bulk poly- or single-crystalline form. Crystal and magnetic structures are studied by powder and single crystal X-ray as well as neutron diffraction methods (outstation at FRM-II/Garching) with special emphasis on complex, defect dominated systems such as partially disordered, incommensurately modulated structures and composite crystals. Among the materials recently studied are superconductors (modulated CaAlSi), fullerenes (C70 high pressure polymer), spin-chain-compounds (vanadates and cuprates) and pyroxene-type multiferroics.

II. Physikalisches Institut (IIA), RWTH Aachen University

C. Stampfer

Our research activities are focused on (i) carbon-based quantum electronics, (ii) semiconductor-based spin-electronics, and on (iii) topological insulators. For instance, we focus on studying electronic and mechanical properties of carbon and Bi_2Se_3-based systems that have critical dimensions on the nanometer scale. Such structures approach the atomic scale and the ultimate limit of solid state miniaturization. In particular we investigate systems based on nanostructured graphene (a monoatomic sheet of graphite) and carbon nanotubes. Current interests include (i) developing advanced processing technologies for fabricating novel nanodevices, (ii) understanding new and interesting transport phenomena that arise in these devices, and (iii) learning how to control and detect the charge, spin and mechanical degrees of freedom in these systems. Potential applications include ultra-fast electronics, new spin-based nanoelectronic device concepts and applied quantum technology.

Peter Grünberg Institut – Elektronische Eigenschaften, Forschungszentrum Jülich

C. M. Schneider

The institute is engaged in the study of electronic and magnetic phenomena in novel materials and is one of the birthplaces of magnetoelectronics. Present research concentrates on the fundamental aspects, properties, and control of spin-transfer processes. The activities cover several facets, e.g., the development of new magnetic materials or the engineering of interfaces to improve the spin injection efficiency. Further important research fields comprise nanomagnetism and nanospintronics, which may form a bridge to quantum information processing. To this end new techniques and procedures are being established. Spintronics is also firmly linked to the condensed matter program, providing access to and knowledge about new material classes for use in the spintronics activities of the present program.

Institut für Anorganische Chemie (IAC), RWTH Aachen University

U. Simon

Our research is devoted to functional metal and metal oxide nanostructures. One focus is the wet chemical tailoring and the characterization of ligand stabilized metal nanoparticles of different geometries, i.e. nanospheres, nanorods and hollow nanospheres, as well as distinct nanoparticle assemblies. On the one hand these nanostructures are investigated with respect to applications as molecular probes, e.g. in photoaccoustic imaging, or as actuators in biomedicine. On the other hand the utilization as fundamental building blocks in nanoelectronic devices is surveyed. Molecules exhibiting distinct functionalities, e.g. anisotropic conductance, or molecules allowing self-organization, e.g. DNA, leading to precisely controllable nanoparticle superstructures are applied. Our characterization involves conventional techniques as IR, NMR, UV-vis, DLS as well as local probe measuring techniques, and investigations on the properties in biological environments.

A further topic deals with the wet chemical synthesis of metal oxide and higher chalcogenide nanostructures, which are applicable as sensor materials, new electrode materials for batteries or as resistive switching elements. In the latter context chemically-based bottom-up approaches for the fabrication of resistively switching nanostructures are explored and aim at the understanding of the switching and its structural consequences of the resistive switching process by using individual nanoparticles as model systems. Furthermore, self-assembly and surface patterning techniques are applied to produce long range order of nanoparticles on solid supports.

Peter Grünberg Institut – Funktionale Nanostrukturen an Oberflächen, Forschungszentrum Jülich

S. Tautz

Our research tackles fundamental issues in the quest towards functional nanostructures at surfaces, with a particular emphasis on nanoelectronics. Since our focus is placed on molecular materials, an important aspect of our work covers the structural investigations and spectroscopy of complex molecular adsorbates on metal, semiconductor and insulator surfaces. Based on these interface studies, the growth of thin films and nanostructures is investigated. Here, our work is directed towards hybrid materials, comprising both organic and inorganic components. Charge transport, being the most important function in the context of nanoelectronics, transport experiments on single molecules and nanostructures round off our activities. It is a specific asset of our institute that we combine well-established surface techniques with the development of new experimental methods.

Lehr- und Forschungsgebiet GaN-Bauelementtechnologie, RWTH Aachen University

A. Vescan

GaN Device Technology is performing fundamental and application-oriented research on the deposition and characterization of compound and organic semiconductor materials as well as on electronic and optoelectronic devices. Major research goals are the development of energy-efficient devices for power and RF electronics, displays, solid-state lighting and next-generation photovoltaics.The III-nitride activities include investigation and development of practical technological building blocks for (opto-)electronic devices and also address fundamental issues of materials growth and device physics. In the field of organic semiconductors, we focus on deposition technologies like organic vapor phase deposition (OVPD), device processing and the development of advanced OLED structures. A special focus is on hybrid structures and the specific properties of inorganic-organic heterojunctions for photovoltaics.

Institut für Werkstoffe der Elektrotechnik 2, RWTH Aachen & Peter Grünberg Institut - Elektronische Materialien, Forschungszentrum Jülich

R. Waser

We focus on the physics and chemistry of electronic oxides and organic molecules, which are promising for potential memory, logic, and sensor functions. Our research aims at a fundamental understanding of nanoelectronic functions based on electrochemical redox processes, memristive phenomena, space charge effects, and ferroelectricity and at the elucidation of their potential for future device applications. For this purpose, our institute provides a broad spectrum of facilities ranging from dedicated material synthesis, atomically controlled film deposition methods, molecular self-assembly routes, and integration technologies, to the characterization of processes, structures, and electronic properties with atomic resolution.

Institute for Integrated Photonics, RWTH Aachen University

J. Witzens

Integration of photonic components and systems in Silicon allows the realization of complex optical systems at the chip scale. At the Institute for Integrated Photonics we are working on the development of Silicon Photonics devices and systems with activities ranging from material science, core device development to system integration. Current activities focus on the development of cost effective, compact and low power electro-optic transceivers based on semiconductor mode-locked lasers, low power and low drive voltage electro-optic modulators, integrated light sources (on-chip comb generation with parametric conversion, GeSn based light sources), and misalignment tolerant fiber-to-chip and laser-to-chip couplers.

I. Physikalisches Institut (IA), RWTH Aachen University

M. Wuttig

The institute's research activities are focused on the development of novel materials for advanced optoelectronic applications. In particular, materials for optical and electronic data storage have been developed in the last few years. For this class of materials, so-called phase change materials, we have established design rules and an atomistic understanding of essential material properties. This work has enabled novel functionalities of phase change materials in applications as non-volatile memories and is part of the SFB 917 (Nanoswitches). Recently, we could demonstrate that some crystalline phase change materials can possess very high levels of disorder, which gives rise to highly unconventional transport properties. Organic materials are a second focus, where we work on routes to tailor material properties for optoelectronic applications ranging from displays, to solar cells and electronic devices.

Selected Research Reports

Molecular Nanomagnets with Switchable Couplings for Quantum Simulation

E. Pavarini[1,2], A.Chiesa[2,3], G.F.S. Whitehead[4], S. Carretta[3], L. Carthy[4], G. A. Timco[4], S.J. Teat[5], G. Amoretti[3], R. E. P. Winpenny[4], and P. Santini[3]

[1] Peter Grünberg Institut-2, Forschungszentrum Jülich, Germany
[2] Institute for Advanced Simulation-3, Forschungszentrum Jülich, Germany
[3] Dipartimento di Fisica e Scienze della Terra, University of Parma, Italy
[4] School of Chemistry and Photon Science Institute, University of Manchester, UK
[5] Advanced Light Source, Laurence Berkeley Laboratory, California, USA

Molecular nanomagnets are attractive candidate qubits because of their wide inter- and intra-molecular tunability. Uniform magnetic pulses could be exploited to implement one- and two-qubit gates in presence of a properly engineered pattern of interactions, but the synthesis of suitable and potentially scalable supramolecular complexes has proven a very hard task. Indeed, no quantum algorithms have ever been implemented, not even a proof-of-principle two-qubit gate. Here we show that the magnetic couplings in two supramolecular {Cr_7Ni}-Ni-{Cr_7Ni} assemblies can be chemically engineered to fit the above requisites for conditional gates with no need of local control. Microscopic parameters are determined by a recently developed many-body *ab-initio* approach and used to simulate quantum gates. We find that these systems are optimal for proof-of-principle two-qubit experiments and can be exploited as building blocks of scalable architectures for quantum simulation.

In the last few years, there have been great advances in the domain of experimental implementation of quantum information processing. A major objective is the construction of quantum simulators (QSs), yielding massively increased computational power in simulating quantum systems. Envisioned 30 years ago by Richard Feynman, QSs are now attracting considerable interest in many areas of physics. The huge Hilbert space of a general quantum system is encoded and stored efficiently on a QS using the wavefunctions of its qubits, whose dynamics can be controlled so as to mimic the evolution of the target system. Many physical properties can be extracted in polynomial time by operating such a device and by performing measurements according to specific algorithms.

Molecular nanomagnets (MNMs) have been proposed as promising candidates for both spintronics and quantum information processing (QIP). The attractiveness of MNMs stems from their wide tunability, both at the intermolecular and at the intramolecular level. One-qubit operations have already been performed on ensembles, and the observed coherence times are long enough to implement more complex algorithmic sequences. In order to implement such sequences, the most direct way would be to use external magnetic fields varying in time and from qubit to qubit and an external tool to switch on and off the qubit-qubit couplings locally for two-qubit gates. This represents an extremely tough experimental challenge.

A much less demanding approach is to use uniform magnetic fields to induce the required time evolution of the register, by exploiting auxiliary states and the structure of intermolecular interactions. This quantum simulation scheme is based on two classes of MNMs that play two distinct roles: effective $S = 1/2$ spins are used to encode the qubits, whereas interposed complexes with a singlet ground state are used as switches of the effective qubit-qubit interaction. In particular, by an appropriate topology and hierarchy of exchange couplings between different molecular units, it would be possible to use uniform pulses to switch on and off intermolecular interactions, thus implementing two-qubit gates and quantum simulation algorithms. However, the engineering of potentially scalable supramolecular complexes fitting these requisites has proven a very hard chemical task.

Here, we show that new supramolecular assemblies have the correct characteristics to implement one- and two-qubits gates with uniform magnetic fields, i.e., with no need of local control. The magnetic couplings are engineered by coordination chemistry and several variants with different geometry are obtained. These two-qubits units are optimal for proof-of-principle experiments and can be exploited as building blocks of scalable architectures for quantum simulation.

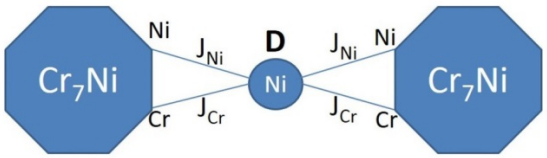

FIG. 1: Scheme of a pair of {Cr_7Ni} rings, linked by a Ni^{2+} ion.

The antiferromagnetically-coupled Cr_7Ni rings behave at low temperature as effective S = 1/2 spins and show long coherence times, and they are therefore excellent candidates for the role of qubits. As a switch we propose a monometallic Ni^{2+} complex, exploiting the axial anisotropy of this S = 1 spin to turn on and off the effective qubit-qubit interaction. A sketch of the here-proposed systems is shown in Fig. 1.

If the Ni ion is frozen in the ground state, the coupling of each ring with the switch merely renormalizes the external magnetic field and single-qubit gates can be implemented. Conversely, two-qubit gates are performed by temporarily bringing the Ni ion to an excited state by a microwave pulse. This scheme requires that the energy of the excited state of the switch is much larger than the qubit-switch coupling. However, this coupling must be large-enough to ensure that the excitation energy of the switch is sufficiently dependent on the state of the qubits to enable conditional dynamics. This requires a chemical engineering of the qubit-switch bond to obtain a suitable hierarchy of the parameters.

Direct physical measurements of ring-Ni exchange interactions are very difficult as variable temperature susceptibility measurements are dominated by the exchange interactions within rings, masking the ring-Ni interaction. Given that our conclusions are grounded on the hierarchy of the different parameters and not on their precise values, we have investigated the possibility of implementing quantum gates by performing an *ab-initio* study of these compounds. We employ the NWChem quantum chemistry code, which is optimized to exploit the power of modern massively parallel supercomputers. These calculations are based on a novel and flexible approach [1] which has already been successfully applied to determine the spin Hamiltonians of three prototype MNMs. Differently from other schemes, such as those based on hybrid functionals or LDA+U,' strong correlation effects are not accounted for at a static mean field level. They are explicitly included in a generalized Hubbard model, which is constructed using localized Boys orbitals to describe the 3d electrons of the transition metal ions. The model accounts for both electron-transfer effects, via the hopping integrals, and strong electron-electron correlations, controlled by the screened Coulomb integrals. The hopping integrals are obtained at the end of a self-consistent DFT run, performed in the Local Density Approximation (LDA). In a subsequent step, the screened Coulomb integrals are also calculated self consistently by means of the constrained LDA method. This leads to a molecule-specific generalized Hubbard model. Finally, the spin Hamiltonian is obtained by means of a canonical transformation applied to such a Hubbard model. In this way, no assumption on the form of this Hamiltonian is needed and all the interactions are deduced systematically, including the subtle anisotropic terms.

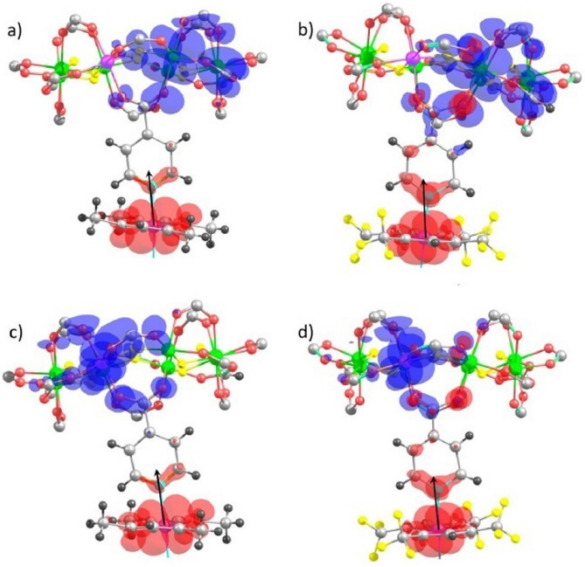

FIG. 2: The substitution of CF_3 groups close to the central Ni ion increases the delocalization of its d-like orbitals.

Our results [2] indicate that single-qubit rotations and two-qubit gates can be implemented with high fidelities by uniform electromagnetic pulses. We find that even if the parameters change significantly in the various compounds, quantum gates can always be implemented. These systems can thus be exploited to implement quantum simulation algorithms, by decomposing the target time evolution into a sequence of elementary operations.

The compounds reported here represent two-qubit units of a potentially scalable quantum simulation scheme. The present switch (the central Ni ion) leads to a non-perfect decoupling of the qubits even in the "off" state. The effect of this small residual interaction increases with N, thus limiting the maximum number of qubits which can be independently rotated. In particular, with the present systems quantum gates can be performed only in short chains with $N \approx 5–6$. This number can be significantly increased, however, by improving the performance of the switch.

In conclusion, the present family of compounds is characterized by the correct hierarchy of parameters to implement sequences of quantum gates and quantum simulation algorithms [2].

[1] A. Chiesa, S. Carretta, P. Santini, G. Amoretti, and E. Pavarini, Phys. Rev. Lett. **110**, 157204 (2013).

[2] A.Chiesa, G.F.S. Whitehead, S. Carretta, L. Carthy, G. A. Timco, S.J. Teat, G. Amoretti, E. Pavarini, R. E. P. Winpenny, P. Santini, Scientific Reports (Nature) **4,** 7423 (2015).

Nonequilibrium transport through a Josephson quantum dot

J. F. Rentrop, S. G. Jakobs, and V. Meden

Institut für Theorie der Statistischen Physik, RWTH Aachen University, Germany

We study the electronic current through a quantum dot coupled to two superconducting leads which is driven by either a voltage V or temperature ΔT bias (beyond linear response). The local two-particle interaction U on the dot is treated with the well established method of Keldysh functional renormalization group. For $V > 0$, "multiple Andreev reflections" might appear. We show that in parameter regimes in which this effect prevails, small $|U|$ approaches become unreliable for interactions of appreciable strength. For $\Delta T > 0$, we find a surprising increase of the current as a function of the superconducting phase difference in the regime which at $T = 0$ becomes the so called doublet phase.

The system of interest is sketched in Fig. 1. The dot is represented by a single spin-degenerate energy level which can be shifted by a gate voltage V_g. The Coulomb energy for double occupation of the dot is represented by the interaction amplitude U. The dot is coupled to the BCS-superconducting leads by a coupling amplitude $\Gamma/2$. Each lead is described by temperature $T_{L/R}$, a superconducting gap Δ, and a superconducting phase factor $e^{i\phi_{L/R}}$. A bias voltage V can be applied across the dot. Experimentally, such a setup is typically realized by a carbon nanotube (the dot) connecting two superconducting leads, see e.g. [1].

We start the discussion with the finite bias voltage case $V > 0$ at zero temperature ($T_{L/R} = 0$). The system is well studied and understood in the noninteracting case $U = 0$ [2]: For intermediate and large values of Δ / Γ the system exhibits an effect which is known as "multiple Andreev reflections" (MAR). Due to the superconducting nature of the leads, new transport channels open up each time the bias voltage crosses the value $(2n+1)/(2\Delta)$, $n \in \mathbb{N}_0$. We are interested in whether and how the interaction on the dot affects the current through the dot in this regime.

In order to treat the interaction U in a non-perturbative manner, we employ the Keldysh functional renormalization group (fRG). This method has been successfully used to investigate the same system with normal, instead of superconducting leads [3]. After tracing out the leads, one works with an effectively zero-dimensional model and aims for a calculation of the dot vertex functions from which observables like the current can be obtained. In principle, this can be done by fRG.

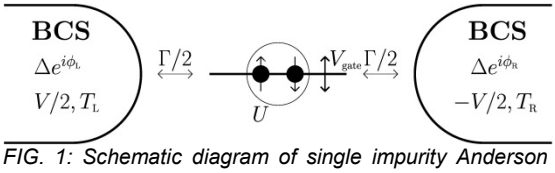

FIG. 1: Schematic diagram of single impurity Anderson model with BCS-superconducting leads.

However, the established method must be adjusted significantly because for $V > 0$ the presence of superconductance causes a periodic time dependence in the Hamiltonian of the system. This can be dealt with by introducing additional discrete Fourier indices in the spirit of Floquet theory. Two fRG flow schemes in which derived and put to use [4]: First, a scheme where the two-particle vertex is fixed to its bare value U which we call P1O. Second, a scheme which allows for a static flow of the two-particle vertex (parameterized by U_Λ; $\rightarrow$ P2O).

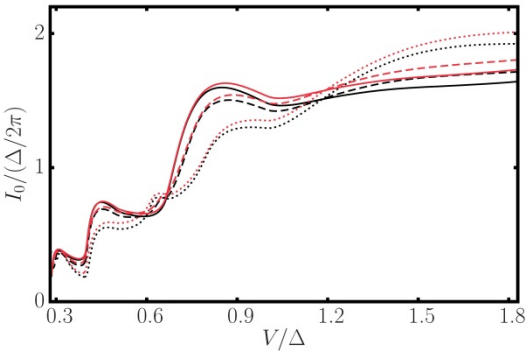

FIG. 2: Time averaged current through the dot for $U/\Gamma = 0.25$ and $\Delta/\Gamma = 1$. $V_g/\Gamma = 0.0$ is the solid line, $V_g/\Gamma = 0.2$ is the dashed line and $V_g/\Gamma = 0.4$ is the dotted line. The red curves are obtained by P1O. The black curves are the U = 0 curves.

Numerical results obtained by P1O (red) for the time averaged current I_0 as a function of V/Δ in the MAR regime are shown in Fig. 2. As we are interested in the interaction effects, they are compared to $U = 0$ data (black). One can clearly see that the MAR have an effect at voltages fulfilling $V/\Delta = 2/(2n+1)$ - this qualitative behavior is not changed by the Coulomb interaction. We now focus on the interaction effects at $V_g = 0$ and plot $\delta I = I_0(U) - I_0(U = 0)$ as a function of $2\Delta/V$, see Fig. 3. Away from the MAR points, the P1O and P2O curves agree quite well. Around the MAR points, however, the curves tend to deviate. Actually, no P2O data points can be calculated around $2\Delta/V = 7,9$ because the flow does not come to an end.

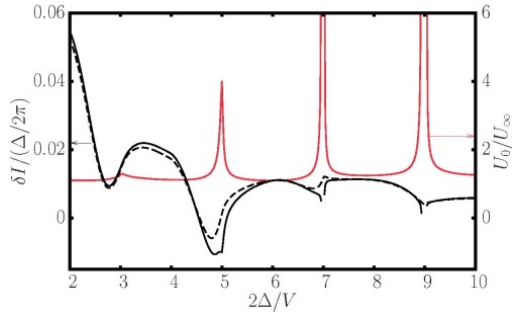

FIG. 3: Difference of interacting and non-interacting current as a function of $2\Delta/V$ for the same parameters as before ($V_g/\Gamma = 0.0$). The dashed line is the P1O data (cf. Fig. 2), the solid line is P2O data. The red solid line is the value of the U_λ at the end of the flow obtained in P2O.

The reason for this can be seen in the solid red line. It shows the value of the RG renormalized interaction U_λ at the end of the flow. Apparently, it diverges if $2\Delta/V$ is too close to the MAR points. This is a clear signal that interaction effects become very important which is plausible because the opening of a new transport channel implies a highly fluctuating occupation of the dot. Furthermore, the U_λ can be interpreted as an indication parameter within the fRG framework and its divergence means that the fRG method is uncontrolled. Moreover, this is a hint that any weak coupling based approach will suffer from problems at the MAR points. This conclusion is augmented by the fact that second order self-consistent perturbation theory exhibits similar problems at the MAR points.

We proceed to discussing the finite temperature bias $\Delta T > 0$ case (with $V = 0$). First of all, we mention that even at $\Delta T = 0$, i.e. a purely equilibrium situation, a current can flow through the dot - the so called Josephson current. This is, again, a superconducting effect which occurs if the complex phases in the two superconductors are not equal, i.e. $\phi = \phi_L - \phi_R \neq 0$. At $T_L = T_R = 0$, the current exhibits a phase transition [5] at a particular $\phi = \phi_c$ which manifests as a change of sign and magnitude of the current (cf. Fig. 4). The phase for $\phi < \phi_c$ is called singlet phase, whereas the phase for $\phi > \phi_c$ is called doublet phase. If one now turns on the temperature $T = T_L = T_R$, this sharp feature is lost but one can still distinguish between the two phases (by the sign change). This equilibrium behavior for finite interactions is well known and "numerically exact" data is available through the numerical renormalization group (NRG) method.

The nonequilibrium situation of $\Delta T > 0$ has hardly been investigated theoretically - which is probably due to the fact that this situation is difficult to realize experimentally. We use again the Keldysh fRG in order to make this investigation [4]. As no challenging periodic time-dependence occurs in this case, the established approach must only be adjusted slightly to account for the superconducting gap of the leads. Again, a static flow of the two-particle vertex is allowed for.

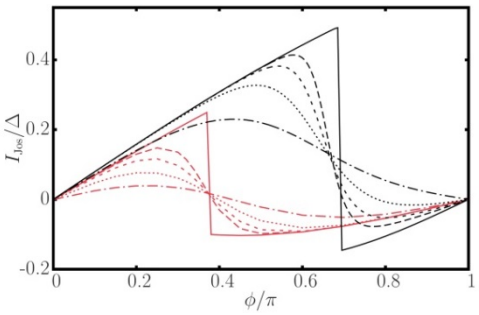

FIG. 4: Josephson current through the dot at $\Delta T = 0$ as a function of the complex phase difference ϕ for $U/\Gamma = 5.2$, $\Delta/\Gamma = 0.37$. T/Δ takes values 0, 0.02, 0.03, 0.05, 0.1 (from solid to dashed-dotted line). fRG data is black, NRG is red.

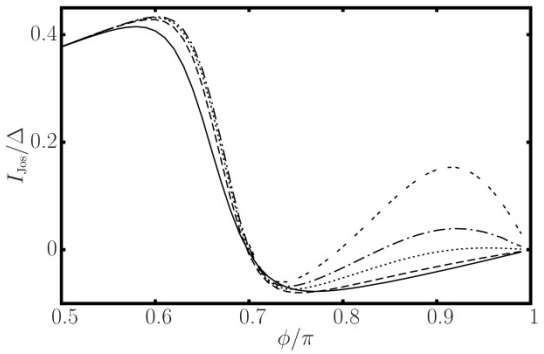

FIG. 5: Josephson current through the dot at $\Delta T \neq 0$ as a function of the complex phase difference ϕ for $U/\Gamma = 5.2$, $\Delta/\Gamma = 0.37$, $T_L/\Delta = 0.02$. T_R/T_L takes values 1, 0.6, 0.5, 0.45, 0.4 (from solid to double-dashed line).

Before we proceed to the new situation of $\Delta T > 0$ nonequilibrium, we benchmark the Keldysh fRG method (black) against existing NRG data [6] (red), see Fig. 4. Even though the position ϕ_c is not reproduced well quantitatively, we can assert that the qualitative features are all reproduced correctly. Thus, we now turn to the nonequilibrium case and fix T_L/Δ to 0.02 but vary T_R/Δ, see Fig. 5. We observe an increase of the current in what used to be the doublet phase. The question arises whether this surprising effect is an artefact of the method. Numerical convergence was assured carefully and several consistency checks were conducted - the effect persists. We hope to stimulate further theoretical (and maybe eventually experimental) research on this situation.

[1] M.R. Buitelaar, W. Belzig, T. Nussbaumer, B. Babic, C. Bruder, and C. Schönenberger, Phys. Rev. Lett. **91**, 057005 (2003)

[2] A. Levy Yeyati, J.C. Cuevas, A. Lopez-Davalos, and A.Martin-Rodero, Phys. Rev. B **55**, R6137 (1997)

[3] S.G. Jakobs, M. Pletyukhov, and H. Schoeller, Phys.Rev. B **81**, 195109 (2010)

[4] J.F. Rentrop, S.G. Jakobs, and V. Meden, Phys. Rev. B **89**, 235110 (2014)

[5] L.I. Glazman, and K. Matveev, JETP Lett. **49**, 659 (1989)

[6] C. Karrasch, A. Oguri, and V. Meden, Phys. Rev. B **77**, 024517 (2008)

Quantum Nature of Edge Magnetism in Graphene Nanoribbons

M. Golor, S. Wessel, and M. J. Schmidt

Institut für Theoretische Festkörperphysik, RWTH Aachen University, Germany

We employ effective theories combined with large-scale quantum Monte Carlo methods to study the quantum nature of graphene edge magnetism. We argue that a subtle crossover from decoherence-dominated classical magnetism to fluctuation-dominated quantum magnetism is experimentally accessible in graphene nanoribbons; the width of a nanoribbon determines whether the edge magnetism is on the classical side, on the quantum side, or in between. In the classical regime, decoherence is dominant and leads to static spin polarizations at the ribbon edges, which are well described by mean-field theories. The quantum Zeno effect is identified as the basic mechanism which is responsible for the spin polarization and thereby enables the application of graphene in spintronics. On the quantum side, however, the spin polarization is destroyed by dynamical processes.

Graphene is usually not considered to be a strongly correlated material, because the vanishing density of states (DOS) at the charge-neutrality point suppresses magnetic correlation effects very efficiently. However, the DOS only vanishes in a perfect bulk crystal. Imperfections, such as edges or vacancies give rise to additional electronic states at the Fermi level [2]. They result in a peak in the local DOS, with the striking consequence that these imperfections enter the regime of strong correlations.

The central phenomenon in this context is the so-called edge magnetism (EM), which is discussed as having possible applications in spintronics [3,4]. The simplest geometry for EM is a nanoribbon with perfect zigzag edges. In this case an extended spin polarization along the edges in the ground state is usually anticipated, with opposite spin directions at opposite edges. One might call this a nonlocal Néel state in the sense that the opposite spins are not neighbors on atomic distances, but are spatially separated. Moreover, this Néel state is implicitly assumed to be classical, i.e., non-fluctuating. This picture is rooted in the often-used mean-field approaches to EM, such as Hartree-Fock or ab initio methods, approximating problem of interacting fermions by a problem of non-interacting fermions, complemented by a self-consistency condition. But, these approaches disregard quantum fluctuations and, in the present context, break the spin symmetry of the initial problem.

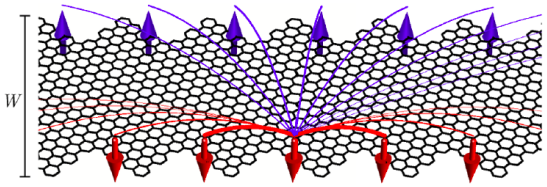

FIG. 1: Special ribbon geometry which allows for a controlled mapping to a spin-1/2 quantum Heisenberg model H_H with a single spin located on each zigzag segment. The effective spin-spin interactions are ferromagnetic (antiferromagnetic) along (across) the edges and sketched here for one reference spin.

More elaborate approaches, such as quantum Monte Carlo (QMC) simulation and the density matrix renormalization group have been applied to EM, but these methods are restricted to rather small systems in which at least the static spin correlations agree well with mean-field results. Thus, the mean-field picture of EM with static spin polarizations prevailed in the community.

Here, we use a recently developed method [4] allowing us to study EM in realistically large systems without the above-mentioned mean-field artifacts [5]. The central idea of this method is the derivation of an effective quantum spin-1/2 Heisenberg theory for the edge states. For special edge geometries in which the edge states are well localized and separated from each other (see Fig. 1), this effective theory has been shown to be in quantitative agreement with numerically exact QMC methods [4]. We restrict our quantitative calculations to this geometry, but our qualitative arguments are expected to extend to more general geometries.

Our work is based on the lattice Hubbard model for graphene, from which we derive an effective spin model H_H that we can study with efficient quantum Monte Carlo methods on large systems. Figure 2 shows the intra-edge spin correlations as well as the spin gap for ribbons of different widths W. In our QMC simulations we mostly used ribbons with size L= 8000, which corresponds to 16 000 edge spins and a physical ribbon length of about 12 µm. We perform all simulations at a temperature T=10 mK, which we verified to be sufficiently low to obtain ground state correlations for ribbons with width at least up to W ~ 6.0 nm. The distance over which the spins are correlated along the same edge grows rapidly with W. We extract the correlation length ξ from the spin correlation function.

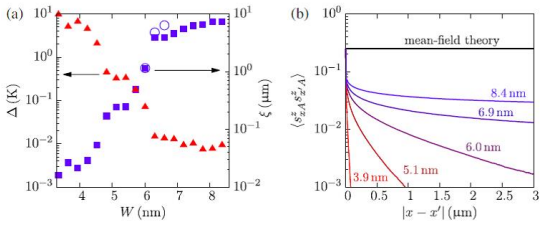

FIG. 2: (a) Spin-spin correlation length ξ and spin gap Δ for different widths W, calculated for 12 μm long ribbons at temperature T=10 mK (errors are smaller than symbol size). Open circles show results for twice as long ribbons (i.e., 24 μm). (b) Spin-spin correlations along the edge for different widths W. For comparison, the black line shows the constant polarization as expected from mean-field theory.

From the analogy with the standard Heisenberg ladders with ferromagnetic leg couplings it is expected that ξ grows exponentially with W, which is in qualitative agreement with our results. The deviations from the exponential behavior of ξ for W $\gtrsim$ 6 nm is a finite size effect, as the total length of the ribbon we simulate is on the order of ξ. Note, however, that we actually consider realistic ribbon lengths, so that this finite size effect is by no means an artifact but an experimentally relevant regime. Results for even longer ribbons (24 μm) support further exponential growth of the correlation length. It should also be noted that mean-field theory predicts infinite ξ at zero temperature in all ribbons considered here. The spin gap Δ is estimated by performing simulations at different temperatures. The spin gap behaves, as expected, inversely to ξ; i.e., it decreases with W, including the finite size effect for W $\gtrsim$ 6 nm. It is remarkable that the spin gap is tunable over more than 2 orders of magnitude via a moderate change in W roughly by a factor of 3. Such small spin gaps are below the resolution of conventional fermionic QMC techniques.

We next discuss the dynamical aspects of the EM. A classical Neel state $|\Psi_N\rangle$ is not an eigenstate of the Heisenberg Hamiltonian, and will therefore decay on a certain time scale τ_{qd}. We extract τ_{qd} by analyzing the quench dynamics of the staggered magnetic moment $D_{st}(t)=\langle\Psi_N(t)|S^z_{st}|\Psi_N(t)\rangle/L$ where $|\Psi(t)\rangle=\exp(-itH_H)|\Psi\rangle$. For general ribbon lengths L and widths W it is difficult to calculate D_{st}. For ribbons with a high aspect ratio ($L \ll W$), however, the interedge antiferromagnetic couplings are essentially independent of distance. If the ribbon width W is twice its length L, we find that the antiferromagnetic couplings are approximately constant $J_{AF}=(5/L)^3$ K. Thus, as far as the antiferromagnetic part is concerned, H_H is equal to the exactly solvable Lieb-Mattis (LM) model of antiferromagnetism. We need to perform a further approximation in order to be able to avail ourselves of the exact solution of the Lieb-Mattis model, namely, the assumption of constant ferromagnetic intraedge coupling J_{FM}. From the size scaling of the intraedge coupling, this assumption is not justifiable. However, we eventually find that, making this assumption, the results are completely independent of J_{FM}, since all spins at the same edge behave as one large superspin. Thus, we do not expect this approximation to affect our results in a qualitative way. We now define the decay time as the first zero of $D_{st}(t)$, and find that $\tau_{qd} \sim 0.1 t_r$ over a wide range of system sizes L, where $t_r \sim J_{AF}^{-1}$ denotes the revival time, specific to the LM model spectrum (in general, the excitation spectrum is incommensurate and thus the revival time is, as usual, exponentially large in the system size). Thus, we have obtained a rough estimate for the quantum decay time of a Néel-like state in a special ribbon geometry, namely, $\tau_{qd} \approx (L/5)^3$ ps [5]. In order to determine whether EM in an actual experiment is a quantum or a classical phenomenon in which the spin polarization is zero or finite, respectively, we consider the environment of the ribbon, including the measurement process. The simplest possible way of doing this is to collapse the complicated system-environment interactions into one single environment time scale τ_{env} on which quantum coherence within the ribbon is destroyed by the environment. One may also understand τ_{env} as the typical time between successive measurements of the spin state of the ribbon by the environment. Such a measurement will be local and will certainly tend to destroy the subtle entanglement of the true ground state $|\Psi_0\rangle$, thereby preparing the ribbon in a classical nonentangled state, say $|\Psi_N\rangle$. We have argued that $|\Psi_N\rangle$ will decay on a time scale τ_{qd} towards the quantum ground state. However, if the time τ_{env} between two measurements is much shorter than τ_{qd}, the ribbon is prepared into the same classical state $|\Psi_N\rangle$ over and over again and thus cannot decay. This phenomenon is known as the quantum Zeno effect. In graphene ribbons τ_{qd} can be tuned via the ribbon dimensions over a wide range, from below a ps up to μs and higher. The environment time τ_{env} is expected in this range as well. Thus, graphene-based nanostructures are perfect candidates for the study of the delicate crossover between classical and quantum behavior. Further details on this research may be found in Ref. [5].

We have profited from discussions with A. Harjun, C. Honerkamp, C. Koop, T. C. Lang, R. Mazzarello, M. Morgenstern, B. Trauzettel, and O. Yazyev. Financial support by the DFG under Grant No. WE 3649/2-1 is gratefully acknowledged, as well as the allocation of CPU time within JARA-HPC and from JSC Jülich.

[1] M. Fujita, K. Wakabayashi, K. Nakada, and K. Kusakabe, J. Phys. Soc. Jpn. **65**, 1920 (1996).

[2] O. V. Yazyev and M. I. Katsnelson, Phys. Rev. Lett. **100**, 047209 (2008)

[3] Y.-W. Son, M. L. Cohen, and S. G. Louie, Nature (London) **444**, 347 (2006).

[4] M. J. Schmidt, M. Golor, T. C. Lang, and S. Wessel, Phys. Rev. B **87**, 245431 (2013).

[5] M. Golor, S. Wessel, and M. J. Schmidt, Phys. Rev. Lett. **112**, 046601 (2014).

Charge carrier scattering in high quality bilayer graphene

S. Engels[1,2], B. Terrés[1,2], A. Epping[1,2], T. Khodkov[1,2], M. Goldsche[1,2], K. Watanabe[3], T. Taniguchi[3], B. Beschoten[2], and C. Stampfer[1,2]

[1] Peter Grünberg Institute-9, Forschungszentrum Jülich, Germany
[2] II. Institute of Physics, RWTH Aachen University, Germany
[3] National Institute for Materials Science, Tsukuba, Japan

Bilayer graphene (BLG) is an interesting material system to explore phase-coherent mesoscopic transport with unique electronic properties. In contrast to single-layer graphene, in BLG a band gap can be opened by an external electric field making local depletion of the two-dimensional electron gas (2DEG) possible, very similar to III/V hetero-structures. So far, BLG devices suffer from the limited device quality which is a consequence of the high sensitivity to its surrounding environment. Recent experiments aimed at tackling this challenge, have shown that a significant improvement in sample quality can be obtained by replacing conventional SiO_2 with hexagonal boron nitride (hBN) [1]. However, a fundamental understanding of the still limiting mechanisms in these systems is not yet established. Here, we show and discuss experimental evidence, that the transport is limited by intra-valley scattering which is likely to be caused by strain fluc-tuations in the BLG lattice.

In the past years, BLG was mostly placed on SiO_2 substrates. In this case, the rough surface, charge traps, and the presence of dangling bonds limit the device quality. One method to overcome the harmful influence of the substrate is to fabricate suspended graphene devices which results in higher mobility samples. However, the fabricated devices are extremely fragile and sensitive to environmental changes. These limitations can be overcome by placing and encapsulating graphene with atomically flat hBN. The perfect interface between the two materials leaves the graphene properties mostly unaltered and leads to high charge carrier mobilites while the present hBN substrate additionally supports the graphene mechanically. An overview over the development, i.e. improvement of the charge carrier mobility μ in BLG supported by the aforementioned substrates is shown in Fig. 1 and illustrates the superior quality of hBN as a substrate material.

To fabricate the graphene hBN heterostructures we use a van-der-Waals pick up technique. In a first step, graphene and hBN with a thickness of around 10–30 nm is exfoliated on two different, highly p-doped Si^{++} substrates with a top layer of SiO_2. Secondly, a glass slide is prepared with an adhesive tape and a copolymer. Hexagonal BN is

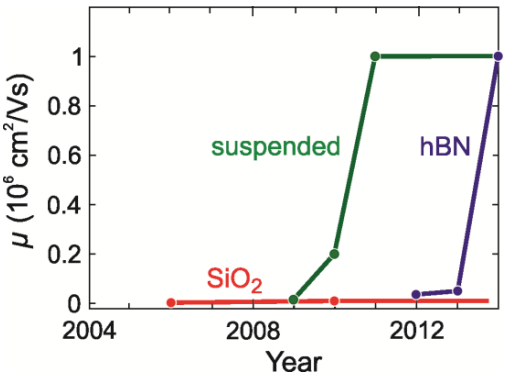

FIG. 1: Development of the charge carrier mobility μ in bilayer graphene from its first isolation in 2006 until 2014 for different substrates (SiO_2, hexagonal boron nitride (hBN) and suspended devices).

then exfoliated onto this stack and the resulting hBN flakes are used to pick up the graphene from the SiO_2 and place it on top of the prepared hBN exfoliated on SiO_2. Finally, the sample is cleaned by organic solvents leaving the hBN–BLG–hBN structure on the SiO_2. For a detailed description please see Ref. [2]. An optical image of a fabricated heterostructure is shown in Fig. 2A. To prove the bilayer nature of the sample, Raman measurements with a wave length of 532 nm are conducted on the structure. A typical spectrum is shown in Fig. 2B which was recorded at the location of the blue dot in Fig. 2A. The spectrum shows the characteristic fourfold splitting of the Raman 2D-peak into four sub-peaks as illustrated by the inset in Fig. 2B. Interestingly, the 2D-sub-peaks exhibit an exceptionally small full width at half maximum, which manifests itself in the dip of the Raman signal between the two leftmost sub-peaks (see arrow in the inset of Fig. 2B). The narrow 2D-sub-peaks are an indication of a high sample quality and can be linked to a low level of strain fluctuations in the BLG lattice [3].

After confirming the bilayer nature and its high quality the hBN-BLG-hBN stack is structured and contacted by standard electron beam lithography, reactive ion etching and metal evaporation steps. The contacted device is shown in the inset of Fig. 2C. Fig. 2C shows the conductivity σ of the device as function of the back gate voltage V_g applied to the highly doped Si^{++} at a temperature of 77 K. From this data we extract the charge carrier mobility μ by performing a linear regression (see

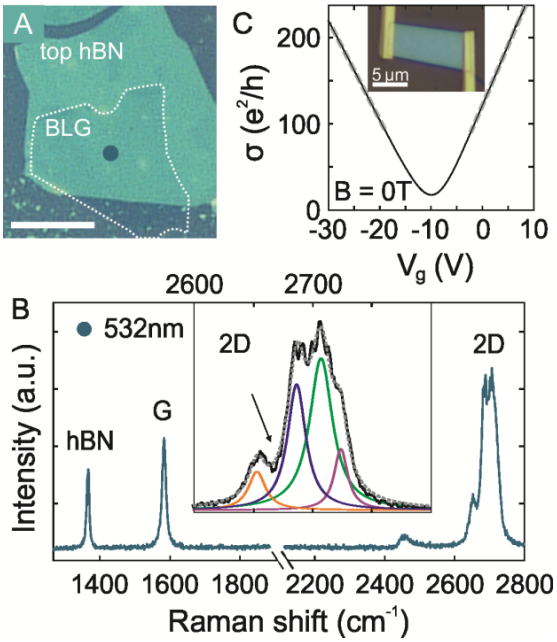

*FIG. 2: **A** Optical image of a hBN-BLG-hBN heterostructure. The scale bar represents 10 µm. **B** Raman spectrum of BLG taken at the position indicated by the blue dot in A. **C** Conductivity in dependence of the back gate voltage V_g applied to the highly doped silicon substrate at an applied magnetic field B = 0 T.*

dashed lines in Fig. 2C) and using Drude's formula $\sigma = en\mu$. Here, e is the elementary charge and n the charge carrier density which can be obtained by $n = V_g\alpha_g$, where α_g is determined by the capacitance between the BLG and the back gate and is $\alpha_g = 6.5 \times 10^{10}$ cm^{-2}V^{-1}. The extracted carrier mobility is μ = 50 000 cm^2/Vs which is among the highest reported for BLG supported by a substrate.

We next focus on weak localization (WL) measurements, from which we extract three fundamental length scales of our device [4]: the phase coherence length, the inter-valley scattering length L_i as well as the intra-valley scattering length L_*. All mentioned length scales can be interpreted as the mean distance the electron travels in between the corresponding scattering events. The dependence of these scattering lengths and the elastic mean free path l_m on the charge carrier density is shown in Fig. 3. The inter-valley scattering length L_i is about 0.4 µm at low carrier densities, and it increases up to 5 µm for larger n. In this regime, L_i exceeds l_m by roughly one order of magnitude, ruling out inter-valley scattering as the mechanism limiting mobility in BLG. This argument is also supported by measurements performed on another BLG sample. This observation clearly points at intra-valley scattering (being the only alternative) as the mobility limiting process in high-quality BLG samples. Additionally, we find that the intra-valley scattering length L_* is roughly one order of magnitude lower than L_i, but similar to l_m. In the literature, the main sources of intra-valley scattering in single-layer and bilayer-graphene have been associated with long-range disorder

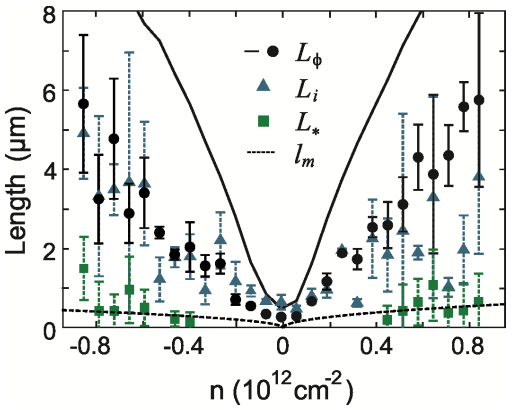

FIG. 3: Dependence of the phase scattering length L_Φ, inter-valley scattering length L_i, intra-valley scattering length L_* and mean free path l_m of the charge carrier density n.

due to either charged impurities or to local mechanical deformations, i.e. strain fluctuations [5]. However, from the observed linear dependence of $\sigma \sim V_g$, we can exclude that the limitations to mobility come from charged impurities which would lead to a super-linear behavior. Vice versa, it can be shown that local strain fluctuations in BLG lead to the correct $\sigma \sim V_g$ dependence [5]. We can therefore conclude that the electron mobility in our sample is limited by intra-valley scattering events that are most likely caused by local strain fluctuations. This conclusion agrees well with evidence we have from confocal Raman experiments that high-mobility samples exhibit reduced local strain fluctuations [3], as well as with recent studies on single-layer graphene, which also identified mechanical deformations as the main source of mobility-limiting scattering processes [5]. This, in turn, strongly suggests that the transport properties of both single- and bilayer graphene are limited by the same physical mechanism.

Support by the Helmholtz Nanoelectronic Facility (HNF), JARA Seed Funds, the DFG (SPP-1459 and FOR-912), the ERC (GA-Nr. 280140) and the EU project Graphene Flagship (contract no. NECT-ICT-604391), are gratefully acknowledged.

[1] C. R. Dean, A. F. Young, I. Meric, C. Lee, L. Wang, S. Sorgenfrei, K. Watanabe, T. Taniguchi, P. Kim, K. L. Shepard, and J. Hone, Nature Nanotechnol. **5**, 722 (2010).

[2] S. Engels, B. Terrés, F. Klein, S. Reichardt, M. Goldsche, S. Kuhlen, K. Watanabe, T. Taniguchi and C. Stampfer, Physica Status Solidi B **251**, 2545 (2014).

[3] C. Neumann, S. Reichardt, P. Venezuela, M. Drögeler, L. Banszerus, M. Schmitz, K. Watanabe, T. Taniguchi, F. Mauri, B. Beschoten, S. V. Rotkin, and C. Stampfer, arXiv: 1406.7771v2

[4] S. Engels, B. Terrés, A. Epping, T. Khodkov, K. Watanabe, T. Taniguchi, B. Beschoten, and C. Stampfer, Phys. Rev. Lett. **113**, 126801 (2014).

[5] N. J. G. Couto, D. Costanzo, S. Engels, D.-K. Ki, K. Watanabe, T. Taniguchi, C. Stampfer, F. Guinea, and A. F. Morpurgo, Phys. Rev. X **4**, 041019 (2014).

Reversible sublattice symmetry breaking in graphene nanomembranes using tip induced strain fields

A. Georgi[1], P. Nemes-Incze[1], R. Carillo-Bastos[2], D. Faria[2,3], S. V. Kusminskiy[4], L. Wirtz[5], M. Pratzer[1], N. Sandler[2], and M. Morgenstern[1]

[1] II. Institute of Physics B, RWTH Aachen University, Germany
[2] Dresden Department of Physics and Astronomy, Nanoscale and Quantum Phenomena Institute, Ohio University, Athens, USA
[3] Instituto de Física, Universidade Federal Fluminese, Niterói, Avenida Litorânea sn, Brasil
[4] Dahlem Center for Complex Quantum Systems and Institut für Theoretische Physik, Freie Universität Berlin, Germany
[5] Physics and Materials Science Research Unit, University of Luxembourg, Luxembourg

Strain engineering in graphene might lead to a new generation of electromechanical devices. However, possibilities to tune the strain on the nanoscale have not been realized so far. Here, we show that the forces exerted by the tip of a scanning tunneling microscope can be used to apply strain on sub-nm length scales, which allows the switching of local strainpatterns on and off, as well as tuning their magnitude. The strain becomes visible as a relative change of the local density of states (LDOS) of the two sublattices by up to 30%. Comparison with tight binding simulations reveals that this contrast pattern is a fingerprint of the induced local strain field.

Exfoliated graphene on SiO_2 is known to show corrugations following the substrate topography like a blanket on top of a rough surface [1], giving rise to spatial varying adhesion energies and even partly suspended graphene areas [2]. It has been shown that these partly suspended areas are easily lifted by the tip of a scanning tunneling microscope (STM). Measurements are conducted at 5K in our home-build system [3]. We show that not only partly freestanding areas, but all graphene can be lifted off the SiO_2-substrate for close tip sample distances and is thereby strained by an induced local deformation. Figure 1a) shows two STM pictures in atomic resolution for different tip sample distances controlled by the tunneling current. As described by the displacement scale bar (right side) the graphene is lifted up to 2Å and thereby exhibits a breaking of symmetry between sublattice A and B.

Figure 1b) shows averaged current distance spectra on two different areas of graphene measured at 0,5V bias voltage. The lifting height Δz of graphene in relation to the substrate can be measured as a difference of the STM current-distance behavior in respect to an exponential tunneling junction characteristic (red line). The amount of tip induced lifting shows spatial changes what is expected because of local variations in the adhesion energies between graphene and the substrate. For some valley areas it is possible to switch the curvature into hills as reported in [2]. The blue spectrum is measured on the valley position that is transformed into a hill, as pictured in Figure 1a), thereby the overall defection of the graphene is up to 3Å. For areas where the curvature of the morphology is preserved, lifting heights of up to 2Å can be realized (black curve).

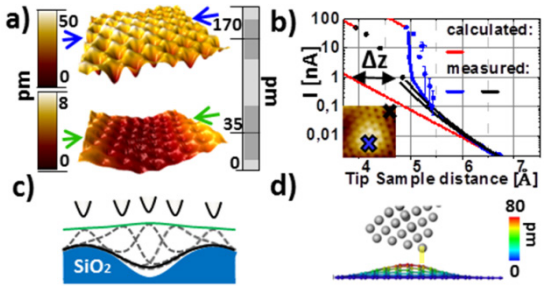

FIG. 1: a) 3D-STM image of monolayer graphene for two different tip sample distance (V_{stab} = 0.5 V, I_{stab} = 50 nA (top) I_{stab} = 0.1 nA (bottom)). Arrows mark area of profile lines in figure (3a) atomic contrast on left color scale, lifting height and topographic height on right colorscale. b) Current distance characteristic for different positions: valley (blue), substrate (black) and quantum tunneling (red). c) Cartoon of the lifting situation. d) Molecular dynamic simulation of graphene and tip. Tunneling position is marked yellow.

We performed molecular dynamic simulations to model the observed lifting behavior, with the LAMMPS software code [4] (Fig. d). The energy minimization shows that a Gaussian deformation forms under the foremost few tip atoms for tip sample distances between 4Å and 7Å. This distance is appropriate for the described experimental tunneling situation and well out of the contact regime. For a pyramidal tungsten tip we find deformation widths b of 5-7Å when the Gaussian is described by $h(r) = A \cdot \exp(r^2/b^2)$. The most likely scanning tip in an experimental setup will show an asymmetric geometry. This we simulated, by applying a tilting angle of up to 30° to the tungsten tip. We find that the position of the

scanning atom with closest distance to graphene is shifted away from the force center.

We further analyzed the influence of a Gaussian strain pattern, in tight-binding approximation for the width found in the molecular dynamic simulation and the measured lifting heights [5]. We find an induced LDOS pattern that is textured in six petals around the deformation center, where the sublattice with enhanced LDOS alternates from petal to petal (Fig 2a). This contrast can be understood geometrically by a local change in the hopping amplitude due to strained SP2 bonds. Figure 2b) shows the LDOS pattern for a Gaussian deformation of amplitude A=1Å and width b=5Å derived from the tight-binding calculations [5]. The relative LDOS contrast change Δv in percent between sublattice A and B can also be calculated in first order perturbation theory [6]. The geometry dependent scaling of the LDOS contrast is given by: $\Delta v = -\frac{\beta A^2}{ba}\sin 3\vartheta \; g(r/b)$ where g(r/b) is an analytic function depending on the Gaussian form. The maximum contrast is located at r=b.

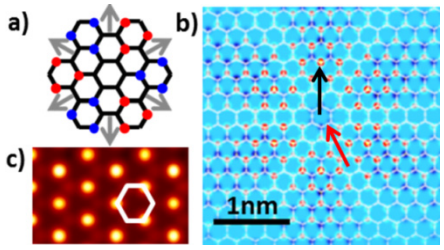

FIG. 2: a) Representation of the central symmetric strain pattern. Enhanced sublattices are marked with sublattice A (red) and sublattice B (blue) b) Tight-binding calculation of the strain induced LDOS contrast pattern for a Gaussian deformation of amplitude A=1Å and width b=5Å.Maximum contrast position at r=b (black arrow) and position of the inner hexagon (red arrow) are indicated. c) Tight-binding calculation of the scanned contrast at the position of maximum contrast with indicated graphene lattice cell (white hexagon).

It is not possible to measure the tip induced LDOS contrast petals in real space within the STM measurement, because the deformation will follow the force center of the tip while scanning (Fig 1c). It is however possible as shown in Figure 1d) to measure inside one of the field petals, if the tip is not rotational symmetric and the scanning atom is disparate from the force center. We conducted tight-binding calculations for tip geometries where the scanning atom is located in the position of maximum contrast. The strain geometry shows only small changes in magnitude, when the positon of the deformation center is changed within the central hexagon. Therefore the scanning situation can be seen as an image of the same strain value at different positions of one unitcell. A simulated scan of a Gaussian deformation yields a completely sublattice symmetry broken graphene lattice, with a reduced contrast of around 40% in relation to the maximum contrast. We measure the induced sublattice contrast by translating the height difference between sublattice A and B into an LDOS difference. For constant current and bias voltage, the height difference is proportional to the LDOS difference.

Figure 3a) shows representative atomically resolved STM picture of a lifted graphene area.

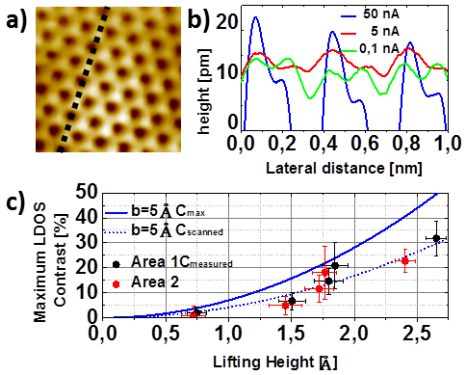

FIG 3: a) STM image of monolayer graphene for close tip sample distance (V_{stab} = 0.5 V, I_{stab} = 50 nA). b) Profile lines for different lifting situations controlled by the tunneling current (I_{stab} = 50nA (green), I_{stab} = 5nA (red), I_{stab} = 0.1nA (sky blue)). The scale shows the sublattice contrast in pm. c) Theoretical- (blue line) vs. measured- (red and black dots) LDOS contrast in respect of the experimental lifting height, additionally we indicated the 40% reduced scanned contrast (dotted blue line).

We always find the same sublattice enhanced, as expected for scanning inside of one LDOS petal. Figure 3b) shows a profile line for different stabilization currents in atomic resolution. The measured height differences of the sublattices scale with the local lifting heights. We measured the height difference of more than 300 atom sites in relation to their lifting heights (Fig 3c). We find a good qualitative agreement with the LDOS contrast for a scanned Gaussian deformation of width b=5Å (dotted blue line) derived from the continuum model [6]. Deviations from the modeled behavior are to be expected, because the width of the Gaussian will depend on the local adhesion forces of the substrate. Also the magnitude of the scanned contrast is further dependent on the relative position of the scanning atom in relation to the position of the maximum contrast inside of the petals which is directly dependent on the width b. It has to be noted that the sublattice symmetry breaking and the lifting behavior are not always visible in the same fashion, but are strongly dependent on the respective microtip and on the adhesion forces between graphene and the substrate. Many atomically resolved carbon structures show similar symmetry broken lattices that could be attributed to this effect. In conclusion we showed that current distance spectra on layered systems in combination with atomically resolved LDOS measurements are a strong tool to check for induced strain patterns in layered systems.

[1] V. Geringer et al., PRL **102**, 146801 (2009)

[2] T. Mashoff et al., Nano Letters **10**, 461 (2010)

[3] T. Mashoff et al., M Rev. Sci. Inst. **80**, 053702 (2009)

[4] S. Plimpton, J Comp Phys. **117**, 1-19 (1995)

[5] R. Carillo-Bastos et al., Phys. Rev. B **90**, 041411 (2014)

[6] M. Schneider et al., Phys. Rev. B **91**, 161407 (2015)

Fault-tolerant quantum computation for singlet-triplet qubits with leakage errors

S. Mehl[1,2], H. Bluhm[2], and D. P. DiVincenzo[1,2]

[1] Peter Grünberg Institut-2, Forschungszentrum Jülich, Germany
[2] JARA-Institute for Quantum Information, RWTH Aachen University, Germany

We describe and analyze leakage errors of singlet-triplet qubits. Even though leakage errors are a natural problem for spin qubits encoded using quantum dot (QD) arrays, they have obtained little attention in previous studies. We describe the realization of leakage correction protocols that can be implemented together with the quantum error correction protocol of the surface code. Furthermore we construct explicit leakage reduction units that need, in the ideal setup, as few as three manipulation steps. Our study shows that leakage errors can be corrected without the need of measurements and at the cost of only a few additional ancilla qubits and gate operations compared to standard quantum error correction codes.

Singlet-triplet qubits (STQs) are a variety of spin qubit, which is coded on the $s_z = 0$ subspace of two electrons that are trapped at a double quantum dot (DQD) [1]. Universal single-qubit control is provided by the exchange interactions between the electrons, when the setup is operated at large magnetic fields with a small, time-independent magnetic field gradient across the DQD. Universal single-qubit control has been realized for STQs coded using GaAs DQDs and Si DQDs. Also the first steps towards the experimental realizations of two-qubit gates have been done. Furthermore the initialization and the readout of STQs has been successfully ahieved. We extends the discussions of fault-tolerant quantum computation for STQs, assuming that the initialization, readout, and universal qubit control have high fidelities.

The leakage of quantum information out of the coding subspace is a generic problem for quantum computers. Because gate operations use couplings to states that are not part of the qubit subspace, the manipulations of quantum states increase the probability of leakage. Besides optimized gate sequences for qubit manipulations that reduce the leakage directly for these operations, there is also the need for an independent gate like operation, a "leakage reduction unit" (LRU). Leakage is especially problematic for spin-qubit encodings because the qubit subspace does not necessarily contain the energetic ground state, and thermal relaxation drives a qubit out of the computational subspace. Many quantum error correction protocols only refocus qubit errors within the Hilbert space that codes the qubit, e.g., they refocus depolarizing or spin-flip errors. It has been shown that if there is additionally a LRU, then fault-tolerant quantum computation can become tolerant to leakage errors.

We introduce two generic approaches to construct LRUs, and apply them specifically to STQs (cf. Fig. 1). In every case, an ancilla qubit $\mathcal{A}$ is used as a resource to correct the leakage of the data qubit $\mathcal{D}$. For the first LRU, $\mathcal{A}$ provides for $\mathcal{D}$ a state from the computational subspace if leakage has occurred, but $\mathcal{D}$ is untouched without leakage events. After this LRU, $\mathcal{A}$ can be discarded. For the second LRU, the state of $\mathcal{D}$ is transferred to $\mathcal{A}$ only if there has been no leakage. For leakage events, $\mathcal{D}$ keeps the leaked state, and $\mathcal{A}$ provides a new state from the computational subspace. In total, the definitions of $\mathcal{D}$ and $\mathcal{A}$ are then interchanged after this LRU.

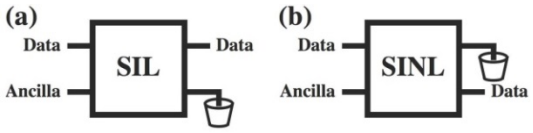

FIG. 1: Circuit diagrams for (a) the SWAP If Leaked (SIL) and (b) the SWAP If Not Leaked (SINL) operations.

Standard quantum error correction protocols neglect leakage errors out of the computational subspace. The surface code is one of the most prominent quantum error correction codes, and it tolerates errors of the gate operations, the qubit initializations, and the readout of every qubit below a threshold of about error per operation. This protocol is especially promising because the error corrections and the manipulations of the encoded quantum information only requires nearest-neighbor interactions between neighboring physical qubits on a lattice (cf. Fig. 2). The surface code setup can be used without changes for the LRUs of Fig. 1. Because the ancilla qubits do not store any relevant information after the parity check operations of the surface code, these qubits can be initialized and the leakage correction procedure can be executed. One ancilla qubit is needed for every data qubit. In the setup of Fig. 2, we therefore add additional ancilla qubits to the edges of the surface code lattice. For the SINL operation, the definitions of data and ancilla qubits swap after the leakage correction procedure, which results in a shift of the surface code layout after one leakage correction step.

We specifically describe LRUs for one data qubit $\mathcal{D}$ and one ancilla qubit $\mathcal{A}$ in close proximity, where the electron transfer between the DQDs is possible, such that the DQDs are coupled by the exchange interaction. We label the two QDs in close proximity as QD_2 and QD_3. It can be desirable that the magnetic fields at individual QDs differ during gate operations. The effective time evolution is

$$U_{\varphi,\psi} = e^{-i\left\{2\pi\left[\frac{\varphi}{4}(\sigma_2\cdot\sigma_3-1)+\frac{\psi}{2}\left(\sigma_2^z-\sigma_3^z\right)\right]\right\}}. \qquad (1)$$

Fig. 3 shows examples of gate sequences to construct LRUs.

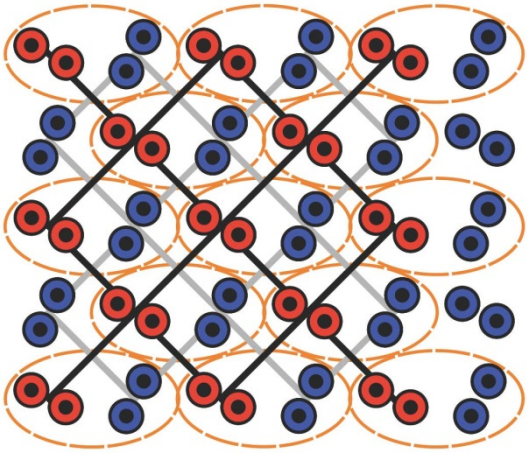

FIG. 2: Setup for fault-tolerant quantum computation with the surface code that also tolerates small leakage errors. A two-electron DQD encodes a qubit. The red DQDs are the data qubits, the blue DQDs are the ancilla qubits. Furthest to the right are some additional ancilla qubits that are needed for the LRUs.

In principle, it is possible to use long-range interactions to construct LRUs for STQs instead of the short-range Heisenberg interactions. Coulomb interactions or cavity-mediated couplings between STQs have been suggested to couple distant STQs. Both coupling mechanisms can be described by an effective two-qubit interaction $\sim \tau_z^D \tau_z^A$ with $\tau_z = |T_0\rangle\langle T_0| + |S\rangle\langle S|$, which acts only on the qubit subspace. One can construct the SINL operation according to

$$H^D e^{-i\frac{\pi}{4}\tau_z^D\tau_z^A} e^{-i\frac{3\pi}{4}\tau_x^D} e^{-i\frac{3\pi}{4}\tau_x^A} e^{-i\frac{\pi}{4}\tau_z^D\tau_z^A} H^A, \qquad (2)$$

with $\tau_x = |S\rangle\langle T_0| + |T_0\rangle\langle S|$. H^D and H^A are the Hadamard gates for $\mathcal{D}$ and $\mathcal{A}$, respectively. The SIL operation cannot be realized with the $\tau_z^D\tau_z^A$ interaction because the s_z quantum number remains unchanged at each QD.

Our study has shown that an array of DQDs realizes a setup for fault-tolerant quantum computation of STQs that even tolerates leakage errors. Experiments have realized excellent single-qubit gates, while high-fidelity two-qubit gates are still to be done.The initialization and the readout of STQs can be done with high fidelities, such that fault-tolerant quantum computation can readily be implemented. To additionally include LRUs, we proposed a lattice of DQDs, where the exchange operations between QDs of the data qubit and the ancilla qubit can be controlled.

The described LRUs use one ancilla qubit for every coded qubit, while the ancilla qubits are only needed during the leakage corrections. We describe two methods for leakage corrections. In one case, the ancilla qubits are only used as a resource to provide a state from the qubit subspace if leakage has occurred. In the other case, the data qubit and the ancilla qubit change their positions if no leakage has occurred. Because the ancilla qubits are required anyway in standard quantum error correction protocols, both approaches to construct LRUs are equally permitted.

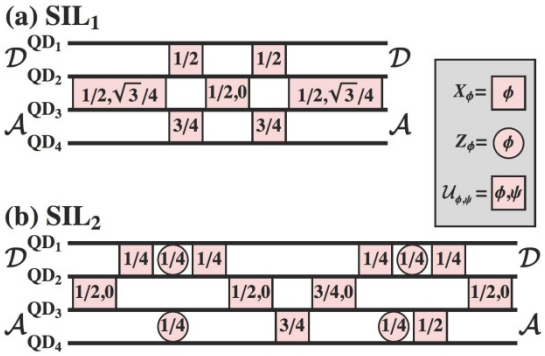

FIG. 3: Gate operations for the SIL operation. Z_ϕ *and* $n.X_\phi$ *label the phase and exchange gates, and* $U_{\phi,\psi}$ *is the effective interaction between the electrons at* QD_2 *and* QD_3 *according to Eq. (1): (a) the magnetic fields at* QD_2 *and* QD_3 *differ, (b) the magnetic fields at* QD_3 *and* QD_4 *are identical.*

Our study can be continued with an in-depth analysis of specific error models for spin qubits to describe leakage errors in addition to the usual gate, initialization, and readout errors. It is especially important to analyze the consequences of imperfectleakage correction sequences more quantitatively. Decoherence is the main obstacle to construct high-fidelity quantum gates for spin qubits, and it will also disturb our leakage correction protocols such that leakage errors are only partly recovered. Furthermore our study should bring attention to the problem of leakage errors in the field of quantum computation with spin qubits, where it has received little attention so far. Not only can our proposed LRUs mitigate leakage errors, but they also show that leakage errors do not present a fundamental problem for fault-tolerant quantum computation.

For more details see [2].

[1] J. Levy, Phys. Rev. Lett. **89**, 147902 (2002)

[2] S. Mehl, H. Bluhm, and D. P. DiVincenzo, Phys. Rev. B , 085419 (2015).

Isolated chiral skyrmions: energy, structure and dynamics

Lukas Döring and Christof Melcher

Lehrstuhl I für Mathematik, RWTH Aachen University, Germany

Chiral skyrmions are vortex-like spin configurations occurring in magnets without inversion symmetry. Predicting static and dynamic stability properties is closely related to the internal multi-scale structure and calls for a thorough mathematical investigation. In a regime of small core size we obtained improved understanding of the subtle interplay between Heisenberg, Zeeman and Dzyaloshinskii-Moriya interaction, and the current-driven dynamics.

The variational description of magnetization configurations in ideally soft noncentrosymmetric magnetic compounds at zero temperature is based on the following energy density for a unit vector field $\boldsymbol{m}$

$$e(\mathbf{m}) = \frac{J}{2}|\nabla \mathbf{m}|^2 + D\,\mathbf{m}\cdot(\nabla\times\mathbf{m}) + \frac{B}{2}|\mathbf{m}-\hat{\mathbf{e}}_z|^2$$

including Heisenberg exchange, Dzyaloshinskii-Moriya interaction (DMI) and Zeeman interaction with an external magnetic field in $\hat{\boldsymbol{e}}_{\boldsymbol{z}}$ direction. DMI is a lower order perturbation of Heisenberg exchange and changes sign upon reflection. This is in contrast to the usual Skyrme mechanism induced by a higher order perturbation preserving $O(3)$ symmetry. After rescaling by $\kappa = D/J$, the normalized density

$$e_h(\mathbf{m}) = \frac{1}{2}|\nabla \mathbf{m}|^2 + \mathbf{m}\cdot(\nabla\times\mathbf{m}) + \frac{h}{2}|\mathbf{m}-\hat{\mathbf{e}}_z|^2$$

only contains one dimensionless system parameter $h = JB/D^2$.

It is well-known that $e_h(\boldsymbol{m})$ features a hierarchy of modulated states. In the planar case (thin layers) the phase diagram encompasses the 1D helical phase at low fields $h < h_{c_1}$, the 2D chiral skyrmion lattice phase (see fig. 1) for intermediate fields $h_{c_1} < h < h_{c_2}$, and the ferromagnetic phase at large fields $h > h_{c_2}$, on which we shall focus from now on. Letting $E_h(\mathbf{m}) = \int_{\mathbf{R}^2} e_h(\mathbf{m})\,dx$, isolated chiral skyrmions may be seen as excited states within the ferromagnetic phase characterized by $E_h(\boldsymbol{m}) \geq 0$ where $\boldsymbol{m} = \hat{\boldsymbol{e}}_{\boldsymbol{z}}$ is the global energy minimizer. From a mathematical perspective, isolated chiral skyrmions are stable equilibria of $E_h(\boldsymbol{m})$ within a non-trivial homotopy class and may be obtained by global minimization of $E_h(\boldsymbol{m})$ subject to the topological constraint $Q(\boldsymbol{m}) = q$, where $Q(\mathbf{m}) = \frac{1}{4\pi}\int_{\mathbf{R}^2}\omega(\mathbf{m})\,dx$ and $\omega(\boldsymbol{m}) = \boldsymbol{m}\cdot\partial_1\boldsymbol{m}\times\partial_2\boldsymbol{m}$ is the topological charge density. Topologically constrained minimization is in general a subtle mathematical task and requires a variety of methods from global and functional analysis. Restricted to the class of radially symmetric configurations, the problem reduces to a boundary value problem for an ordinary differential equation that for appropriate h can be solved by phase plane methods as shown by Bogdanov and Hubert in their seminal work. Recently we have shown that the symmetry constraint can be dropped and established the first global existence result [1]:

Theorem. *If $h > 1$, then the minimum of $E_h(\boldsymbol{m})$ among all admissible finite energy configurations with $Q(\boldsymbol{m}) = -1$ is attained by a smooth field $\boldsymbol{m} = \boldsymbol{m}_h$ in this homotopy class.*

The result slightly underscores the estimate for the critical field $h_{c_2} \sim 0.8$ obtained by numerical calculations for the radially symmetric model by Bogdanov and Hubert. Whether the global minimum is obtained by a radially symmetric configuration is a major open question.

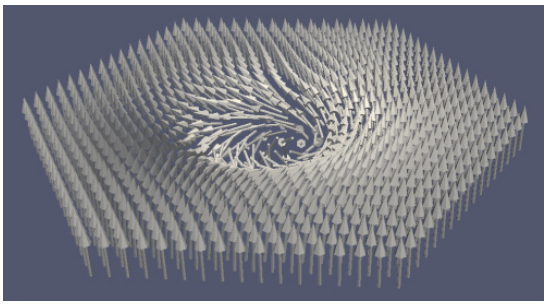

FIG. 1: A chiral skyrmion in a hexagonal lattice, courtesy of O. Sander [2]

Energy asymptotics for large fields. We are interested in effective properties of isolated skyrmions in the regime when $h \gg 1$. Of particular relevance to us are energy asymptotics, which are used in order to study the dynamic stability of skyrmions. Closely related to the energy asymptotics is the decay of the skyrmion profile at moderate distances from its core and the corresponding transition length scales. A guiding idea is that when $h \gg 1$ the suitably rescaled skyrmion profiles approach those of a sigma model soliton.

Proposition. *There exist magnetization configurations $\boldsymbol{m}_h$ with topological charge $Q(\boldsymbol{m}_h) = -1$ and*

$$E_h(\mathbf{m}_h) \leq 4\pi\left(1 - \frac{1}{h\log h}\right), \text{ if } h \gg 1.$$

Hence, the same upper bound holds for the minimal energy $\min_{Q(\boldsymbol{m})=-1} E_h(\boldsymbol{m})$.

In order to rigorously identify the scaling of minimal energies in large fields, one has to establish a matching "ansatz-free" lower bound.

However, a straightforward argument only yields the lower bound

$$E_h(\mathbf{m}) \geq 4\pi(1-\frac{1}{h}) \quad \text{if } Q(\mathbf{m}) = -1 \text{ and } h \gg 1.$$

Nevertheless, our considerations strongly support that in the regime $h \gg 1$, the logarithmic correction to the energy cannot be avoided and also a logarithmic correction to the expected skyrmion-core radius has to be taken into account; in fact, the energy $E_h(\boldsymbol{m})$ exhibits several competing terms which cannot be minimized simultaneously in the given homotopy class: While Heisenberg exchange is scaling invariant and minimized by conformal maps in this homotopy class, DMI favors a widening of the curling configuration, i.e. a large skyrmion. On the other hand, the Zeeman interaction favors small regions of misalignment with the external field, i.e. a small skyrmion. As the upper and lower bounds already show, to leading order in $h \to \infty$, $\min E_h(\boldsymbol{m})$ is given by the exchange energy of a minimizer $\mathbf{m}_h$.

Thus, we expect that $\mathbf{m}_h$ arises as perturbation of a conformal map such as a rescaled inverse stereographic projection Φ. However, $|\Phi - \hat{e}_3|^2 = 2(1-\Phi_3)$ decays only quadratically as $|x| \to \infty$. In particular, the Zeeman energy of Φ diverges logarithmically. This introduces a cut-off length scale at which a faster, presumably exponential decay of $\mathbf{m}_h$ sets in. This modification of Φ, however, will increase Heisenberg exchange. The radius of the skyrmion core will be determined by a competition of DMI and Zeeman interaction. The logarithmic growth of the Zeeman energy suggests that similar corrections to the radius of the skyrmion core and the total energy will appear. However, since our upper and lower bounds to $\min_{Q(\boldsymbol{m})=-1} E_h(\boldsymbol{m})$ do not match, it is unclear whether the additional logarithm in the energy is an artifact of our ansatz. In order to improve the lower bound, one may try to use a projection argument as in [3]; a major open problem, though, consists in proving a suitable spectral-gap type estimate for the Hessian of the exchange energy along a sequence of minimizers $\mathbf{m}_h$ of E_h in the class $Q(\boldsymbol{m}_h) = -1$.

Dynamic stability and Thiele equation. We have examined the current-driven dynamics of chiral skyrmions in the framework of the governing Landau-Lifshitz-Gilbert equation (LLG)

$$\partial_t \mathbf{m} + (\mathbf{v}\cdot\nabla)\mathbf{m} = \mathbf{m}\times\big(\alpha\,\partial_t\mathbf{m} + \beta(\mathbf{v}\cdot\nabla)\mathbf{m} - \gamma\mathbf{H}_{\text{eff}}\big),$$

where $\mathbf{v}$ is the spin drift velocity field. We claim that in the regime $h \gg 1$, when the topological charge density concentrates near the skyrmion center $\omega\,(\boldsymbol{m}_h(t)) \sim 4\pi q\,\delta_{X(t)}$ (compare [4]), i.e. the skyrmion degenerates to a charged particle at position $X = X(t)$, Thiele's equation

$$q(\dot{X} - \mathbf{v})^{\perp} + (\alpha\dot{X} - \beta\,\mathbf{v}) = 0,$$

captures the effective dynamics - at least on short time scales. A crucial aspect and difficulty in this reduction is that LLG may develop singularities in finite time. In our situation, this singularity is inherently connected with the creation and collapse of skyrmions. In fact below a certain level of smoothness, the topological charge is no longer a preserved quantity for LLG dynamics. For $\mathbf{v} = 0$, almost skyrmionic solutions relax smoothly to the equilibrium state, merely as a consequence of almost minimality and the dissipative character of LLG. In the case $\mathbf{v} \neq 0$ the system may however accumulate configurational energy, resulting in a collapse beyond the critical barrier of 4π. The energy increase between time 0 and t is controlled by

$$\big[\Delta E_h(\mathbf{m}_h)\big](t) \leq c\,\mathbf{v}^2\,\frac{\alpha}{\gamma}\int_0^t Excess(\mathbf{m}_h)\,ds,$$

where $c = (1-\beta/\alpha)^2$ is supposed to be a uniformly bounded quantity as $h \gg 1$ and

$$Excess(\mathbf{m}) = \int_{\mathbf{R}^2} \frac{|\nabla\mathbf{m}|^2}{2}dx - 4\pi,$$

which may be interpreted as conformal energy excess. In fact, for arbitrary almost skyrmionic configurations $\mathbf{m}$, i.e. $Q(\boldsymbol{m}) = -1$ and $E_h(\boldsymbol{m}) < 4\pi$ we have for $h > 1$

$$0 \leq Excess(\mathbf{m}) \leq \frac{4\pi}{h-1}.$$

According to the regularity theory for LLG, an energy barrier $E_h\big(\boldsymbol{m}_h(t)\big) = 4\pi$ needs to be overcome in order to create a singularity. In view of the energy upper bound $E_h(\boldsymbol{m}_h) - 4\pi \leq -1/(h\log h)$ at initial time, this provides a uniform life span of smooth solutions $\boldsymbol{m}_h(x,t)$ in the regime $h \gg 1$ and $\alpha/\gamma \lesssim log(h)^{-1}$. The quadratic mean distance $[\Delta\mathbf{m}_h](t)$ between the exact Thiele translation of a minimizing skyrmion $\boldsymbol{m}_h(x)$ and exact LLG solution decays to zero when $h \gg 1$

$$[\Delta\mathbf{m}_h](t) \leq c\,t\,\mathbf{v}^2\int_0^t Excess(\mathbf{m}_h)\,ds = O((t\mathbf{v})^2/h).$$

Theorem. In the regime $h \gg 1$ and $\alpha/\gamma \lesssim 1/\log h$ chiral skyrmions are dynamically stable with uniform life span that only depends on the velocity $\mathbf{v}$. Their dynamics is well-approximated by Thiele's equation of motion.

By the assumption on α/γ this is only a short time result. An improved understanding of the structure of almost skyrmionic configuration and the conjectured excess decay $Excess(\boldsymbol{m}) \lesssim 1/(h\,\log h)$ would enable us to formulate a long time result.

[1] C. Melcher, Proc. R. Soc. Lond. Ser. A Math. Phys. Eng. Sci. **470,** 20140394 (2014)

[2] O. Sander, IMA J. Numer. Anal. (2015)

[3] L. Döring and R. Ignat, Asymmetric domain walls of small angle in soft ferromagnetic films, *submitted*.

[4] M. Kurzke, C. Melcher, R. Moser, D. Spirn, Calc. Var. Partial Differential Equations **49**, 1019 (2014)

Quantum Well states and amplified spin-dependent Friedel oscillations in thin films

M. Bouhassoune, B. Zimmermann, P. Mavropoulos, D. Wortmann, P. H. Dederichs, S. Blügel, and S. Lounis

Peter Grünberg Institut-1 and Institute for Advanced Simulation, Forschungszentrum Jülich, Germany

The interactions between atoms in a material are mainly governed by electrons whose propagation in a solid determine its thermal, electrical, optical, magnetic and transport properties. Thus, the constant energy contours characterizing the electrons, in particular the Fermi surface, have a principal impact on the behavior of materials. The anisotropy of the Fermi surface induces strong directional dependence in the electronic propagation at the nanoscale in the Friedel oscillations surrounding impurities. Using density functional theory, we find a spin-dependent gigantic anisotropic charge density oscillations along specific directions after scattering at an oxygen impurity embedded in the surface of a ferromagnetic thin film of Fe grown on W(001). We demonstrate that by changing the thickness of the Fe films, we design quantum well states confined to two dimensions that manifest as multipleflat energy contours, impinging and tuning the strength of the induced charge oscillations which allow to probe the impurity at large distances (50nm).

Friedel oscillations result from the charge screening of localized defects by the electron gas of metals. The form and the magnitude of these oscillations are related to the shape of the host Fermi surface and to the nature of the defects. When the energy contour is isotropic such as in some surface states, ring-like isotropic Friedel oscillations emanate from step edges and adatoms on the surface of noble metals [1,2]. However, when the energy contour is anisotropic and bears flat regions where its curvature is small or vanishes, a focusing effect with a strong directional bundling of group velocities can shape the electronic propagation at the nanoscale after scattering with defects. This has been shown for Co impurities buried below copper surfaces by measurements performed with a scanning tunneling microscope (STM) combined with density functional theory (DFT) based simulations using the Korringa-Kohn-Rostoker Green function (KKR) method [3,4]. As a consequence, in real bulk materials Friedel oscillations are strongly anisotropic and can decay slower than $1/R^3$ contrary to the general wisdom stating that the confinement or dimensionality (*D*) of the electron gas defines the decay of the charge oscillations (R^{-D}). It was anticipated to utilize the focusing effect in a nanosonar device that would allow to detect hidden buried impurities as well as buried nanostructures [3].

Besides being fundamentally important, these oscillations mediate the interaction between atoms and can lead to superstructures of adatoms or to complex magnetic states. Thus, controlling and understanding the decay of these interactions, intimately related to the decay of the Friedel oscillations, is decisive if these atoms are used as building blocks in nano-spintronic devices.

The ability to manipulate the energy contours, and in particular Fermi surfaces, with appropriate properties such as their flatness, is desirable in order to control the decay of Friedel oscillations. In our work [5], we use quantum well states (QWS) in thin films to design two-dimensional (2D) Fermi surfaces with layer-dependent multi-flat energy contours leading to a super-slow lateral decay of the Friedel oscillation. Depending on the quantum number defining the QWS, the spatial localization of these states changes from layer to layer which is different from the case of a surface state that is strongly confined on the surface layer. This idea concretized after the experimental observation of unexpected anisotropic charge oscillations around the Fermi energy (E_F) due to a non-magnetic impurity, most probably oxygen, implanted in the surface of a thin Fe film grown on W(001) surface [6]. These Friedel oscillations show fourfold in-plane symmetry and are focused along the diagonal [110] directions of the crystal as observed in the dI/dU map for 3 monolayers (MLs) Fe on W(001).

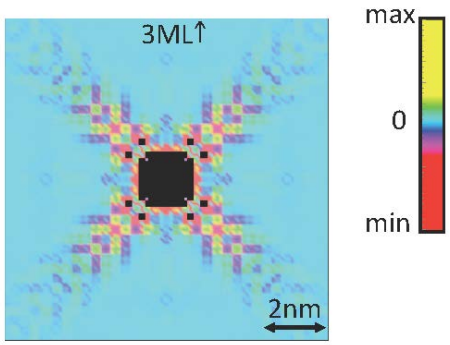

FIG. 1: Majority-spin density oscillations induced around an oxygen impurity on thin Fe films on W(001) at the E_F .

Surprisingly, these oscillations extinguish if a thinner Fe film is considered, i.e. 2 instead of 3 MLs. To understand this experimental result, we used DFT to evaluate the charge density induced by the insertion of an oxygen impurity in the ferromagnetic surface of 2 and 3 MLs Fe deposited on W(001) surface. The spatial modulation at E_F of the induced charge density by oxygen calculated in the vacuum at a distance of 3.165 Å above the Fe surface layer is illustrated for 3MLs Fe majority-spin channels (Fig. 1). The fourfold symmetry of the anisotropic oscillations observed in the experiment is obtained theoretically and is notably pronounced for the majority-spin channel of 3 MLs Fe and much stronger than those of its minority-spin channel or those obtained from both spin channels of 2 MLs Fe. The charge oscillations of the majority-spin channel in the [110] direction have the highest amplitude and survive the longest away from the impurity. These results imply spin-filtering in that the spin-nature of the oscillations observed experimentally are of majority-spin type. As explained below, this surprising behavior is related to confinement effects in the Fe films.

This behavior is explained, as stated earlier, by the shape of the Fermi surface of the host metal which deviates from the spherical symmetry. Using the stationary phase approximation, the energy-dependent charge density induced at a large distance *R* from the impurity reads [5]

$$\Delta n(\vec{r};E) = \sum_{k_j - k_j} |t_{\vec{k}_j - \vec{k}_j}| \frac{\sin(2k_{zj}R + 2\varphi_j + \delta_{\vec{k}_j})}{R^{d-1}C} \quad (1)$$

Where $C = \frac{\partial^2 E}{\partial k_{xj}^2}\frac{\partial^2 E}{\partial k_{yj}^2}|$ is the curvature measuring the flatness of the Fermi surface at a point *j*. *t*, δ and φ are energy dependent quantities defining, respectively, the scattering-strength, the phase-shift that Bloch wave functions experience after scattering and a contour related phase. When the curvature *C* goes to zero, the energy contour is flat, which leads to a large variation of the induced charge density and consequently to highly focused beam intensity.

The Fermi surface of our materials can be observed in the 2D Bloch spectral function at E_F for both spin channels (majority and minority). We notice the presence of extremely flat regions on the diagonal [110] direction in the majority-spin of 3 ML Fe/W(001). Here the change in density according to equation (1) is maximized in the direction normal to these flat regions and thus having a higher directional beam intensity than in other directions. Actually, it is these states that are responsible for the well pronounced long range anisotropic Friedel oscillations. We notice by increasing the number of Fe MLs (more than 3MLs) the presence of multiple flat regions, which belong to QWS. These QWS are created because the Fe majority-spin states cannot propagate into the gap regions found in the substrate. Their number increases from 2 to 5 when increasing the number of layers from 5 to 11 ML (Fig. 2). These will strengthen the amplitude of the Friedel oscillations and slower their decay. In the majority-spin channel of the 2D Bloch spectral function of 2 ML Fe/W(001), the flat areas disappear. Since the QWS do not cross the Fermi level, they do not contribute to the Friedel oscillations measured at E_F. This explains the extinction of the charge ripples at large distances.

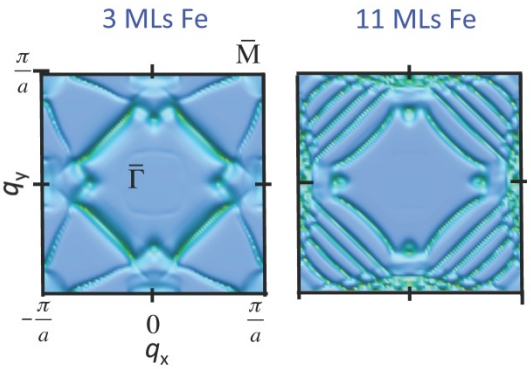

FIG. 2: Majority-spin 2D Bloch spectral function at E_F in the first Brillouin zone projected on the Fe surface layer.

We find large focused long-range and large amplitude majority-spin density oscillations at the Fe surface created by spin-polarized quantum well states of Fe films on W(100). Our finding demonstrates the possibility to design and control of quantum well states in supported thin layers that lead to a super-amplification of interaction effects. This can impact on the lateral coupling of magnetic nanostructures at the vicinity of the surface. For magnetic films, in particular, there is a strong amplification of a selected spin component (spin filtering) which can be detected at large distances from embedded non-magnetic defects. This may have an impact in nanotechnology, since spin-information can be transmitted laterally to large distances. The choice of the substrate and the thickness of the film are of crucial importance in terms of their electronic structure to obtain a giant laterally focused signal far away from the imperfections located in the surface of thin films.

This work was funded by the HGF-YIG programme Funsilab - Functional Nanoscale Structure Probe and Simulation Laboratory (VH-NG-717). B. Z. is supported by the HGF-YIG programme VH-NG-513.

[1] M. F. Crommie, C. P. Lutz, and M. D. Eigler, Science **262**, 218 (1993)

[2] F. Silly, M. Pivetta, M. Ternes, F. Patthey, J. P. Pelz, and W. D. Schneider, Phys. Rev. Lett. **92**, 16101 (2004)

[3] A. Weismann, M. Wenderoth, S. Lounis, P. Zahn, N. Quaas, R. G. Ulbrich, P. H. Dederichs, and S. Blügel, Science **323**, 1190 (2009)

[4] S. Lounis, P. Zahn, A. Weismann, M. Wenderoth, R. G. Ulbrich, I. Mertig, P. H. Dederichs, and S. Blügel, Phys. Rev. B **83**, 35427 (2011)

[5] M. Bouhassoune, B. Zimmermann, Ph. Mavropoulos, D. Wortmann, P. H. Dederichs, S. Blügel, S. Lounis, Nature Comm. **5**, 5558 (2014)

[6] K. von Bergmann, PhD Thesis, University of Hamburg (2004)

Robust Quantum Anomalous Hall Effect from First Principles

C. Niu[1], P. Buhl[1], G. Bihlmayer[1], H. Zhang[2], D. Wortmann[1], S. Blügel[1], and Y. Mokrousov[1]

[1] Peter Grünberg Institut-1 and Institute for Advanced Simulation-1, Forschungszentrum Jülich, Germany
[2] Department of Physics and Astronomy, Rutgers University, Piscataway, New Jersey 08854, USA

Realizing the quantum Hall effect at room temperature and without external magnetic field has always been a dream of researchers in the field of condensed-matter physics. The recent interest for new large band gap quantum anomalous Hall (QAH) insulators is based on their potential for showing dissipationless charge transport at the edges of these materials. Here we predict, based on density functional theory (DFT) calculations, that the band gap of QAH states can be as large as 0.35 eV in a half H-decorated Bi(111) film. Moreover, we find that the QAH state is maintained when half H-decorated Bi(111) lies on a ($\sqrt{3}\times\sqrt{3}$) MoS_2 substrate. Our results indicate the feasibility of the QAH effect in the room-temperature regions.

The QAH effect, which was first suggested to occur in a honeycomb lattice model, has been achieved recently in Cr-doped topological insulators $(Bi,Sb)_2Te_3$ [1] via suppressing one of the spin channels, but requires extremely low temperatures (30 mK). For obtaining the room temperature QAH-based electronic devices, searching for novel materials with large band gaps as well as stable atomic and magnetic structures has been a fairly important topic in the field. As the heaviest atom with effectively stable isotope and strong SOC, bismuth is an important ingredient for both two-dimensional (2D) and three-dimensional topological insulators (TIs). The Bi(111) bilayer has drawn much attention due to a relatively large band gap of the 2D system (~0.2 eV) and the QAH effect was predicted with the ferromagnetism induced by a 3d transition metal [2, 3]. However, on weakly interacting substrates ultrathin, (111) oriented films are unstable with respect to transformation into another allotrope of Bi and turn out to be topologically trivial. If the interaction is stronger, doping shifts the bandgap out of the transport regime.

Based on first-principles calculations, we show that both the electronic and topological properties of ultrathin Bi films can be drastically modified when decorated by H, and the stability is confirmed by DFT phonon calculations that show no imaginary frequency [4]. H-decorated Bi(111) films (H-Bi(111)) exhibit a topological energy gap of 1.01 eV, that is much larger than those in known TIs. To identify the band topology, the Z_2 invariant is investigated by evaluating the wave function parities at four time reversal invariant momentum (TRIM) points, i.e. the Γ and three M points. The calculated Z_2 = 1 verifies that the H-Bi(111) is a QSH insulator. The existence of gapless edge states is a prominent feature of QSH insulators. To see it explicitly, we construct nanoribbon structures of H-Bi(111) with symmetric edges and plot the band structures in Fig. 1(a). The width of zigzag H-Bi(111) and armchair H-Bi(111) nanoribbons are 8.2 and 8.8 nm, respectively, which are large enough to avoid interactions between the edge states. The dangling bonds of edge atoms are saturated by H. One can easily see that gapless edge states, which bridge the conduction and valence bands of the 2D system, appear and cross linearly at the Γ (Y) point. This Dirac-like behavior demonstrates further the topological nontrivial character of H-Bi(111).

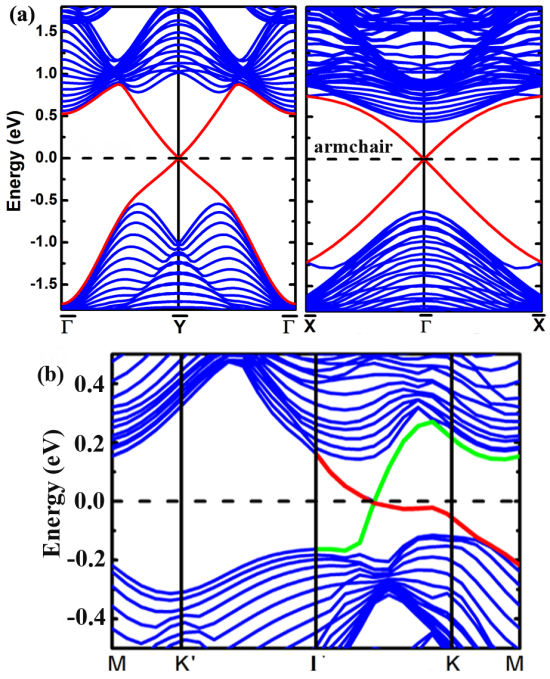

FIG. 1: Calculated band structure of (a) full H-decorated and (b) half H-decorated Bi(111) nanoribbon. The gapless edge states (red lines) appear and cross linearly for full H-decorated case (both the zigzag-terminated and armchair-terminated). For half H-decorated case, the states located at different edges, which exhibit valley-polarized QAH states, are indicated by different colors (red/green).

When the hydrogen atoms are removed from one side of H-Bi(111) [what we call half H-decorated Bi(111)], a stable ferromagnetic ordering is

realized with a sizable indirect energy gap of 0.35 eV, and the spin-polarization is mainly carried by the p_z states of the unhydrogenated Bi atoms [4]. To identify the topological properties and predict a stable QAH state resulting from the sizable energy gap, we calculate the anomalous Hall conductivity $\sigma_{xy} = (e^2/h)C$, where C is quantized and known as the first Chern number in case of an insulator. It can be obtained as an integral of the Berry curvature of the occupied states, $\Omega(\mathbf{k})$, over the Brillouin zone. An integer value of +1 confirms the QAH effect in semihydrogenated Bi(111) bilayer.

However, half H-decoration of the Bi(111) bilayer leads to the breaking of time-reversal symmetry and inversion symmetry simultaneously. The valleys *K* and *K′* are distinguishable and the valley-polarized QAH state, which exhibits properties of both QAH state and quantum valley Hall (QVH) state ($C_K = 1$ and $C_{K'} = 0$), is obtained. To further confirm the valley-polarized QAH state, edge states of zigzag-terminated half H-decorated Bi(111) at valleys *K* and *K′* are calculated and are shown in Fig. 1(b). The number of edge states in each valley indeed corresponds to the corresponding valley Chern number.

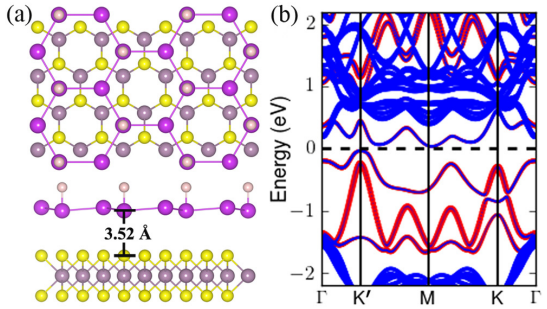

FIG. 2: (a) Top and side view of the energetically favored structure and (b) band structures with SOC of a half H-decorated Bi(111) bilayer on a substrate of (√3 × √3) MoS_2. Bi and H atoms are shown in purple and white, while Mo and S are depicted as grey and yellow spheres, respectively. The number in panel (a) shows the spacing between the top S and the lowest Bi layer. States shown in red in (b) are derived from the semihydrogenated Bi bilayer, while blue indicates states originating from the substrate.

For device applications, it is important to support the 2D materials on a substrate. Given a large enough bulk band gap of the lattice-matching substrate, which is aligned with the Bi-originated 2D gap, one has to make sure that the predicted topological properties are preserved. While owing to the enlarged lattice constant of the H-Bi(111) both Bi(111) and Bi chalcogenides are not suitable for the purpose, we demonstrate this taking MoS_2 (√3 × √3) as an example substrate, which fits the hydrogenated Bi nicely both in lattice constant as well as in alignment of the band gaps. Fig. 2(a) shows the top and side view of the energetically favored structure, and the corresponding band structures with SOC is shown in Fig. 2 (b). Similar to the case without substrate, the Fermi level is pinned inside the gap and the band structures at valleys *K* and *K′* have different patterns, demonstrating that the valley- polarized QAH state survive for half H-decorated Bi(111) on the MoS_2 substrate.

In summary, by performing DFT calculations for semihydrogenated Bi(111), we have demonstrated that the QAH states with giant band gaps can be realized. It exhibits the properties of both QAH state and QVH state, realising a new quantum state, called valley-polarized QAH insulator. We further verify that valley-polarized QAH states survive even if the decorated Bi bilayers are on an appropriate substrate.

Besides the TI-based QAH state, the recently predicted topological crystalline insulators (e.g. SnTe) bear great potential for the investigation of the QAH states with exotic phenomena, such as with the large Chern number and with the variable magnetic direction. We demonstrated by DFT calculations that also ultrathin PbTe and SnTe layers can be stabilized in NaCl quantum well structures with sizable bandgaps and robust QAH states [5].

This work was supported by the Priority Program 1666 of the German Research Foundation (DFG), the Virtual Institute for Topological Insulators (VITI) and the Project No. VH-NG-513 of the Helmholtz Association (HGF).

We acknowledge computing time on the supercomputers JUQUEEN and JUROPA at the Jülich Supercomputing Centre and JARA-HPC of RWTH Aachen University.

[1] C. Z. Chang, J. Zhang, X. Feng, J. Shen, Z. Zhang, M. Guo, K. Li, Y. Ou, P. Wei, and L. L. Wang, Science **340**, 167 (2013).

[2] H. Zhang, F. Freimuth, G. Bihlmayer, S. Blügel, and Y.Mokrousov, Phys. Rev. B **86**, 035104 (2012).

[3] H. Zhang, F. Freimuth, G. Bihlmayer, M. Ležaić, S. Blügel, and Y. Mokrousov, Phys. Rev. B **87**, 205132 (2013).

[4] C. Niu, G. Bihlmayer, H. Zhang, D. Wortmann, S. Blügel, and Y. Mokrousov, Phys. Rev. B **91**, 041303(R) (2015).

[5] C. Niu, P. M. Buhl, G. Bihlmayer, D. Wortmann, S. Blügel, and Y. Mokrousov, accepted in Phys. Rev. B **91**, 201401 (2015)

Exploring the chemical-bonding nature of amorphous GeTe

V. L. Deringer[1], W. Zhang[2,3], M. Lumeij[1], S. Maintz[1], M. Wuttig[3], R. Mazzarello[2], and R. Dronskowski[1]

[1] Institute of Inorganic Chemistry, RWTH Aachen University, Germany
[2] Institute for Theoretical Solid-State Physics, RWTH Aachen University, Germany
[3] I. Institute of Physics A, RWTH Aachen University, Germany

Phase-change materials are crucial chemical ingredients for modern information technology: their crystalline and amorphous phases encode "ones" and "zeroes" in digital media, respectively. Nonetheless, even the binary germanium telluride, GeTe, continues to pose fundamental questions. Here, we explore one of them: the chemical nature of diverse local structural fragments which coexist in its amorphous phase. To do so, large-scale *ab initio* molecular-dynamics simulations are combined with novel bond-analytical tools [1].

In crystalline materials, atoms are periodically ordered and often form aesthetically pleasing structures. Amorphous or "glassy" solids lack such long-range order, but they are no less interesting for scientists and industry alike. Amorphous phase-change materials (PCMs) are prominent examples [2], with structural diversity in the first coordination shell already: take amorphous GeTe, in which octahedra and tetrahedra coexist, and short Ge–Ge contacts occur, unlike in the crystalline counterpart [3]. The property contrast between crystalline and amorphous PCMs is a direct consequence of such atomic-scale complexity (Fig. 1).

Not surprisingly, the structure of amorphous PCMs has been under thorough study (and debate) over the recent years. Besides experiments such as extended X-ray absorption fine structure (EXAFS) spectroscopy, a key role is increasingly played by theory and simulation. Today, amorphous PCMs are quite routinely investigated by a complementary combination of experiments and *ab-initio*-quality molecular dynamics (MD) simulations [2,3].

To handle the sheer numerical effort associated with such simulations, plane-wave based density-functional theory (DFT) has become the workhorse of choice. Plane-wave basis sets are highly efficient, but due to their delocalised nature, they do not allow intuitive "chemical" interpretation of the simulation output in terms of atom-resolved, local quantities [4]. Fortunately, it is principally possible to retrieve the latter information: namely, by a basis-set transfer or *projection* from the plane-wave expansion into an auxiliary set of atom-centred orbitals (say, one 4s and three 4p at each Ge atom). Over the recent years, we have developed such projection techniques [5] and implemented them into the LOBSTER code (www.cohp.de). This makes it possible to study the output of large-scale DFT computations, including *ab initio* MD results for amorphous materials.

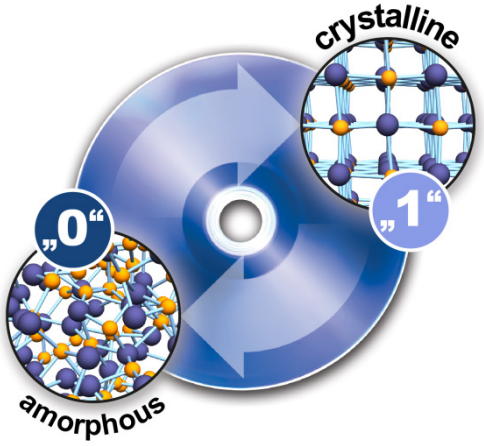

FIG. 1: Structural models for crystalline and amorphous GeTe which iconise "one" and "zero" bits in phase-change data storage devices. Chemically, the binary compound is a close relative of the material $Ge_8Sb_2Te_{11}$ which is used in re-writeable Blu-ray disks [2].

The recipe follows from the classical chemical notion of bonding (stabilising) and antibonding (destabilising) pairwise interactions: the crystal orbital overlap population (COOP) identifies such interactions between neighbouring atoms based on the overlap of the valence orbitals involved [4]. For crystalline GeTe, such analysis is straightforward: all atoms reside in slightly distorted octahedral environments (Fig. 1). In amorphous GeTe, the situation is more delicate: there is no translational symmetry, so *each* bond in the simulation cell is unique, and the supercell models used for GeTe each contain thousands of close contacts. In a first step, we inspect projected COOPs integrated up to the Fermi level, yielding a quantity (henceforth "bond population") which may be correlated with individual bond strengths [4,5], and the results for amorphous GeTe as retrieved from LOBSTER output have been plotted in Fig. 2a.

How to handle and interpret such large datasets? Similar questions already arise for purely structural analyses, and in the latter case, the radial distribution function (RDF) is used to visualise the frequency of pairwise contacts in an MD trajectory. We follow a similar train of thought here and introduce what we call the "bond-weighted distribution function" (BWDF), obtained by collecting or "binning" the distribution of bond populations.

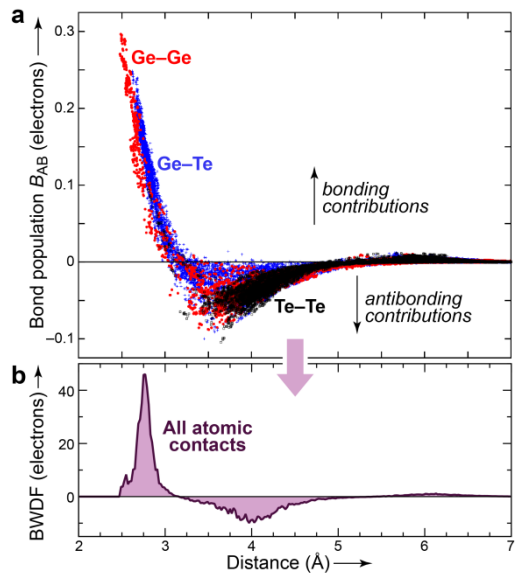

FIG. 2: (a) Bond populations (pCOOPs energy-integrated up to ε_F) for atomic contacts in amorphous GeTe; positive values identify stabilisation. Data have been collected for all A–B contacts up to 7 Å and over a total of ten relaxed MD snapshots. (b) The newly introduced bond-weighted distribution function (BWDF), which condenses the above dataset into a single line as described in the text. Reproduced from Ref. [1]. © 2014 Wiley-VCH Verlag GmbH & Co. KGaA, Weinheim.

The results are shown in Fig. 2b: one obtains a single curve, reminiscent of the RDF, but the new indicator takes positive or negative values as it additionally carries bonding information. This gives a first "fingerprint" of local chemical interactions in amorphous GeTe: short contacts below ≈ 3 Å are strongly stabilising, as expected, while at larger interatomic distances repelling interactions become predominant (BWDF < 0), best seen at around 4 Å. The latter is easily understood as mainly Te·Te contacts occur in these regions (Fig. 2a). At even larger interatomic separation, the BWDF curve approaches zero, naturally so as covalent bonding requires the valence orbitals to overlap.

The results so far allow for a first glimpse, but to be really useful one needs to separate the data further. Once more in analogy to the RDF, one may calculate a "partial" BWDF which contains only certain atomic species. Fig. 3 provides such partial BWDFs which have been further resolved according to local atomic environments (the aforementioned coexistence of tetrahedral- and octahedral-like motifs is sketched in Fig. 3a). The partial BWDF curves reveal particularly interesting behaviour for homopolar Ge–Ge bonds in amorphous GeTe: the latter notably stabilise tetrahedral fragments (evidenced by a positive BWDF peak around 2.6 Å), but they do not significantly stabilise defective octahedral environments. Such a bonding contrast is not observed for the heteropolar Ge–Te contacts (Fig. 3c), which appear rather insensitive to the local structure.

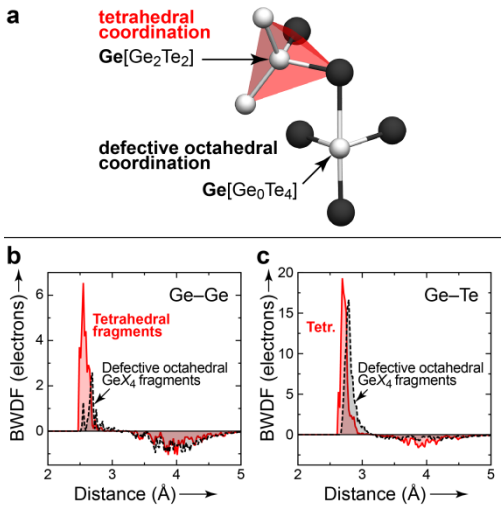

FIG. 3: (a) Structural fragment from amorphous GeTe, highlighting the different coordination environments (tetrahedral vs octahedral) in which Ge atoms are found. (b,c) Selective BWDFs, obtained by summing only over homopolar (Ge–Ge) and heteropolar (Ge–Te) contacts, and also resolved according to the different local environments which are sketched above. Reproduced from Ref. [1]. © 2014 Wiley-VCH Verlag GmbH & Co. KGaA, Weinheim.

In conclusion, we have developed new tools to study chemical bonding in amorphous materials, thereby combining *ab initio* MD simulations with projection-based bond-analytical tools. They afford an unprecedented local view into atomic interactions, as we have shown here for amorphous GeTe. Future work will explore how the amorphous network and the structural motifs therein evolve over time, with implications for the technologically relevant long-term stability of amorphous "zero bits".

This work was supported by the Deutsche Forschungsgemeinschaft (SFB 917 "Nanoswitches") and the Studienstiftung des deutschen Volkes (scholarship to V.L.D.). Large amounts of CPU time were provided by JARA-HPC.

[1] V. L. Deringer, W. Zhang, M. Lumeij, S. Maintz, M. Wuttig, R. Mazzarello, R. Dronskowski, Angew. Chem. Int. Ed. **53**, 10817 (2014).

[2] M. Wuttig and N. Yamada, Nat. Mater. **6**, 824 (2007).

[3] S. Caravati, M. Bernasconi, T. D. Kühne, M. Krack, M. Parrinello, Appl. Phys. Lett. **91**, 171906 (2007).

[4] R. Dronskowski, Computational Chemistry of Solid-State Materials, Wiley, Weinheim (2005).

[5] S. Maintz, V. L. Deringer, A. L. Tchougréeff, R. Dronskowski, J. Comput. Chem. **34**, 2557 (2013); see references therein for further information on the underlying projection and analysis techniques.

Crystallization in the canonical phase-change material $Ge_2Sb_2Te_5$: a new memory effect

R. O. Jones[1], J. Akola[2], and J. Kalikka[3]

[1] Peter Grünberg Institut-1, Forschungszentrum Jülich, Germany
[2] Tampere University of Technology, Finland
[3] Singapore University of Technology and Design, Singapore

The crystallization of amorphous $Ge_2Sb_2Te_5$ (GST) has been studied using four extensive (460 atoms, up to 5 ns) density functional (DF)/ molecular dynamics (MD) simulations at 600 K. An amorphous sample obtained from heating a previously crystalline structure shows a "memory effect", since it crystallizes completely in 1.2 ns, while crystallization in other samples was slower and less complete after 5 ns. Crystallization is accompanied in all cases by an increase in the number of "*ABAB* squares" (*A*: Ge, Sb; *B*: Te), percolation of crystalline clusters, and the occurrence of low-frequency localized vibration modes. Three structures display phases (> 1 ns) with sub-critical nuclei (10-50 atoms) ranging from nearly-cubical blocks to string-like configurations of *ABAB* squares and *AB* bonds extending across the cell. Cavities play a crucial role, and the final ordered structure is distorted face-centered-cubic with a sublattice containing predominantly Te atoms. GST is a rare system where crystallization can be simulated without adjustable parameters over the physical time scale, and the results could provide insight into order-disorder processes in general.

Phase change (PC) materials are chalcogenide (group 16) alloys that are ubiquitous in the world of rewritable optical storage media, familiar examples being digital versatile disk (DVD-RW) and Blu-ray Disc. Nanosized bits in a thin polycrystalline layer are switched reversibly and extremely rapidly between amorphous (a-) and crystalline (c-) states by laser irradiation or resistive heating, and the state can be identified by changes in resistivity or optical properties. The rate limiting process in the write/erase cycle is the re-crystallization of the amorphous bit, and demands for increasingly rapid transfer have focused much attention on this process. Two families of chalcogenide alloys dominate practical applications: $(GeTe)_{1-x}(Sb_2Te_3)_x$ pseudobinary alloys and doped alloys of Sb and Te near the eutectic composition $Sb_{70}Te_{30}$. Digital versatile disk (DVD)-RAM and Blu-ray Disc are examples of the first family, where $Ge_2Sb_2Te_5$ (GST, x=1/3) is often taken as a prototype, and DVD-rewritable disks provide examples of the second.

Crystallization of the amorphous bit is the rate-limiting step in the write/erase cycle, and much attention has been focused on this process. We have performed four 460-atom DF/MD simulations of amorphous GST at 600 K and monitored changes in the distribution of cavities, the diffusion of atoms of the different elements, the vibration frequencies, and percolation of crystalline units in each sample. Crystallization takes place in just over 1 ns in one sample (*run0*), but it is significantly slower in the other three *(run1-3).* The differences provide insight into the crystallization process, which is favoured in these materials by the presence of cavities.

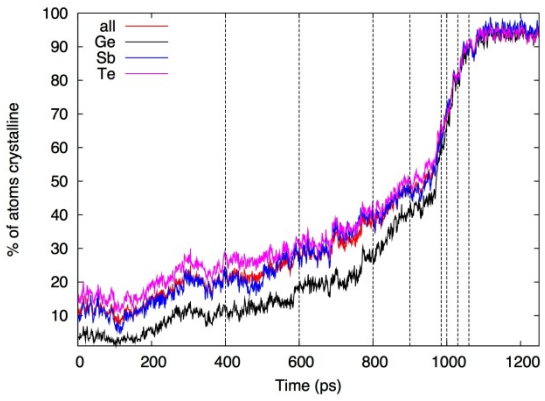

FIG. 1: Percentage of crystalline atoms by element (Ge, Sb, Te). The vertical dashed lines mark reductions in the supercell size to reflect density changes. See Ref. [1].

An example of the results for *run0* is shown in Fig. 1, where the percentages of crystalline atoms for Ge, Sb, Te and all atom types are shown. Rapid crystallization occurs at 600 K between 900 ps and 1100 ps, where the process is essentially complete. The coordinates and velocities of all atoms are monitored throughout the simulations, and this enables us to follow details of the process that are difficult to determine in amorphous materials by other means. In Fig. 2, we compare the structures of GST at the beginning (215 ps) and end (1100 ps) of *run0*. Full details of all simulations and their analysis are given in Ref. 1.

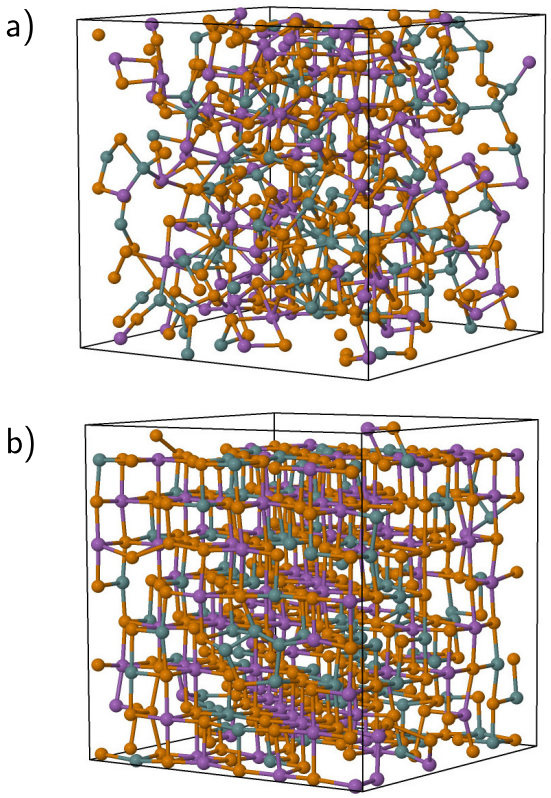

FIG. 2: Crystallization in GST alloy at 600~K. (a) Amorphous structure after 215 ps, (b) crystalline structure after 1045 ps. Green: Ge, purple: Sb, Orange: Te

The simulation *run0* required over 400,000 self-consistent DF calculations of energies and forces for a 460-atom sample, and it was exciting to witness the gradual transition from an amorphous sample to a crystal without driving it in any way. A crucial pattern in the process is the increase in the number of *ABAB* squares (*A*: Ge, Sb; *B*: Te) [2], and the final structure is similar to that proposed by Yamada [3]: a rock salt structure with Te atoms on one sublattice and a random assembly of Ge and Sb atoms and vacancies on the other. The suggestion of Yamada has been accepted by most workers in the field, but the speed of the phase change means that a distorted structure is inevitable.

The starting structure for *run0* showed no signs of order, but the speed of crystallization and the alignment of the final structure along the axes of the simulation cell were not found in the other simulations *runs1-3.* The starting configuration of the latter simulations was the amorphous structure found in Ref. [2], the only difference being the initial velocity distributions at 600 K. These apparently small differences led to large differences in the crystallization pocess.

Runs1-3 have been carried out to 5 ns, which means that each involves over 1.6 million (!) self-consistent DF calculations for a system with 460 atoms. Calculations of this scale were unthinkable only a few years ago. The simulation trajectories show crystallization directions that are unrelated to the axes of the simulation cell, and they show subcritical phases with ordered clusters of 10-50 atoms prior to the onset of crystallization. The speed of crystallization from the subcritical phases is similar in all samples, although the onsets differed. Two of the simulations show multiple clusters and 'polycrystalline' final structures. The final structure in all cases show the existence of low-frequency, localized vibrational modes that are not present in the original amorphous structures. Percolation initiates the rapid phase of crystallization and is coupled to the directional p-type bonding in metastable GST. The apparent acceleration of crystallization in a sample with an ordered history could lead to improved optical storage media.

These four simulations have provided much new information about crystallization in a material of technological importance, but the stochastical nature of the process limits the information that they provide. Nevertheless, they involve many more atoms and much longer times than all previous DF studies of the process, and they raise questions about the findings of most, in particular those of a recent study [4] that indicated that all cavities segregate to the amorphous-crystalline boundary, leaving a cavity-free crystal. There is no evidence for this mechanism in any of our simulations.

It is very unusual for a phase transition to be fast enough (nanoseconds in this case) to be accessible to DF calculations, which are free of adjustable parameters, under the actual conditions of temperature and timescale. The details of the structural change should shed light on the mechanisms of other phase transitions.

Essential to the success of such calculations has been the steady improvement in numerical algorithms and computer programs during the past decades, but they also require computers of the highest performance class. These calculations have been made possible by grants of computer time by the JARA-HPC Vergabegremium on the JARA-HPC partition of the supercomputer JUQUEEN in the Forschungszentrum Jülich and by time granted on the supercomputer JUROPA at Jülich Supercomputer Centre.

[1] J. Kalikka, J. Akola, and R. O. Jones, Phys. Rev. B **90**, 184109 (2014).

[2] J. Akola and R. O. Jones, Phys. Rev. B **76**, 235201 (2007); Phys. Rev. Lett. 100, 205502 (2008).

[3] N. Yamada, MRS Bulletin **21**, 48 (1996).

[4] T. H. Lee and S. R. Elliott, Phys. Rev. B **84**, 094124 (2011).

Simulations of Crystallization of Phase-Change Materials

W. Zhang[1,2], I. Ronneberger[1], P. Zalden[2,3], M. Xu[2], M. Salinga[2], M. Wuttig[2,4], and R. Mazzarello[1,4]

[1] Institute for Theoretical Solid State Physics, RWTH Aachen University, Germany
[2] I. Physikalisches Institut A, RWTH Aachen University, Germany
[3] Stanford Institute for Materials and Energy Sciences, SLAC National Accelerator Laboratory, Menlo Park, USA

Phase-change materials (PCMs) are very promising candidates for non-volatile memories of next generation, due to a) their ability to switch rapidly and reversibly between the crystalline and the amorphous phase at high temperature, b) the stability of both states at room temperature and c) the pronounced resistivity contrast between the two phases [1]. Recently, time-resolved reflectivity measurements of the PCM $Ag_4In_3Sb_{67}Te_{26}$ (AIST) showed that the glass transition temperature T_g of this material depends significantly on the cooling/heating rates and its growth velocity obeys the Arrhenius law below 550 K, with high activation energy [2]. Here we report on *ab initio* molecular dynamics (AIMD) simulations of crystallization of AIST, which employ density functional theory (DFT) [3]. We show that, at high temperature, the computed crystallization speed is in good agreement with experimental data and we provide an in-depth understanding of the crystallization mechanisms at the atomic level. On the other hand, at lower temperatures, discrepancies between simulations and experiments are observed. We attribute these deviations to the high fragility of the system, in combination with the very fast quenching rates employed in the simulations.

We consider models of AIST containing 810 atoms. The AIMD simulations are carried out using Quickstep, a mixed Gaussian-plane wave code included in the package CP2K [4]. We employ gradient-corrected exchange -correlation functionals and Goedecker pseudopotentials. Since it is known that crystallization of small amorphous marks of AIST surrounded by a crystalline region is dominated by the growth at the interface, we study amorphous and supercooled liquid models of AIST inside a crystalline matrix and investigate the growth of the interface at different temperatures.

We start our analysis focusing on the crystallization process at high temperature (585 K). We consider crystal growth along the [0001] direction of the hexagonal lattice formed by AIST. Crystallization is observed to occur at the amorphous-crystalline interface, in agreement with experiments. Some snapshots of one of our AIMD trajectories is shown in Fig. 1. Based on the crystallization trajectories, we derive the growth velocity v_g. Specifically, we calculate the evolution of the number of crystalline-like particles, N_c. By multiplying the ratio N_c/N (where N is the total number of particles) by the cell parameter along the growth direction and dividing by the corresponding time t, v_g is obtained. Averaging over four trajectories, we obtain v_g = 7.8 m/s, which is consistent with the time-resolved reflectivity measurements [2].

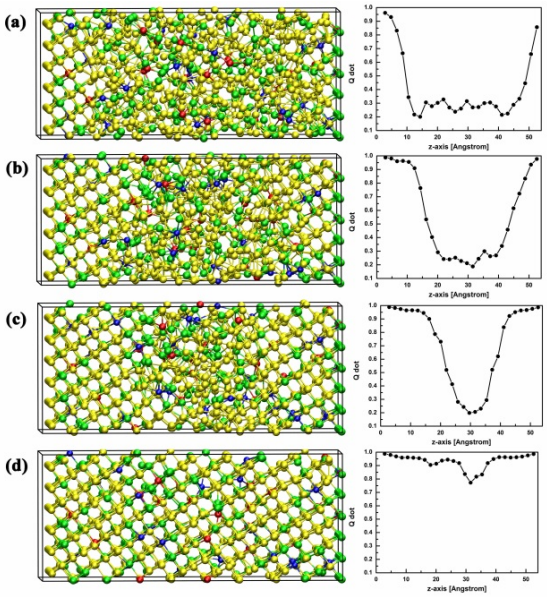

FIG. 1: (a-d) Snapshots of the crystallization process of AIST (at T=585 K) at 0, 60, 120 and 170 ps and corresponding profiels of the bond order parameter Q_4^{dot}. This parameter can appropriately discriminate between the crystalline and amorphous states. Ag, In, Sb and Te atoms are rendered with blue, red, yellow and green spheres respectively. Q_4^{dot} is averaged both over the atoms within each slab and over time (0.6 ps).

To better understand the crystallization mechanisms, we inspect the properties of the amorphous-crystalline interface. We calculate the profiles of the atomic population, the bond order parameter Q_4^{dot} (see Fig. 1) and the diffusion coefficient *D* along the growth direction. These profiles indicate that the interface is thin: it extends over 8 Å only. The sharp interface, together with the large diffusion coefficients in the amorphous state, ensures a very high mobility of the atoms near the crystalline surface. To better quantify the

growth process, we calculate the sticking coefficient for atoms impinging on the surface. This coefficient turns out to be large [3]. Hence, the interplay between large diffusivities, large sticking coefficients and sharp crystal/amorphous interfaces results in fast crystal growth

We now consider the growth velocity of AIST at lower temperatures. We calculate v_g at 3 additional temperatures (550 K, 500 K and 455 K). The obtained values range between 5 and 7 m/s. It turns out that the values at T = 455 K and 500 K are in very poor agreement with experiments, which yielded growth velocities between 10^{-2}–10^{-5} m/s in this temperature range [2]. This discrepancy mainly stems from the large difference between the calculated and experimental diffusion coefficients, as shown in Fig. 2.

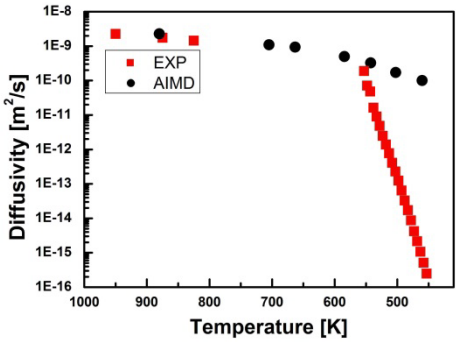

FIG. 2: Calculated and experimental diffusion coefficients of AIST [3]. The theoretical coefficients are obtained by evaluating the atomic mean square displacements in the amorphous models on an 80 ps time scale. Experimental values of D at T below 600 K are obtained from the growth velocity measurements in [2].

At low temperature, experimental diffusivities are extracted from the growth velocity data of Ref. 2 using the Wilson-Frenkel formula. The diffusivities exhibit Arrhenius behaviour with high activation energy E_a = 2.78 eV and large prefactor D_0 = 2×10^{15} m^2/s [2]. In contrast, at higher temperatures, an activation barrier of about 0.24 eV and a prefactor of 4.1×10^{-8} m^2/s were observed experimentally for similar compounds [5]. The very pronounced change in E_a and D_0 near T_g indicates that AIST is highly fragile. Fragility ensures the combination of fast recrystallization at elevated T and high stability of the amorphous phase at low T. The two properties are crucial for the utilization of PCMs in data storage applications. The change in E_a and D_0 reflects the slowing down of the kinetics, which stems from an increasingly cooperative character of the atomic motion.

On the other hand, by fitting the theoretical data for the diffusion coefficients in the temperature range between 450 K and 585 K, we obtain E_a = 0.30 eV and D_0 = 2.2×10^{-7} m^2/s, which are in fair agreement with the high-temperature experimental data, but not with the low-temperature values. We have been able to rule out the possibility that these deviations are due to finite size effects [3]. Instead, we attribute the discrepancy to the difference in quenching rates, namely, 10^{13} K/s (simulations) versus 10^{10} K/s (experiments). If the cooling rate applied to a fragile system is too fast, the resulting glass is less stable and more prone to crystallization. Fast quenching generally results in poor sampling of the potential energy landscape. In a fragile system, due to the complex topography of the energy landscape, which typically consists of well-separated large basins [6], poor sampling leads to markedly different dynamical properties. Strong glasses are expected not to exhibit this behaviour.

Very recently, we have also performed high temperature (600 K) AIMD simulations of crystallization of $Ge_2Sb_2Te_5$ (GST), an important PCM used in DVD-RAM and phase-change memories [7]. Recrystallization of GST is known to be triggered by nucleation events. In our work, we simulate the stochastic processes of nucleation by using metadynamics, an enhanced sampling method [8] which enables us to accelerate the formation of sizable nuclei, and then we let the nuclei grow by performing standard “unbiased” simulations. Similarly to the simulations of AIST, we also consider amorphous models inside a crystalline matrix, so that crystallization occurs via growth from the interface. With decreasing cell size in non-volatile phase-change memories, this recrystallization mechanism is expected to prevail over nucleation even in GST, eventually. The two sets of simulations yield growth velocities of the order of 1 m/s, which are in fair agreement with previous experimental work [9]. These simulations also provide evidence that, upon fast crystallization from the amorphous phase on a subnanosecond time scale, a disordered cubic phase of GST is formed, in which the distribution of vacancies, Ge and Sb appears to be uncorrelated. Hence, the simulations corroborate the existence of vacancy clusters in rapidly crystallized GST, which have been shown to induce localization of the electronic states at the Fermi energy [10].

[1] M. Wuttig and N. Yamada, Nature Mater. **6**, 824 (2007).

[2] M. Salinga, E. Carria, A. Kaldenbach, M. Bornhöfft, J. Benke, J. Mayer, and M. Wuttig, Nature Comm. **4**, 2371 (2013).

[3] W. Zhang, I. Ronneberger, P. Zalden, M. Xu, M. Salinga, M. Wuttig, and R. Mazzarello, Sci. Rep. **4**, 6529 (2014).

[4] J. VandeVondele et al., Comput. Phys. Commun. **167**, 103 (2005).

[5] F. W. Herwig, Z. Metallkd. **83**, 35 (1992).

[6] P. G. Debenedetti and F. H. Stillinger, Nature **410**, 259 (2001).

[7] I. Ronneberger, W. Zhang, Eshet, H. and R. Mazzarello, Adv. Funct. Mater., *in press* (2015) DOI: 10.1002/adfm.201500849

[8] A. Laio and M. Parrinello, Proc. Natl. Acad. Sci. USA **99**, 12562 (2002).

[9] A. Sebastian, M. Le Gallo, and D. Krebs, Nature Comm. **5**, 4314 (2014).

[10] W. Zhang, A. Thiess, P. Zalden, J.-Y. Raty, R. Zeller, P. H. Dederichs, M. Wuttig, S. Blügel, and R. Mazzarello, Nature Mater. **11**, 952 (2012).

Tuning the Carrier Concentration of n-Bi_2Te_3 / p-Sb_2Te_3 Topological Insulator Junctions

G. Mussler[1], M. Lanius[1], C. Weyrich[1], M. Luysberg[2], L. Plucnski[3], M. Eschbach[3], and D. Grützmacher[1]

[1] Peter Grünberg Institut-9, Forschungszentrum Jülich, Germany
[2] Peter Grünberg Institut-5, Forschungszentrum Jülich, Germany
[3] Peter Grünberg Institut-6, Forschungszentrum Jülich, Germany

Owing to inevitable point defects, the topological insulators (TIs) Bi_2Te_3 and Sb_2Te_3 are intrinsically n-type and p-typed doped, respectively. Because of these high doping levels, it is difficult to probe surface carriers by means of transport experiments. In order to circumvent this problem, we have realized Bi_2Te_3 /Sb_2Te_3 n-p junctions. By varying the top Sb_2Te_3 thicknesses, the built-in voltage tunes the carrier concentration from n- to p-type, determined by means of magneto-transport studies. Besides, a gate-dependent non-linear I-V characteristics is observed in nearly intrinsic Bi_2Te_3/Sb_2Te_3 material.

Topological insulators (TIs) have great potential for next-generation electronic or spintronic device applications owing to the fascinating properties of their surface states. Carriers at the surface of TIs have a topologically protected linear energy dispersion, which allows them do travel spin-locked at a very high speed without dissipation [1]. However, making use of these surface carriers requires intrinsic TI material, which still poses a severe problem due to point defects. It is known that Bi_2Te_3 is intrinsically n-type doped due to Te_{Bi} antisites, whereas the p-type doping in Sb_2Te_3 is attributed to Sb vacancies.

A possible avenue to circumvent the large bulk carrier concentration in Bi_2Te_3 and Sb_2Te_3 is to realize an n-Bi_2Te_3 / p-Sb_2Te_3 heterostructure. Like in conventional semiconductors, an n-p junction results in a built-in voltage, which causes a depletion of charge carriers in the vicinity of the interface, as depicted in figure 1b. Bi_2Te_3 is known to grow epitaxially on Si(111), forming films of high structural quality [2]. Since Bi_2Te_3 and Sb_2Te_3 have very similar lattice constants (Bi_2Te_3: a = 4.385 Å, c = 30.49 Å; Sb_2Te_3: a = 4.264 Å, c = 30.458 Å), Sb_2Te_3 grows epitaxially on Bi_2Te_3. For this study, we have grown four Bi_2Te_3/Sb_2Te_3 samples. The thickness of the underlying Bi_2Te_3 layer was kept constant for all samples (6 QLs = 6 nanometers), whereas the Sb_2Te_3 layer thickness h was varied between 3 – 28 QL (or nanometers). The growth rates were kept constant at v(Bi_2Te_3) = 11 nm/h and v(Sb_2Te_3) = 9 nm/h in order to avoid the formation of twin domains [3]. Figure 1c shows a cross-sectional STEM image of the sample capped with 17 QL Sb_2Te_3. A relatively sharp contrast between Bi and Sb is seen at the Bi_2Te_3/Sb_2Te_3 interface, despite the tendency of Bi and Sb atoms to diffuse into neighboring layers.

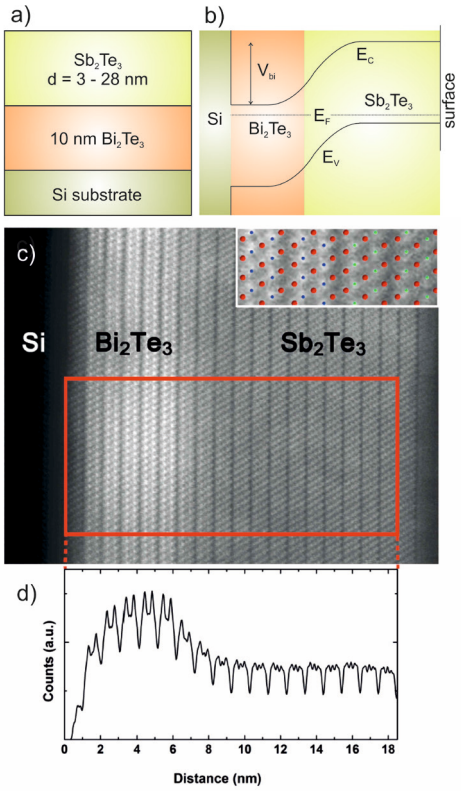

FIG. 1 a) Cross section of the grown Bi_2Te_3/Sb_2Te_3 structures. b) Schematics of the valence of the conduction band alignment including the built-in voltage. c) Structural analysis of the 17 QL Sb_2Te_3 / 6 QL Bi_2Te_3 sample via STEM. HAADF image of atomic resolution. The large overview image reveals the high quality of the crystal. Van der Waals separated quintuple layers can be observed. The contrast in the image is related to the size of the atoms on which electrons are scattered, i.e. chemical contrast is obtained. To estimate the size of the intermixed interface region a line profile is plotted integrated over the red rectangle. This line profile additionally serves as a scale. The inset shows a magnified region across the interface of the two layers with a structural model superimposed (blue atoms = Bi; green atoms = Sb and red atoms = Te).

The sharp interface between Bi_2Te_3 and Sb_2Te_3 is quantitatively analyzed by means of Auger

spectroscopy on a Bi_2Te_3/Sb_2Te_3 sample sputtered for several cycles in order to obtain depth-dependent Sb and Bi concentration profiles. Indeed, a strong chemical contrast between Bi and Sb is seen, despite some Bi/Sb interdiffusion. However, it should be noted that the sputtering itself may cause a Bi/Sb interdiffusion. Hence the Bi and Sb concentration profiles of the unprocessed sample may be less interdiffused than the concentration profiles determined from the Auger spectroscopy experiments.

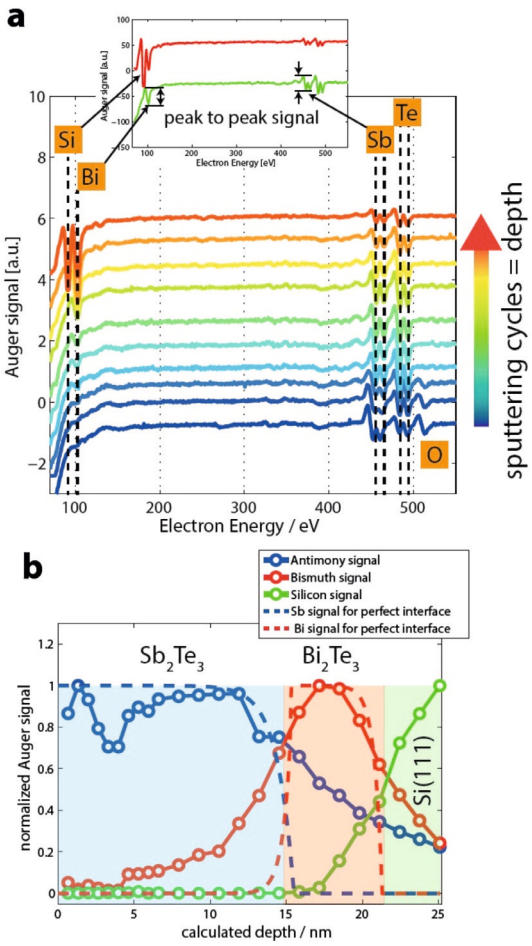

FIG. 2: A Structural analysis of the 17 QL Sb_2Te_3 / 6 QL Bi_2Te_3 sample via AES depth profiling after cleaning procedure in the ARPES apparatus. (a) Single AES spectra obtained after repeated cycles of ion sputtering (from blue = untreated to red). The inset shows how the peak-to-peak signal was obtained. (b) The peak-to-peak signal from Bi (red), Sb (blue) and Si (green) is plotted against sputtering time.

Magnetotransport measurements were performed on Hall bars that were patterned from the films via photolithography and Ar^+ ion beam etching. The bars have widths of the order of 20 – 60 µm and a contact separation of 150 or 300 µm. All measurements were done in a cryostat at 1.5K in 4-point geometry with a DC current of 50 µA. In Fig 3 a) Hall curves for films with different Sb_2Te_3 thicknesses h are shown. From the sign of the slope it is obvious that the dominant carrier species changes from electrons to holes as the Sb_2Te_3 thickness increases. The sheet carrier concentration has been determined to about 8.5×10^{13} cm^{-2} at the lowest for h = 17 nm.

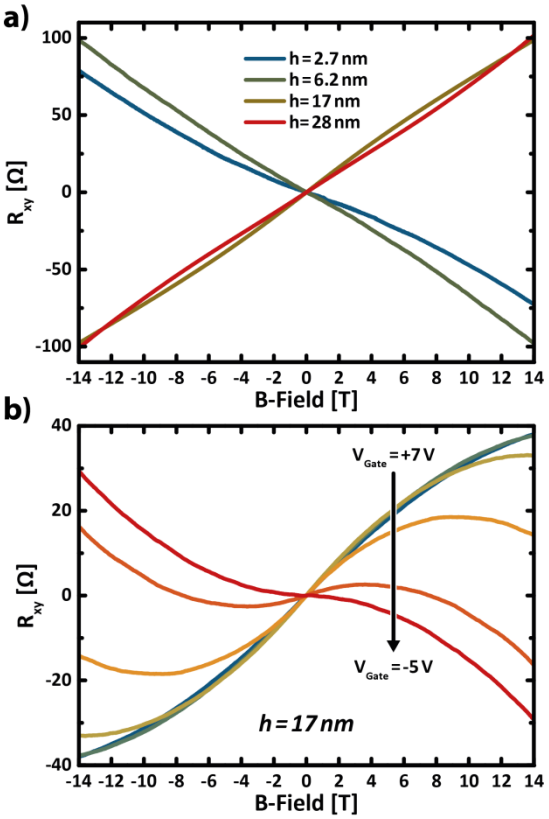

FIG. 3: Hall resistances R_{xy} measured at magnetic fields up to 14T. (a) Results for different films with increasing thickness h of the top Sb_2Te_3 layer. (b) Curves from a single sample with h=17 nm at different gate voltages. For the gate oxide a 50nm thick layer of high-k dielectric $LaLuO_3$ was deposited at room temperature via pulsed laser deposition.

Using a top gate we were further able to tune the carrier concentration as shown in Fig.3 b). From the strong non-linearity of the curves it becomes evident, that all the films host at least two transport channels. Most probably they originate from a few lowermost/uppermost layers of the Bi_2Te_3/Sb_2Te_3 stack that are the furthest away from the intrinsic area of the films. Therefore, we aim at decreasing the total width of the heterostructures to further reduce the carrier concentration, possibly leading to a fully depleted film.

This work was supported by the Virtual Institute for Topological Insulators (VITI) and the Priority Programme SPP1666.

[1] J. E. Moore, Nature **464**, 194 (2010).

[2] J. Krumrain et al., J. Crystal Growth **324**, 115 (2011).

[3] J. Kampmeier at al., Crystal Growth Des. **15**, 390–394 (2015).

Topological insulator nanostructures realized via MBE selective area growth

C. Weyrich[1,2], T. Heider[1,2], M. Lanius[1,2], P. Schüffelgen[1,2], G. Mussler[1,2], Th. Schäpers[1,2], and D. Grützmacher[1]

[1] Peter Grünberg Institut-9, Forschungszentrum Jülich, Germany
[2] VITI – Virtual Institute for Topological Insulators, RWTH Aachen University, Germany

3D topological insulators like Bi_2Te_3, Sb_2Te_3 and Bi_2Se_3 are hot topics due to their novel intrinsic properties including protected surface states, spin-momentum locking and the possibility to host Majorana fermions in combination with superconductors [1,2]. To access these phenomena by means of electrical transport it is imperative to reduce the intrinsic bulk conductance as much as possible, since it easily masks all effects that arise due to surface transport. One way of achieving this goal is to reduce sample sizes since this will severely increase the surface to volume ratio and enable better tunability of the Fermi level via gating. In order to produce samples with dimensions in the nm-regime, we chose to work with pre-patterned substrates to ensure that the films grow only on selected areas. This enables us to avoid several problems during processing samples from entire films. Those arise due to the low durability of the material regarding most process steps as well as many chemical substances needed to clean the samples. Here, we present two distinct methods to achieve selective area growth (SAG) that are based on different kinds of substrates and produce different results regarding the final structures.

Prior to the methods described hereafter the samples were patterned using optical photo-lithography and Ar^+ ion beam etching (IBE). The latter usually results in hardening the resist based etching mask, making it difficult to strip it afterwards using only acetone or similar organic solvents. Due to the softness of the material and its chemical vulnerability to most acids and bases, removing the resist with other means like ultrasound, resist stripper or oxygen plasma are not an option. This problem can be completely circumvented by (SAG), since all the critical process steps are performed on the substrate before the topological insulator is even grown. By using silicon-on-insulator (SOI) or Si_3N_4-covered Si(111) substrates we were able to produce structures of Bi_2Te_3 with lateral dimensions down to 100nm and less. Additionally, we were able to grow suspended films over distances of more than 150nm without any further etching after growth.

The first approach for SAG is realized with SOI-wafers that are compromised of 70nm Si(111) / 300nm SiO_2 / Si(100). As shown in Fig. 1 a) first a photoresist mask (purple) is realized with ebeam lithography. After that the topmost Si(111) layer (red) is removed by reactive ion etching (RIE) using Cl_2/Ar-plasma to expose the buried SiO_2 oxide layer (black). Before transferring it into the molecular beam epitaxy (MBE) chamber, the resist mask is stripped and the substrate is cleaned with Piranha and HF. Owing to the different growth dynamics on the remaining crystalline Si mesa compared to the amorphous SiO_2, SAG restricted to the mesa can be achieved.

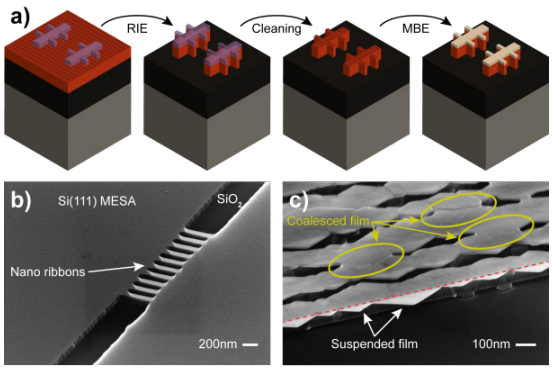

FIG. 1: a) Schematic of the SOI wafer preparation for SAG. b) SEM picture of a nano-ribbon array after RIE etching. The array consists of 10 ribbons with a length of 500nm, 100nm width and a separation of 140nm. c) SEM picture of an array after a 15nm thick Bi_2Te_3 film has been grown. One edge of the mesa is indicated by the dashed red line.

Structures with sizes down to 100nm can be achieved as shown in Fig. 1 b).The flip side of this approach is plotted in Fig. 1 c). It is apparent, that the lateral growth of the film is not restricted by the edges of the mesa. Therefore, protruding structures spanning up to 150nm from the edges (marked with a dashed line) can be observed. Furthermore it is possible for films that emerge from two different mesa to coalesce in between, as the separation becomes smaller. This effect occurs once the size of the mesa is reduced to roughly 200nm in at least one dimension. While this makes the SOI wafers unsuitable to realize well defined structures on the nm-scale, it gives rise to the possibility to analyze transport properties of MBE grown films without the influence of the underlying substrate, as depicted in Fig. 4 a).

In order to grow films with defined shapes, a second approach to obtain nanometer sized SAG has been developed. In this case the substrates are Si(111) wafers with different doping levels that were covered by 100nm Si_3N_4 via low-pressure

chemical-vapor-deposition (LPCVD). Silicon nitride was chosen due to its good insulating properties and stability towards HF. Fig 2 a) shows the process of patterning the substrate. This time the photoresist mask (purple) is a negative of the previously used one for SOI. Then the Si_3N_4 (green) is locally removed by RIE with CHF_3/O_2-plasma. After stripping and cleaning, the TI film is grown using the nitride as a mask.

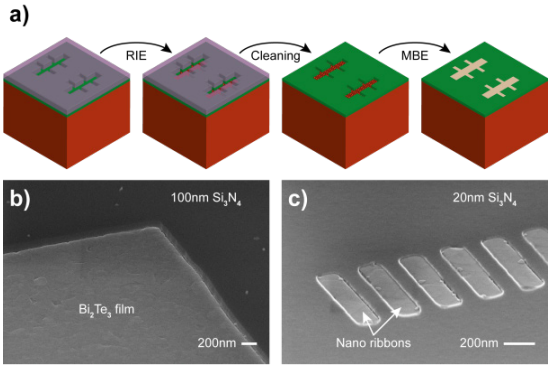

FIG. 2: a) Schematic of the Si/Si_3N_4 wafer preparation for SAG. b) SEM picture of the edge of a 20nm thick TI film, grown on a 20x20µm^2 area where the nitride was removed. c) SEM picture of an array of Bi_2Te_3 nano-ribbons grown within holes of a thinned Si_3N_4 mask. The ribbons are 170nm wide, 750nm long and are separated by 125nm.

As shown in Fig. 2 b) a closed TI film has been grown on top of the silicon surface but no growth took place on the nitride mask. Again SAG is possible due to the difference in growth dynamics between the Si(111) and the nitride surface. To further achieve planar samples, the nitride layer can also be thinned to thicknesses comparable to those of the TI films prior to MBE growth. This is shown in Fig. 2 c), where the nitride thickness has been reduced to 20nm using RIE, before a 15nm film was grown. It can also be used to probe transport properties perpendicular to the film surface normal by using highly doped Si(111) substrates (see Fig. 4 b)). This way the TI can be contacted on the bottom surface using the substrate while contacting the top surface via standard metallization. The nitride then acts as a mask for SAG as well as insulating barrier between the substrate and the conductive substrate.

Preliminary magnetotransport measurements on the first grown ribbons show clear universal conductance fluctuations (UCF) due to phase-coherent transport in low dimensional systems [3]. They arise from coherent superposition of charge carrier wavefunctions as they scatter at inhomogeneous scattering sites. This effect leads to an aperiodic modulation of the conductance when an applied magnetic flux is varied. The modulations are also symmetric regarding field reversal. An exemplary measurement is plotted in Fig. 3. It was done at 1.5K with an applied AC current of 100nA. The sample consists of 5 parallel ribbons with an identical length of 4.6µm, 140nm width and a separation of about 150nm.

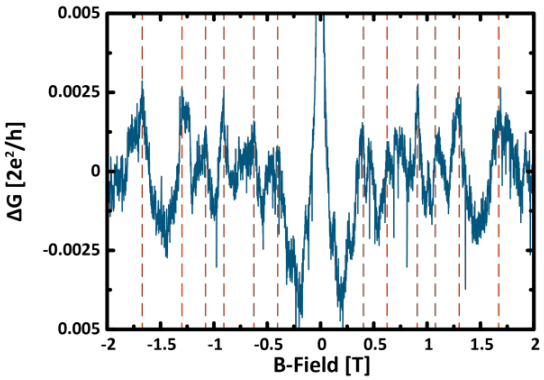

FIG. 3: UCF measured on an array of 5 ribbons grown on a patterned SOI wafer after subtracting the background. The dashed lines mark some of the local maxima. The central peak is attributed to weak anti-localization (WAL), which is another effect originating from self-interference of scattered charge carriers. This effect reduces direct back scattering at B=0T, resulting in an increase of conductance, but diminishes when the field is increased.

It has been predicted, that the unusual surface states of TI give rise to an Aharonov-Bohm like effect in nano-wires, if a magnetic field is applied parallel to the wire axis [4]. Obviously one requires nano-wires with a mostly uniform cross-sectional area to observe this effect. This renders samples grown on SOI wafers unsuitable for this task, since it can be seen from Fig. 1 c) that the ribbons have very irregular diameters along the main axis, due to the film expanding beyond the MESA. Therefore these measurements will have to be attempted using samples on nitride based substrates.

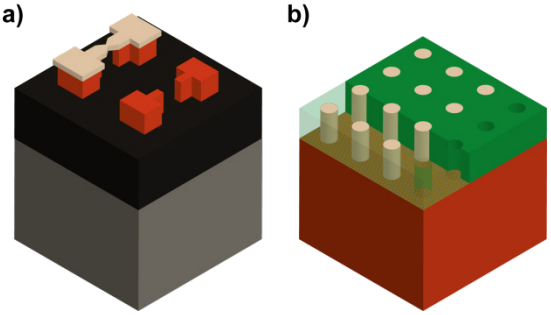

FIG. 4: Schemes for two different experiments that enable access to transport properties of TI films which are very difficult to probe without SAG. a) SOI wafers are useful to grow suspended films, eliminating every possible influence of the underlying substrate. b) Si_3N_4 covered wafers readily enable transport measurements along a different crystal axis in contrast to commonly used lateral transport setups.

This work within VITI was supported by a research grant provided by Helmholtz Association.

[1] M. Z. Hasan and C. L. Kane, Reviews of Modern Physics **82**, 3045 (2010).

[2] P. Roushan et al., Nature, **460**, 08308 (2009).

[3] P. A. Lee and A. Douglas Stone, PRL **55**, 1622 (1985).

[4] J. H. Bardarson and P. W. Brouwer and J. E. Moore, PRL **105**, 156803 (2010).

Subnanometre-wide electron channels on the dark side of a weak topological insulator

C. Pauly[1], B. Rasche[2], K. Koepernik[3], M. Liebmann[1], M. Pratzer[1], M. Richter[3], J. Kellner[1], M. Eschbach[4], B. Kaufmann[1], L. Plucinski[4], C. M. Schneider[4], M. Ruck[2], J. van den Brink[3], and M. Morgenstern[1]

[1] II. Institute of Physics B, RWTH Aachen University, Germany
[2] Department of Chemistry and Food Chemistry, TU Dresden, Germany
[3] Leibnitz Institute for Solid State and Materials Research and Dresden Center for Computational Science, IFW Dresden, Germany
[4] Peter Grünberg Institute-6, Forschungszentrum Jülich, Germany

Weak topological insulators are the counterpart of strong topological insulators such as Bi_2Se_3, Bi_2Te_3 and Sb_2Te_3. They are predicted to exhibit topologically protected surface states on most of their surfaces, but typically not on their cleavage planes. Here, we demonstrate by scanning tunneling spectroscopy on $Bi_{14}Rh_3I_9$ (001) that fingerprints of the topologically protected states appear as edge states on the topologically dark cleavage planes. We reveal these edge states to be continuous in energy throughout the non-trivial band gap and to be continuous in space. The edge states are absent in the closely related "dimerized" layer compound $Bi_{13}Pt_3I_7$, as proposed by theory. For the title compound, our results provide final evidence of its weak topological nature. The new type of edge states might permit carved one-dimensional quantum networks for electrons.

Using scanning tunneling microscopy (STM) and spectroscopy (STS) at 6 K, we probe the local atomic and electronic structure of the weak topological insulator (WTI) $Bi_{14}Rh_3I_9$ [1]. In [001]-direction, the material is built from stacks of 2D topologically insulating, graphene-like planes (red layer in Fig. 1a) separated by trivial insulators (blue layer in Fig. 1a). Thus, the surfaces of the 2D topological insulator (TI) layer, which are the natural cleaving planes of the material, exhibit a non-trivial band gap however with topologically protected states only at each step edge. These edge states are immune to backscattering as long as time-reversal symmetry persists. Thus, perfect conduction of these channels with conductivity e^2/h is anticipated [2,3]. Moreover, partially interfacing these channels with superconductors is predicted to induce Majorana fermions at the rim of the interfacial region [4].

STM on the cleaved surface of $Bi_{14}Rh_3I_9$, i.e. the surface perpendicular to the stacking direction, identifies the spacer layer and the 2DTI layer by their different appearances (Fig. 1c). An atomically resolved STM image of the 2DTI layer is shown in the upper part of Fig. 2a) revealing its honeycomb structure and exhibiting the unit cell size known from XRD [1]. The locally resolved differential conductivity dI/dV(V) as recorded on the 2DTI layer (red curve), on the spacer layer (blue curve) and at the step edge (grey curve) is shown in Fig. 1b). On the 2DTI layer, we find a gap between V = -180 mV and V = -360 mV which is in excellent agreement with the gap measured by ARPES [1]. Importantly, there is strong dI/dV intensity within this 2DTI gap if measured at the step edge. This indicates the edge state. The peak maximum is at the lower part of the band gap in accordance with the dispersion from tight-binding calculations [5]. A larger gap is revealed on the insulating spacer layer as expected. These properties are present on all areas of the sample, partly with a different intensity distribution, which is attributed to different local chemistry or to a different density of states of the probing tip.

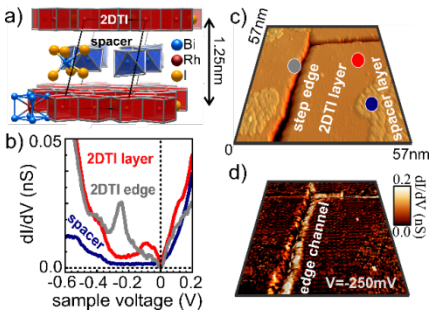

FIG. 1: a) Atomic polyhedron model of $Bi_{14}Rh_3I_9$ as deduced from XRD [1]. b) dI/dV(V) spectra taken at the different layers as marked in (c) by respectively colored circles (V_{stab} = 0.8 V, I_{stab} = 100 pA, V_{mod} = 4 mV). Notice the linearly vanishing dI/dV intensity around E_F which is attributed to a 2D Coulomb gap of Efros-Shklovskii type [6]. c) STM and d) dI/dV image within the 2DTI band gap of a region with step edges of the 2DTI layer (V = -250 mV, I = 100 pA, V_{mod} = 4 mV). Spacer layer is also present.

Additionally, Fig. 1d) shows a spatially resolved *dI/dV* map corresponding to the topography of Fig. 1c) and measured at a sample voltage within the band gap of the 2DTI. Bright stripes at all step edges indicate the presence of an edge mode, as also found on all other step edges of the 2DTI layer.

In addition, we checked that the edge state covers the whole non-trivial band gap as predicted for a topological state. Fig. 2b) is a stack of dI/dV images at energies within the non-trivial band gap for a 2DTI layer including a step edge. It reveals pronounced edge state intensity throughout the whole band gap and slightly weaker intensity even in the energy region below. Further, we analyzed the ubiquity of the edge state along the step edge and found signatures of a spatially continuous edge state within all investigated step edges. Even in the presence of the strong disorder, the edge state is not interrupted. Moreover, no standing wave pattern has been observed pointing to a lack of back-scattering, as expected for a topologically protected state.

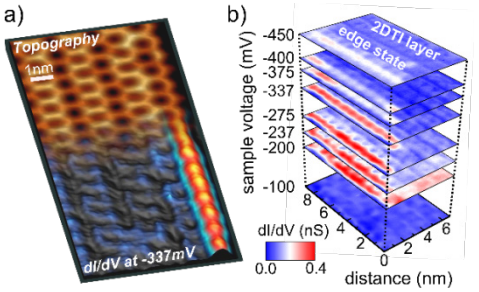

FIG. 2: a) STM topography image of the 2DTI layer (honeycomb lattice) with overlaid dI/dV data (V_{stab} = -337 mV) at the bottom part of the image. Sub-nm wide edge state (orange stripe) is present at the step edge of the 2DTI layer. b) Stacked dI/dV images of the step edge area of the 2DTI layer recorded at voltages across the band gap as marked on the left. The edge state is visible throughout the whole band gap region.

The width of the edge state is found to exhibit a FWHM of 0.8 nm only (Fig. 2a) showing that it is confined to a single unit cell (width: 0.92 nm [1]). Such a width is much smaller than for edge states of the buried 2DTI made of HgTe quantum wells (edge state width: ~200 nm) [3,7] implying the possibility of much smaller devices. As the topological edge state is found and also predicted by theory to remain robust even in the vicinity of disorder, simply scratching the surface deeper than a single layer induces a one-dimensional electron channel with a robust conductivity of at minimum e^2/h [2]. Fig. 3a shows that edges can be carved artificially into the surface of $Bi_{14}Rh_3I_9$ using atomic force microscopy (AFM) offering the possibility of designing well defined quantum networks in order to exploit the topological nature of this sub-nm wide states.

To further consolidate the topological character of the edge states in $Bi_{14}Rh_3I_9$, we have investigated the very similar system $Bi_{13}Pt_3I_7$. Its stacking consists of a 2DTI layer (as revealed by DFT) but with two different spacer layers, leading to an alternating coupling between adjacent 2DTI layers and thus giving rise to a dimerization. Our DFT study reveals that the dimerization drives the system trivial, basically due to a band number doubling, such that the topologically protected edge states disappear. This is in agreement with our STS data, which do not show any edge states at the step edges of the 2DTI layers within the energy regions of the band gaps (Fig. 3b). Prior to the STS measurements, the energy position of these band gaps has been determined by DFT and ARPES, again showing reasonable agreement. Thus, the "dimerized" structure of $Bi_{13}Pt_3I_7$, where stacks are built from pairs of 2DTIs, is a trivial insulator without protected edge states, thereby corroborating the topological nature of $Bi_{14}Rh_3I_9$´s edge states.

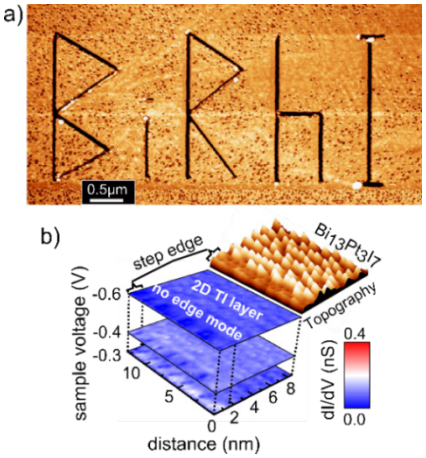

FIG. 3: a) AFM image of $Bi_{14}Rh_3I_9$ surface with letters BiRhI scratched into the surface by a carbon coated silicon cantilever in AFM contact mode. b) Stacked dI/dV images of the 2DTI layer (see topography) of $Bi_{13}Pt_3I_7$ and recorded within the band gaps at voltages marked on the left. No edge state is visible. Same contrast as in Fig. 2 b.

Hence, this new type of helical edge states in $Bi_{14}Rh_3I_9$ might offer the opportunity to design spin filters [8] with extremely small footprint compared to 2DTIs in heterostructures [3]. Moreover, the interfacing with other materials such as superconductors or magnetic insulators required for advanced quantum circuitry [4,9,10] would become accessible directly by shadow mask evaporation. In this sense, the discovery of the first weak 3DTI $Bi_{14}Rh_3I_9$ might offer similar advantages as graphene does with respect to conventional semiconductor heterostructures [11].

Results have been published in [12].

[1] B. Rasche et al., Nature Mat. **12**, 422 (2013)

[2] Y. Yoshimura et al., Phys. Rev. B **88**, 045408 (2013)

[3] M. König et al., Science **318**, 766 (2007)

[4] J. Alicea, Rep. Prog. Phys. **75**, 076501 (2012)

[5] L. Cano-Cortes et al., Phys. Rev. Lett. **111**, 146801 (2013)

[6] A. L. Efros et al., J. Phys. **C8**, L49 (1975)

[7] B. Zhou et al., Phys. Rev. Lett. **101**, 246807 (2008)

[8] M. Brüne et al., Nature Phys. **8**, 485 (2012)

[9] V.Mourik et al., Science **336**, 1003 (2012)

[10] J. Alicea et al., Nature Phys. **7**, 412 (2011)

[11] A.H. Castro Neto et al., Rev. Mod. Phys. **81**, 109 (2009)

[12] C. Pauly et al., Nature Phys. **11**, 338 (2015)

Memristive Electrochemical Metallization Cell Model Simulations for Sequential Logic-in-Memory

E. Linn[1], S. Ferch[1], R. Waser[1,2], and S. Menzel[2]

[1] Institut für Werkstoffe der Elektrotechnik II, RWTH Aachen University, Germany
[2] Peter Grünberg Institut-7, Forschungszentrum Jülich, Germany

A memristive model of an Electrochemical Metallization Cell (ECM) was implemented as SPICE behavioral model to enable accurate simulation of complementary resistive switch (CRS) cells in passive crossbar arrays. All 14 of 16 Boolean logic functions, which can be realized with a single CRS cell were simulated. The basic CRS-logic functionality could be demonstrated and the influence of series resistances, applied voltage scheme, and pulse height was studied. The switching energies were compared to the basic sequential memristor logic-in-memory approach revealing the advantages of CRS-logic, also in terms of array compatibility.

Redox-based resistive switching devices (ReRAM) are a promising class of emerging non-volatile memory devices. ReRAMs offer high endurance, high retention and low power consumption and excellent scaling properties [1]. According to the ITRS roadmap ReRAMs could replace FLASH memory in upcoming technology nodes, or enable a novel memory hierarchy level, so called storage class memory.

Since ReRAMs are two-terminal devices they can be embedded in $4F^2$ (F: feature size) passive crossbar array structures enabling ultra-dense memories. The key element to realize those architectures is either a ReRAM-matched selector element, e.g. a bipolar diode or a complementary resistive switch (CRS) consisting of two ReRAM cells connected anti-serially.

In combination with external CMOS periphery hybrid CMOS/crossbar circuits are realized. Moreover, novel computing concepts become feasible in ReRAM-based passive crossbar arrays by using sequential logic-in-memory approaches. In principle any bipolar resistive switching material is suited for this approach.

There are two device classes offering bipolar switching mode according to the ReRAM classification scheme: Valence Change Mechanism (VCM) devices and Electrochemical Metallization Cell devices.

In this work we concentrated on ECM devices where a conductive filament (either Ag or Cu) grows from the inert (Pt) electrode to the active electrode (Cu or Ag) under positive bias, and is dissolved under negative bias (Fig. 1).

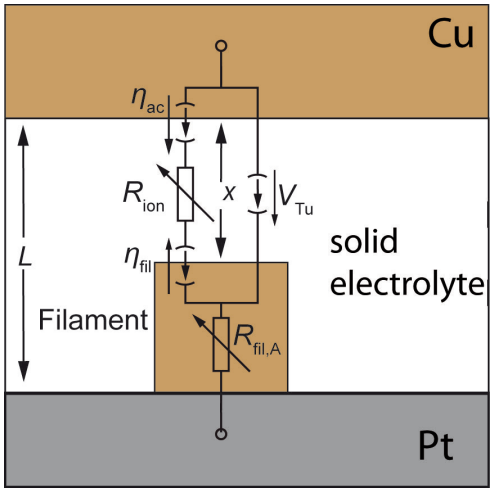

FIG. 1: A. Equivalent circuit model of the Cu/solid electrolyte/Pt ECM-type ReRAM devices.

For ECM devices accurate compact models have been introduced recently [2]. In Fig. 1 the underlying equivalent circuit model is depicted where the state variable x is the width of the gap between the filament and the active electrode. The ionic current path is mainly described by the Butler-Volmer equation and the electronic current path is implemented as tunneling resistance which depends on the gap width x. In the simulation two ECM devices are connected anti-serially (Fig. 2a).

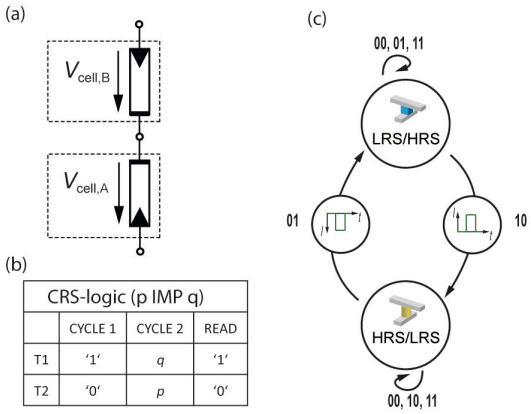

CRS-logic (p IMP q)			
	CYCLE 1	CYCLE 2	READ
T1	'1'	q	'1'
T2	'0'	p	'0'

FIG. 2: (a) CRS cell consisting of two anti-serially connected ECM cells. (b) Table showing the sequential steps for the IMP operation. (c) Finite state machine depicting the CRS-logic functionality.

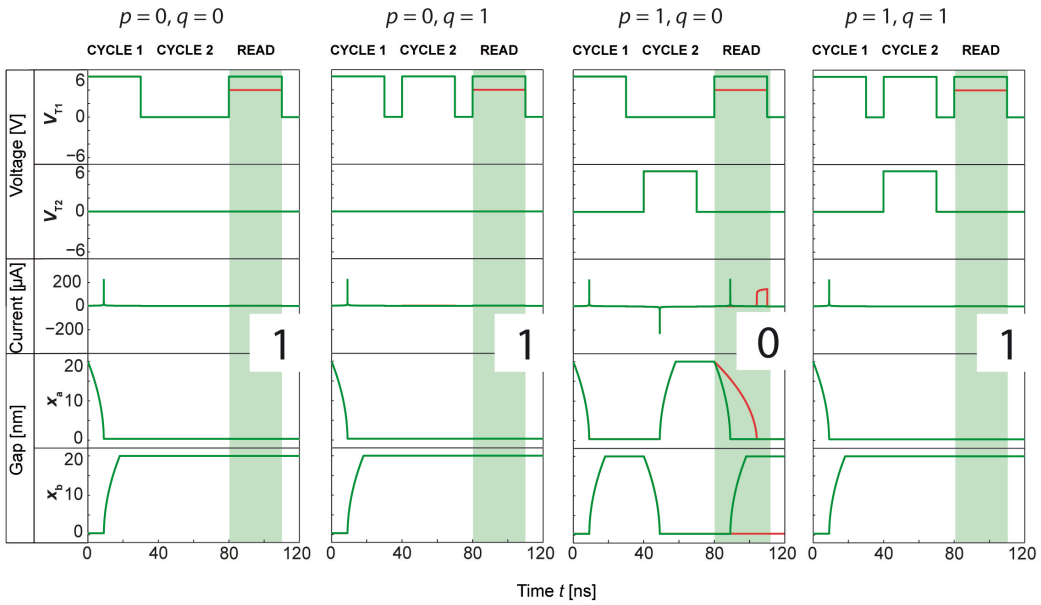

FIG. 3: Simulation of the logic function p IMP q. All four input signal combinations are shown. In the first two rows the voltage inputs at terminal T1 (top electrode) and T2 (bottom electrode) of the ECM-type CRS cell are depicted. In the third row the current response is shown. If there is a current response (spike read: green spike; level read: red current pulse) in the READ phase a logic 0 is present whereas no current response corresponds to a logic 1. The last two lines highlight the width of the filament gap of each ECM part cell, cf. also Fig. 1.

To realize a CRS-logic function a sequence of signals is required, e.g. two cycles are required for the function *p* IMP *q* (Fig. 2b). In the first cycle the CRS cell is initialized to state HRS/LRS (state 1) by applying 1 to the top electrode T1 and 0 to the bottom electrode T2 (cf. also Fig. 3). Being in this state the cell switches only back to LRS/HRS (state 0) if *q* = 0 and *p* = 1. In a last step a read-out can be performed. Here, either a level read or spike read can be applied [3].

For the IMP function with all input combinations the memristive simulation of an ECM-type CRS cell is shown in Fig. 3. In the first cycle 6 V is applied to the top electrode T1 and GND is applied to the bottom electrode. Since the previous state was 0 (LRS/HRS) a current spike is visible in each first cycle. Next, the logic operation is conducted in cycle 2.

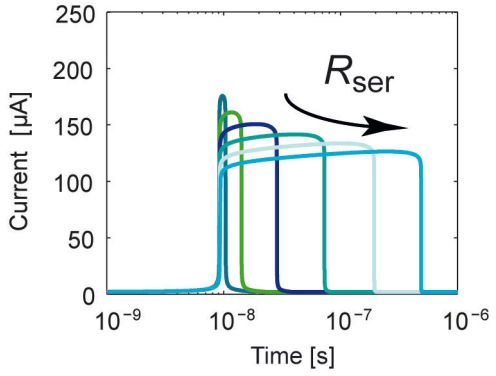

FIG. 4: CRS current response for increasing series resistances on a log time scale.

For *q* = *p* = 0, *q* = *p* = 1 no change of state may occur since the overall voltage drop is zero. Also for *q* = 1 and *p* = 0 no change of state is observed due to the overall positive voltage polarity which cannot induce a state change for a device in state HRS/LRS. However, for *q* = 0 and *p* = 1, the CRS devices is switched to LRS/HRS (compare current spike in cycle 2). For read-out two schemes were used. For the spike read a voltage of 6 V is used (green colored lines) whereas for level read a voltage of 4 V was used (red colored lines). This lower read voltage is insufficient for switching to LRS/HRS completely during the pulse and induces switching to LRS/LRS.

In Fig. 4 one can see that not only pulse height, but also the value of the series resistance affects the current response. With increasing series resistances the LRS/LRS regime is increased, thus tuning of the series resistances enables ON-window engineering.

In terms of switching energy CRS-logic is preferable compared to the basic memristor-logic [4]: For the IMP operation the energy saving is about a factor of 20 [3]. Due to the better array compatibility of CRS cells compared to pure ReRAM cells, the energy efficiency of CRS-logic is further increased in large scaled arrays.

[1] R. Waser, R. Dittmann, G. Staikov, and K. Szot, Adv. Mater. **21**, 2632 (2009).

[2] S. Menzel, U. Böttger, and R. Waser, J. Appl. Phys. **111**, 014501 (2012).

[3] S. Ferch, E. Linn, R. Waser, and S. Menzel, Microelectronics Journal **45**, 1416 (2014).

[4] J. Borghetti et al., Nature **464**, 873 (2010).

Statistical Modeling of Electrochemical Metallization Memory Cells

S. Menzel[1], S. Tappertzhofen[2], I. Valov[1], U. Böttger[2], and R. Waser[1,2]

[1] Peter Grünberg Institut-7, Forschungszentrum Jülich, Germany
[2] Institut für Werkstoffe der Elektrotechnik II, RWTH Aachen University, Germany

Redox-based resistive switching devices have attracted great interest for future nonvolatile memory application. The electrochemical metallization memory (ECM) cell is one variant of these devices. One issue is the variability of the resistive switching in ECM cells. Thus, statistical models that capture the variability of ECM cells are required to enable circuit design. This works presents a statistical model for the resistive switching in ECM cells that is based on the electrochemical driven growth and dissolution of a metallic filament. The simulation results are validated using experimental data.

Electrochemical metallization memory (ECM) cells are a promising candidate for next generation non-volatile, high speed and highly scalable memory cells [1, 2]. The switching is attributed to the electrochemical growth and dissolution of a Cu or Ag nano-sized filament. Typically, ECM cells consist of a Cu or Ag active electrode, an ion conducting switching layer (SL) and an inert electrode. During the SET process a positive potential is applied to the active electrode which is oxidized. Ag or Cu cations are driven out of the active electrode and migrate through the switching layer. At the inert cathode the cations are reduced and a metallic filament grows towards the anode resulting in a low resistive state (LRS). To RESET the device to a high resistive state (HRS), the voltage polarity is reversed and the filament dissolves. Here we report on a statistical 1D simulation model for ECM switching, which also incorporates conductance quantization.

In order to set up a statistical model, we extended our previous continuous deterministic model [3]. The resistance of the cell is now described as function of the number of atoms in the growing filament rather. In addition, the addition/removal of single atoms to/from this filament is modeled using a kinetic Monte Carlo approach.

The considered filament model is shown in Fig. 1(a). It consists of a filament stub of K_L complete atomic layers with cross-sectional area A_{fil} and an incomplete top layer A_{in}. In this configuration one can distinguish between two areas A_{in}/A_{res} with different distances x_{in}/x_{res} to the counter electrode. The equivalent circuit diagram for this filament model is shown in Fig. 2(a). There are two parallel electron tunneling path $I_{Tu,res}$ and $I_{Tu,in}$, which can be calculated with the fitting factor C, the electron effective mass m_{eff} and the tunneling barrier height ΔW_0 according to Simmons as

$$I_{\mathrm{Tu,res/in}} = \frac{3CK}{2x_{\mathrm{res/in}}}\left(\frac{e}{h}\right)^2 \exp\left(-\frac{4\pi x_{\mathrm{res/in}}}{h}K\right) A_{\mathrm{res/in}} V_{\mathrm{res/in}}.$$

Here, it is $K = (2m_{eff}\,\Delta W_0)^{0.5}$. The resistance of the incomplete top layer depends on the filament resistivity ρ_{fil} and the layer thickness d, i.e. the atomic diameter. It reads $R_{in} = \rho_{fil} d/A_{in}$ as long as a tunneling gap remains. If a galvanic contact is formed $R_{in} = R_0/N_{in}$ results, where R_0 = 12.9 kΩ and N_{in} corresponds to the number of atoms in the top layer. The resistance of the filament stub is calculated according to $R_{fil} = K_L \rho_{fil} d/A_{in}$.

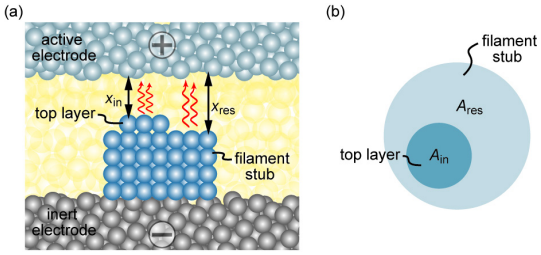

FIG. 1: (a) Vertical and (b) lateral cross-section of the filament model. (Redrawn from [4])

The equivalent circuit diagram for the statistical model is shown in Fig. 2(b). The two voltage-controlled current sources η_{ac} and η_{fil} describe the electron-transfer reactions at the boundaries. The corresponding ionic current densities are calculated using the Butler-Volmer equation

$$j_{et} = j_{0,et}\left\{\exp\left(\frac{(1-\alpha)ez}{k_B T}\eta_{et}\right) - \exp\left(-\frac{\alpha ez}{k_B T}\eta_{et}\right)\right\},$$

which depends on the charge transfer coefficient α and the number of electrons z involved in the electron transfer reaction. The ion transport within the insulating layer and the corresponding current density can be calculated by the Mott-Gurney Law:

$$j_{hop} = j_{0,hop}\sinh\left(\frac{aze}{2k_B T}E\right).$$

Here, a is the mean ion hopping distance and $E = \eta_{hop}/x$ the electric field. Prior to filamentary growth a stable nucleus with N_C atoms needs to be formed. The mean nucleation time can be calculated according to

$$t_{\mathrm{nuc}} = t_{0,\mathrm{nuc}} \exp\left(-\frac{(N_c+\alpha)ze}{k_B T}\eta_{\mathrm{nuc}}\right).$$

Here, $t_{0,\mathrm{nuc}}$ is a time pre-factor and η_{nuc} the nucleation overpotential.

The rates for addition/removal of one atom to the filament can be deduced from the Butler-Volmer equation and read

$$\frac{1}{\tau_{\mathrm{red}}} = \Gamma_{\mathrm{red}} \exp\left(-\frac{\alpha ez}{k_B T}\eta_{\mathrm{et}}\right)$$

for the attachement of one atom and

$$\frac{1}{\tau_{\mathrm{ox}}} = \Gamma_{\mathrm{ox}} \exp\left(\frac{(1-\alpha)ez}{k_B T}\eta_{\mathrm{et}}\right)$$

for the removal. Here, $\Gamma_{\mathrm{ox}}/\Gamma_{\mathrm{red}}$ are rate constants. Using a kinetic Monte Carlo approach one of the processes is randomly chosen. The time for this event to occur is calculated to $\tau = ln(U)\ \tau_{\mathrm{mean}}$, where U denotes a random number between 0 and 1 and τ_{mean} equals the addition/removal rates.

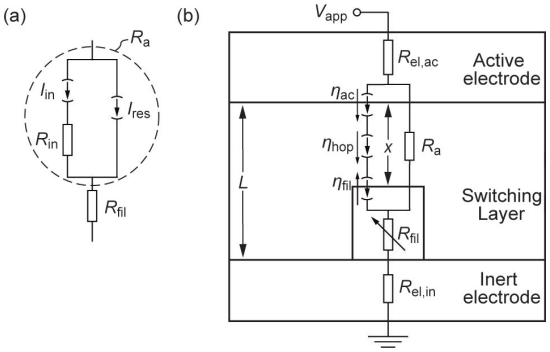

FIG. 2: (a) Equivalent circuit diagram of the filament resistance model. (b) Schematic of the switching model with equivalent circuit diagram. A switching layer of thickness L is sandwiched between the active top electrode and the inert bottom electrode. A cylindrical filament (the form is arbitrary chosen for simplicity) grows within the electrolyte film and modulates the tunneling gap x between the filament and the active electrode. In the switching layer both ionic and electronic current paths are present, respectively. (Redrawn from [4]).

The simulation of the switching kinetics is divided into two steps: nucleation and filamentary growth. First, the nucleation time is calculated and then the kMC model is used to simulate the ECM switching. The used simulation parameters are given in Table 1.

The SET switching kinetics is simulated using voltage pulses with different amplitude. For each voltage amplitude 50 simulations were carried out and the mean value is determined. Fig. 3 shows the simulated switching kinetics statistics for different voltages compared to experimental

Table 1: Simulation model parameters

Symbol	Value	Symbol	Value
Γ_{ox}/Γ_{red}	$8.5\cdot10^{5}$ s^{-1}	$t_{0,nuc}$	$5.4\cdot10^{5}$ s
z	1	N_c	3
ΔW_0	3.36 eV	A_{is}	12.57 nm^2
m_{eff}	0.2 m_0	L	20 nm
α	0.34	ρ_{fil}	$5\cdot10^{-7}$ Ωm
$j_{0,et}$	$3.2\cdot10^{5}$ A/m^2	R_{el}	76,4 mΩ
$j_{0,hop}$	$1.1\cdot10^{11}$ A/m^2	d	0.3 nm
a	0.3 nm	C	0.27

data obtained from 20 nm thick AgI based ECM cells [3]. The simulated data is displayed using open circles and the experimental data using squares. The simulation model reproduced the experimental data very well. The distributions are very tight for voltages V> 0.4 V. In this regime the switching kinetics are limited by filamentary growth, i.e. electron-transfer reactions and ion hopping. At lower voltages, however, the Weibull plot shows a bigger spread. This is due to the assumed statistical distribution in the calculations. In this regime, the switching kinetics are strongly determined by the nucleation process, which is modeled using an exponential distribution.

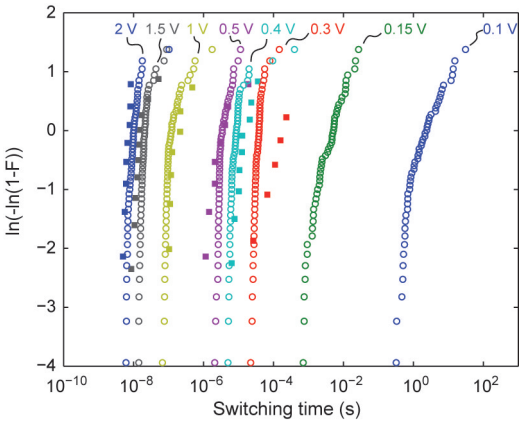

FIG. 3 Weibull statistics of the SET switching kinetics for different voltage amplitudes (open circles) compare to experimental data of a AgI-based ECM cell. (Redrawn from [4])

In conclusion, we presented a 1D statistical model for resistive switching in ECM cells. It is capable of modeling the switching variability obtained from experimental data. In addition, the model can be used to simulate quantized conduction steps.

[1] R. Waser and M. Aono, Nat. Mater. **6**, 833 (2007)

[2] I. Valov, ChemElectroChem **1**, 26 (2014)

[3] S. Menzel, S. Tappertzhofen et al., Phys. Chem. Chem. Phys. **15**, 6945 (2013)

[4] S. Menzel, B. Wolf et al., 6th IEEE International Memory Workshop (IMW), Taipeh Taiwan (2014)

Electrochemical Dynamics of Metallic Nanoclusters in Dielectrics

Y. Yang[1], P. Gao[2], L. Li[2], X. Pan[2], S. Tappertzhofen[3], S.H. Choi[1], R. Waser[3,4], W.D. Lu[1], and I. Valov[4]

[1] Dept. Electr. Eng. and Computer Science, University of Michigan, USA
[2] Dept. Mater. Sci. and Engineering, University of Michigan, USA
[3] Institute für Werkstoffe der Elektrotechnik II, RWTH Aachen University, Germany
[4] Peter Grünberg Institut-7, Forschungszentrum Jülich, Germany

Nanoscale metal inclusions in or on solid-state dielectrics are an integral part of modern electrocatalysis, optoelectronics, capacitors, meta-materials and memory devices. By *in situ* TEM studies, we show that fundamental electrochemical processes can lead to universally observed nucleation and growth of metal clusters, even for inert metals like platinum. The clusters exhibit diverse dynamic behaviours governed by kinetic factors including ion mobility and redox rates, leading to different filament growth modes and structures in memristive devices. These findings reveal the microscopic origin behind resistive switching, and provide general guidance for the design of novel devices involving electronics and ionics.

Studies focused on the microscopic mechanism and filament growth processes in redox-based resistive switching memories (ReRAM) have been carried out using scanning probe microscopy (SPM) and high-resolution transmission electron microscopy (TEM) techniques. For example, a recent experiment reveals different filament growth modes and shows that filament formation can be achieved in the form of metal nanoclusters [1]. However, a critical question was raised regarding the fundamental, microscopic origin of the growth and migration of the nanoclusters inside dielectrics [2], and whether the different and seemingly contradicting experimental results can be reconciled within the same theoretical framework.

We directly reveal the microscopic origin of the dynamic growth and migration processes of metal nanoclusters in dielectrics and show that the field-driven migration is an universal behaviour, even for inert metals such as Pt. We show the different migration modes can be explained in the electrochemical model framework, driven by both thermodynamic and kinetic factors. Specifically, we show that in conventional insulators the metal clusters can be treated as bipolar electrodes (BPEs), and can dissolve from their original locations and nucleate and redeposit at new positions closer to the counter electrode in a process driven by the competing electrochemical processes occurring at the two polarized sides [3].

Fig. 1 shows the bipolar shift of Cu nanoclusters within SiO_2 matrix.

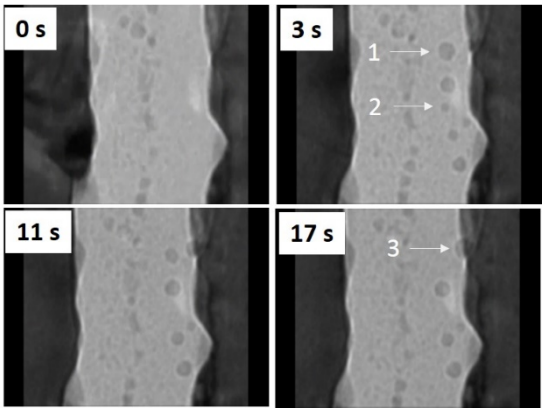

FIG. 1. Dynamic growth and migration of Cu nanoclusters in a dielectric film. Figure adapted from [3].

The evolution of the shape and size of a cluster can be determined by the competition between the oxidation and reduction rates on the cathode and anode sides of the BPE, which can be described as:

$$\frac{dV^i}{dt} \propto \Gamma^i_{\text{red}} - \Gamma^i_{\text{ox}} \qquad (1)$$

where V^i is the volume of cluster *i*, and Γ^i_{ox} (Γ^i_{red}) is the oxidation (reduction) rate for the Ag atoms (ions) on the anode and cathode sides of cluster *i*, respectively.

For two adjacent clusters (*i* and *i*-1) with small distance, we can approximate the ion exchange as:

$$\Gamma^i_{\text{red}} = \Gamma^{i-1}_{\text{ox}} \qquad (2)$$

accounting for the conservation of the Ag material. In systems with more clusters interacting electrostatically, the different growth rates will be affected by the distance between the clusters, their relative position to each other and their sizes. These factors account for the electric field strength and the overall evolution of the system (e.g. the conducting filament in a memristive device).

More surprisingly, we found that even inert metals as Pt can dissolve and form nanoclusters within the dielectric as shown in Fig. 2

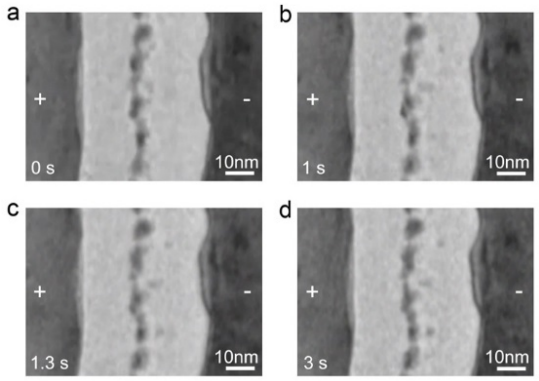

FIG. 2 Dynamic behavior of Pt within SiO_2 matrix

When the ion mobility (μ) and the redox rates Γ^i are high and homogeneous, the ions can reach the inert electrode without agglometration, thus avoiding nucleation within the insulating film so filament growth initiates from the inert electrode, and the large amount of ion supply (due to high Γ^i) leads to an inverted cone shaped filament with its base at the inert electrode interface (as in conventional ECM devices).

In contrast, in the other extreme of low and inhomogeneous μ and low Γ^i, the ions can pile and reach the critical nucleation conditions inside the dielectric and further filament growth is fulfilled by cluster displacement via the repeated splitting → merging processes. An experimental example is the filament growth in amorphous Si, which shows the filament is initiated from the active electrode and grows towards the inert electrode as discrete nanoclusters.

Instead, if the ion mobility is low while the redox rates are high, nucleation can occur inside the dielectric while large amounts of atoms can be deposited onto the cathode sides of the nuclei, leading to gap filling. After a connection between the nuclei and the active electrode is made, the process is repeated thus again leading to an effective forward growth towards the inert electrode.

Finally, if the ion mobility μ is high while the redox rates Γ^i are low, nucleation only occurs at the counter electrode but the limited ion supply means reduction predominately occurs at the edges with high field strengths thus leading to branched filament growth towards the active electrode.

Additionally we have studied the dynamics at the Ag/SiO_2 interface and observed the dissolution and deposition of Ag and the related structural changes into the matrix. The device was directly formed inside the TEM column by connecting a high-purity Ag wire with a movable W probe coated with the SiO_2 film (Fig. 3). After ~ 4 min we detected the appearance of several Ag clusters near the Ag electrode. These clusters then behave as BPEs during subsequent growth. As expected, over time these clusters move closer to the inert electrode, following the splitting → merging processes. Due to the higher concentration of Ag^+ ions near the Ag electrode therefore the higher probability to overcome the nucleation barrier, more Ag clusters will be nucleated near the Ag electrode inside SiO_2 and the repeated nucleation.

The overall growth of the filament can then be characterized by the step-by-step movements of Ag cluster components driven by the electrochemical kinetics.

Additionally, a feature reminiscent of a void was observed in the SiO_2 film at the interface region in Figs. 3c,d after large amounts of Ag atoms have passed through. The void formation is a clear sign of plastic deformation of the dielectric film due to increased mechanical stress that was introduced into the SiO_2.

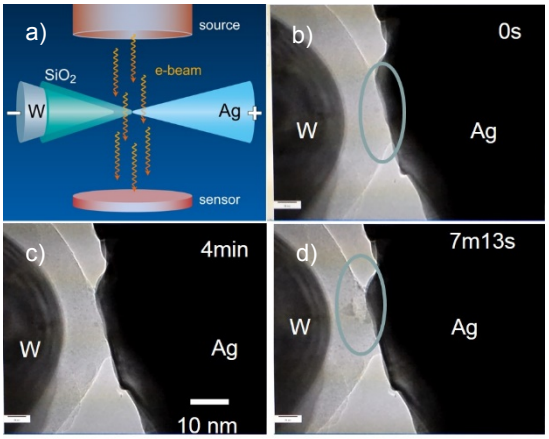

FIG. 3 Interface dynamics at the Ag/SiO_2 interface

The cluster interactions and formation processes are strongly affected by kinetic factors leading to different shapes and growth modes of the clusters that can be observed experimentally. We suggest a generalized framework governing the electrochemical dynamics of the metal clusters. The nanoclusters were found to act as BPEs under electric field, with their dissolution and nucleation processes mediated by the competing electrochemical reactions on both sides. By controlling the kinetic factors including ion mobility and redox rates, different growth modes can be achieved and verified experimentally. This framework explains well the apparently contradicting experimental observations of filament growth in memristive devices, and provides critical insight into the principle of device operations. Our qualitative model may help to develop a more quantitative and microscopic model for electric field-induced nanoionics based on two main kinetic factors, ion mobility and redox rate. These findings can be readily expanded to material and device systems where controlling the metal inclusion dynamics (or avoiding such) is critical and will have significant theoretical and practical impacts.

[1] Y. Yang et al., Nature Communications **3**, 732 (2012).

[2] I. Valov and R. Waser, Advanced Materials **25**, 162 (2013).

[3] Y. Yang et al., Nat. Commun. **5**, 4232/1 (2014).

Nanoscale electro-reduction at the triple phase boundaries of memristive oxide devices

C. Lenser [1], M. Patt [2], St. Menzel [1], A. Köhl [1], C. Wiemann [2], C. M. Schneider[2], R. Waser [1,3], and R. Dittmann[1]

[1] Peter Grünberg Institut-7, Forschungszentrum Jülich, Germany
[2] Peter Grünberg Institut-6, Forschungszentrum Jülich, Germany
[3] Institute für Werkstoffe der Elektrotechnik II, RWTH Aachen University, Germany

The nanoscale electro-reduction in a memristive oxide is a highly relevant aspect for future non-volatile memory materials. We use photoemission electron microscopy to identify the conducting filaments and correlate them to structural features of the top electrode that indicate a critical role of the three phase boundary (electrode-oxide-ambient) for the electro-chemical reduction. Based on simulated temperature profiles, we demonstrate the essential role of Joule heating through localized currents for electro-reduction and morphology changes.

In recent years resistive switching in transition metal oxides received a lot of research interest due to the proposed application as non-volatile data memory [1]. The resistive switching process is usually attributed to the diffusion of oxygen vacancies driven by the applied voltage and an associated valence change of the transition metal cations. However, explicit detection of valence changes is found rarely in the literature since these changes are expected to take place not within the whole device volume but within small filaments. We have elucidated the impact of the presence of the electrode, the applied electric field and local Joule heating on the filament formation in Au/ Fe-doped $SrTiO_3$ (Fe:STO)/ Nb-doped $SrTiO_3$ (Nb:STO) memristive devices.

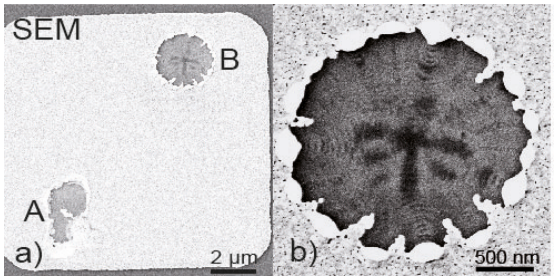

FIG. 1: SEM micrograph of the formed electrode. Features "A" and "B" mark the contact point of the probe and forming crater, respectively, with an higher magnification image of the crater in b).

In particular, we have investigated in detail the nanoscale structural and chemical changes on the surface of a Nb:STO/Fe:STO/Au device after electroforming. The initially high resistance of the stack (> $10^{12}\Omega$) breaks down at a voltage of +7 V, forming into a low resistance state ($10^{6}\Omega$). Fig. 1 a) depicts an electron microscopy image of the electrode after forming recorded in a conventional scanning electron microscope (SEM). The Au electrode shows two distinctive features, marked "A" and "B". Feature "A" is a scratch in the electrode caused by the W-probe used to establish electrical contact. Feature "B" is a result of the electrical treatment (hereafter called the forming crater) and shows a remarkable contrast pattern, depicted in higher magnification in figure 2 b). The forming crater has a diameter of approximately 2 µm and is circular in shape. The rim of the crater is decorated with globules of Au, which can be seen as bright areas. The smooth, rounded character of these globules strongly indicates that Au from the crater location has been enabled to flow in a liquid-like state to the crater rim.

To correlate the structural changes with the local chemical state of the oxide, we have performed X-ray absorption spectroscopy of the Ti $L_{2,3}$-edge in the photoemission electron microscope (PEEM). The spectra recorded in the forming crater are presented in fig. 2 a), with the corresponding regions of interest (ROI) marked in the PEEM image in the inset. The rim of the crater ROI-2 (red line, marked red in the inset) clearly shows a shoulder at the L_3 e_g line, as well as a much more shallow dip between the two components of the L_2 edge, indicating a valence change at the Ti-site from Ti^{4+} to Ti^{3+} [2].

A direct comparison of the spectra recorded in ROI-1 and ROI-2, normalized to the respective pre-edge intensity, shows the spectral differences of the Ti L_3 edge directly (figure 2b)). The increased intensity of the Ti^{3+} shoulder between t_{2g} and e_g components facilitates a spatial distinction of lightly (ROI-1) and heavily (ROI-2) reduced regions in the PEEM image, displayed as a false color image in figure 2 c). Note that the dark red region around the forming crater is covered by Au, and therefore no Ti is visible. The yellow regions correspond to a strong contribution of the Ti^{3+} component, while the red regions indicate the absence of this component, as marked by the color bar in fig. 2 b).

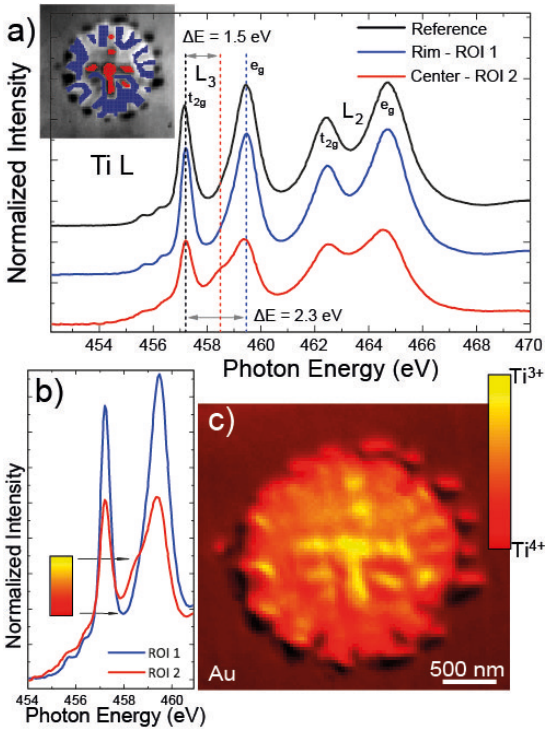

FIG. 2: a) Ti L-edge absorption spectra recorded in the three regions of interest: ROI 1 ("rim", blue) and ROI 2 ("center", red), as well as a reference spectrum (black) recorded in the needle contact area. Inset: PEEM image with ROI 1 and 2 marked in blue and red, respectively. b) Direct comparison of the Ti L3 edge spectra from ROI 1 and 2, normalized to the background. c): False color map depicting the distribution of Ti3+ (yellow) and Ti4+ (red) states in the forming crater.

We suggest that the reduction of the Ti^{4+} and the melting of the Au is related to a local temperature increase through Joule heating and could confirm it by finite element calculations [3]. In particular, we could show that the temperature strongly increases at the interface between the conducting filament and the Au electrode and becomes sufficiently hot to melt the Au electrode.

From the contrast pattern visible in the crater, we can reconstruct the spatial and temporal evolution of the nanoscale reduction process. A schematic visualization is displayed in fig. 3, based on the geometry of the SEM image given in fig. 1 b). We start by assuming that the reduction reaction takes place initially at the center of the crater. In the first stage of the forming step, the current flows in confined pre-filaments [4], which can be related to structural defects [5]. Above a certain critical current density in the pre-filaments, the electro-reduction takes place through a self-accelerated process where Joule heating leads to enhanced mobility of the oxygen ions, which accelerates the reduction and in turn enhances the conductivity of the filaments and thereby the Joule heating.

As soon as a significant current starts to flow and a filament is formed, the localized Joule heating melts the Au electrode, causing it to flow away from the "hot spot" through a gradient of the surface tension induced by the temperature gradient.

The mobile Au forms small globules and retreats away from the hot spot of the first filament. As soon as the Au has retreated from a reduced region, the electrical contact to the conducting filament is disconnected, and new filaments are formed at the new edge of the electrode. The fact that these disconnected filaments are arranged along the traces reveals that the Au globules do not reach their final position immediately, but that filaments are formed sequentially. The localized reduction of the material takes places only at an electrode edge, which is usually the physical edge of the electrode or a defect in the electrode. These edges represent a triple phase boundary (TPB), where oxide, metal and the ambient atmosphere are in contact. The TPB facilitates the release of oxygen gas, marking these areas as preferred reduction sites. Our findings have two important implications for resistive switching devices, namely, that the nanoscale structure of the top electrode can play a key role and that filament formation can be a dynamic process and might not be terminated after the first voltage sweep.

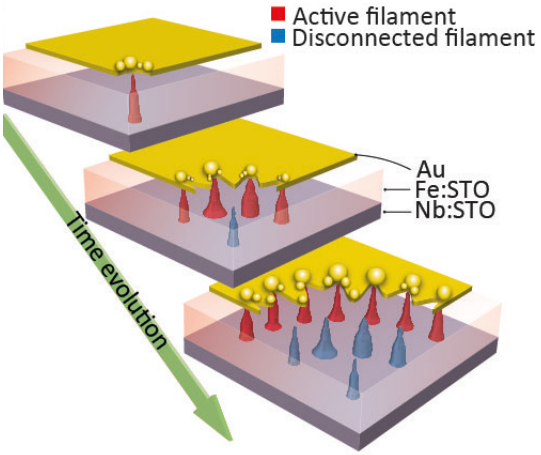

FIG. 3: Schematic representation of the time evolution of the forming crater, indicating the growth of the crater and the concomitant formation of additional filaments at each position of the electrode edge.

This work was performed within the SFB 917 “Nanoswitches”.

[1] R. Waser, R. Dittmann, G. Staikov, and K. Szot, Adv. Mater. **21**, 2632 (2009).

[2] M. Abbate, F.M.F. de Groot, et al., Phys. Rev. B **44**, 5419 (1991)

[3] C. Lenser, M. Patt, S. Menzel, A. Köhl, C. Wiemann, C. Schneider, R. Waser and R. Dittmann, Adv. Funct. Mat. **24**, 4466 (2014)

[4] A. Koehl, H. Wasmund, A. Herpers, P. Guttmann, S. Werner, K. Henzler, H. Du, J. Mayer, R. Waser, R. Dittmann, APL Materials **1**, 042102 (2013).

[5] Ch. Lenser, Z. Connell, A. Kovacs, R. Dunin-Borkowski, A. Köhl, R. Waser and R. Dittmann, Appl. Phys. Lett. **102**, 183504 (2013)

3-bit Read Scheme for Single Layer Ta_2O_5 ReRAM

V. Rana[1], A. Schoenhals[2], S. Menzel[1], D. Wouters[2], and R. Waser[1,2]

[1] Peter Grünberg Institut-7, Forschungszentrum Jülich, Germany
[2] Institut für Werkstoffe der Elektrotechnik II, RWTH Aachen University, Germany

Physical orientation of conductive filament in complementary switching plays a crucial role in defining the state of the device. This makes it possible to store and read 3-bit information in the single Ta_2O_5 ReRAM device. We report a novel read scheme, makes it possible to distinguish 8 different states only by using 4 different resistive states during pulse measurements. Variability and cycle-to-cycle stability of the single layer Ta_2O_5 complementary switching are also discussed.

Complementary Resistive Switching (CRS) [1], two anti-serially integrated bipolar ReRAM devices overcomes the sneak path problem in passive crossbar arrays. However, similar behavior has also been observed in several single layer metal-oxides Ta_2O_5, HfO_2 and $SrTiO_3$ ReRAM devices with symmetrical electrode configuration [2]. In literature, it is referred to as complementary switching (CS) [3]. The CS devices can also be implemented into the passive crossbar array without the selector device and further can allow logic-in-memory operation. Additionally, data density capabilities of these devices can be enhanced by multi-level storage (at least 3-bit operation). During the multi-state writing procedure, intermediate states can be accessed by limiting the maximum voltage/current. It has been reported that the HfO_2-based CS device stores 3-bit information in 8 different physical states of the conductive filament only by using 4 different resistive states [4]. The 3-bit information [3] using only 4 different resistance levels in the CS based ReRAM device is a promising feature for ultra-high data density electronic applications. In this paper, we present a 3-bit read scheme for Ta_2O_5-based CS device that uses a sequence of two read voltage pulses.

Fig. 1 shows the SEM image of a single layer Ta_2O_5 device. The experimental details can be assessed in ref. [5]. The quasi static *I-V* measurements of the single layer Ta_2O_5 device shows highly uniform cycle-to-cycle complementary switching characteristics as illustrated in Fig. 2a. Using write voltage sweeps with defined voltage polarities, maximum voltages and current compliances, we can precisely tune the device resistance. Three exemplary write sweeps are shown in Fig. 2b. Applying the negative voltage sweep without any current compliance forces the device to set and reset subsequently. The resulting state is defined as a high resistive state (HRS) written at negative (N) polarity or NHRS. Limiting the maximum current during the SET process makes it possible to stop the SET process at an intermediate state.

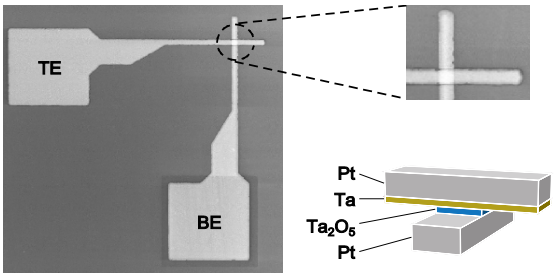

FIG. 1: SEM image of the single layer Ta_2O_5 CS device with 3D device stack schematic.

The device is set to a lower resistance state than NHRS but a higher resistance state compared to the state when the SET process is completed (i.e. state NLRS – 0 shown in Fig. 2b). Such state is defined as a low resistance state (LRS) written at negative (N) polarity or NLRS. The subsequent RESET process starts once the RESET current of about 0.8 mA is reached. Thus, the current compliance during the write procedure should be kept significantly lower.

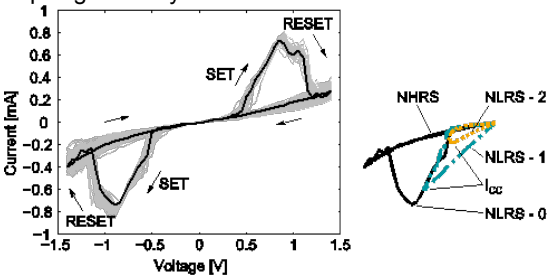

FIG. 2: (a) I-V characteristic of the single layer Ta_2O_5 CS device (b) Multiple resistive levels can be reached by applying different current compliance levels (I_{CC}) during CS SET process.

The symmetrical CS characteristics of single layer Ta_2O_5 ReRAM device can be explained by a theoretical model that considers the modification of the excess-donor density profile at the interfaces between Pt electrode and Ta_2O_5 thin film and between Ta_2O_5 thin film and Ta electrode, respectively. Consequently, the electron transport through the interface barriers is modulated rather than the bulk electron transport. Such donors can be mobile oxygen vacancies or Ta interstitials, the excess of which leads to *n*-conductivity [5].

Fig. 3 shows the evolution of the PLRS and the PHRS resistances during cycling. Here, the PLRS is defined as the state, where the SET process is completed, i.e. the turning point in the *I-V* curve

where the RESET process begins. Because of the symmetry of the *I-V* characteristics, both the PLRS and the PHRS have nearly the same resistance states as the corresponding NLRS and NHRS. Therefore, it is enough to evaluate the resistances only at one polarity. After a few tens of cycles, the resistances of both the PLRS and the PHRS start to increase. In addition, the cycle-to-cycle variability of the resistance states increases dramatically, especially in the case of the PLRS. In order to prevent the device failing due to increased variation of the resistance values, we refresh the device by applying a full voltage sweep with slightly increased voltages that allows us to maintain resistances to its initial values.

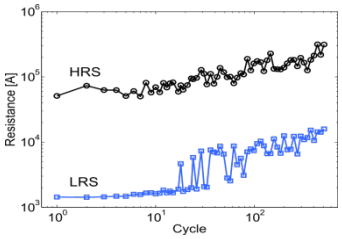

FIG. 3: Resistance evolution of PLRS - 0 and PHRS over more than 500 cycles. The PLRS - 0 is analogue to the NLRS - 0 state in Fig. 2b.

The control over the excess-donor density profile in the CS device allows us to define different resistance levels. This is achieved by applying an appropriate current compliance during the SET process. Such two states would have the same overall resistance but different excess-donor profiles, depending on the write voltage polarity. According to the conduction model, the PLRS exhibits lower excess-donor concentration at the Pt/Ta_2O_5 interface, whereas the NLRS exhibits the lower excess-donor concentration at the Ta_2O_5/Ta interface.

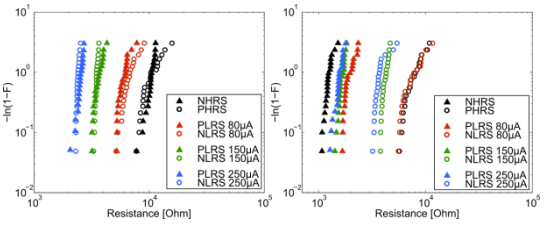

FIG. 4: (a) Cumulative resistance distribution calculated from the current response of the Ta_2O_5 CS device to the first read pulse with +0.1 V voltage amplitude. (b) Cumulative resistance distribution for the second pulse with +0.7 V voltage amplitude.

A sequence of two read voltage pulses is applied. The amplitude of first read pulse is between zero and the SET transition voltage whereas the second pulse amplitude is higher than the SET voltage but smaller than the RESET voltage. The voltages for the pulse sequence were set to +0.1 V for the first read pulse and +0.7 V for the second read pulse, respectively. Initially, the Ta_2O_5 -based CS device is programmed to one of the 8 defined resistive states by using the current compliance. Best distribution of the low resistive states was achieved with the current compliances of ±250 µA, ±150 µA and ±80 µA for the PLRS and the NLRS, respectively. Positive current value corresponds to PLRS state whereas negative value shows the NLRS state. The first voltage pulse of the read sequence provides the device resistance after the write procedure. The cumulative distribution of the written resistances is shown in Fig. 4a. The response to the first read pulse gives 4 subsets of states depending on the overall device resistance. Each subset contains 2 states with the same resistive state but different atomic profile in the device. The response to the second read pulse depends on the polarity of the programming voltage sweep. The state subsets measured during the first read pulse split into two groups below and above a certain threshold according to the programming voltage polarity as shown in Fig. 4b.

In the presented device, the threshold was set to 2.5 kΩ. The states PLRS@250 µA and NLRS@ −250 µA show both the same resistance value of ~ 2.5 kΩ for the first read pulse (Fig. 4a). In contrast, the resistances measured with the second pulse are ~1.5 kΩ for the PLRS@250 µA state and ~3.6 kΩ for the NLRS@−250 µA state, respectively (Fig. 4b). The response to each read pulse gives a related subset of states with the measured resistive state. However, the correlated response to both read pulses allows for clearly distinguishing between all 8 CF states and thus encoding 3-bit information. By applying only the first read pulse 2-bit information can be read without destroying the written state. The second read pulse increases the requirements on the electronic periphery and is a destructive read-out, but it also doubles the information density per device.

In conclusion, we have demonstrated a novel read scheme in Ta_2O_5 CS device, which makes it possible to distinguish between all 8 physical states into only 4 resistive states. This concept implies a sequence of two read voltage pulses and is based on the complementary switching mechanism. Both read pulse response gives one of the 8 unique combinations of two resistive state subsets and thus allows for clearly distinguishing between all 8 states, i.e. 3-bit information. This read scheme allows for improving the information density of the ReRAM devices.

This work was supported by the German Science Foundation (DFG) within the framework of SFB 917, Nanoswitches and Forschungszentrum Jülich.

[1] E. Linn, R. Rosezin, C. Kuegeler, and R. Waser, Nat. Mater. **9**, 403 (2010).

[2] Y. Yang, P. Sheridan, and W. Lu, Appl. Phys. Lett. **100**, 203112/1-4 (2012).

[3] F. Nardi, S. Balatti, S. Larentis, D.C. Gilmer, and D. Ielmini, IEEE Trans. Electron Devices **60**, 70 (2013).

[4] S. Balatti, S. Larentis, D. C. Gilmer, and D. Ielmini, Advanced Materials **25**, 1474 (2013).

[5] A. Schönhals, S. Menzel, V. Rana, and R. Waser, Non-Volatile Memory Technology Symposium (NVMTS),14th Annual (2014).

Impact of Composition and Morphology of ALD $SrTiO_3$ Films on the Resistive Switching of Pt/$SrTiO_3$/TiN Devices

N. Aslam[1], V. Longo[2], C. Rodenbücher[1], F. Roozeboom[2], W. M. M. Kessels[2], K. Szot[1], R. Waser[1], and S. Hoffmann-Eifert[1]

[1] Peter Grünberg Institut-7, Forschungszentrum Jülich, Germany
[2] Dept. of Applied Physics, Eindhoven University of Technology, Netherlands

The resistive switching (RS) behavior of atomic layer deposited (ALD) strontium titanate (STO) films were studied regarding the impact of composition and morphology. STO films of 12 nm thickness and ([Sr]/([Sr]+[Ti]) composition of 0.57, 0.50 and 0.46 were grown with adjusted ALD parameters. Clear stoichiometry effects on the film morphologies were observed after crystallization anneal. Nevertheless, all nano-crosspoint Pt/STO/TiN devices showed stable bipolar RS with non-linear current-voltage characteristics for both resistance states. The switching polarity agrees well with the filamentary character of the underlying valence change mechanism. In addition, effects of the films' composition on the RS properties were identified.

Towards the industrial application of ReRAM devices vertical crosspoint architectures are intensively discussed for reaching the required high integration density. Atomic layer deposition (ALD) will be the preferred technique for the integration of films into such 3-dimensional structures. Therefore, a deeper understanding of the relations between composition and morphology and RS properties in such films is of superior importance.

In this work [1], ALD $SrTiO_3$, films were integrated into Pt/STO/TiN nano crosspoint devices for future ReRAM applications (see Fig. 1). The composition and thickness of the STO films was controlled by the ALD parameters [2]. Main focus was on the effect of the cation ratio [Sr]/([Sr]+[Ti]) of 0.57 (Sr-rich), 0.50 (stoichiometric) and 0.46 (Ti-rich) on the morphology after crystallization and finally on the RS performance.

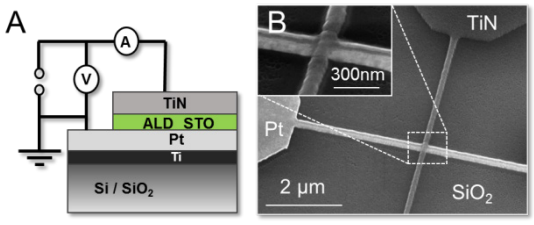

FIG. 1: A. Stack sequence and electrical measurement setup of the Pt/STO/TiN devices. B. SEM micrographs of a nano-crossbar Pt/STO/TiN structure.

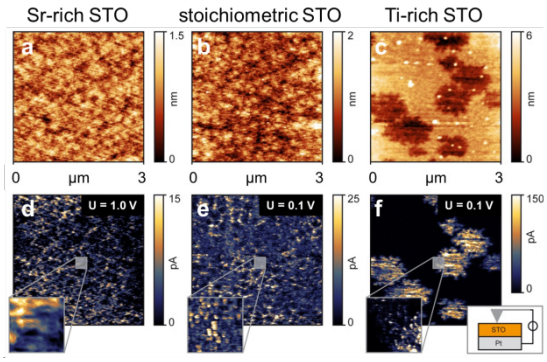

FIG. 2: (a-c) AFM and (d-f) LC-AFM pictures showing the topography and the corresponding current maps, respectively, of the 12 nm STO thin films grown on Si/Pt substrates and annealed for 5 min 600 °C in N_2; the STO compositions are arranged from the left to the right Sr-rich (a,d), stoichiometric (b,e), and Ti-rich (c,f). The LC-AFM measurements were performed at 200°C under UHV conditions with the voltage applied to the Pt/Ir coated AFM tip.

X-ray diffraction and X-ray photoemission spectroscopy (XPS) of the 600°C annealed STO films revealed perovskite-type crystalline phases with contributions from intergrowth of excess-cation oxide [1]. XPS data suggest the possibility of SrO intergrowth in the Sr-rich STO films. Ti-rich STO films show a broadening of the Ti 2p lines which could indicate additional Ti oxidation states.

Topography and current maps under UHV conditions at 200 °C were performed by local-conductivity atomic force microscopy (LC-AFM). The pronounced changes in the crystallization behavior of the Ti-rich films compared to the others could be explained by an increased thermal budget to achieve crystallization of the first [2]. The LC-AFM results (Fig. 2) clearly reveal locally inhomogeneous current spots which relate to the film's morphology being influenced by a stoichiometry-affected nucleation and crystallization behavior. Therefore, in order to interpret the electrical properties of the RS devices correct, both, the influence of the [Sr]/([Sr]+[Ti]) composition as well as the morphology of the STO thin films have to be considered, including phase separation in non-stoichiometric parts.

The current-voltage (*I*-*V*) characteristics of the Pt/STO/TiN crosspoint devices were recorded in a

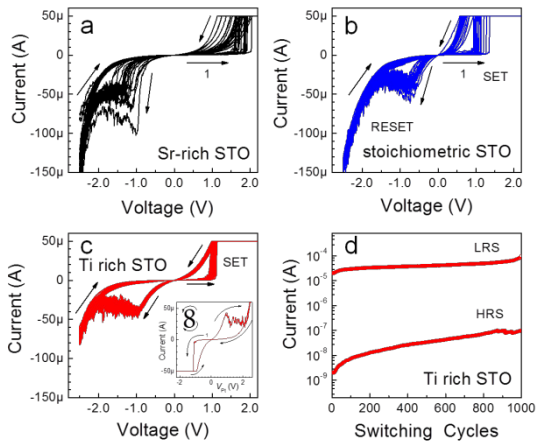

FIG. 3: (a-c) I-V hystereses of nano-crosspoint Pt/STO/TiN devices of 0.01 μm² size with 12 nm polycrystalline STO films of different compositions for a current compliance of 50 μA. The inset in (c) shows the 'counter-eight-wise' RS with respect to the actively switching Pt/STO contact. (d) Endurance plot over 1000 quasistatic switching cycles (I_{cc} = 100 μA) for a Pt/Ti-rich STO/TiN device at V_{read} = +0.3 V.

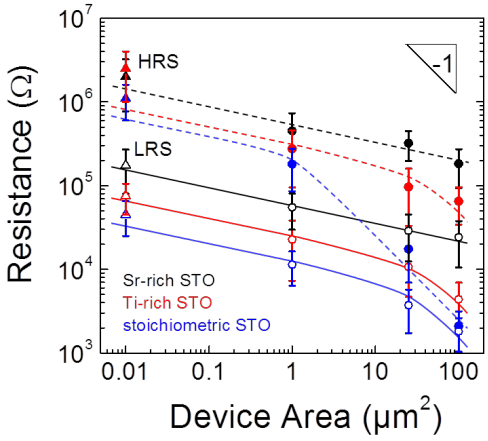

FIG. 4: Area dependency of the resistance states of the Pt/STO/TiN devices determined at V_{read} = +0.3 V from stable, quasistatic I-V hystereses. The colors encode the films composition, Sr-rich (black), Ti-rich (red), and stoichiometric STO (blue). Resistance values of the ON-state (LRS) and OFF-state (HRS) are given in open/filled symbols. The slope of (-1) is plotted for easier identification of area-scaling.

quasi-static mode using an Agilent B1500A semiconductor analyzer with the voltage signal applied to the TiN top electrode and the Pt electrode grounded (see Fig. 1A). All studied devices required an electroforming step into the ON state under positive polarity and a negative reset step prior to the reversible bipolar switching. The electroforming voltage (between 4 and 5 V) of the Pt/STO/TiN devices was found to be affected by the STO composition in two ways; intrinsically, by a change in the conduction mechanism and, extrinsically, by the different films' morphologies.

Figs. 3 (a-c) show representative (*I-V*) curves for electroformed 12 nm STO film devices obtained for equal values of current compliance and reset voltage. As a rather general trend an increase of the mean switching voltage with increasing Sr-content in the STO thin films was observed. This difference might be explained by a variation in the 'strength' of the conductive filament which is formed during the SET-process. This description is consistent with the higher ON-state non-linearity in the Sr-rich STO devices in comparison to the other compositions which can be interpreted as a difference in the redox-chemical processes involved in the VCM-type RS. For the constituents of STO the standard free energies of formation of oxides ΔG_0 differ significantly, i.e. $|\Delta G_0(SrO)| \gg |\Delta G_0(TiO_2)|$ at given conditions. Therefore, the SrO intergrowth found for the Sr-rich STO films might impede local reduction reactions resulting in a lower concentration of oxygen vacancies and therefore in a weaker conductive filament. In contrast, the small $|\Delta G_0(TiO_2)|$ value for TiO_2 might enable easy reduction of the material leading to a low SET-voltage and stable SET-operation. These effects in the RS behavior of nano-crystalline ALD grown STO thin films as a function of the [Sr]/[Sr]+[Ti] composition were confirmed for various device sizes (Fig. 4).

In low resistance state (LRS), all STO devices of the three compositions show a considerably weak area-dependency of their resistance values. This is interpreted in the way that the area-independent VCM-type filamentary mechanism dominates the RS characteristics of the Pt/STO/TiN devices after electroforming. The area-dependency of the high resistance state (HRS) values demonstrates the important effect of the films microstructure and morphology on the RS properties.

Once the microstructural effects of the polycrystalline thin films have been assessed, a clear effect of the STO composition on the RS behavior was observed. Nano-crossbar devices from stoichiometric STO films could be switched at lowest voltages of about 1.0 V between the lowest LRS values of $R_{ON} \approx 40$ kΩ, and reasonable HRS values of $R_{OFF} \approx 1$ MΩ determined at +0.3 V. Non-stoichiometry in the ALD grown STO films, especially Sr-excess, increases the devices R_{ON} values, i.e. result in LRS of lower conductance.

This work has been supported in parts by the European Community's Seventh Framework programme (FP7/2007-2013) under Grant ENHANCE 238409 and by the Deutsche Forschungsgemeinschaft (SFB 917).

[1] N. Aslam, V. Longo, C. Rodenbücher, F. Roozeboom, W. M. M. Kessels, K. Szot, R. Waser, and S. Hoffmann-Eifert, J. Appl. Phys. **116**, 064503 (2014).

[2] N. V. Longo, F. Roozeboom, W. M. M. Kessels, and M. A. Verheijen, ECS Transactions **58**, 153 (2013).

[3] N. Aslam, V. Longo, W. Keuning, F. Roozeboom, W.M.M. Kessels, R. Waser, and S. Hoffmann-Eifert, Phys. Status Solidi A **211**, 389 (2014).

Resistive switching of a quasi-homogeneous distribution of filaments on reduced TiO_2 surfaces

C. Rodenbücher[1], M. Rogala[1,2], G. Bihlmayer[3], W. Speier, and K. Szot[1,4]

[1] Peter Grünberg Institut-7, Forschungszentrum Jülich, Germany
[2] Faculty of Physics and Applied Informatics, University of Lodz, Poland
[3] Peter Grünberg Institut and Institute for Advanced Simulation-1, Forschungszentrum Jülich, Germany
[4] A. Chełkowski Institute of Physics, University of Silesia, Poland

We developed a heat treatment procedure involving reduction and oxidation steps in order to induce nanofilaments in TiO_2 (110)-surface layers. They can be switched between a high-resistive OFF state and a low-resistive ON state and thus promise high storage density in a redox-based random access memory (ReRAM). We demonstrate that it is possible to imprint quasi-homogeneous switchable regions over several square micrometers, which can be switched easily by low-voltage electrical stimulation using the conducting tip of an atomic force microscope. These regions consist of nanofilaments crossing the surface with a density of around 10^{12} cm^{-2}, much higher in density than observed for single crystals so far. Experimental evidence is given that these nanofilaments are not related to inherent structural imperfections such as dislocations, but may originate from a linear agglomeration of oxygen vacancies. Ab initio calculations and electrical simulations are performed to analyze the filamentary structures and their network to gain insight into the switching mechanism on the nanoscale.

By investigations of TiO_2, a prototypical transition metal oxide, it was found that resistive switching is not a material property by itself but is a highly localized phenomenon in the bulk material related to reduction processes and filamentary structures [1,2]. These structures may develop in single crystalline materials along structural imperfections such as dislocations through oxygen redistribution in an initializing electroforming step. However, the nanofilaments were found to evolve in unpredictable locations and irregular structures, which is a serious drawback for device development. Since the resistive switching in Ti-based oxides is related to the modification of the local oxygen content resulting in a valence change of the neighbouring Ti atoms, a change of the resistance can be achieved by application of an electrical field, or by thermal reduction.

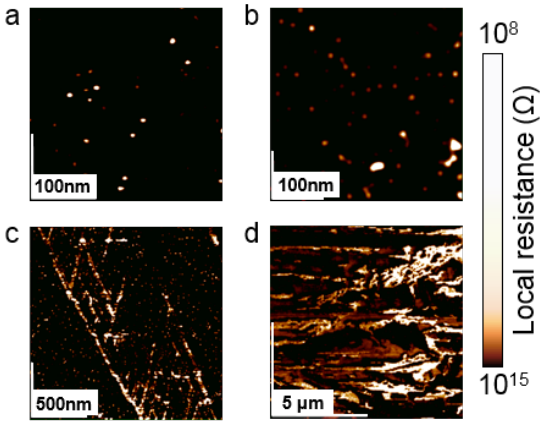

FIG. 1: LC-AFM maps of the TiO_2 (110) surface after different reduction steps: a) stoichiometric crystal, b) slightly reduced crystal (after 1-2 h at 800-1000 °C in UHV), c) strongly reduced crystal (24h; 1000°C; UHV), d) heavily reduced crystal (a few days; 1100 °C; UHV)

As illustrated in Fig. 1 this process is highly local and heterogeneous in nature. Here, we use electrical mapping of the surface employing a local conductivity atomic force microscope (LC-AFM) where the tip of the microscope acts as a point electrode in contact with the surface. Current maps of TiO_2 are presented for a reference stoichiometric crystal without any pre-treatment (Fig. 1a), thermally treated crystals with different level of reduction, here light (Fig. 1b), strong (Fig. 1c) to heavy (Fig. 1d) reduction. While the maps for lightly reduced crystals show only a statistical distribution of exits of filaments, they tend to accumulate in linear structures with increasing reduction. Simultaneously, the filaments gain conductivity as an effect of the removal of oxygen, which can even lead to the creation of new crystallographic phase as identified by X-ray diffraction. This small gallery of “switched crystals” exemplifies that the homogeneity of the distribution and the density of filaments in heat-treated TiO_2 is far from what one would consider as being useful for the application as nano-devices for information storage.

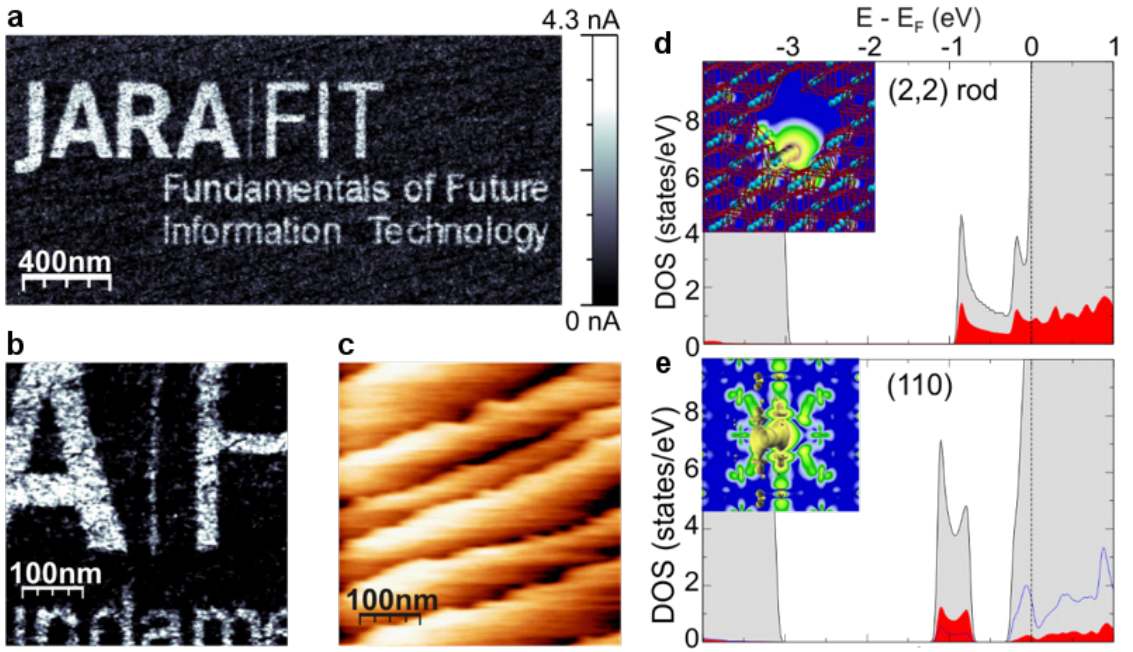

FIG. 2: a) LC-AFM current map of TiO_2 previously patterned by selectively applying a low voltage (U < 4 V) in the scanned area. b) magnification of the center of the scanned region. c) corresponding topographical image. Right: Ab initio simulation of the charge density and electronic structure of two types of linear defects in TiO_2: d) a large defect with a (2,2)-nanorod removed from the TiO_2 matrix, e) row of oxygen vacancies in (110) direction. The inset shows the structure with oxygen atoms in red and Ti atoms in blue.

It came as a surprise that, when we tried to test different low-level reduction and reoxidation procedures we were able to electrically imprint an astonishingly high concentration of conducting filaments (density ~ 10^{12}/cm^2) with LC-AFM using only low voltages. This is illustrated in Fig. 2, showing the current map after selectively switching the surface in the shape of the JARA-FIT logo. Regions become visible with a quasi-homogenous distribution of high-conducting states at the micrometre scale. These regions are, however, still found to be filamentary in nature but, do not seem to be related to structural imperfections with an invariant Burgers vector such as dislocations (type I) but may be regarded as a new type of linear defects (type II). This is underlined by the fact that dislocation-like type I filaments, which can be identified on etched crystals, are much harder to reoxidize than the new type II defects. To gain an understanding of the conductive properties of different types of defects, we performed density functional theory calculations of idealized, one-dimensional models of defects in the ground state: For the model of a “type I” large-scale defect we simulated the removal of a so-called (2,2)-nanorod. As shown in Fig. 2d, the additional removal of a O row from such a defect leads to the formation of a one-dimensional band close to the conduction band edge. Hence it is easily conceivable that such a defect is electronically conductive, even when additional oxygen atoms are diffusing into this 1D channel. For the type II defect we assumed one-dimensional oxygen defects, such as those predicted in [3]. We calculated the electronic structure of these defect arrangements exemplarily shown for the (110) direction in Fig. 2e. It can be seen that more or less extended defect states split off the conduction band and reside in the gap. In contrast to larger defects or defect-bundles, the metallic pathways in these oxygen-vacancy rows are easily disrupted by adding oxygen atoms. Thus, these structures would be compatible with the electrically active type II defects. A statistical analysis of the current distribution at the surface for different oxidation stages shows that they are connected to the stable type I filaments that connect the surface to the electrode [4].

In summary, our results indicate that the formation of filaments related to one-dimensional defects could be used for a tailoring of resistive switching filaments and to an improvement of switching performance.

We acknowledge the financial support by the Deutsche Forschungsgemeinschaft, SFB 917 Nanoswitches and computing time granted at the RWTH Compute Cluster in Aachen.

[1] K. Szot, G. Bihlmayer, and W. Speier, Solid State Physics **65**, 353 (2014).

[2] K. Szot, M. Rogala, W. Speier, Z. Klusek, A. Besmehn, and R. Waser, Nanotechnology **22**, 254001 (2011).

[3] S.-G. Park, B. Magyari-Köpe, and Y. Nishi, Electron Device Letters, IEEE, **32**, 197 (2011)

[4] M. Rogala, G. Bihlmayer W. Speier, Z. Klusek, C. Rodenbücher, and K. Szot, Adv. Funct. Mater. *in press* (2015); doi: 10.1002/adfm.201500855.

GISAXS Simulations of Filamentary Inhomogeneities with Gradients in Resistively Switching $SrTiO_3$

O. Faley and U. Klemradt

II. Physikalisches Inst. B, RWTH Aachen University, Germany

We investigated the influence of geometrical and chemical gradients in structures buried in a layer on the grazing incidence small angle X-ray scattering (GISAXS) pattern by simulation. Geometrical and chemical gradients as well as their combinations produce distinct scattering patterns, whereas the inversion of gradients has very little impact.

In metal-insulator-metal (MIM) devices with $SrTiO_3$ as the insulating layer, resistive switching can be achieved through the valence change of Ti cations owing to the diffusion of oxygen vacancies [1]. The resistive switching mechanism in $SrTiO_3$ is presumably of filamentary nature, with oxygen vacancies agglomerating along dislocations.

GISAXS measurements of resistively switching MIM structures exhibit patterns with distinct lateral lobes, which originate from tapered filamentary inhomogeneities within the insulating layer [2]. For a quantitative characterization of such structures, simulations of scattering patterns from increasingly complex structures have been calculated.

Fig. 1 shows a sketch of a structure embedded in a layer, with the z–axis pointing upwards in growth direction. This axis is also distinguished with respect to the scattering geometry, since it corresponds to the $\vec{q}_z = \vec{k}_f - \vec{k}_i$ direction under specular conditions.

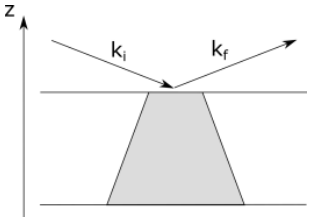

FIG. 1: The direction of sample growth is defined as z-axis, here shown with a structure embedded in a layer. This axis is also distinguished in scattering.

To define structural gradients, we consider the electron density ρ(z), e.g. the laterally averaged electron density, which is solely a function of z. For homogeneous layers, ρ(z) is stepwise constant ("box model"). By definition, a structural gradient exists if the derivative $d\rho/dz$ is non-zero within a layer.

Structural gradients can have different causes. We distinguish here between geometrical and chemical gradients, the latter referring to a variation of the chemical composition in z-direction with respect to the embedded material. For example, an embedded homogeneous cylinder does not lead to a structural gradient, but a homogeneously filled cone does.

Geometrical and/or chemical gradients in the filaments can influence the GISAXS pattern strongly. To study their impact, we implemented a conical form factor [3] modulated by a factor *τ(z)* in the freely available software FitGISAXS [4]

$$F = \int_0^H \tau(z) \cdot 2\pi \, {R_z}^2 \cdot \frac{J_1(q_\parallel R_z)}{q_\parallel R_z} \cdot \exp(iq_z z) dz$$

with $\tau(z) = \frac{n_z^2 - n_{layer}^2}{n_{base}^2 - n_{layer}^2}$ and $R_z = R_{base} - \frac{z}{\tan\alpha}$.

The refractive index is defined at the bottom and at the top of the filament and the refractive index decrement and the absorption coefficient are varied linearly between these limits. The simulations are calculated using the distorted wave Born approximation (DWBA), neglecting all interfacial roughness as well as multiple scattering.

For the simulations we choose the MIM system of Nb:$SrTiO_3$ (substrate) / Fe:$SrTiO_3$ (20 nm) / Ti (5 nm), a grazing angle of 0.65° and a wavelength of 1.38 Å. The sample structure, experimental parameters and dimensions of the filaments are based on measurements [2, 5].

According to Ref. [6] the reduction of oxygen compared to stoichiometric $SrTiO_3$ is about 15 % to 30 %, which corresponds to Fe:$SrTiO_{2.5}$ and Fe:$SrTiO_{2.1}$. To study the effect of chemical gradients, we therefore chose a gradient in the oxygen concentration varying between Fe:$SrTiO_{2.1}$ and Fe:$SrTiO_{2.9}$. The average composition of Fe:$SrTiO_{2.5}$ was used to describe chemically homogeneous filaments. The refractive indexes were calculated from the stoichiometry and calculated density of each compound.

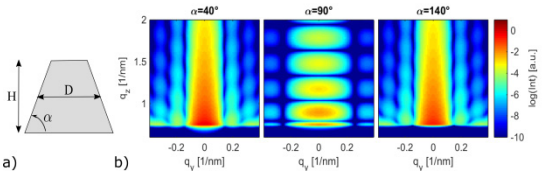

FIG. 2: Simulated GISAXS patterns from chemically homogeneous cylindrical and conical structures embedded in a Nb:SrTiO$_3$/ Fe:SrTiO$_3$/ Ti layered system. a) Sketch of the simulated structure with height H = 20 nm, an average width D = 30 nm and base angle α=40°, 90° and 140°. b) The left and right patterns show scattering from the same conical structure but with opposite orientation, while the central pattern shows scattering from a cylinder.

In Fig. 2 the GISAXS patterns for cylindrical and conical structures embedded in an insulating layer are displayed for homogeneous filaments. Whereas the opening angle α strongly influences the patterns, opposite orientations of the cones result in very similar patterns (Fig. 2 b, α = 40° and α=140°). The detailed value of the opening angle influences in particular the vertical shift between the lateral and the central lobes as well as the distinction of the oscillations on the off-specular line q_y = 0 (Fig. 3).

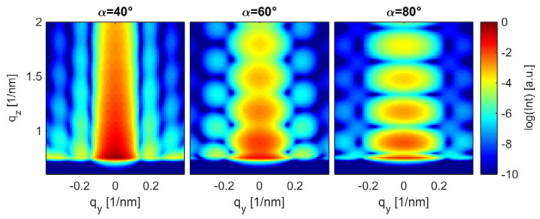

FIG. 3: GISAXS patterns from conical structures for the same parameters as in Fig. 2, showing the influence of the cone angle. The oscillations in the q_z direction become more pronounced as the filament approaches cylindrical shape.

Fig. 4 shows GISAXS patterns for cylindrical structures (α = 90°, H = 20 nm, D = 30 nm) with different oxygen vacancy concentrations. Chemical gradients are visualized in the inset, with higher oxygen deficiencies being represented by darker shading. Whereas the existence of a gradient is clearly observable from the washing-out of oscillations, the orientation of the chemical gradient (upward or downward) appears to have very little impact on the patterns. This is similar to our finding for a purely geometrical gradient (cf. Fig. 2 b).

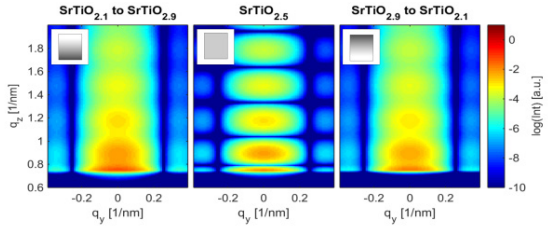

FIG. 4: Simulated GISAXS patterns for cylindrical structures with chemical gradients. Left: variation of oxygen concentration from Fe:SrTiO$_{2.1}$ at the bottom to Fe:SrTiO$_{2.9}$ at the top of the structure; right: vice versa. Middle: homogeneous cylinder of Fe:SrTiO$_{2.5}$ for comparison.

However, if both a geometrical and a chemical gradient are present, a more complex situation arises. As depicted in Fig. 5, filaments with parallel and antiparallel orientation of the two gradients give rise to strongly differing scattering patterns. However, the simultaneous inversion of both gradients results again in similar patterns, which is analogous to our previous findings. It should be noted that the scattering intensity exhibits a small difference for upward and downward oriented cones. Whether this difference is significant and could potentially be exploited experimentally, will be the subject of further studies.

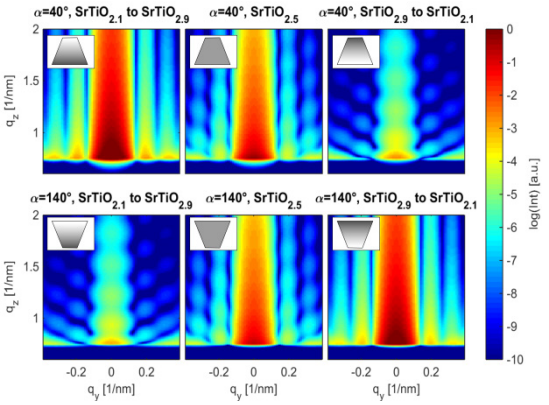

FIG. 5: GISAXS patterns for conical structures with a base angle of 40° and 140° and variation of refractive index between the top and the bottom of the structure, showing the influence of a combined chemical and geometrical gradient.

The presented research is part of the efforts of the Collaborative Research Group (SFB 917) on the topic of “Resistively Switching Chalcogenides for Future Electronics – Structure, Kinetics and Device Scalability” [7].

[1] R. Waser, R. Dittmann, G. Staikov, and K. Szot, Adv. Mater. **21**, 2635 (2009)

[2] S. Stille, Ch. Lenser, R. Dittmann, A. Koehl, I. Krug, R. Muenstermann, J. Perlich, C.M. Schneider, U. Klemradt, and R. Waser, Appl. Phys. Lett. **100**, 223503 (2012)

[3] R. Lazzari, J. Appl. Cryst. **35**, 406-421(2002)

[4] D. Babonneau, J. Appl. Crystallogr. **43**, 929 (2010)

[5] S. Stille, C. Baeumer, S. Krannich, C. Lenser, R. Dittmann, J. Perlich, S.V. Roth, R. Waser, and U. Klemradt, J. Appl. Phys. **113**, 064509 (2013).

[6] K. Szot, G. Bihlmayer, and W. Speier, Solid State Physics **65,** 353-559 (2014)

[7] Further information on the homepage of SFB 917: http://www.sfb917.rwth-aachen.de

Limiting factors for 2D Electron Transport in $LaAlO_3/SrTiO_3$ Bilayers

F. Gunkel[1], S. Wicklein[1], S. Hoffmann-Eifert[1], P. Meuffels[1], P. Brinks[2], M. Huijben[2], G. Rijnders[2], R. Waser[1], and R. Dittmann[1]

[1] Peter Grünberg Institut-7, Forschungszentrum Jülich, Germany
[2] MESA + Institute for Nanotechnology, University of Twente, The Netherlands

The electrical properties of the 2-dimensional electron gas (2DEG) at the metallic interface of $LaAlO_3/SrTiO_3$ (LAO/STO) bilayers are investigated. Systematic growth-control of the STO thin film cation stoichiometry (defect-engineering) yields a relation between cationic defects in the STO layer and electronic properties of the bilayer-interface. Hall measurements reveal a stoichiometry-effect primarily on the electron mobility. The results indicate an enhancement of scattering processes in as-grown non-stoichiometric samples indicating an increased density of defects. As revealed, growth-induced defects in thin film STO ultimately limit the transport properties in LAO/STO thin film interfaces even under ideal growth conditions. This result is of significant importance for the technical use of such electron systems [1].

The discovery of the conducting interface between the wide band gap perovskite insulators, $SrTiO_3$ (STO) and $LaAlO_3$ (LAO), has sparked enormous scientific and technological interest. In analogy to similar interface effects in semiconductor heterostructures, the supposed 2-dimensional electron gas (2DEG) formed at the LAO/STO interface represents a promising candidate system to emulate the achievements of semiconductor technologies in all-oxide devices. A general understanding of the conduction mechanism at oxide interfaces - as developed in recent years [2,3] - is an important prerequisite for the development of real electronic devices. Furthermore, it is desirable to obtain a transfer from the scientifically relevant STO-*single crystal-based* LAO/STO interface to the technologically more relevant STO-*thin-film-based* interface system and superlattices. However, given the crucial impact of crystal defects on the electronic properties of LAO/STO interfaces, the use of STO thin films adds new challenges to the field, namely understanding and controlling the defect structure of thin film STO.

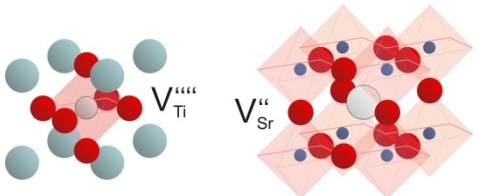

FIG. 1: Sketch of cationic point defects in STO; Red spheres = O anions, light blue = Sr cations, dark blue = Ti cations. Gray spheres indicate vacancies (V).

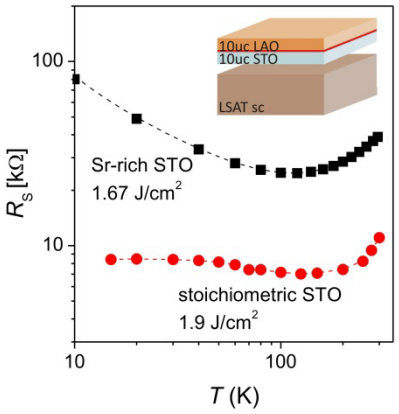

FIG. 2: Temperature dependence of the sheet resistance of LAO/STO bilayer interfaces for (red) stoichiometric STO composition and (black) Sr-rich STO composition.

Here, we follow the potential approach to alter the intrinsic cation stoichiometry in STO by growth-control [1]. We investigated the electrical properties of LAO/STO bilayers comprising STO thin films grown under varied growth conditions and a LAO layer grown under constant conditions. In particular, the laser fluence, F, during the pulsed laser deposition (PLD) of the STO thin film was the only parameter varied in this study. This procedure enables to continuously tune the composition of the STO thin film from being Sr-rich to stoichiometric to Ti-rich, while keeping the LAO top layer unchanged. In order to accommodate non-stoichiometric growth, the STO thin film is expected to incorporate defects such as strontium vacancies and/or titanium vacancies (see fig.1).

The electric properties of the resulting LAO/STO bilayer interfaces are presented in fig. 2. For the stoichiometric growth of STO, the sheet resistance of the stoichiometric bilayer interface decreases with decreasing temperature generally reflecting a metallic temperature dependence. A resistance upturn is observed around 150 K, while R_S saturates at a value of several kilo ohms at temperatures below 50 K. This low temperature limiting value is about one to two orders of magnitude higher than the typical residual resistance observed for standard LAO/STO interfaces to single crystals (typically a few hundred ohms). This result hints at an increased defect density in the stoichiometric STO thin film compared to STO single crystals. Non-stoichiometric samples deliver even higher sheet resistance values than stoichiometric samples, as

displayed for an LAO/STO interface to slightly SrO-rich STO (see fig. 2). Starting at 300 K, the non-stoichiometric sample exhibits a metallic temperature dependence. Below 120 K, the resistance shows an upturn and increases constantly indicating an even more pronounced effect of defect scattering and/or carrier freeze-out than for the stoichiometric case. Fig. 3 depicts the room temperature sheet resistance of all as-grown LAO/STO bilayers as a function of the laser fluence applied during growth of the STO layer. For comparison, the *c*-lattice expansion of the homoepitaxial reference samples – used as a measure of the cation non-stoichiometry of the STO films – is added to the plot. Obviously, R_S exhibits a minimum for the heterostructures with almost stoichiometric STO layers indicated by the vanishing *c*-lattice expansion of the homoepitaxial films at F_{STO} = 1.9 J cm^{-2}. For Sr-rich as well as Ti-rich STO layers, the sheet resistance of the LAO/STO bilayer increases with increasing non-stoichiometry, finally reaching several hundreds of kilo-ohms at F_{STO} = 1.1 J cm^{-2} and at F_{STO} = 3.05 J cm^{-2}, respectively. Thus, the interface conduction is affected for both types of non-stoichiometry, Ti-rich composition and Sr-rich composition. In fact, the sheet resistance of the LAO/STO interface can be tailored and controlled by the (non-) stoichiometry of the involved STO layer. As revealed by Hall measurements, the non-stoichiometry of the STO layer primarily influences the electron mobility which exhibits an opposite dependence on laser fluence as R_S. For a stoichiometric growth of the STO layer, the electron mobility reaches its maximum value of 1.6 cm^2 V^{-1}s^{-1}. For Sr-rich and Ti-rich growth of the STO layer, the mobility is reduced by up to one order of magnitude. An increased amount of defects in the non-stoichiometric STO layers thus causes additional scattering centers for the electrons at the LAO/STO interface. In contrast to that, the electron density, n_S, is for all samples of the same order of magnitude, while it shows a slight tendency to increase with increasing laser fluence.

In bulk STO (or standard LAO/STO heterostructures), the room temperature electron mobility is typically limited by phonon scattering yielding μ_{Ph} ≈ 5–10 cm^2 V^{-1}s^{-1}. Hence, the low mobility values (μ_n ≤ 1–2 cm^2 V^{-1}s^{-1}) obtained for LAO/STO bilayers in our study (as well as in literature) indicate that defect scattering affects and ultimately limits μ_n in thin film LAO/STO interface samples even at 300 K. This is the case also for stoichiometric STO thin film composition. The further decrease in mobility when tuning the STO stoichiometry indicates that non-stoichiometry of the STO layer causes a further increase in the concentration of scatter centers, i.e. defects, in the vicinity of the LAO/STO interface.

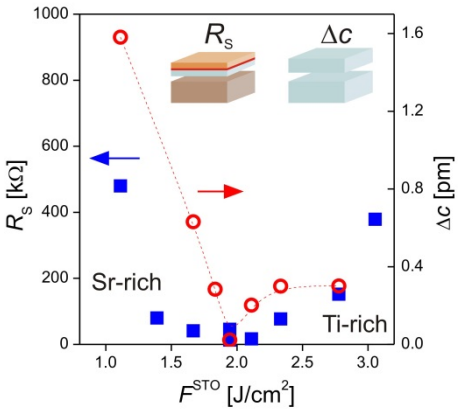

FIG. 3: Sheet resistance of LAO/STO bilayers comprising STO thin films with varied cation stoichiometry (squares). As a measure of (non-) stoichiometry, we use the c-lattice expansion of homoepitaxial STO films grown at various laser fluences (circles).

In summary, we addressed the influence of the STO cation stoichiometry on the electronic properties of the LAO/STO interface. As-grown LAO/STO heterostructure devices obtained by PLD are shown to exhibit a drastic non-equilibrium defect structure involving both oxygen and cation species. One possible way of manipulating and controlling the defect structure of the STO layer adjacent to the LAO/STO interface is the growth-induced variation of the cation stoichiometry (a defect engineering process). As shown, the variation of the STO growth parameters primarily tailors the electron mobility at the LAO/STO interface due to the incorporation of defects in non-stoichiometric STO thin films, while the amount of acceptor-type point defects induced during growth seems insufficient to significantly alter the effective charge density and the resulting electron concentration at the LAO/STO interface.

A more detailed study of the bilayer properties [1] shows that both point defects as well as extended defects, such as Ruddlesden-Popper-like defects induced during non-stoichiometric growth, contribute to electron scattering. Extended defect structures are found to partially heal during thermal treatment resulting in a mobility-increase in non-stoichiometric samples.

The results of this study underline the direct interrelation between interfacial conductivity and cationic defects in the STO layer adjacent to the LAO/STO interface. Such defects evidently exist even in nominally stoichiometric STO and limit the electron mobility in the 2DEG at LAO/STO bilayer interfaces.

[1] F. Gunkel et al., Nanoscale **7** (3), 1013-22 (2015).

[2] F. Gunkel et al., Appl. Phys. Lett. **100**, 052103 (2012).

[3] F. Gunkel et al., Appl. Phys. Lett. **97**, 012103 (2010).

Momentum-resolved electronic structure at a buried interface from soft X-ray standing-wave angle-resolved photoemission

L. Plucinski[1,2], A. X. Gray[3,4,5], J. Minár[6], M. Huijben[7], A. Bostwick[8], E. Rotenberg[8], S.-H. Yang[9], J. Braun[6], A. Winkelmann[10], G. Conti[3,4], D. Eiteneer[3,4], A. Rattanachata[3,4], A. A. Greer[3,4], J. Ciston[11], C. Ophus[11], G. Rijnders[7], D. H. A. Blank[7], D. Doennig[12], R. Pentcheva[12], J. B. Kortright[4], H. Ebert[6], C. M. Schneider[1,2], and C. S. Fadley[3,4]

[1] Peter-Grünberg-Institut-6, Forschungszentrum Jülich, Germany
[2] Fakultät für Physik and Center for Nanointegration Duisburg-Essen (CeNIDE), Duisburg University, Germany
[3] Department of Physics, University of California Davis, USA
[4] Materials Sciences Division, Lawrence Berkeley National Laboratory, USA
[5] Stanford Institute for Materials and Energy Science, Stanford University and SLAC National Accelerator Laboratory, USA
[6] Department of Chemistry, Physical Chemistry Institute, Ludwig-Maximilians University-Munich, Germany
[7] Faculty of Science and Technology, MESA + Institute for Nanotechnology, University of Twente - Enschede, Netherlands
[8] Advanced Light Source, Lawrence Berkeley National Laboratory, USA
[9] IBM Almaden Research Center - San Jose, USA
[10] Max-Planck-Institut für Mikrostrukturphysik, Halle (Saale), Germany
[11] National Center for Electron Microscopy, Lawrence Berkeley National Laboratory, USA
[12] Department of Earth and Environmental Sciences and Center of Nanoscience (CENS), Ludwig-Maximilians University-Munich, Germany

Angle-resolved photoemission spectroscopy (ARPES) is a powerful technique for the study of electronic structure, but it lacks a direct ability to study buried interfaces between two materials. We address this limitation by combining ARPES with soft X-ray standing-wave (SW) excitation (SWARPES), in which the SW profile is scanned through the depth of the sample. We have studied the buried interface in a prototypical magnetic tunnel junction $La_{0.7}Sr_{0.3}MnO_3/SrTiO_3$. Depth- and momentum-resolved maps of Mn 3d e_g and t_{2g} states from the central, bulk-like and interface-like regions of $La_{0.7}Sr_{0.3}MnO_3$ exhibit distinctly different behavior consistent with a change in the Mn bonding at the interface. We compare the experimental results to state-of-the-art density-functional and one-step photoemission theory, with encouraging agreement that suggests wide future applications of this technique.

A significant disadvantage of the conventional ARPES technique is its extreme surface sensitivity, due to the very low inelastic mean-free paths (IMFPs) of the electrons photoemitted using radiation in the range 25 eV < hν < 150 eV. Even at soft X-ray photon energies (500 < hν < 1200 eV), the photoemission signal originating closer to the surface will be stronger than the signal originating from below according to $I(z) = I_0 \exp[-z/\Lambda \sin(\theta_{TOA})]$, where z is the depth, Λ is the IMFP, and θ_{TOA} is the electron take-off angle relative to the surface.

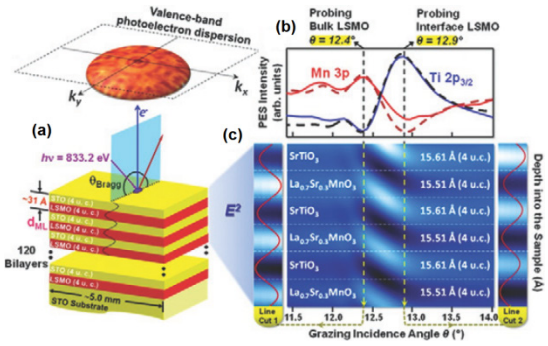

FIG. 1: (a) Schematic diagram of the investigated epitaxial multilayer structure consisting of 120 bilayers of STO and LSMO (b) SW-excited photoemission intensity rocking curves (RCs) for Ti 2p 3/2 and Mn 3p core-levels (solid curves), as well as the X-ray optical simulations fitted to them (dashed curves) (c) Simulated intensity of the X-ray SW electric field (E^2) inside the sample as a function of the depth and grazing incidence angle. The line-cuts indicate that, for incidence angles <12.4°, the SW field highlights the bulk or center of the LSMO layer, but for angles >12.9° the interface regions of the LSMO layer are emphasized.

We add depth selectivity to ARPES by combining more bulk-sensitive soft X-ray excitation at 833.2 eV corresponding to IMFPs of about 19Å with the SW approach (SWARPES) to provide a unique depth- and *k*-resolved probe of buried layer and interface electronic structure [1]. We illustrate this capability of SWARPES on a prototypical oxide magnetic tunnel junction (MTJ), $La_{0.7}Sr_{0.3}MnO_3/SrTiO_3$ (LSMO/STO) by comparing experiment to theory of several types, including, in particular, state-of-the-art one-step photoemission calculations. The details of the sample are presented in Fig. 1.

The SWARPES measurements were carried out at the Electronic Structure Factory (ESF) endstation at Beamline 7.0.1 of the Advanced Light Source (Lawrence Berkeley National Laboratory) using a Scienta R4000 spectrometer. The measurements were performed at a temperature of 20 K and with an overall energy resolution of ~ 300 meV, with some reference data taken at 300 K. In order to maximize reflectivity and thus also the contrast of the SW, and therefore to better define the depth-resolved photoemission within the sample, the excitation energy was set to 833.2 eV, which is just below the La $3d_{5/2}$ absorption edge [2].

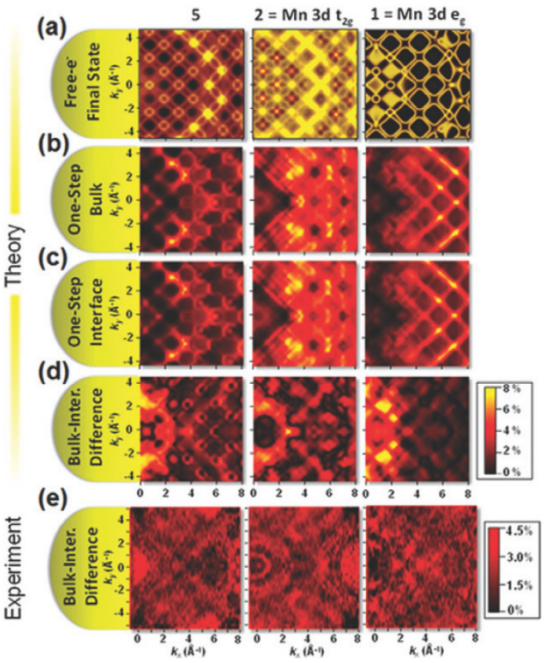

FIG. 2: Theoretical calculations for SWARPES from levels Mn 3d e_g (1), Mn 3d t_{2g} (2) and the bottom of the valence bands (5). (a) Simple free-electron final-state theory with direct transitions from an LDA+U-based band structure. Yellow corresponds to spin-up (majority) bands, and red to spin-down (minority). (b), (c), and (d) More accurate one-step photoemission theory summing over both spin polarizations and with the SW intensity profile included, for a bulk-LSMO–sensitive geometry (b), an interface-sensitive geometry (c), and the bulk-minus-interface difference (d), respectively. The amplitudes of the effects are again indicated. (e) shows experimental bulk-interface difference panels.

In order to verify the presence of the SW in the superlattice, and to most quantitatively model the intensity profile of it within the sample, we first performed core-level SW-XPS measurements shown in Fig. 1(b). Strong SW rocking curve (RC) intensity modulations near the Bragg condition for the superlattice were observed for Ti $2p_{3/2}$ and Mn 3p core-levels; these are fully consistent with momentum-integrated study of a similar LSMO/STO sample [2].

By combining soft X-ray ARPES with SW-excited photoelectron spectroscopy, we have devised a unique technique for probing the k-resolved electronic structure of buried layers and interfaces. By generating an X-ray SW inside a multilayer sample, and then translating it up and down within the sample by varying the incidence angle, we can selectively probe the electronic structure emphasizing the bulk of a layer or its interface, and then directly compare the two. We have applied SWARPES to the investigation of the electronic properties of the buried interface within a magnetic tunnel junction composed of $La_{0.7}Sr_{0.3}MnO_3/SrTiO_3$, and discovered that the bulk-like and interface-like regions of the buried $La_{0.7}Sr_{0.3}MnO_3/SrTiO_3$ layer exhibit a distinctly different behavior, consistent with a change in the Mn bonding geometry at the $La_{0.7}Sr_{0.3}MnO_3/SrTiO_3$ interface observed previously [2], but now elaborated with *k* resolution. This can be seen in the distinct features in the bulk-interface difference maps, which are the most clear for the binding energies related to the Mn orbitals in the valence band, as shown in Fig. 2(e). The experimental results are validated via agreement with free-electron final-state model calculations and more precise state-of-the-art one-step photoemission theory including matrix-element effects, as shown in Fig. 2(d). Future theoretical treatments should involve the inclusion of atomic distortions near the interface, e.g. incorporating a crystal-field distortion near the interface that is suggested by our prior angle-integrated SW-XPS study of the same system, as well as a more accurate inclusion of the interface mixing/roughness that is also seen in the prior SW-XPS study of this system, as well as transmission electron microscopy (TEM) + electron energy loss spectroscopy (EELS) data from the present sample, the SW intensity profile and phonon effects. We thus suggest that the SWARPES method should be of broad use in the future studies of buried layers and interfaces in various types of epitaxial multilayer structures, including those exhibiting spintronic, ferroelectric, multiferroic, and superconducting properties.

[1] A. X. Gray, J. Minar, L. Plucinski, M. Huijben, A. Bostwick, E. Rotenberg, S.-H. Yang, J. Braun, A. Winkelmann, G. Conti, D. Eiteneer, A. Rattanachata, A. A. Greer, J. Ciston, C. Ophus, G. Rijnders, D. H. A. Blank, D. Doennig, R. Pentcheva, C. M. Schneider, H. Ebert, and C. S. Fadley, Europhys. Lett., **104**, 17004 (2013)

[2] A. X. Gray, C. Papp, B. Balke, S.-H. Yang, M. Huijben, E. Rotenberg, A. Bostwick, S. Ueda, Y. Yamashita, K. Kobayashi, E. M. Gullikson, J. B. Kortright, F. M. F. de Groot, G. Rijnders, D. H. A. Blank, R. Ramesh, and C. S. Fadley, Phys. Rev. B **82**, 205116 (2010),

Polarity of Translation Boundaries in Antiferroelectric $PbZrO_3$

X.-K. Wei[1,2], C.-L. Jia[2], K. Roleder[3], and N. Setter[1]

[1] Ceramics Laboratory, Swiss Federal Institute of Technology Lausanne (EPFL), Lausanne, Switzerland
[2] Ernst Ruska-Centrum and Peter Grünberg Institute-5, Forschungszentrum Jülich, Germany
[3] Institute of Physics, University of Silesia, Katowice, Poland

The peculiar properties possessed by domain walls in ferroic materials find potential applications in designing novel nanoelectronic devices. Here, the polarity of translation boundaries (TBs) in antiferroelectric $PbZrO_3$ is investigated. We show that previous experimentally reported polar property of $\boldsymbol{R}_{III\text{-}1}$ type TB can be well approximated by a strain-free rigid model. Based on this, the modeling investigation suggests that there are two additional polar TBs, three antipolar-like TBs and one antipolar antiphase boundary. High-resolution scanning transmission electron microscopy study reveals that the straight $\boldsymbol{R}_{III\text{-}1}$ type TB can split into "sub-domains" with possible polarization reversal, suggesting the occurrence of ferroic orders at the TBs.

Since the discovery of peculiar properties at domain walls, the topological defects residing intrinsically in ferroelectrics and multiferroics have attracted a great deal of attention for their potential applications in designing nanoelectronic devices [1]. In particular, against the insulating domains, conductivity at ferroelectric domain walls is investigated with emphasis. In nonpolar materials, domain boundaries are also found to have fascinating properties, which promises an alternative material basis towards future device applications. For example, the twin boundary in ferroelastic $CaTiO_3$ predicted to be ferri-electric is qualitatively verified by using probe-corrected scanning transmission electron microscope (STEM). In $SrTiO_3$, the hard APB is theoretically predicted to be ferroelectric at low temperatures. Associated with first-principles calculations, recently, the polar property at an $\boldsymbol{R}_{III\text{-}1}$ = 1/4[0 2 n] (n = 0 or 2) type APB of antiferroelectric (AFE) $PbZrO_3$, which has a spontaneous polarization (P_S) about 14 μC/cm^2, is quantitatively determined by using negative spherical-aberration (C_S) imaging (NCSI) technique in an aberration-corrected TEM [2].

Translation boundary (TB), an interface between two domains, arises from the translation symmetry breaking of unit cells. It is characterized by a displacement vector of $\boldsymbol{R}$ associated with a phase shift ($\Delta\phi$) for the separated but neighboring unit cells. In this letter, we report that the polar property of the $\boldsymbol{R}_{III\text{-}1}$ type can be nicely approximated by results from a strain-free rigid model. Based on this, the polarity of other types of TBs in $PbZrO_3$ is deduced. High-resolution STEM study reveals that "sub-domains" exist inside the $\boldsymbol{R}_{III\text{-}1}$ type TB, inside of which the polarization tends to orient independently.

Thermal treatment changes the octahedral rotation behavior, and by simulating a perfect AFE domain, the initial rigid structure model is determined. Fig. 1A and 1B show the lattice parameter *b* changes across the APB with a displacement vector of $\boldsymbol{R}_{III\text{-}1}$ = 1/4[0 2 n] (n = 0 or 2). The inset shows the displacement characteristics of Pb atoms inside this APB. It is clearly seen that parameter *b* strongly fluctuates inside the APB region. Meanwhile, changes of parameter *b* in the initial rigid model exhibit the essential feature of the experimentally determined APB structure. Ideally, when adjacent crystal planes containing parallel and antiparallel Pb displacements inside the APB keep the same spacings as that in perfect domains, such an interface is regarded as strain-free.

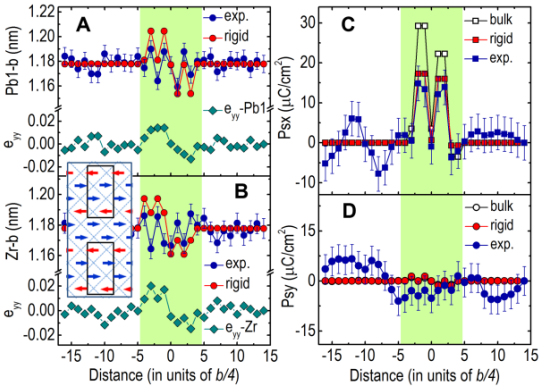

FIG. 1. A,B. Lattice parameter b and strain changes across the $\boldsymbol{R}_{III\text{-}1}$ type APB determined by Pb1 and Zr atom based on experimental results (blue) and initial rigid APB model (red). The insert shows the schematic APB structure according to Pb displacements. C,D. The calculated P_{SX} (squares) parallel and P_{SY} (circles) perpendicular to the boundary plane, respectively.

Therefore, the strain component of e_{yy} and P_S can be calculated with respect to the strain-free rigid model. It is found that the internal strain inside the APB is very small and a good match of the P_S, either parallel or perpendicular to the boundary, is found between the experimental one and the initial rigid modal. With the atomic positions from the bulk, the maximum P_{SX} is up to 29 mC/cm^2, even higher than that of ferroelectric $BaTiO_3$ (P_S = 26 mC/cm^2).

Accordingly, the polarity of other types TBs are calculated based on their rigid models with atomic positions from the bulk $PbZrO_3$ [3]. When

constructing the TB interfaces, two prerequisites are abided: (1) the interfaces are kept free of strain; (2) when different oxygen atoms conflict at the interfaces, the one leading to the smallest net polarization is adopted. Fig. 2 shows the calculated polarization results for other possible types of TBs, their insets show the schematic TB characteristics according to Pb displacements. It can be seen that there are two polar TBs with $\boldsymbol{R}_{I\text{-}1}$ = 1/4[2 1 n] and $\boldsymbol{R}_{III\text{-}3}$ = 1/4[0 2 n], three antipolar-like TBs with $\boldsymbol{R}_{I\text{-}2}$ = 1/4[2 1 n], $\boldsymbol{R}_{II\text{-}1}$ = 1/4[2 -1 n] and $\boldsymbol{R}_{II\text{-}2}$ = 1/4[2 -1 n], and one anti-polar APB with $\boldsymbol{R}_{III\text{-}2}$ = 1/4[0 2 n].

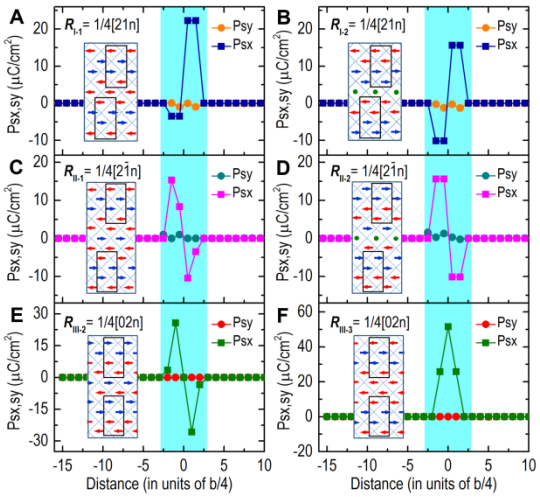

FIG. 2. Polarity of TBs calculated based on the strain-free rigid model. The P_{SX} and P_{SY} for TBs with displacement vectors of A,B, $\boldsymbol{R}_{I\text{-}1}$ and $\boldsymbol{R}_{I\text{-}2}$, C,D, $\boldsymbol{R}_{II\text{-}1}$ and $\boldsymbol{R}_{II\text{-}2}$, E,F, $\boldsymbol{R}_{III\text{-}2}$ $\boldsymbol{R}_{III\text{-}3}$. The schematics are inserted to show the boundary characteristics according to Pb displacements.

Analysis of the high-resolution high-angle annular-dark-field (HAADF) image reveals that the APB, at atomic scale, can split into "sub-domains". Fig. 3A shows a HAADF image of the $\boldsymbol{R}_{III\text{-}1}$ type APB, positions of the TB and the "sub-domain walls" inside the TB are outlined by the yellow and white dotted lines. By mapping positions of Pb columns, locations of the sub-domains are indicated by the cyan shaded areas inside the APB, as illustrated in Fig. 3A and 3B. With respect to atomic positions of the cubic phase, Fig. 3B presents the averaged Pb displacements (along the boundary direction) as a function of the distance from domain I to domain II. In comparison with the bilateral sub-domains, it is seen that the middle sub-domain shifts upward by *b*/2, and width of the sub-domain walls is *a*. According to our previous results [2], the displacements of Pb shown in Fig. 3B suggest that the polarization inside the left- and right-side sub-domains points to the -x direction, while the polarization inside the middle sub-domain tends to adopt the opposite direction, as the color arrows indicated in Fig. 3A. Although the exact polarization orientation inside the sub-domains can only be determined when all atomic positions (Pb, Zr and O) are imaged and considered, the tendency of polarization reversal inside the sub-domains of the TB suggests the occurrence of ferroic orders at structural domain walls [4].

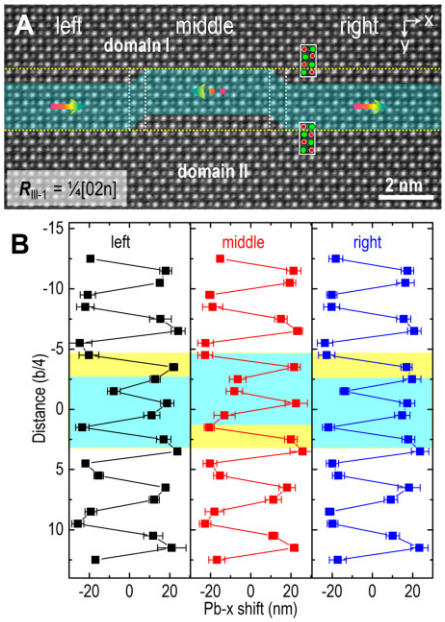

FIG. 3. A. High-resolution HAADF image of $\boldsymbol{R}_{III\text{-}1}$ type APB in $PbZrO_3$ recorded along [0 0 1] direction. The yellow and white dotted lines outline positions of the APB and the "sub-domain walls" inside the APB, respectively. The color arrows indicate the possible polarization direction inside each "sub-domain". B. The average Pb displacement profiles (along the boundary direction) for the left, middle and right part of A. Schematic unit cells are overlapped on the images: Pb – green circles, Zr – red circles.

In conclusion, by comparing the lattice parameter changes and the spontaneous polarizations inside the $\boldsymbol{R}_{III\text{-}1}$ type TB, we find a good approximation of the results obtained from the strain-free rigid TB model to the experimental one in AFE $PbZrO_3$. Based on the strain-free rigid models, the polarity of other types of TBs is proposed. High-resolution STEM experiments reveal that the straight TBs may consist of many "sub-domains", as observed in the $\boldsymbol{R}_{III\text{-}1}$ type TB, which suggests the occurrence of ferroic orders at structural domain boundaries according to the probable inverse polarization orientation. Our results not only enrich the understanding on the polar property of the TBs in AFE $PbZrO_3$, but also are instructive for future applications of these nanoscale domain boundaries.

The research leading to these results has received funding from the European Research Council under the EU 7th Framework Programme (FP7/2007-2013)/ERC grant agreement no (268058) Mobile-W and from the EU 7th Framework Programme under Grant Agreement 312483—ESTEEM2 (Integrated Infrastructure Initiativel3).

[1] G. Catalan, J. Seidel, R. Ramesh, J.F. Scott, Rev. Mod. Phys. **84**, 119 (2012).

[2] X.-K. Wei, A. K. Tagantsev, A. Kvasov, K. Roleder, C.-L. Jia, and N. Setter, Nat. Commun. **5**, 3031 (2014).

[3] K. Yamasaki, Y. Soejimaa, K.F. Fischer, Acta Cryst. **54**, 524 (1998).

[4] X.-K. Wei, C.-L. Jia, K. Roleder, and N. Setter, Mater. Res. Bull. **62**, 101 (2015).

Ultrafine-Grained Thermistor-Ceramics from Micro-Emulsion Mediated Synthesis of Donor-Doped $BaTiO_3$ Nanoparticles

C. Pithan[1], H. Katsu[2], J. Dornseiffer[3], R. Waser[1], G. Roth[4], and H.Takagi[2]

[1] Peter Grünberg Institut-7, Forschungszentrum Jülich, Germany
[2] Murata Manufacturing Corporation Limited, Kyoto, Japan
[3] Institute of Energy and Climate Research-1, Forschungszentrum Jülich, Germany
[4] Institute of Crystallography, RWTH Aachen University, Germany

The practical possibility for realizing ultrafine-grained thermistor ceramics on $BaTiO_3$ basis with an average grain-size well below the theoretically predicted lower limit has been demonstrated for the first time. This contribution presents processing procedures as well as the resulting electric functionality.

Along with the ongoing technological trend to promoted miniaturization of many kinds of passive electronic components, also multilayer thermistors (PTCR) based on semiconducting ferroelectric $BaTiO_3$ exhibiting a positive temperature co-efficient of resistivity above the Curie temperature T_C, should be as small as possible. It is the continuous reduction of dimensions in electronic circuitry that has been driving this development requiring high performing miniaturized components without forfeiting a loss in their functionality. Insulating dielectric devices based on $BaTiO_3$ are at present produced as multilayer ceramic capacitors with a layer thickness of merely a few hundreds of nm consisting of ceramic grains of only a few tens of nm. On the other hand advanced industrial modern multilayer thermistors based on reduction- resistant $BaTiO_3$ have a layer thickness of approximately 20 µm that are built up by grains with an average size of a few µm.

Up to the present the theoretical understanding of defect chemistry [1, 2] in these materials anticipates a lower limit in grain size of a few µm only, below which the PTCR characteristics are assumed to vanish because of an overlap of the insulating Schottky-barriers at the grain-boundaries, that bring about the physical effect of a positive temperature coefficient of these electrically inhomogeneous materials. In this scenario, it is expected that the material becomes completely insulating or at least charge neutrality requires that the characteristics of the insulating space charge layers of the grain boundaries essentially change. The fundamental scientific question of the present study was to clarify, whether it is generally and practically possible to realize $BaTiO_3$-based PTCR ceramics with a grain size of only a few hundreds on nm and whether the formerly postulated lower grain size limit exists or not.

For this purpose micro-emulsion mediated synthesis of nano-crystalline La-doped $BaTiO_3$ powders [3] having a very narrow particle size distribution in combination with consolidation by spark plasma sintering [4] were used to prepare ultrafine-grained ceramics.

Fig. 1 shows a typical TEM image recorded for as-synthesized stoichiometric $BaTiO_3$ nano-particles doped with 0.2 at.-% La with an average particle size of 10 to 20 nm used in the present investigation.

FIG. 1: TEM micrograph of as prepared stoichiometric La-doped $BaTiO_3$ nano-particles. The inset shows on the right side a transparent solution of $BaTiO_3$ particles (typically 5 – 15 wt.-%) in comparison with ultrapure water on the left side.

Alternatively, hypo-stoichiometric powders with 2 mole-% of BaO have been prepared. Before consolidation by SPS all powders were calcined for 1 hour in air at 700°C in order to remove physically or chemically adsorbed water and more importantly organic residues from the synthesis. After this treatment, the average particle diameter determined by N_2-gas adsorption was approximately 220 nm (stoichiometric case) and 140 nm (case of excessive BaO). XRD measurements were used to confirm crystallinity and phase purity. The as-synthesized powders were amorphous whereas the calcined products were pseudocubic regarding their crystallographic structure.

A dilatometric profile recorded for ultrafine $(Ba_{0.998}La_{0.002})TiO_3$ processed at 1000°C for 5 min. in Ar at a mechanical uniaxial pressure of 75 MPa (heating rate 90 K/min, electrical current: 400 – 600 A) and the resulting ceramic pellet is represented in fig. 2.

Shrinkage starts at about 800 °C and consolidation is completed within a few minutes after the maximum temperature upon heating is reached.

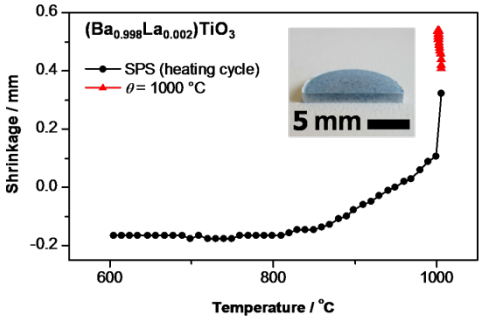

FIG. 2: Shrinkage during sintering upon SPS of $(Ba_{0.998}La_{0.002})TiO_3$ nano-powders processed at 1000°C for 5 minutes in Ar at a mechanical uniaxial pressure of 75 MPa (red curve). The black curve and symbols represent the heating cycle under pressure (heating rate: 90 K/min, electrical current: 400 – 600 A). The inset shows a cut sample piece of the compressed ceramics.

Fig. 3 shows the resulting microstructure by TEM after re-oxidation at 500 °C in air. Clearly, the presence of ferroelectric domains, a prerequisite for the reduction of electric resistivity of grain-boundary regions below T_C [5] is evident. The grain size amounts to 200 – 300 nm in average, meaning that practically no grain growth occurred during densification. These values are by far below (one order of magnitude) those observed in typical thermistor ceramics on $BaTiO_3$ basis, where anomalous grain growth usually takes place.

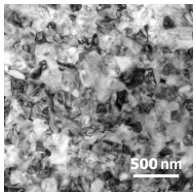

FIG. 3 TEM image of the sample shown in fig. 2 after re-oxidation at 500°C in air.

As can be recognized from fig. 2 the consolidated nano-crystalline ceramics are bluish in color. The densities determined by the Archimedes method of both stoichiometric and hypo-stoichiometric pellets were well above 96 % of the theoretical value for $BaTiO_3$. XRD inspection of the consolidated ceramics revealed a considerable broadening of Bragg reflections that relates to high mechanical distortions introduced during the compaction via SPS. Even after spark plasma, sintering at 1000°C no tetragonal splitting of XRD-reflections could be detected.

Since the partial pressure of oxygen $p(O_2)$ is relatively low (~ 10^{-21} MPa), re-oxidation of the grain boundaries turns out to be essential for realizing the thermistor effect. This indispensable heat treatment, typically carried out at temperatures as low as 500°C, avoided substantial grain growth. It has to be noted here that this thermal regime is far below the one used for conventional coarse-grained materials (800 – 1200°C). It is believed, that the small grain size also implies an improved diffusivity of oxygen during re-oxidation through enhanced grain-boundary diffusion. Excellent thermistor performance is obtained for the stoichiometric case, revealing a resistivity jump of more than three orders of magnitudes upon heating above T_C as shown in fig. 4. Compositions with BaO-excess (not presented here) only revealed a resistivity increase of merely one order of magnitude.

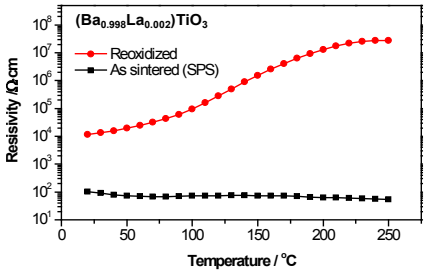

FIG. 4: Temperature dependence of resistivity for ultrafine-grained $(Ba_{0.998}La_{0.002})TiO_3$ thermistor ceramics after sintering under reductive conditions (black curve) and after re-oxidation (red curve).

Fig. 5 shows a comparison of oxygen desorption and uptake monitored by thermogravimetry for the case of a ceramic pellet with ultrafine microstructure after SPS and one that has been – as a reference – subsequently annealed at 1300°C for 2 hours in addition in order to achieve considerable grain-growth. It is evident that the exchange of oxygen with the ambient, presumably mainly via grain-boundaries, is significantly large at 500°C in the fine-grained case. When switching from reductive (Ar + 4% H_2) to oxidizing (Ar + 20% O_2) conditions the oxygen uptake amounts to 0.27 mole-%. In the coarse case this measured value drops down to only 0.07 mole-%). The enhanced oxygen uptake in the case of ultrafine-grained ceramics is believed to originate from a lower enthalpy of oxidation.

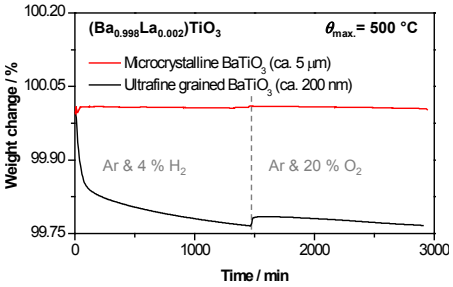

FIG. 5 Reduction- and oxidation-behavior at 500°C of ultrafine-grained (200 nm) and coarse-grained (5 mm) $(Ba_{0.998}La_{0.002})TiO_3$.

In the coarse grained reference sample the PTCR-effect was absent.

[1] J. Daniels and R. Wernicke, Philips Res. Repts **31**, 544 (1976).

[2] S.-H. Cho, J. Kor. Ceram. Soc. **43**, 673 (2006).

[3] C. Pithan, Y. Shiratori, J. Dornseiffer, F. H. Haegel, and R. Waser, J. Am. Ceram. Soc. **89**, 2908 (2006).

[4] J. Liu and Z. Shen, J. Am. Ceram. Soc. **89**, 2689 (2006).

[5] G. H. Jonker, Solid-State Electon. **7**,895 (1964).

Periodic cation segregation in $Cs_{0.44}[Nb_{2.54}W_{2.46}O_{14}]$ quantified by HRSTEM

M. Heidelmann[1,2], J. Barthel[1,2], G. Cox[3], and T. E. Weirich[1,4]

[1] Gemeinschaftslabor für Elektronenmikroskopie, RWTH Aachen University, Germany
[2] Ernst Ruska-Centrum, Forschungszentrum Jülich, Germany
[3] BASF SE, Polymerphysik, Mannheim, Germany
[4] Institut für Kristallographie, RWTH Aachen University, Germany

The atomic structure of $Cs_{0.44}[Nb_{2.54}W_{2.46}O_{14}]$ closely resembles the structure of the most active catalyst for the synthesis of acrylic acid, the M1 phase of MoVNbTeO. Consistently with observations made for the latter compound, the high-angle electron scattering signal recorded by scanning transmission electron microscopy shows a significant intensity variation, which repeats periodically with the projected crystallographic unit cell. The occupation factors for the individual mixed Nb/W atomic columns are extracted from the observed intensity variations. For this purpose, experimental images and simulated images are compared on an identical intensity scale, which enables a quantification of the cation distribution.

The compound CsNbWO became of interest recently for the development of new catalytic materials since it closely resembles the so-called M1 phase of MoVNbTeO. The latter compound has been identified as the active part in the hitherto best heterogeneous catalyst for the partial and selective gas-phase oxidation of propane with molecular oxygen to acrylic acid [1]. In several initial studies of CsNbWO the basic crystallographic structure parameters such as the lattice constants, the symmetry, the chemical composition, as well as the positions of the heavy elements Cs, Nb, and W have been determined. The structure models extracted from the previous investigations until now assume an equal distribution of niobium and tungsten atoms for the mixed cation sites. The assumption of an equal Nb/W distribution for all sites within the unit cell contradicts findings for the related structure of the M1 phase of MoVNbTeO and for other compounds from the Nb-W-O system, with a similar structural complexity. According to these investigations, the individual cation sites have individual Mo/V or Nb/W occupation values, respectively. Occupancy differences have been determined via refined x-ray diffraction data and by analysis of significant intensity variations in the high-angle scattering signal recorded by scanning transmission electron microscopy (STEM). To quantify the occupancy of the mixed Nb/W positions we applied in particular the approach of [2], where the STEM detector response is calibrated with respect to the current of the incident electron beam.

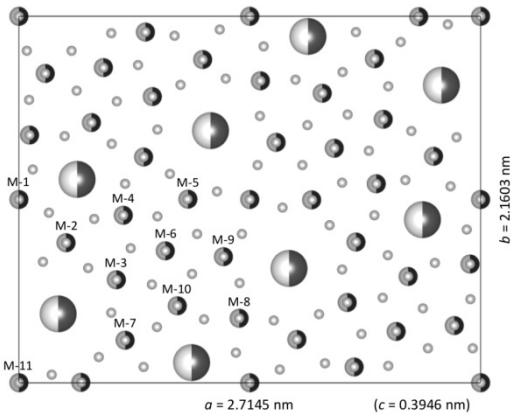

FIG. 1: Structure model of CsNbWO projected along the c-axis of the orthorhombic unit cell. Large spheres represent the partially occupied Cs positions, spheres of medium size represent metal atom positions M-1 to M-11 with a mixed Nb/W occupation, and small spheres represent pure oxygen atom positions..

The atomic structure model of CsNbWO as shown in Fig.1 contains 11 distinct metal atom positions M-1 to M-11 per asymmetric unit. All these positions have a mixed Nb/W occupancy. The structure models developed so far assign the same Nb/W occupation to all of the 11 positions. The metal positions, which are not labeled in Fig.1 are related to one of the 11 labeled positions applying the space group symmetry Pbam (No. 55).

The image displayed in Fig. 2 represents the average over 20 consecutively acquired HAADF-STEM images of a thin CsNbWO crystallite projected along the [001] zone axis. The image contrast in Fig. 2 is dominated by the signal of the mixed Nb/W-O columns amounting up to approximately 5% of the incoming beam current. A strong increase of the average peak intensity is observed from the top-left region to the lower-right region of the image, which is due to a respective increase of the object thickness. In addition there is an obvious local variation of the Nb/W-O peak intensities repeating periodically over the whole image. The period of the repeating local intensity

variations corresponds to the crystal structure period of the projected unit cell. Compared to the local average peak intensity, the peaks at the M-4 and M-10 position show significantly higher intensities, whereas the M-8 and M-11 positions show significantly lower intensities. The peak intensities at the Cs position in the six-fold channels are significantly higher than the intensities observed in the seven-fold channels.

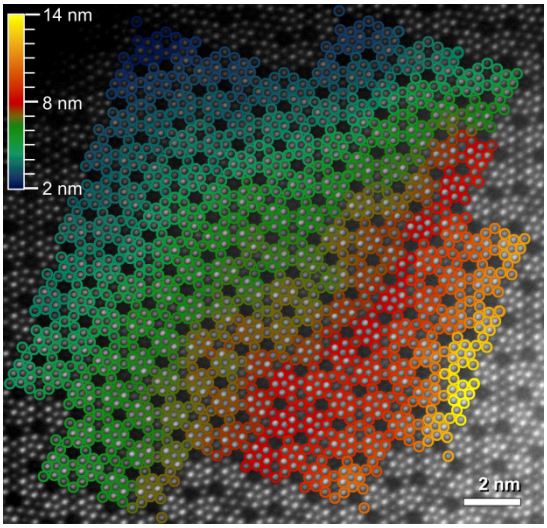

FIG. 2: Calibrated experimental HAADF STEM image in a gray-scale display ranging from 0% (black) to 5% (white) of the incident beam current. The color of the overlaid circles denotes the local object thickness determined at the respective atom column position.

Variations of the HAADF signal within the projected unit cell as observed in Fig. 2 indicate differences in the projected atomic structure of the individual mixed Nb/W-O columns. The target of our data evaluation is to determine the average W-concentration for each metal atom position. The following strategy is applied to overcome the problem, that the absolute value of the HAADF intensity depends simultaneously on the W-concentration and on the so far unknown object thickness, and that the respective dependencies are not known a priori on a quantitative level (for details see [3]):

1. Experimental image intensities and simulated image intensities are evaluated on the same absolute scale of integrated peak intensities in order to allow for a direct comparison.

2. The relations between the W-concentration and the resulting integrated peak intensity attributed to a Nb/W-O atomic column are determined from image simulations for each M position and for a sufficiently large range of object thicknesses.

3. Given the relations determined in (2) and the average W-concentration of 0.49 in the M sub-lattice, as verified by EDX on several CsNbWO crystallites, the local object thickness in the experimental image is estimated by matching local average intensities of the experimental image to those of simulated images

4. The W-concentration corresponding to each peak in the experimental image is calculated from the integrated peak intensity by inverting the appropriate relation determined in (2).

The resulting average tungsten concentrations range between 0.25 for the M-11 position, which exhibits also the lowest image intensity, up to approximately 0.72 for the positions M-4 and M-10, which show the highest image intensities. Image simulations based on an improved structure model of CsNbWO, which incorporates the measured average tungsten concentration are in excellent agreement with the experimental image intensity distribution. Fig. 3 shows a set of such simulated images which are compared on the same intensity scale to a stripe cut-out of the experimental image displayed in Fig. 2.

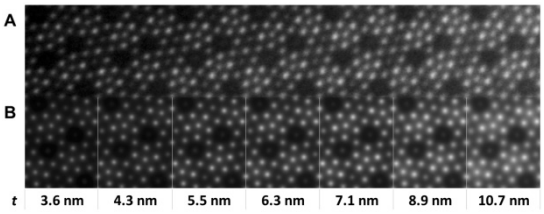

FIG. 3: Comparison between experimental and simulated HAADF STEM images on the same intensity scale as used in Fig.2. (A) shows a consecutive stripe, which has been cut out from the experimental image. (B) shows the best matching simulated images on a unit-cell scale. The local object thickness t is denoted below and has been extracted from the respective area of the experimental image.

A radical improvement is made in the understanding of the atomic structure of CsNbWO, revealing a non-uniform distribution of the two cation species Nb and W over the unit cell. A strong accent of tungsten is measured for the positions M-4, and M-10, whereas the positions M-1, M-2, M-7, M-8 and M-11 are more frequently occupied by niobium than by tungsten. The remaining positions M-3, M-5, M-6, and M-9 have tungsten concentrations close to 50%, corresponding to the average Nb/W ratio of the structure. The measured tungsten occupancies range range between 0.25 and 0.72. The Nb/W cation segregation in the crystallographic unit of CsNbWO correlates well with the V/Mo distribution measured for the structurally related catalyst compound MoVNbTeO [4]. Similarities of the atomic structure of the two compounds extend thus also to the level of the distribution of the two cation types, which build the metal-oxide framework of the M1 phase.

This work was supported by the DFG (WE 2579/3-1, MA 1280/40-1).

[1] H. Hibst, F. Rosowski, G. Cox, Catal. Today **117**, 234 (2006).

[2] J.M. LeBeau, S.D. Findlay, L.J. Allen, S. Stemmer, Phys. Rev. Lett. **100**, 206101 (2008).

[3] M. Heidelmann, J. Barthel, G. Cox, T.E. Weirich, Microsc. Microanal. **20**, 1453 (2014).

[4] X. Li , D.J. Buttrey, D.A. Blom, T. Vogt, Top Catal. **54**, 614 (2011).

Enhanced ferrimagnetism in auxetic $NiFe_2O_4$ in the crossover to the ultrathin film limit

M. Hoppe[1], S. Döring[1], S. Cramm[1], M. Gorgoi[2], and M. Müller[1,3]

[1] Peter Grünberg Institut-6, Forschungszentrum Jülich, Germany
[2] Helmholtz-Zentrum Berlin für Materialien und Energie, Berlin, Germany
[3] Fakultät für Physik, Universität Duisburg-Essen, Germany

We investigate the sensitive interplay between magnetic, electronic and structural properties in the ferrimagnetic oxide $NiFe_2O_4$. Emphasis is placed on the impact of reduced dimensionality in the crossover from bulk-like to ultrathin films. We observed an enhanced saturation magnetization M_S for ultrathin $NiFe_2O_4$ films on Nb-$SrTiO_3$ (001) substrates that co-occurs with a reduced out-of-plane lattice constant under compressive in-plane epitaxial strain. We found a bulk-like cationic coordination of the inverse spinel lattice independent of the $NiFe_2O_4$ film thickness – thus ruling out a cationic inversion that nominally could account for an enhanced M_S.

The competition of charge, spin and orbital degrees of freedom in complex oxides leads to intriguing physical phenomena, including ferromagnetism, ferroelectricity or multiferroicity. Fertilized by the continuously advancing art of oxide growth, the controlled synthesis of high-quality oxide heterostructures now approaches a monolayer-precision. Designing electronic properties in ultrathin oxide films and interfaces thereby opens up routes to explore novel nanoelectronic functionalities for applications.

In the context of spin-based electronics, oxides featuring both magnetic and insulating properties reveal a highly effective spin filter effect, where spin-polarized electron currents are generated by a spin-dependent tunnelling process. In this pursuit, ferrite materials are envisioned as high-T_c spin filters with the ultimate goal to realize efficient spin filtering for application at room temperature. For example, $NiFe_2O_4$ shows ferrimagnetic ordering up to T_c = 865 K and grows epitaxially on Nb-doped $SrTiO_3$ (001) perovskite electrodes. Its inverse spinel lattice of the type $Fe^{3+}[Ni^{2+}Fe^{3+}]O_4$ however, exhibits a high structural complexity: Ni^{2+}-cations are situated on octahedrally (O_h) coordinated lattice sites, while Fe^{3+}-cations are equally distributed across both tetrahedral (T_d) and O_h sites (Fig. 1). The electronic and magnetic properties of spinel ferrites thus sensitively depend on the details of the interatomic coordinations. In particular, magnetic ordering is dominated by superexchange interactions between T_d- and O_h-coordinated cations on two antiferromagnetically coupled sublattices.

In previous studies, an unexpected magnetic behaviour, i.e. an enhanced saturation magnetization was reported for $NiFe_2O_4$ films in the ultrathin film limit. The origin of this phenomenon was explained by a cationic inversion from an inverse to a partly normal spinel lattice, since this structural redistribution of Fe cations nominally accounts for an increased magnetic moment. An experimental proof for this model is however still lacking.

In this work, we explore the details of the electronic and magnetic properties of single-crystalline $NiFe_2O_4$ films in the crossover from bulk-like to the ultrathin film limit [1,2]. The goal of our studies is to uncover modifications of the structural, electronic and magnetic properties with regard to the reduced film dimensionality. We performed a complementing spectroscopic analysis employing the bulk- and surface sensitive photon spectroscopy techniques HAXPES, XANES and XMCD, respectively, which allow for a precise quantification of the element-specific cationic valencies and spatial coordinations.

First, $NiFe_2O_4$ films were investigated with regard to their magnetic properties. Hereby, special attention is payed to changes dependent on their film thickness. Hysteresis loops of all samples were recorded at T = 5K, which are shown in Figure 1.

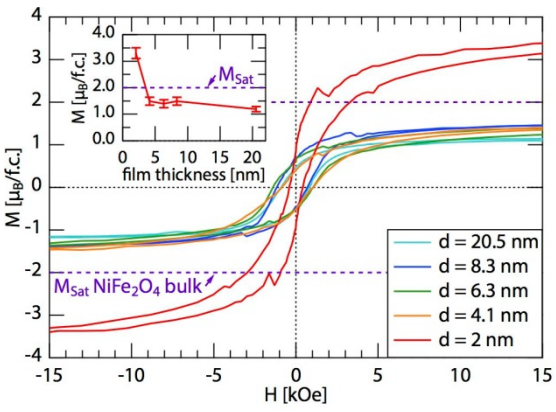

FIG. 1: Details of the in-plane M-H hysteresis loops of $NiFe_2O_4$ on $SrTiO_3$ (001) recorded at T = 5K with a maximum applied field of up to 36 kOe. The inset shows the saturation magnetization M_S as a function of $NiFe_2O_4$ film thickness.

As the film thickness scales below 6 nm, we find the saturation magnetization enhancing up to 3 μ_B/f.u.- thus significantly exceeding the bulk value. This result is in agreement with previous studies on $NiFe_2O_4/SrTiO_3$ and $CoFe_2O_4$ /$SrTiO_3$. In order to evidence the existence or absence of a cationic inversion, we investigate the chemical properties and cationic distribution of $NiFe_2O_4$ as a function of the film thickness in more detail.

HAXPES measurements have been performed to quantify the valence states of each cation species. Therefore, Ni 2p and Fe 2p core level spectra are taken from $NiFe_2O_4$ films of 8 nm to 2 nm, and compared to a bulk reference. Since both shape and energy position of the thin film samples core level and satellite peaks perfectly match that of the $NiFe_2O_4$ bulk spectra, we conclude, that all films grow in bulk-like stoichiometry and cationic distribution – without any sign for a cationic inversion. In order to rule out also any smaller effect, we investigate the spatial cationic distribution by further spectroscopic means.

Therefore, we investigated XMCD asymmetry spectra of the Fe $L_{2,3}$-edge, which is reflecting the superposition of the individual asymmetry spectra from cations occupying T_d or O_h sites. Due to the antiferromagnetic alignment of the cation spins between T_d and O_h sites, the asymmetry signals are of opposite sign. Consequently, these signals mainly cancel out in the observable sum asymmetry signal, leaving the resulting difference spectrum extremely sensitive to subtle changes in the cationic distribution. Site- and valency-specific Fe $L_{2,3}$-edge XMCD model spectra were computed by LFM calculations utilizing the software CTM4XAS. A linear combination of them is fitted to the experimental data, thus allowing us to quantify the fraction of each configuration.

Fig. 2 exemplary shows the MCD spectrum of the Fe $L_{2,3}$-edge for the 2 nm thick $NiFe_2O_4$ film with the corresponding fit. The L_3-edge exhibits a pronounced -/+/- asymmetry structure, caused by the antiparallel oriented Fe moments. The positive (+) peak at 709.7 eV (II) is dominated by tetrahedral Fe^{3+} and the high energy negative (-) peak at 710.5 eV (III) by octahedral Fe^{3+} cations.

However, the result gives no indication for a cationic inversion of the film, which would result in a decrease of the positive peak (II) and strong enhancement of the high energy negative peak (III). These results are also observed for all other investigated $NiFe_2O_4$ film thicknesses, which give no clue for an increased octahedral Fe^{3+} fraction, as would be characteristic for a cationic inversion to the normal spinel structure.

The striking consistency from the analysis of the XMCD data and the bulk-sensitive HAXPES and XANES techniques provides clear evidence for the absence of a cationic inversion in $NiFe_2O_4$ in the crossover to the ultrathin film limit, and thus rules out this mechanism as the origin of the observed enhanced M_S in ultrathin $NiFe_2O_4$films.

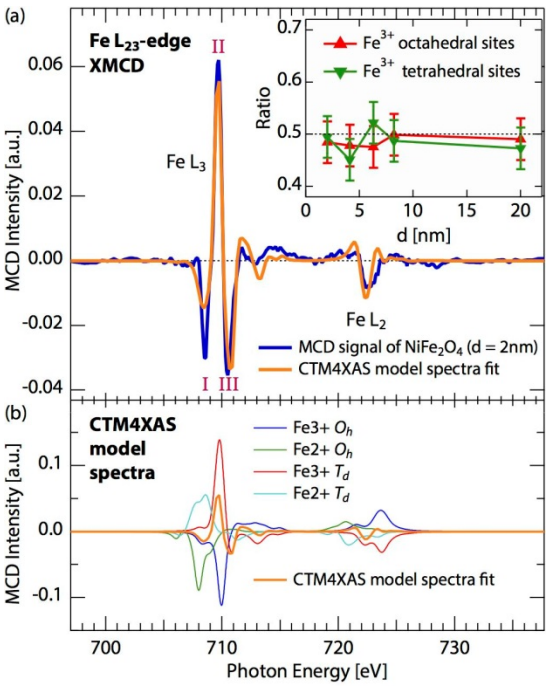

FIG. 2: Experimental XMCD spectrum from the Fe $L_{2,3}$-edge of the 2 thick $NiFe_2O_4$ film and the corresponding fit. The resulting lattice site occupancy for various film thicknesses is depicted in the inset.

In summary, we have investigated single-crystalline $NiFe_2O_4$ thin films grown cube-on-cube on Nb-doped SrTiO3 (001) substrates, with thicknesses scaling down from 20 – 2 nm [1,2]. In this crossover to the ultrathin film limit, we focussed on the impact of reduced dimensionality on the structural, electronic and magnetic $NiFe_2O_4$ properties. Foremost, we observed an enhanced saturation magnetization M_S in ultrathin $NiFe_2O_4$ films. In order to investigate the cationic distribution in the $NiFe_2O_4$ thin films, complementing bulk- and surface-sensitive analyses using HAXPES, XANES and XMCD spectroscopy techniques have been performed, and special attention was paid to the element-specific cation valencies and -coordinations. We find a bulk-like inverse spinel structure being present in all samples – independent of the $NiFe_2O_4$ film thickness. Thereby, our results consistently reveal the absence of a cationic inversion from the inverse to the normal spinel structure, as was so far held responsible for an enhanced M_S in ultrathin spinels.

[1] M. Hoppe, S. Döring, M. Gorgoi, S. Cramm, and M. Müller, Phys. Rev. B **91**, 054418 (2015).

[2] M. Hoppe, M. Gorgoi, C. M. Schneider, and M. Müller, IEEE Trans. Magn. **50**, 2506204 (2014).

Electron microscopy investigation showing anisotropic growth of shaped Pt-Ni fuel-cell catalyst nanoparticles

M. Heggen[1], L. Gan[2], C. Cui[2], Fabio Dionigi[2], S. Rudi[2], and P. Strasser[2]

[1] Ernst Ruska-Centrum and Peter Grünberg Institut-5, Forschungszentrum Jülich, Germany
[2] Department of Chemistry, Technical University Berlin, Germany

Shape control can be an effective approach for tuning the physical and chemical properties of inorganic nanocrystals. While much is known about the growth mechanisms of monometallic shaped nanocrystals, understanding the anisotropic growth of shaped alloy nanocrystals is still at its infancy. Using aberration-corrected scanning transmission electron microscopy combined with electron energy loss spectroscopy at the 'PICO' microscope, we reveal an element-specific anisotropic growth mechanism of bimetallic nano-octahedra where compositional anisotropy couples to geometric anisotropy [1].

Because of the existence of a catalytically highly active (111) oriented surface [2], octahedral bimetallic Pt-Ni NCs have been considered the ultimate "dream electrocatalysts" for the technologically important oxygen reduction reaction (ORR) in hydrogen fuel cells. Although a variety of shaped bimetallic Pt alloy nanocrystals (NCs) have been prepared by solution-phase co-reduction of metal precursors, their detailed elemental surface compositions have been largely overlooked, rarely addressed, and have thus remained poorly understood. Contrary to the widely held notion of essentially homogenous elemental distribution, recent studies uncovered an unusual compositional segregation in shaped Pt alloy NCs, e.g. Pt-rich frames and Ni-rich facets in Pt-Ni nano-octahedra [3]. The elemental distribution resulted in complex structural corrosive degradation patterns of the alloy octahedra during the ORR electrocatalysis.

Using aberration-corrected microscopy at the Ernst Ruska-Centre, the atomic growth mechanism of bimetallic nano-octahedra was revealed. Octahedral $PtNi_{1.5}$ NCs were synthesized by solvothermal reduction of 4 mmol/L Pt(acac)2 (acac=acetylacetonate) and 28 mmol/L Ni(acac)2 in 100 mL dimethylformamide (DMF) at 120 °C, where DMF acted as both reducing agent and solvent [4]. Unlike other methods requiring capping agents such as oleylamine, no dedicated surfactants were needed to induce the shape-selective growth, leaving clean particle surfaces for catalytic applications. The low-temperature solvothermal synthesis is also slow (up to 42 hours), which allowed us to capture intermediate structures at different growth stages (after 4, 8, 16, and finally 42 hours). The collected NCs were characterized by using a spherical aberration corrected FEI Titan transmission electron microscope (TEM) operated at 300 KV for atomic imaging and an FEI Titan scanning transmission electron microscope (STEM), the 'PICO' microscope, operated at 80 KV for high-angle annular dark field (HAADF) imaging and electron energy loss spectroscopy (EELS) elemental mapping.

After 4 hours of reaction time, most of the particle have near-spherical shape of 2 to 8 nm diameter size, some particles show branched structure at larger size between 6-12 nm. After a reaction time of 8 hours, most nanoparticles evolved into a hexapod structure (Fig. 2 A,B) with average size around 11 nm. The average composition ($Pt_{73}Ni_{27}$) implies that the growth of the Pt-rich phase along the multi-pod arms dominates the growth process. To gain element-specific insight in the nanoparticle growth mechanism, a microstructural and compositional analysis using aberration-corrected STEM and EELS elemental mapping at 80 KV was done.

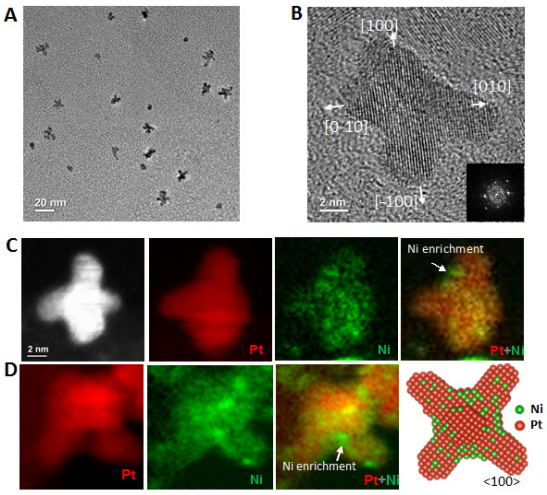

FIG 1: Characterization of Pt-Ni NCs after 8 hours reaction time. A, typical low-magnification TEM image, B, TEM image and the corresponding FFT pattern of a branched NC along <100> direction. C, D, HAADF images (red) mainly representing Pt and EELS spectrum images of Ni (green), showing Ni segregation at the concave surface of the Pt-Ni hexapod NCs.

Fig. 1, C and D, shows two branched nanoparticles oriented along two different directions combining high angle annular dark field (HAADF) STEM images (red) that mainly represent the distribution of Pt and EELS mapping images of the Ni L-edges (green). The overlaid images demonstrate the segregation of Ni at the concave surfaces of the hexapods, whereas Pt is distributed more homogeneously. This result implies an initiated deposition of Ni-rich phase at the concave surfaces of the hexapod NCs. Extending the reaction time to 16 hours, a transformation of the hexapod NCs to "concave octahedra" (Fig. 2A) was observed. The Ni content of the NCs increased substantially to $Pt_{62}Ni_{38}$, while the NCs maintained their average size. These results suggest an accelerated deposition of Ni-rich phase at the concave surfaces, whereas the growth of the Pt-rich phase along the hexapod arms, which were responsible for increasing particle size, slowed down due to the depletion of the Pt precursor. As illustrated in Fig. 2B, the preformed Pt-rich hexapods after 8 hours featured intrinsic {111} surface steps at the concave surfaces and {100}/{110} steps at the sidewalls of the arms. Compared to the terrace sites, Ni ad-atoms energetically prefer the step sites because of a higher coordination number, thus the process being thermodynamic in nature. Deposition of a Ni atom at the step results in the advance of the atomic step and thus leads to a continuous, step-induced deposition of primarily Ni atoms. In this context, the sidewalls play an important role in providing the initial step sites to induce a layer-by-layer growth of Ni-rich {111} facets. Taken together, the entire particle formation proceeded spontaneously in a one-pot still highly geometric and compositionally anisotropic co-reduction. Thus, the current synthesis also enables us to control the extent of concavity by simply controlling the reaction time.

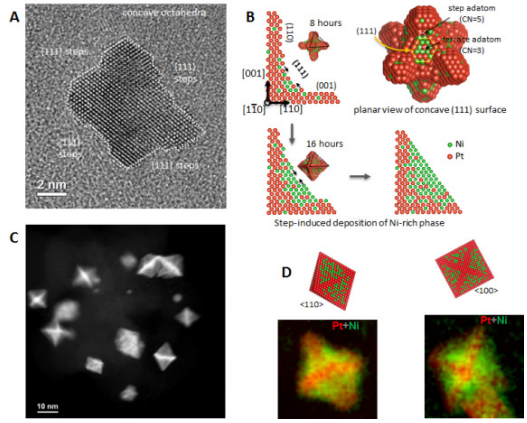

FIG 2: A, TEM image of a "concave octahedral NC" along <110> direction after a growth of 16 hours, showing the atomic surface steps at the concave {111} facets. B, sketch of the delayed anisotropic growth of Ni-rich phase through a step-induced, layer-by-layer deposition of Ni-rich atoms at the concave {111} surfaces of the pre-formed Pt-rich hexapods. C, D, Characterization of the final Pt-Ni nanooctahedra after 42h reaction time. C, HAADF-STEM image. D, HAADF images (red) mainly representing Pt and EELS spectrum image of Ni (green) of the octahedral PtNi1.5 NCs showing Pt-rich frames along the edges/corners and Ni-enriched facets.

Ultimately, a complete transformation to octahedral Pt-Ni NCs with smooth {111} surfaces occurred after a reaction time of 42 hours (fig. 2C). The Ni average composition increased to $Pt_{40}Ni_{60}$, whereas the particle size increased only slightly. This change is consistent with a continued, selective anisotropic deposition of Ni-rich phase at the concave {111} surfaces. As soon as the filling of Ni-rich phase has reached the top of the hexapod arms and flat {111} surfaces formed, there are no more step edges available, which makes metal deposition to cease, with the octahedron completed. Elemental STEM-EELS mapping of the octahedral NCs (Fig. 2 D) unambiguously shows Ni enrichment at the {111} facets versus Pt enrichment at the corners and edges, consistent with our previous findings [3]. The Pt enrichment at the edges in addition to at the corners also indicates a refined anisotropic growth trajectory of the Pt-rich phase, that is, the rapid growth of Pt-rich hexapods along <100> directions was probably followed by a slower growth along <110> direction.

Our results reveal a previously overlooked element-specific compositionally anisotropic growth mechanism, where rapid growth of Pt-rich hexapods/concave octahedra along <100> directions precedes delayed deposition of Ni-rich phase at the concave {111} sites. While the growth of Pt-rich hexapod is a ligand-controlled kinetic process, the step-induced deposition of the Ni-rich phase at the concave surface resembles a thermodynamically controlled process accomplished in much longer time. The revealed element-specific anisotropic growth provides the root of our previously-reported compositional segregation and chemical degradation pathway of the Pt-Ni octahedra [3], which underwent a selective etching of the Ni-rich {111} facets and thus activity instability during the ORR electrocatalysis in acidic electrolyte. The selective etching of the Ni-rich {111} facets resulted in concave octahedra with the exposure of less-active facets such as {100} and {110}. Extended potential cycling further resulted in the formation of Pt-rich hexapods back again and almost none of the catalytically active {111} surfaces survived, leading to significant activity degradation. In this context, the fate of the shaped Pt bimetallic NCs during long-term ORR electrocatalysis was substantially determined by their very beginning element-specific anisotropic growth during synthesis. Our results highlight the importance of understanding the element-by-element growth mechanism of shaped alloy NCs and may aid rational synthesis of shaped alloy catalysts with desired compositional patterns and properties.

[1] L. Gan, C. Cui, M. Heggen, F. Dionigi, S. Rudi, P. Strasser, Science **346**, 1502 (2014).

[2] V.R. Stamenkovic, B. Fowler, B.S. Mun, G.F. Wang, P.N. Ross, C.A. Lucas, N.M. Markovic, Science **315**, 493 (2007).

[3] C. Cui, L. Gan, M. Heggen, S. Rudi, P. Strasser, Nature Materials **12**, 765 (2013).

[4] C. Cui, L. Gan, H.H. Li, S.H. Yu, M. Heggen, P. Strasser, Nano Lett. **12**, 5885 (2012).

The interplay between structure, energy level alignment and chemical bonding strength at organic–metal interfaces

M. Willenbockel[1], D. Lüftner[2], B. Stadtmüller[1], G. Koller[2], C. Kumpf[1], S. Soubatch[1], P. Puschnig[2], M. G. Ramsey[2], and F. S. Tautz[1]

[1] Peter Grünberg Institut-3, Forschungszentrum Jülich, Germany
[2] Institute of Physics, University of Graz, NAWI Graz, Austria

What do energy level alignments at metal–organic interfaces reveal about the metal–molecule bonding strength? Is it permissible to take vertical adsorption heights as indicators of bonding strengths? To provide exemplary answers to these questions, we study adsorption of perylene-tetracarboxylic-acid-dianhydride (PTCDA) on the three canonical low index Ag surfaces employing angular resolved photoemission spectroscopy (ARPES) for a systematic study of the energy level alignments in ordered monolayer phases of PTCDA. Combining this with density functional theory (DFT) calculations and the generic Newns–Anderson chemisorption model, we analyse the alignments of highest occupied and lowest unoccupied molecular orbitals (HOMO and LUMO) with respect to the vacuum levels of bare and molecule-covered surfaces [1].

The alignment of molecular energy levels at metal–organic interfaces is important for the engineering of organic electronic devices and has been studied in great detail for many years. A large body of experimental data has been assembled, and powerful models have been developed that describe the phenomenology well. It is clear that ultimately the energy level alignments will be determined by the atomistic structure of the interface. Evidently, this link will always be taken into account automatically when the electronic properties in general and energy level alignments in particular are calculated using atomistic first-principles methods, such as DFT, albeit within the error of the chosen functional. However, in many experiments on energy level alignments, the interface structure is not so well controlled, sometimes not even known, and it is therefore often difficult to establish the link between electronic and geometric structures on the basis of the available experimental data. We attempt a discussion of both aspects on the same footing. To approach this goal, we study the electronic structure of the PTCDA molecule on Ag(100), Ag(110) and Ag(111) surfaces. This material system PTCDA/Ag(hkl) is ideally suited to attempt a comprehensive and unified view of geometric and electronic interface structures, because a complete set of lateral and vertical structural data is available for these interfaces and has been published, see e.g. [2]. Moreover, there are large variations in the surface reactivity of these three surfaces, allowing to study how this parameter influences geometric and electronic interface structures.

Applying a tomographic deconvolution technique of ARPES (cf. e.g. [3]), we obtained electronic structure data in the form of energy level alignments of the two uppermost frontier orbitals of PTCDA in four different bonding configurations on three Ag resolving different surface species within the unit cell (Fig. 1). This leads to empirical observation that the *openness* of the surface controls orbital binding energies E_B of HOMO and LUMO, because in the sequence (111)→(100)→(110), i.e. from the most close-packed to the most open surface, E_B increases. At the same time, the surface openness appears to influence the molecular adsorption heights, which decrease in the same sequence from 2.86 Å via 2.81 Å to 2.56 Å. Consequently, adsorption heights and orbital binding energies are also linked, in the sense that smaller adsorption heights go along with larger orbital binding energies (Fig. 2).

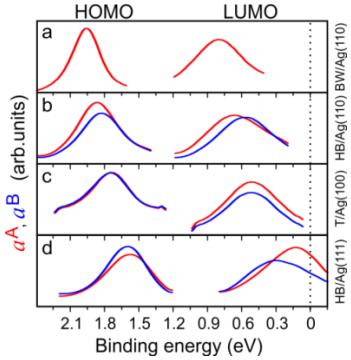

FIG. 1: Experimental partial density of states (PDOS) of PTCDA HOMO and LUMO in (a) brick-wall phase (BW) on Ag(110), (b) herring-bone phase (HB) on Ag(110), (c) T-phase on Ag(100), and (d) HB phase on Ag(111). In (b–d), the red and blue curves correspond to different molecules (A and B) in the unit cell.

The central quantity both for determining the adsorp- tion height and the energy level alignment at an organic–metal interface and therefore naturally linking them is the surface work function. Unfortunately, the thorough review of available database on the experimentally determined surface work functions of Ag surfaces in focus reveals a significant scatter caused by

nonequivalent and barely reproducible details of experimental conditions used in various works. We therefore apply a unified theoretical approach to calculate work function by means of DFT. Corresponding calculations demonstrate the expected tendency of increasing work function with atomic density in the sequence Ag(110)→Ag(100)→Ag(111). For all three surfaces DFT also predicts an increase of the work function as a PTCDA monolayer is adsorbed.

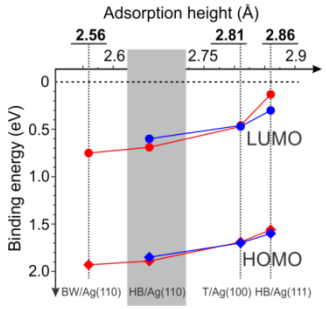

FIG. 2: Orbital binding energies of HOMO and LUMO as a function measured average adsorption height of the carbon skeleton of PTCDA (cf. [1] and Refs. therein).

Using the mentioned above experimental data in conjunction with the theoretical work function data, we can now analyse the energy level alignments of PTCDA HOMO and LUMO relative to the vacuum levels $E^{hkl}_{vac,0}$ of the three bare Ag surfaces and the vacuum levels E^{hkl}_{vac} of surfaces covered by molecules (Fig. 3). Inspection of Fig. 3a reveals that the hypothetical ionization energies $I_0=E_B^{HOMO,hkl}+\Phi_0^{hkl}$ of the adsorbed PTCDA are identical ($I_0\approx5.95$ eV) for all three Ag surfaces to within 55 meV, in spite of HOMO binding energies ranging from 1.58 to 1.93 eV. Thus different HOMO binding energies $E_B^{HOMO,hkl}$ on the three metal surfaces are precisely offset by different bare metal work functions Φ_0^{hkl}. This suggests a weak interaction of the PTCDA HOMO with the metal. In particular, the ionization energy of the adsorbate is affected only unspecifically (i.e., in the same way on all three surfaces) by the adsorption. On another hand, LUMO E_B increases in the sequence HB/Ag(111)→ T/Ag(100)→BW/Ag(110) more rapidly than the HOMO E_B. Since in the same sequence $\Delta\Phi=\Phi-\Phi_0$ decreases, we find (Fig. 3b) that $I'= E^{LUMO,hkl} + \Phi^{hkl}$ is nearly identical for all three surfaces ($I'\approx4.95$ eV), within 65 meV, in spite of LUMO E_B ranging from 0.215 to 0.75 eV. I' corresponds to the ionization potential of the occupied LUMO. Thus, Fig. 3b shows that the ionization energy from the filled LUMO is largely independent of the substrate surface on which PTCDA is adsorbed. The near identity of the ionization energies I' from the LUMO for different surfaces is remarkable, because the different amounts of charge transfer into LUMO from metal, different adsorption heights and ensuing different degrees of hybridisation and charge reorganization, and the different molecular distortions all have an influence on the orbital. This finding indicates that as far as removing an electron from the filled LUMO into the vacuum is concerned, there does not appear to be too much difference between the three surfaces. Accordingly, for the negatively charged molecule we observe approximate pinning of the LUMO to the vacuum level of the PTCDA-covered surface, $S^{LUMO}=dE_B^{LUMO}/d\Phi\approx-1.1$. Thus the LUMO seems to be related to Φ as the HOMO is related to Φ_0.

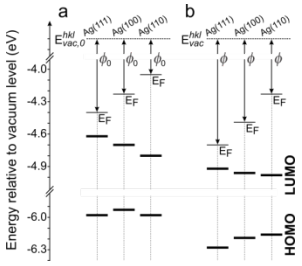

FIG. 3: HOMO and LUMO positions in PTCDA monolayers on Ag(111), Ag(100) and Ag(110). (a) Vacuum levels of the bare surfaces $E^{hkl}_{vac,0}$ are aligned. (b) Vacuum levels of the molecule covered surfaces E^{hkl}_{vac} are aligned.

The different behaviours of HOMO and LUMO show clearly that primarily the latter plays a pivotal role in the p–metal interaction, while the HOMO is rather more passive. In particular, the LUMO of PTCDA at the interface with metal is subject to massive bond stabilization, and this varies between the different interfaces which we have studied in a way that cannot be accounted for in the common model of energy level alignment at metal–organic interfaces, i.e. the model based on an induced density of interface states (IDIS) (cf. [1] for details). The behaviour of the HOMO, contrary, can be explained on the basis of the IDIS model. The Newns–Anderson model of chemisorption reveals that the orbital binding energy of the LUMO scales with the π–metal chemisorption energy, because the latter is to a large extent determined by the energy gain due to the charge transfer of electrons from the Fermi level of the metal into the stabilized LUMO. Within the same model we can also identify a causal link between the differential bond stabilization of the LUMO and the adsorption height. This means that the overall adsorption height of PTCDA on Ag surfaces is primarily determined by the interaction of the molecular π-system with the metal, not by the functional groups. Finally, the central property which controls a surface's reactivity towards an extended adsorbate (and thus quantities such as adsorption height, bond stabilization and chemical interaction strength) is the work function.

Summarizing, the observed relations between adsorption height, frontier orbital binding energies and π–metal bonding strength can be understood from very general principles and constitute the 'normal (canonical) case' that can serve as a reference when considering deviations from the canonical behavior [4].

[1] M. Willenbockel et al., Phys. Chem. Chem. Phys. **17**, 1530 (2015).

[2] O. Bauer et al., Phys. Rev. B **86**, 235431 (2012).

[3] M.Willenbockel et al., New J. of Phys. **15**, 033017 (2013).

[4] B. Stadtmüller et al., Nat. Commun. **5**, 3685 (2014).

More than the sum of parts: Bonding height and energy level alignment at heteromolecular interfaces

B. Stadtmüller[1], D. Lüftner[2], M. Willenbockel[1], S. Schröder[1], F. C. Bocquet[1], C. Henneke[1], C. Kleimann[1], T. Sueyoshi[1], S. Soubatch[1], E. M. Reinisch[2], G. Koller[2], M. G. Ramsey[2], P. Puschnig[2], F. S. Tautz[1], and C. Kumpf[1]

[1] Peter Grünberg Institut-3, Forschungszentrum Jülich, Germany
[2] Institut für Physik, Karl-Franzens-Universität Graz, Austria

Although geometric and electronic properties of any physical or chemical system are always mutually coupled by the rules of quantum mechanics, counterintuitive coincidences between the two are sometimes observed. The coadsorption of organic molecules, i.e., molecular blends on a noble metal surface, represents such a case, since geometric and electronic structures appear to be decoupled: One molecule moves away from the substrate while its electronic structure indicates a stronger chemical interaction, and vice versa for the other. A systematic investigation of four different pairs – one charge donating and one accepting species – adsorbed on Ag(111) using the X-ray Standing Wave (XSW) technique demonstrates the general trend [1]: In all cases the molecules align themselves to an adsorption height between those observed in the respective homomolecular structures. Spectroscopic investigations and ab-initio theoretical studies for one of the systems reveals that, mediated by the metal surface, both species mutually amplify their charge donating and accepting characters, respectively [2,3]. This resolves the apparent paradox, and demonstrates with exceptional clarity how geometric and electronic bonding parameters are intertwined at metal-organic interfaces.

In chemistry, there is a general tendency that stronger bonds go along with shorter bond lengths. For covalent bonds this is well-known; for instance, in the sequence from single to triple bonds, the bond length decreases while the bond strength increases. Shorter bonding distances imply more wave function overlap, stronger hybridization, and (in case of polar bonds) more charge exchange, all of which promote stronger chemical interaction and can thus be interpreted as electronic signatures thereof. Therefore, it would be very surprising if observations that normally go along with a stronger chemical interaction coincided with a larger bonding distance. Yet, such a counterintuitive relationship is precisely what we observe in the particular case of metal-organic hybrid interfaces presented here.

For adsorbed organic molecules it is the smaller adsorption height at a surface that corresponds to shorter bond lengths and is therefore usually coincided by signs of stronger chemical interaction. In the electronic structure this is a downshift of the lowest unoccupied molecular orbital (LUMO) that, in the case of "weak chemisorption", becomes partially filled. Two effects are at the origin of this relationship between adsorption height and LUMO binding energy: The spatial extent of the charge spill-out of the metal and the image dipole of the negatively charged LUMO. The normal relationship between geometric and electronic structure for molecules adsorbing on metal surfaces therefore is: A smaller bonding distance, which is the geometric signature of a stronger chemical interaction, coincides with an increased binding energy of the relevant frontier orbital (the LUMO).

This relationship has been demonstrated for many organic materials. Here we concentrate on four pairs of molecules with either CuPc or SnPc as donor and PTCDA or NTCDA as acceptor. We first concentrate on the adsorption height. It can be measured with the highest precision and chemical sensitivity by the NIXSW technique. In Fig. 1 a schematic illustration of the vertical adsorption geometries is shown, which in principle is valid for

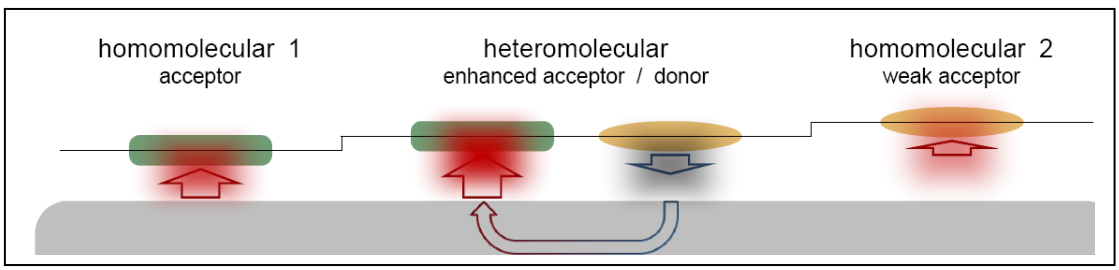

FIG. 1: Schematic illustration of the adsorption height alignment found for donator-acceptor blends consisting of either PTCDA or NTCDA and CuPc or SnPc, adsorbed on Ag(111) (from [3]).

all systems investigated here [1]. It demonstrates that the molecules are adjusting their heights upon formation of the mixed phase: The adsorption height of the perylene/naphthalene core of the charge accepting molecule (PTCDA/NTCDA) increases, that of the donor molecules decreases. The effect is most strongly observed for the PTCDA/SnPc case [1,3].

The fingerprints of the interaction strength in the electronic properties of the adsorbates, i.e., in the energetic positions of the relevant frontier molecular orbitals, are investigated by (angular resolved) ultraviolet photoelectron spectroscopy (AR)PES, and orbital tomography. Fig 2a shows the valence band structure of a mixed PTCDA/CuPc film and of both homomolecular structures, recorded by conventional UPS. All HOMO peaks are clearly visible, as well as the former LUMOs since they become partially filled due to charge transfer from the substrate and shift below the Fermi edge. While for the heteromolecular structure the HOMO region simply shows a superposition of the two homomolecular spectra, the situation close to the Fermi edge is different: Only one LUMO peak is visible, and is significantly shifted towards larger binding energies compared to both homomolecular films. The question whether this peak corresponds to the LUMO of PTCDA or CuPc was answered by an orbital tomography analysis of ARPES data. In Fig. 2b the *k*-resolved data cube of photoelectron intensities close to the Fermi edge is displayed. From this data the orbital specific experimental projected densities of states (pDOS) is extracted for all relevant LUMOs (Fig. 2c, for details see [2]).

This analysis clearly shows that only the LUMO of PTCDA contributes to the peak at the Fermi edge (dark green line in Fig. 2c), not the CuPc LUMO (vanishing pDOS, red line). This demonstrates that in the mixed phase the LUMO binding energy of CuPc has decreased. Consequently CuPc releases all of its acquired charge, which in turn is taken up by the PTCDA LUMO showing an increased filling. Hence, for PTCDA, the electronic signatures, which normally go along with *shorter* bonding distances and thus *stronger* chemical interaction, appear here in conjunction with *larger* bonding distances (and vice versa for CuPc).

Our experimental results appear paradoxical, and we therefore performed density functional theory calculations for the PTCDA/CuPc system [2]. These calculations yield adsorption heights in very good agreement with the experiment, and moreover confirm the measured frontier orbital binding energies and charging states of the CuPc and PTCDA LUMOs. They furthermore reveal the reorganization of the charge density (i.e., charge accumulation and depletion at PTCDA and CuPc sites, respectively) that goes along with the equalization of adsorption heights upon formation of the mixed phase. A comparison with model calculations performed for the adsorbate layer with

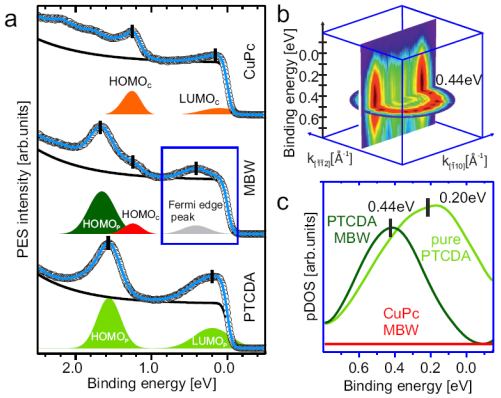

FIG. 2: (a) Conventional UPS data for homo- and heteromolecular PTCDA/CuPc phases. (b) Full tomographic 3D data cube. For an animated illustration see online version of Ref. [2]. (c) pDOS (resulting from the orbital tomography analysis) for the LUMOs of PTCDA and CuPc in the mixed phase as well as for the LUMO of PTCDA in its homomolecular phase (from [2]).

and without substrate (for details see [2]) identifies the interaction of the frontier orbitals with the metal states as an important element leading to the population/depopulation of the respective LUMOs. As a consequence, the Pauli-repulsion between the adsorbates and the metal is modified, which is the direct reason for the two molecules to equalize their heights in the heteromolecular phase: The electronic charge which CuPc sheds from its LUMO and repels from its site is redirected towards PTCDA, with the result that PTCDA both floats upon this `cushion' of charge and accepts more of it into its LUMO, while CuPc sinks into the remaining `depression' of the electron density. The necessity to equalize the heights of the two adsorbates thus harmonizes very well with the different chemical characters (relative donor vs.\ relative acceptor) of the two molecules [2,3].

The apparently paradoxical behavior between geometric structure (adsorption height) and electronic properties (frontier orbital binding energy) of the heteromolecular MBW phase is resolved, and has thus revealed very clearly how observables such as vertical adsorption height, frontier orbital binding energies and charge transfer, for homomolecular as well heteromolecular systems, are linked and influence each other. The insight at this level has an obvious impact on the challenge of engineering the interfaces of heteromolecular materials for applications.

[1] B. Stadtmüller, S. Schröder, F.C. Bocquet, C. Henneke, C. Kleimann, S. Soubatch, M. Willenbockel, B. Detlefs, J. Zegenhagen, T.-L. Lee, F.S. Tautz, and C. Kumpf, Phys. Rev. B **89**, 161407(R) (2014).

[2] B. Stadtmüller, D. Lüftner, M. Willenbockel, E.M. Reinisch, T. Sueyoshi, G. Koller, S. Soubatch, M.G. Ramsey, P. Puschnig, F.S. Tautz, and C. Kumpf, Nature Communications **5**, 3685 (2014).

[3] B. Stadtmüller, S. Schröder, and C. Kumpf, J. Electron Spectrosc. Relat. Phenom., *in press* (2015), doi: 10.1016/j.elspec.2015.03.003.

Patterning a hydrogen-bonded molecular monolayer with a hand-controlled scanning probe microscope

M. F. B. Green, T. Esat, C. Wagner, P. Leinen, A. Grötsch, F. S. Tautz, and R. Temirov

Peter Grünberg Institut-3, Forschungszentrum Jülich, Germany

One of the paramount goals in nanotechnology is molecular-scale functional design, which includes arranging molecules into complex structures at will. The first steps towards this goal were made through the invention of the scanning probe microscope (SPM), which put single-atom and single-molecule manipulation into practice for the first time. Extending controlled manipulation to larger molecules is expected to multiply the potential of engineered nanostructures. Here we report an enhancement of the SPM technique that makes the manipulation of large molecular adsorbates much more effective. By using a commercial motion tracking system, we couple the movements of an operator's hand to the sub-angstrom precise positioning of an SPM tip. Literally moving the tip by hand we write a nanoscale structure in a monolayer of large molecules, thereby showing that our method allows for the successful execution of complex manipulation protocols even when the potential energy surface that governs the interaction behaviour of the manipulated nanoscale object(s) is largely unknown.

The scanning probe microscope (SPM) is an excellent tool for the manipulation of atoms and molecules on surfaces due to its high spatial imaging resolution and atomic-scale precision. Today, controlled SPM manipulation of individual atoms and small molecules is a routine operation. Since most of the detailed studies of SPM manipulation have been performed on such atoms or small molecules adsorbed on surfaces with a highly symmetric structure, their success can be explained to a large extent by the fact that the high symmetry of the surface reduces the potential of the junction in multi-dimensional state space considerably. Unfortunately, the behaviour of large molecules on surfaces is generally not well understood, and full and quantitative reconstruction of the adsorption potential in such a situation does not seem realistic in the nearest future.

How can we nevertheless manipulate large molecules successfully, despite lacking full knowledge of their complex interaction potential? Generally, manipulation is defined as a trajectory that connects the initial and final states of the junction in its multi-dimensional state space. In reality, since the potential is not known 'successful' trajectories can only be determined with the help of an experiment in which the relevant regions of the potential landscape are explored in a trial and error fashion and the information obtained is finally used for learning. We demonstrate the possibility of such learning through a human operator controlling the position of the SPM tip with their hand. Our experiments directly show that the operator efficiently finds trajectories for the intentional manipulation of large organic adsorbates without prior knowledge of the potential to which the manipulated system is subjected, which in the future could allow for a related computer-driven approach to the problem.

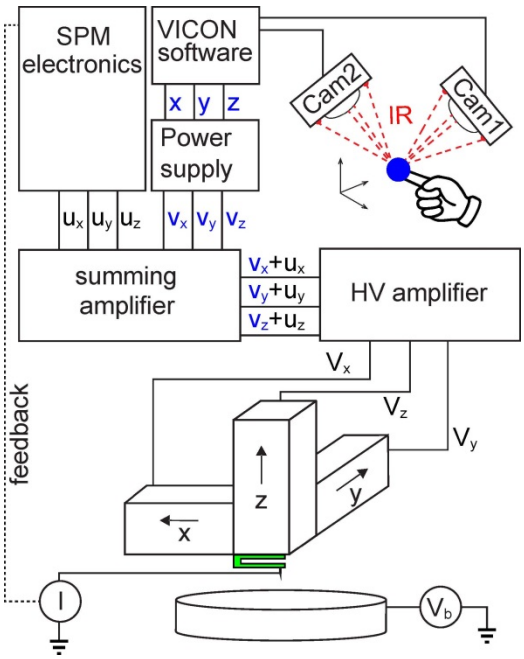

FIG 1: Scheme of the set-up for manual control of the SPM tip. Lamps mounted on the front of the two cameras emit infrared light that is reflected by a single marker fixed rigidly to the hand of the operator. The reflected light is captured by the cameras; with two cameras full three-dimensional triangulation is achieved. At the system output the real-time x(t), y(t), z(t)-coordinates of the marker are extracted. These coordinates are converted into a set of three voltages vx, vy, vz that are further added to the ux, uy, uz voltages of the SPM software used to control the scanning piezo-elements of the microscope.

For the demonstration of our manipulation technique we chose one of the best-studied cases of the adsorption of complex organic molecules: the well-ordered interface formed by the archetypal organic semiconductor 3,4,9,10-perylene tetracarboxylic acid dianhydride (PTCDA) on a single-crystalline Ag(111) surface. Due to the lack of quantitative information on the strong hydrogen bonds holding the molecules together in the monolayer (Fig. 2), it is not clear a priori which trajectories will be successful. Hand-controlled manipulation (HCM) allows us to find a manipulation protocol that removes single PTCDA molecules from the molecular monolayer very reliably, as shown below.

We performed the molecular manipulation with a commercially available SPM. Our instrument, the low-temperature combined non-contact atomic force/scanning tunnelling microscope (NC--AFM/STM) from CREATEC operated under ultra-high vacuum, allows for a stable and precise positioning of the tip, while simultaneously measuring the current flowing through the junction (I) and the frequency shift of the oscillating tip (Δf). Measuring Δf provides additional information about the microscopic junction structure [1,2].

The essence of our approach lies in the coupling of the sub-angstrom precise positioning of the tip of our instrument to the motion of the operator's hand [3]. This is achieved with the help of a commercial motion tracking system from VICON (Fig. 2). The VICON software was used to obtain Cartesian coordinates of a marker attached to the hand of the operator and feed them into a high precision power supply from STAHL ELECTRONICS that generated three voltages, v_x, v_y and v_z, which were added to the voltages u_x, u_y, u_z used by the scanning probe software to control the position of the SPM tip.

Each individual HCM started by parking the tip over the carboxylic oxygen atom of PTCDA that had been selected for contacting. The contact to the molecule was established by approaching the tip vertically towards the surface; this approach was effected by downward movement of the hand of the operator. Over the course of HCM the junction current I and the frequency shift Δf were displayed on an oscilloscope and served as feed-back signals for the operator. After establishing contact between the tip and the molecule (a sharp kink in I), the operator retracted the tip along an arbitrary three-dimensional trajectory. If the contact to the molecule was lost prematurely, the tip was moved back to the initial parking position by zeroing the v_x, v_y and v_z voltages and the manipulation was re-initiated. If contact was maintained up to retraction distances of 10–15 Å, the tip was moved, with the help of the SPM software, laterally at constant height to a clean silver surface area, where the molecule was then deposited back to the surface [3].

To illustrate the reliability of HCM, we present a structure 'drawn' into PTCDA/Ag(111) by sequentially removing single molecules from the layer (Fig. 2). Importantly, the images report the very first attempt, with no previous experience and without training. Remarkably, it was possible to re-deposit 40 of the removed molecules onto the clean Ag(111) surface nearby, showing that the molecules are not damaged during their extraction. Therefore, as Figure 4 shows, manual manipulation can also be used to 'correct' errors by filling a created vacancy with a molecule that has been extracted from a different location. For more information on the trajectories used to manipulate the 48 molecules see [3].

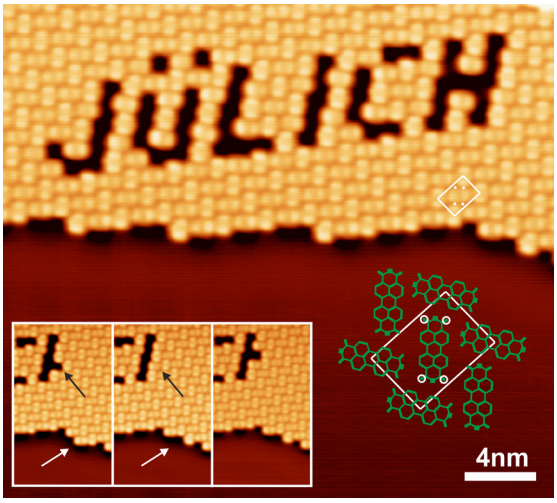

FIG. 2: Constant current STM image (I = 0.1 nA and V = -0.34 V) of a structure consisting of 47 vacancies that were created by removing individual PTCDA molecules from the PTCDA/Ag(111) monolayer. The three insets show the "repair" of a vacancy created by mistake. The black arrow marks the position of the error vacancy. The white arrow marks the molecule at the edge of the molecular island that was used to fill the error vacancy. The molecule from the edge was removed by using the same manipulation protocol as for all other vacancies and was then placed into the error vacancy by approaching the tip to the vacancy and increasing the voltage steadily to 0.6 V [3].

In summary, HCM allows for the straightforward manipulation of single molecules of large organic adsorbates in bound assemblies. The strength of the method derives from the direct manual control of the AFM/STM tip. This allows the operator to explore the unknown potential in the state space of the manipulated system, quickly determining the manipulation trajectories that steer the system into the desired final state(s). By using HCM we were able to find the trajectories of the AFM/STM tip that break the intermolecular bonds in the molecular monolayer of PTCDA/Ag(111) and write the first ever complex structure with *large* molecules. Lastly, the HCM method reported here brings us a step closer to the possibility of building functional nanoscale molecular structures.

[1] Fournier et al, Phys. Rev. B**, 84**, 035435. (2011)

[2] Wagner et al, Phys. Rev. Lett.**, 109**, 076102. (2012)

[3] Green et al, Beilstein J. Nanotechnol., **5**, 1926-1932 (2014)

Structural integrity of $NdPc_2$ molecules on metal surfaces of different reactivity

S. Fahrendorf[1], F. Matthes[1], D. E. Bürgler[1], C. M. Schneider[1], N. Atodiresei[2], V. Caciuc[2], S. Blügel[2], C. Besson[3], and P. Kögerler[3]

[1] Peter Grünberg Institut-6, Forschungszentrum Jülich, Germany
[2] Peter Grünberg Institut-1 and Institute for Advanced Simulation-1, Forschungszentrum Jülich, Germany
[3] Institute of Inorganic Chemistry, RWTH Aachen University, Germany

Magnetic molecules are auspicious candidates as functional units in molecular spintronics. Integrating molecules in devices requires their deposition as intact entities onto substrates. Here, we show for $NdPc_2$ molecules deposited on differently reactive metal surfaces that the molecule-surface interaction affects the intramolecular bonding. We explain these findings by substrate-dependent partial charge transfer to the Pc ligands, which strengthens the predominantly electrostatic intramolecular bonding.

The implementation of molecular magnets with high-spin ground states is a promising path to realize molecular spintronic devices [1]. Their primary advantages, small size, tuneable multiplet spectra, and the possibility to produce them in large quantities with identical properties, promise devices with high integration density and low power consumption. However, it is a priori unclear if and to what extent the geometric, electronic, and magnetic properties inherent to the molecule in the gas phase are modified upon adsorption. Here, we study the structural integrity of single bis(phthalocyaninato)-neodymium(III) molecules ($NdPc_2$) deposited by sublimation on three differently reactive surfaces, namely Au(111), Cu(100), and Fe/W(110) [2]. Fe/W(110) refers to a Fe film with a thickness of about 1.5 atomic layers on W(110), which is a well-known model system for magnetic surfaces. We find a strongly substrate-dependent structural integrity of the adsorbed $NdPc_2$ molecules, which tend to decompose into single-decker species upon deposition. Surprisingly, we observe the lowest decomposition probability on the most reactive Fe/W(110) surface, a clearly larger decomposition probability on the medium reactive Cu(100), and no intact double-decker molecules at all on the least reactive Au(111) surface. We attribute this counterintuitive behavior to partial charge transfer from the substrate to the Pc ligands of the molecule, which increases with molecule-surface interaction strength but also strengthens the intramolecular, predominantly electrostatic interaction and, thus, increases the stability of the adsorbed molecule [2].

In-house synthesized $NdPc_2$ molecules are sublimed at 850 K in a multichamber UHV-system equipped with a low-temperature scanning tunneling microscope (STM) and facilities for substrate preparation and characterization. In order to make sure that thermally induced processes in the evaporator, *e.g.* transformation of the double-decker $NdPc_2$ into the triple-decker Nd_2Pc_3, do not interfere with our experiments on the different surfaces, we use Cu(100) as a reference system meaning that after each experiment on other surfaces we check whether the observations on Cu(100) remain the same. Cu(100), Au(111), and Fe/W(110) substrates were all prepared and characterized *in-situ* prior to the $NdPc_2$ deposition.

Fig. 1a shows an STM overview image of the Cu(100) surface after $NdPc_2$ deposition. There are three characteristic features with different size, apparent height, and symmetry. The crosses with four lobes (Fig. 1b) are identified as single-decker Pc molecules [3]. The eight-lobe structure with a three times larger apparent height (Fig. 1c) is the STM image of double-decker Pc molecules [4].

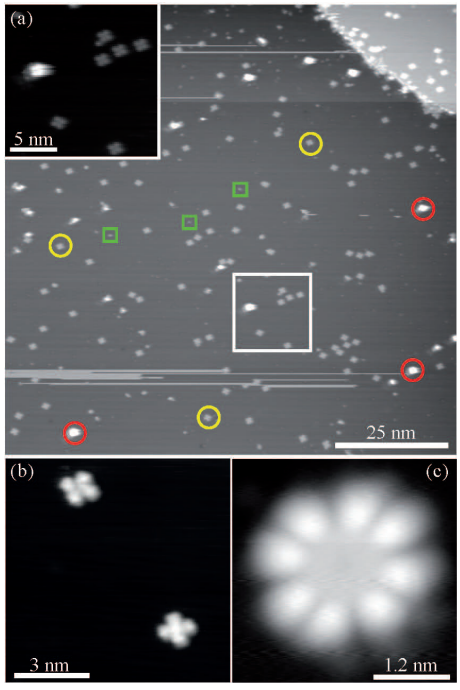

FIG. 1: STM images taken after $NdPc_2$ deposition on Cu(100): a) Overview showing single-decker (yellow) and double-decker (red) Pc as well as some smaller features (green). The inset is a zoom of the region inside the white frame. b) Single-decker and c) double-decker Pc molecules.

Both species appear in two different orientations (e.g., Fig. 1b) that can be explained by the coordination of the (lower) Pc ligand and the Cu(100) surface [5]. The third feature type (green squares in Fig. 1a) are about a quarter of a single Pc molecule in size and most likely correspond to phthalonitrile-like fragments of Pc molecules. The large number of single-decker molecules clearly exceeding the number of double-deckers suggests that the $NdPc_2$ decompose upon deposition. The analysis of such images yield a decomposition probability of $NdPc_2$ on Cu(100) of $P^{Cu(100)}$ = 78% − 82%. The analysis of similar data sets for $NdPc_2$ on Au(111) and Fe/W(110) [2] yield significantly different decomposition probabilities (Table 1) revealing a clear dependence of the structural integrity after deposition on the substrate material.

Several mechanisms can play a role for the decomposition of the double-decker structure during thermal sublimation and adsorption on the surface. First, heating of the molecule powder in the evaporator increases the thermal energy (850 K correspond to 70 meV), which may become sufficient to overcome the activation energy barriers for certain chemical reactions that release single-decker molecules. However, our reference measurements on the Cu(100) surface and the fact that the number of released single-decker molecules would not depend on the substrate material rule out that the thermal energy for sublimation plays a decisive role for the observed substrate-dependent structural integrity. The same arguments rule out an influence of the kinetic energy of the molecules when they reach the surface (also of the order of 70 meV). The only substrate-dependent energy contribution involved in the deposition process is the adsorption energy that is released when the molecule chemically binds to the surface. Lacking detailed density functional theory (DFT) for $NdPc_2$ on all three substrates, we compile in Table 1 calculated adsorption energies of the model system benzene on Au(111), Cu(100), and Fe/W(110) $E_{ads}^{benzene}$ taken from literature.

Surface	$E_{ads}^{benzene}$ [eV]	P
Au(111)	-0.55	≈ 100%
Cu(100)	-0.68	78-82%
Fe/W(110)	-0.98	45-55%

TABLE 1: Calculated adsorption energy of benzene $E_{ads}^{benzene}$ and measured decomposition probability P of $NdPc_2$ on different surfaces.

The values are one order of magnitude larger than the thermal energy required for sublimation (70 meV) and thus confirm that the adsorption energy is the dominant energy contribution of the deposition process. The relative magnitudes reproduce the increasing reactivity from Au(111) to Cu(100) and Fe/W(110). However, the comparison of the decomposition probabilities *P* with the adsorption energies contradicts the simple-minded assumption that the structural integrity of the molecule decreases with increasing adsorption energy. Counterintuitively, we find the lowest decomposition probability on the surface with the largest adsorption energy.

Fig. 2 shows local d*I*/d*V*-spectra measured above the center of $NdPc_2$ molecules adsorbed on Cu(100) and Fe/W(110). Based on the DFT calculations for $NdPc_2$ on Cu(100) [5] the peaks close to -1.0 V and the shoulder/peak above 1.0 V are assigned to occupied and unoccupied Nd 4*f*-states, respectively. Their ligand-field splitting is a measure for the intramolecular interaction between the central Nd-ion and the Pc ligands, which is predominantly of electrostatic character.

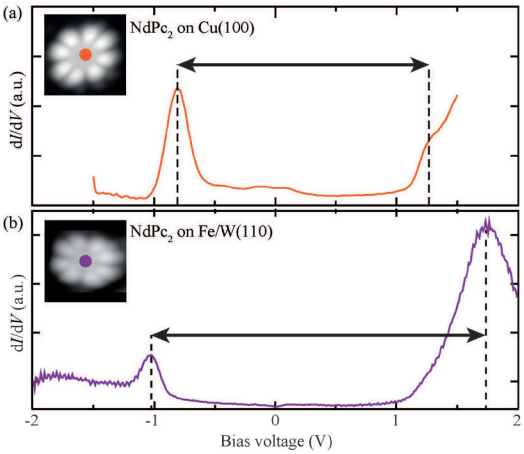

FIG. 2: dI/dV-spectra measured above the center of $NdPc_2$ molecules adsorbed on a) Cu(100) and b) Fe/W(110). Arrows indicate the ligand-field splitting of the 4f-derived states.

The obviously larger splitting in Fig. 2b) indicates that the intramolecular interaction within $NdPc_2$ adsorbed on Fe/W(110) is stronger than on Cu(100). Based on this observation we propose the following mechanism to explain the observed substrate-dependent structural integrity [2]: The bonding of $NdPc_2$ to metal surfaces occurs via strong hybridization and partial charge transfer [5]. The more reductive the surface, the more charge is transferred to the not fully occupied ligand states. The additional negative charge on the ligands strengthens the intramolecular electrostatic interaction and thus increases the molecular stability. As a consequence the structural integrity of the molecule increases with increasing surface reactivity.

In conclusion, the structural integrity of organic molecules after chemisorption on metallic surfaces is governed by a subtle balance of competing interactions. Upon adsorption organic molecules cannot be considered as chemically and geometrically rigid entities with fixed internal interactions.

[1] L. Bogani and W. Wernsdorfer, Nature Mater. **4**, 79 (2008)

[2] S. Fahrendorf et al., SPIN **4**, 1440007 (2014)

[3] P. H. Lippel et al., Phys. Rev. Lett. **62**, 171 (1989)

[4] L. Vitali et al., Nano Lett. **8**, 3364 (2008)

[5] S. Fahrendorf et al., Nature Commun. **4**, 2425 (2013)

Differential Adsorption of Gold Nanoparticles to Gold/Palladium and Platinum Surfaces

C. Kaulen[1], M. Homberger[1], S. Bourone[1], N. Babajani[2], S. Karthäuser[2], A. Besmehn[3], and U. Simon[1]

[1] Institute of Inorganic Chemistry, Forschungszentrum Jülich, Germany
[2] Peter Grünberg Institut-7, Forschungszentrum Jülich, Germany
[3] Central Institute for Engineering, Electronics and Analytics-3, Forschungszentrum Jülich, Germany

Integration of hybrid materials, like molecule capped gold nanoparticles (AuNP) into nanoelectronic devices requires detailed knowledge about the AuNP-electrode interface. Here, we report the pH-dependent adsorption of amine or carboxylic acid terminated gold nanoparticles on platinum or gold/palladium (30%Pd) alloy, respectively. We synthesized amine terminated AuNP by applying a new solid phase supported approach as well as AuNP exhibiting carboxylic acid as terminal groups. The pH-induced agglomeration of the AuNP was investigated by UV-vis, DLS and ζ-potential measurements. Preferential adsorption was observed on the different metals depending on the pH and the ionic strength of the AuNP solution. Thereby, we demonstrate that by choosing the appropriate functional group and adjusting the pH as well as the ionic strength a directed binding can be achieved, which is an essential prerequisite for applications of these particles in nanoelectronics.

The application of ligand stabilized gold nanoparticles (AuNP) as building blocks for the fabrication of nanoelectronic devices is considered promising, due to their unique size dependent properties, their high stability and their versatile surface chemistry [1]. However, the integration of AuNP in 2D or 1D arrays or even 0D devices for electronic applications requires a highly controllable immobilization of AuNP onto respective substrates. In this work, we report the adsorption properties of carboxylic acid and amine terminated AuNP with a gold core size of 13 nm on platinum and gold/ palladium surfaces [2]. We used citrate stabilized AuNP as starting compound and applied mercaptooctanoic acid (MOA) and aminooctane-thiol (AOT), respectively, in a ligand exchange reaction. While the ligand exchange with MOA is straightforward, for the capping with AOT a new solid phase assisted synthetic route has been developed. We applied these two types of particles to platinum substrates with line structures of gold/palladium alloy on top of it. The substrate design ensures that both AuNP types can adhere to both metals under identical conditions and eventually discriminate the two metal surfaces. By variation of the pH value and adjustment of the ionic strength we analyzed the adsorption properties of the carboxylic acid and amine terminated AuNP. Fig. 1 shows their pH-dependent differential binding, reflected by the preferred binding of the carboxylate groups to gold at pH 5 but to platinum at pH 9 (not shown), while the ammonium functionality exhibits preferred binding to platinum at pH 3.

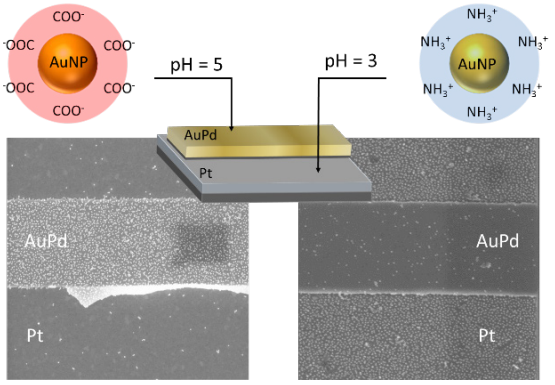

FIG. 1: Schematic of the pH dependent adsorption of AuNP-MOA on AuPd at pH 5 and of AuNP-AOT on Pt at pH 3.

For the pH-dependent measurements the purified particles were dispersed in HEPES buffer solution at pH 3, 5, 7 and 9. Distinct absorption maxima (λ_{max}) for AuNP-MOA at 522 nm in the range from pH 5 to 9 approve the presence of isolated non-interacting particles and consequently the respective colloid solutions appear red. Within this pH range the carboxylic acid groups are deprotonated and therefore, negatively charged, also visible by a negative ζ-potential. Decreasing the pH into the acidic range leads to protonation of the carboxylic group and consequently, an increase of the ζ-potential from -40 mV to a positive value. Furthermore, a red-shift and the broadening of λ_{max} is detected. At pH ≤ 4 electrostatic repulsion is reduced with stepwise protonation of the carboxylic group, leading to the formation of AuNP-MOA agglomerates. Thereby a color change of the AuNP-MOA solution from red to blue can be followed by the naked eye (Fig. 2).

The AuNP-AOT reveals contrary properties. Acidified colloid solutions (pH = 3) exhibit a positive value for the ζ-potential as well as a

distinct λ_{max} at 522 nm corresponding to individual AuNP with protonated ammonium groups. Whereas, at pH ≥ 5 the plasmon peak broadens, the UV-vis spectra show a red-shift of $\lambda_{max,}$ and hydrodynamic diameters up to 1500 nm are detected by DLS. These results correspond to large particle agglomerates caused by the decreased electrostatic stabilization due to the deprotonation of the terminal ammonium group.

pH	3	5	7	9
Au-MOA	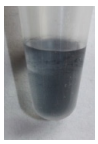	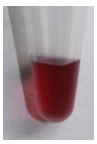	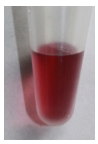	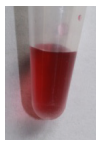
Au-AOT				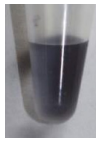

FIG 2: Photographs of AuNP-MOA and AuNP-AOT solutions at different pH values.

In order to investigate the pH-dependent adsorption of AuNP-AOT and AuNP-MOA, we performed immobilization studies on structured substrates consisting of AuPd lines on Pt. First, solutions of the respective AuNP in HEPES were coated on the structured substrates and imaged with SEM to visualize the covering density (Fig. 3).

At pH 5 the AuNP-MOA adsorb preferably on AuPd, whereas at pH 9 these particles are adsorbed almost exclusively on the Pt surface. In case of AuNP-MOA in neutral HEPES buffer solutions (pH = 7) adsorption neither on AuPd nor on Pt was observed. At pH 3 AuNP-MOA tend to aggregate as described above and thus no preferred immo-bilization of individual particles could be observed. The same holds for AuNP-AOT at pH 9, 7 and 5, whereas at pH 3 they exhibit preferential adsorption on Pt. These results already point towards differential binding.

In order to get precise insight to the influence of the ionic strength on the adsorption process the experiments were repeated in HEPES buffer brought to the respective pH with citric acid (pH = 5) or Tris (pH = 9). Thus, a good buffer capacity was ensured, while the ionic strength was kept low. In addition, a value in the high ionic strength regime, I = 0.02 molL^{-1}, was selected and adjusted by addition of 0.01 molL^{-1} NaCl to the HEPES buffer solutions. We restricted the investigations to those pH values, where adsorption of individual particles on the metal surfaces was observed in the initial experiments (pH 5 and pH 9 for AuNP-MOA and pH 3 for AuNP-AOT). The covering density was derived from SEM images for the low as well as for the high ionic strength regime, respectively.

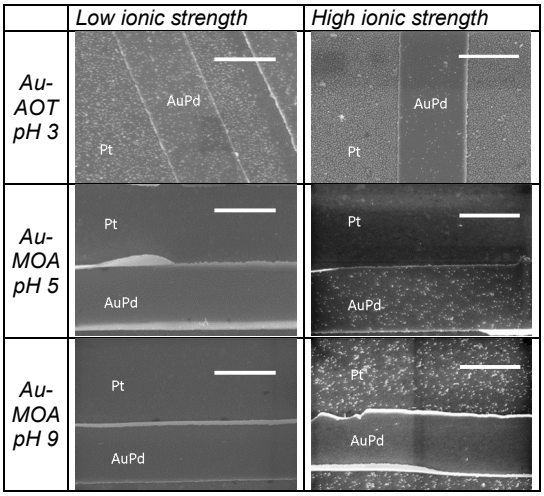

FIG 3: SEM images of AuPd structured Pt substrates with adsorbed AuNP-AOT and AuNP-MOA at different pH values and ionic strengths.

It turned out that for both particle types a higher ionic strength results in higher particle coverage. Furthermore, the selectivity of particle adsorption on Pt increases for AuNP-AOT solutions with higher ionic strength. For AuNP-MOA at pH 9 and AuNP-AOT at pH 3 on platinum a preferred binding due to the formation of an ionic adlayer is assumed, i.e., AuNP capped with charged molecules are adsorbed on the metallic substrate.

In summary, we analyzed the adsorption properties of carboxylic acid and amine terminated AuNP (AuNP-MOA and AuNP-AOT) on metallic sub-strates consisting of Pt and AuPd. We discovered preferred binding of AuNP-MOA to AuPd at pH 5 but to Pt at pH 9, and preferred binding of AuNP-AOT to Pt at pH 3. An increased ionic strength of the buffer solution improves the adsorption at any pH value. Hence, the study reveals differential adsorption to AuPd and Pt surfaces. These results allow for controlling the adsorption of ligand stabilized AuNP on electrode surfaces consisting of different metals. This was demonstrated in a further investigation regarding electrical characterization of Janus–AuNP, bearing carboxylic groups as well as amino groups, trapped within a heterometallic nanogap formation [3].

[1] M. Homberger and U. Simon, Phil. Trans. A **368**, 1405 (2010).

[2] C. Kaulen, N. Babajani, S. Bourone, M. Homberger, S. Karthäuser, A. Besmehn, and U. Simon, Langmuir **30** 574 (2014).

[3] C. Kaulen, N. Babajani, M. Homberger, S. Karthäuser, R. Waser, and U. Simon, J. Phys. Chem. C **118** (46), 27142 (2014).

Janus-AuNP in Heterometallic Nanogaps – a Key Step Towards Integration of Functional Molecular Units in Nanoelectronics

N. Babajani,[1] C. Kaulen[2], M. Homberger[2], M. Mennicken[1], R. Waser[1], U. Simon[2], and S. Karthäuser[1]

[1] Peter Grünberg Institut-7, Forschungszentrum Jülich, Germany
[2] Institute of Inorganic Chemistry, RWTH Aachen University, Germany

We present a highly promising approach for the formation of novel nanoscale organic/inorganic hybrid architectures. For this purpose we prepared ligand stabilized Janus-type gold nanoparticles (AuNP), which were immobilized in between customized heterometallic nanogap structures, consisting of two different metal electrodes. The Janus-type AuNP were equipped with carboxyl- and amine-terminal functionalities on opposite hemispheres. By choosing appropriate immobilization conditions we could control the immobilization direction in between the heterometallic nanoelectrode gap structures. Our results demonstrate the striking potential of this approach with respect towards the utilization of functional molecular units in nanoelectronics.

One of the great challenges in integrating ligand stabilized AuNP or molecules in nanoelectronic devices is the reproducible and reliable contact formation with solid-state electrodes. A reliable contact formation is the prerequisite for controlling the charge transfer at the molecule-metal junction and for allowing selective addressing and exploitation of the intrinsic molecular functionalities. If this challenge could be met, molecule-defined devices with functionalities of rectifiers or memristors would come into reach.

In order to meet this challenge we developed an approach involving heterometallic nanogap structures consisting of different metals (Pt and AuPd) and ligand stabilized Janus-type AuNP equipped with different terminal functionalities on opposite hemispheres (-NH_2 and -COOH). Based on our previously reported findings on ligand stabilized AuNP and investigations on molecule/metal junctions, these selected molecular terminal group/metal combinations should allow to control the immobilization direction of these Janus-AuNP, as depicted in figure 1a [1,2].

Furthermore, the resulting devices should exhibit highly reproducible asymmetry of the measured *I/U*-characteristic, due to the proposed directed immobilization.

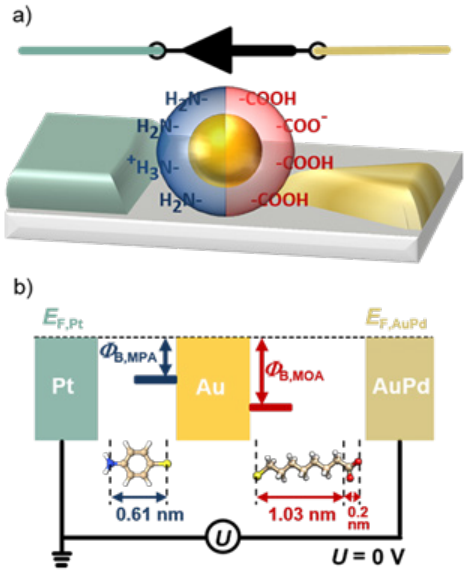

FIG. 1: a) Schematic of the "Pt-MPA/AuNP/MOA-AuPd" device; b) the Fermi energies (E_F), tunneling barrier heights (ϕ_B), as well as the respective molecular lengths are indicated. Reprinted with permission from [4]. © 2014 American Chemical Society.

Janus-type AuNPs were synthesized based on a concept applying sequential ligand exchange and a solid phase support, as already described for the preparation of AuNP dimers [3]. We applied 1,8-mercaptooctanoic acid (MOA) and 4-mercapto-phenylamine (MPA) exhibiting the desired terminal groups (-NH_2 and -COOH). Additionally both molecules are equipped with a thiol moiety, guaranteeing proper binding to the AuNP´s surface and thus, sufficient stabilization.

XPS measurements on monolayers of the Janus-type MOA-MPA AuNP adsorbed on Pt in comparison with simple MOA and MPA stabilized AuNP adsorbed on Pt verify the proposed Janus-character. Furthermore, the XPS data foster the assumption that the strongest bond, which is in this case the N-Pt bond, determines the adsorption direction of the Janus-AuNPs to the Pt-substrate [4].

Heterometallic nanostructures comprising gap sizes within the range of the prepared Janus-type AuNP were fabricated utilizing electron beam lithography (EBL) in combination with shadow mask technique. Thereby an aluminum-layer was deposited on top of EBL defined nanoelectrode structures in the first step. The thickness of this aluminum layer determines the overhang of the resulting Al_2O_3 after oxidation, which builds the shadow mask for a subsequent EBL-step. In the last EBL-step the second nanoelectrode is formed, and thus separated from the first nanelectrode by the distance corresponding to the Al_2O_3 overhang [4].

AuNP were immobilized by dielectrophoretic trapping (DEPT) from phosphate buffer solution at pH 5. From 270 fabricated devices 37 functional device were obtained exhibiting conductances (for U_{SD} = 1 V) in the range from 1 pS to 100 nS, whereby the utmost number of devices exhibit conductances in the range 40 pS – 1 nS. Figure 2 displays representative *I/U*-measurements (averaged over about 50 cycles). All *I/U*-curves show a distinct increase in conductance in the negative voltage regime (Pt-electrode grounded). Furthermore, the striking result is, that this increase of more than 10% in conductance (at U_{SD} ~ 0.7 V) is observed in the same way for 80% of the Janus-AuNP devices (25 out of 31). This result strongly supports an immobilization of the Janus-AuNPs in a controlled and directed way.

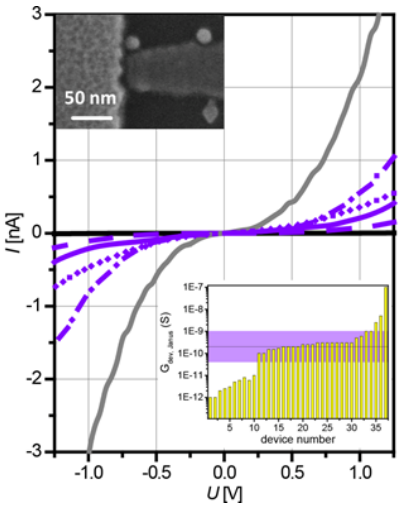

FIG. 2: I/U-curves of 6 representative Janus-AuNP devices. Insets: SEM image of a Janus-AuNP device taken after electrical characterization (left) and statistics of experimental conductance of 37 devices at U_{SD} = 1 V (right, black line depicts the calculated $G_{dev,Janus}$ = 0.21 nS, violet bar marks the conductance range 40 pS to 1 nS). Reprinted with permission from [4]. © 2014 American Chemical Society

In principle such a device can be approximated as a double barrier tunnel junction, meaning two molecular junctions connected in series. Corresponding to the assumed geometry depicted in figure 1 the following equation for the conductance ($G_{dev,Janus}$) through our device "Pt-MPA/AuNP/MOA-AuPd" is valid:

$$1/G_{\mathrm{dev,Janus}} = 1/G_{\mathrm{MPA}} + 1/G_{\mathrm{MOA}}$$

From this equation a theoretical device conductance of $G_{dev,Janus}$ = 0.21 nS at U_{SD} = 1 V is deduced, which corresponds impressively to the experimentally obtained values (Figure 2, inset, $G_{exp,Janus}$ = 0.04 to 1 nS).

Additionally analysis of I/U-curves that correspond to the theoretical conductance value of Janus-AuNP devices, reveal a pronounced asymmetry in the voltage range 0.4 - 0.8V that vanishes for U_{SD} > 1 V (Figure 3).

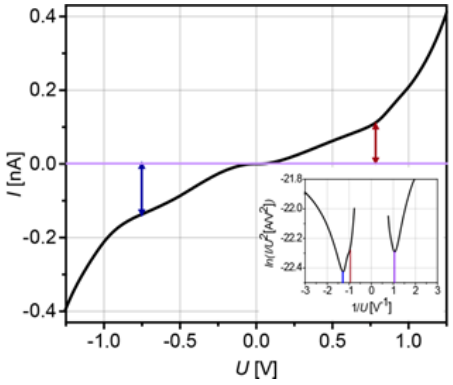

Fig. 3: I/U-measurement of a Janus-AuNP device with a conductance corresponding to $G_{dev,Janus}$; Inset: corresponding Fowler-Nordheim plot. Reprinted with permission from [4]. © 2014 American Chemical Society

A Fowler-Nordheim plot was used to analyze these results (Figure 3, inset). Thereof, for negative voltages two minima can be deduced corresponding to U_{trans1} = 0.75 ± 0.1 V and U_{trans2} = 1.2 ± 0.1 V while for positive voltages one minimum corresponding to U_{trans3} = 0.95 ± 0.1 V can be identified. U_{trans1} is in good agreement with tunneling barrier heights obtained for the reference particles MPA-AuNPs ($\Phi_{MPA,exp}$ = 0.85 ± 0.1 V) while U_{trans2} corresponds to MOA-AuNP, ($\Phi_{MOA,exp}$ = 1.25 ± 0.1eV). These results support the assumption that both molecules are involved in the charge transport through the Janus-type AuNP device. Furthermore, the observed asymmetry of the *I/U*-characteristics can be attributed to the different molecules forming the junction between AuNP and metal.

Our results indicate that the directionality of the Janus-AuNP immobilization and thus, the rectification direction of the formed nanoscale device can be controlled.

This work was supported by the Excellence Initiative of the German federal and state government and by JARA Seed Funds.

[1] S. Karthäuser, J. Phys.: Condens. Matter. **23**, 013001, 16pp (2011).

[2] C. Kaulen, M. Homberger, N. Babajani, S. Karthäuser, R. Waser, U. Simon, Langmuir **30**, 574-583 (2014).

[3] R. Sardar, T. B. Heap, J. S. Shumaker-Parry, J. Am. Chem. Soc. **129**, 5356-5357 (2007).

[4] N. Babajani, C. Kaulen, M. Homberger, M. Mennicken, R. Waser, U. Simon und S. Karthäuser , J. Phys. Chem. C **118** (46), 27142-27149 (2014).

Surface and Step Conductivities on Silicon

S. Just[1], M. Blab[1], S. Korte[1], V. Cherepanov[1], H. Soltner[2], and B. Voigtländer[1]

[1] Peter Grünberg Institut-3, Forschungszentrum Jülich, Germany
[2] Central Institute of Engineering, Electronics and Analytics (ZEA-1), Forschungszentrum Jülich, Germany

The increasing importance of surface conductance compared to conductance through the bulk in modern nanoelectronic devices calls for a reliable determination of the surface conductivity in order to minimize the influence of undesired leakage currents on the device performance or to use surfaces as functional units. Electrical four-point measurements using a multi-tip scanning tunneling microscope (STM) are carried out in order to determine surface and step conductivities on Si(111) surfaces.

A model system for corresponding investigations is the Si(111)-(7x7) surface. Over the years a wide range of values for the conductivity of this surface has been reported, spanning several orders of magnitude [1], and the latest measurements deviate still by a factor of 2 to 3 [2, 3]. The main difficulty in measuring the surface conductivity is to separate the 2D conductance at the surface from the conductance through other channels, e.g. the bulk and the space charge layer.

Here, we use a four-tip scanning tunneling microscope [4] for distance-dependent measurements of the four-point resistance on Si(111), as shown in the inset in Fig. 1 for a linear tip arrangement, in combination with a three-layer model for charge transport. This method allows the separation of the surface conductance from other contributions due to the characteristic probe spacing dependency of different conductance channels. Further on, we analyze the anisotropy of the surface conductance caused by the influence of atomic steps, which allows to determine the conductivity of a single step and the step-free surface.

Analytic equations relating the measured four-point resistance to a conductivity can be obtained easily for pure 2D or 3D geometries, i.e. four tips positioned on a conducting sheet (surface) or on a half space (bulk).

In order to minimize the number of tips to be repositioned, we preferentially use a non-equidistant spacing, in which three tips remain at a mutual distance of s = 50 µm, while only the distance x between tip 1 and tip 2 is varied (Fig. 1). In this non-equidistant setup the hallmark of the constant four-probe resistance is lost for the 2D case, but there still exist analytical equations.

The measured distance dependence of the four-point resistance on a clean Si(111)-(7x7) sample for the non-equidistant configuration with distances $x \leq s$ = 50 µm, and for the equidistant configuration with distances $x = s \geq 50$ µm is shown in Fig. 1. The observed decreasing four-point resistance for increasing equidistant probe spacing s indicates that a non-surface channel contributes to the charge transport, since a pure 2D conduction exhibits a constant behavior in the equidistant region. Thus, the measured four-point resistance should be modeled by a conductance channel through the surface states as well as additional contributions from the bulk and a near-surface space charge layer.

Often an approximation of a parallel circuit consisting of the four-point resistance of the surface and the bulk (plus space charge layer) is used, but this approach has two shortcomings. First, a complete separation of the surface conduction channel and the bulk is assumed. Second, the two-point resistances, not the four-point resistances, determine, which amount of current flows through the surface layer and which part through the bulk/space charge layer. So, the preferred way for the current to split up depends on the details of the injection, e.g. the size of the current injecting contact (tip diameter). Thus, if more than one current path exists, the four-point resistance depends on possible transitions between charge transport channels as well as on the properties of the current injecting contacts, so that the well-known statement that the four-point

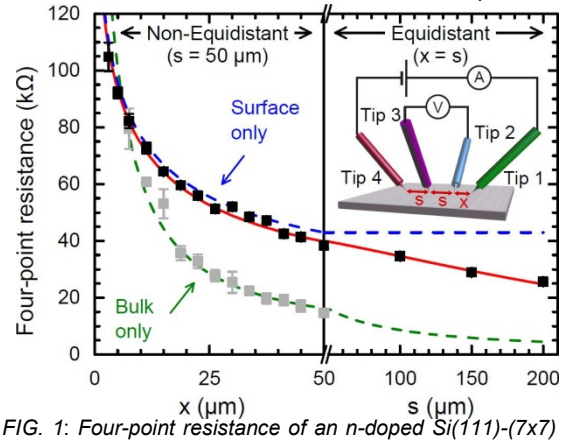

FIG. 1: Four-point resistance of an n-doped Si(111)-(7x7) sample as function of the probe distances s and x for the equidistant and the non-equidistant configuration. A three-layer model for charge transport yields the solid red line with $\sigma_{2D} = (5.1 \pm 0.7) \cdot 10^{-6}$ $\Omega^{-1}/\square$ located between the two limiting cases of a pure surface conductance (dashed blue line) and a pure bulk conductance (dashed green line). After removing the surface channel, the bulk can be measured directly (gray data points). In the inset the linear measurement configuration is shown.

resistance measured on the surface is independent of the contact resistances is not completely true.

In order to describe the charge transport through the different channels more accurately, we use an analytically derived three-layer model for conductance. In this model, the bulk enters with its known conductivity, while the surface conductivity is the parameter to be determined by a fit to the data. The space charge layer is approximated by an intermediate layer with a certain thickness and conductivity.

The best fit to the measured four-point resistance using the three-layer model is shown as a solid red line in Fig. 1 and results in a surface conductivity of $\sigma_{2D} = (5.1 \pm 0.7)\cdot 10^{-6}\ \Omega^{-1}/\square$. For comparison the two limiting cases are marked in Fig. 1: The four-point resistance arising from a pure 2D conductivity σ_{2D} is shown as dashed blue line, while the four-point resistance induced by a pure 3D conductance, with its $1/s$ behavior in the equidistant configuration, is indicated as dashed green line. So, the three-layer model including the intermediate space charge layer describes the experimentally observed behavior of a mixed 2D/3D transport very well.

If the Si(111) surface is hydrogen-terminated by a treatment in HF, which removes the surface states present on the 7x7 surface, a pure 3D transport results and the bulk conductivity can be measured directly (gray data points in Fig. 1).

While the distance-dependent four-point measurements could disentangle the surface conductivity from non-surface contributions to charge transport, the influence of atomic steps located on the (7x7)-reconstructed Si surface has not been considered up to now. This influence of steps can be described on average by an anisotropic surface conductance with $\sigma_{\parallel}$ along the step edges and $\sigma_{\perp}$ perpendicular to the step edges. The linear four-point measurement configuration (Fig. 1) is not sensitive to a two-dimensional conductance anisotropy, but in a square arrangement of the four probes, as shown in Fig. 2(b), an angle-dependent four-point resistance is obtained and the two tensor components can be measured. Results for this anisotropic four-point resistance on an Si(111)-(7x7) sample are shown in Fig. 2(a) as a function of the rotation angle θ relative to the average step direction. A fit of a model, which describes a 2D conductance anisotropy, to the experimental data is shown as solid red line in Fig. 2(a) describing the angle dependence quite well and results in $\sigma_{\parallel} = (9 \pm 2)\cdot 10^{-6}\ \Omega^{-1}/\square$ and $\sigma_{\perp} = (1.7 \pm 0.4)\cdot 10^{-6}\ \Omega^{-1}/\square$ with an anisotropy ratio of $\sigma_{\parallel} / \sigma_{\perp} \approx 5$.

In a last step, we convert the measured mean field anisotropic conductivities to the conductivities of a step-free terrace σ_{surf} and a single step σ_{step} resulting in $\sigma_{surf} = (9 \pm 2)\cdot 10^{-6}\ \Omega^{-1}/\square$, and $\sigma_{step} = (29 \pm 9)\cdot 10^{-6}\ \Omega^{-1}/\square$.

From a comparison of the surface resistivity and the step resistivity, the following relation is obtained. The resistance of one step (per unit length) corresponds to the resistance of a segment of the step-free Si(111)-(7x7) surface (per unit length) of a width of 300 nm. For our sample with a step density of 14 steps/µm, the contribution of the step resistance to the total resistance has a substantial amount of 80 % for a current flowing in the perpendicular direction. In general, the presence of steps will reduce the surface conductivity of the Si(111)-(7x7) considerably, however, in a well predictable manner.

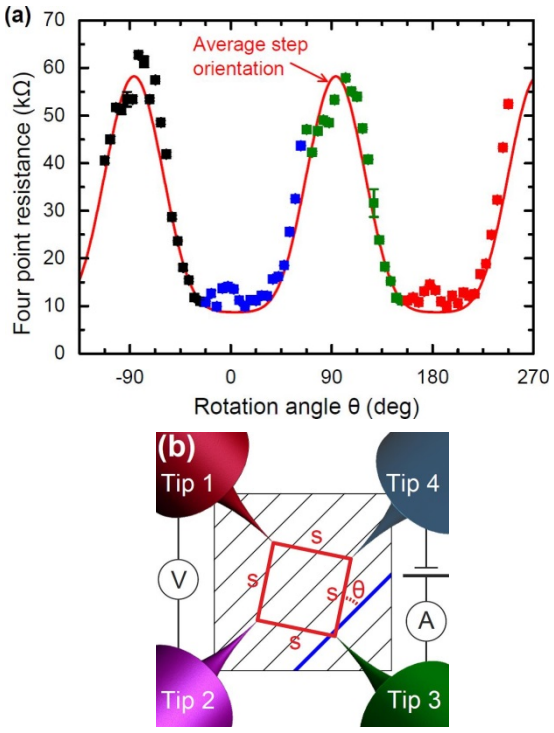

FIG. 2: (a) Four-point resistance measured on a Si(111)-(7x7) surface in the square configuration (shown in (b)) with s = 50 µm as a function of rotation angle θ between the average step orientation and the line connecting the current injecting tips (colored data points). The fit to the data is indicated as solid red line.

In conclusion, we combined the distance-dependent linear configuration for four-point resistance measurements on Si(111) surfaces with a three-layer model for charge transport in order to disentangle the surface conductivity from non-surface contributions (bulk and space charge layer conductivity). The influence of atomic surface steps is obtained by measurements in the angle-dependent square configuration. These two generic methods can easily be used to determine surface conductivities of other mixed 2D/3D systems, like different semiconductors or topological insulators.

[1] P. Hofmann and J. W. Wells, J. Phys.: Condens. Matter 21, 013003 (2009).

[2] M. D'angelo, K. Takase, N. Miyata, T. Hirahara, S. Hasegawa, A. Nishide, M. Ogawa, and I. Matsuda, Phys. Rev. B 79, 035318 (2009).

[3] B. V. C. Martins, M. Smeu, L. Livadaru, H. Guo, and R. A. Wolkow, Phys. Rev. Lett. 112, 246802 (2014).

[4] S. Just, M. Blab, S. Korte, V. Cherepanov, H. Soltner, and B. Voigtländer, Phys. Rev. Lett. (in press)

Determination of the 3D shape of a nanoscale crystal with atomic resolution from a single image

C. L. Jia[1,2,3], S. B. Mi [3], J. Barthel[2,4], D. W. Wang[3], R. E. Dunin-Borkowski [1,2], K. W. Urban [1,2] and A. Thust[1,2]

[1] Peter Grünberg Institute-5, Forschungszentrum Jülich, Germany
[2] Ernst Ruska-Centre (ER-C), Forschungszentrum Jülich, Germany
[3] International Center for Dielectric Research, Xi'an Jiaotong University, Xi'an 710049, China
[4] Central Facility for Electron Microscopy, RWTH Aachen University, Germany

Although the overall atomic structure of a nanoscale crystal is in principle accessible by modern transmission electron microscopy, the precise determination of its surface structure is an intricate problem. Here we show that aberration-corrected transmission electron microscopy, combined with dedicated numerical evaluation procedures, allows the three-dimensional shape of a thin MgO crystal to be determined from only one single high-resolution image. The sensitivity of the reconstruction procedure is not only sufficient to reveal the surface morphology of the crystal with atomic resolution, but also to detect the presence of adsorbed impurity atoms. The single-image approach that we introduce offers important advantages for three-dimensional studies of radiation-sensitive crystals.

The accurate description of the physical and chemical properties of nanoscale materials is a long-standing goal in nanoscience and technology. Many of the interesting properties of such dimensionally limited systems result from the dominant part played by their surface structure and chemistry, which are related intimately to their functionality [1]. In the present work, we report on the experimental three-dimensional (3D) shape reconstruction of a thin MgO crystal with single-atom precision from only a single image [2]. Our approach follows a different route from the classical tomographic multi-image approach. At the same time, we demonstrate that single-atom sensitivity is not only obtainable for high nuclear charge elements, but can be extended to include light chemical elements, such as oxygen. We restrict our treatment to the case of a periodic crystal, which does not contain impurities or vacancies in significant density.

3D reconstruction from a single high-resolution TEM image is possible due to the fact that the physical principle of electron diffraction is an intrinsically three-dimensional process. We demonstrate that the signal that is related to the 3D nature of electron diffraction can be recorded and interpreted by combining three major methodical building blocks. The first is the choice of a highly sensitive imaging mode for experimental data acquisition. The second building block is a structure refinement procedure, in which a structure model and the optical parameters are varied stepwise in such a way that the image calculated on this basis provides a best fit to the experimental image. A very important feature of this refinement procedure is the use of absolute image intensity levels [4,5] instead of commonly used relative values. The third building block is a statistical confidence check that provides precise quantitative statements about the uniqueness of the final 3D structure model.

Figure 1A shows an image of MgO acquired along the [001] crystal direction using the negative spherical-aberration imaging (NCSI) technique. This technique provides high contrast that is localized, to the greatest possible extent, at the positions of the atomic columns (seen end-on), which appear bright on a dark background.

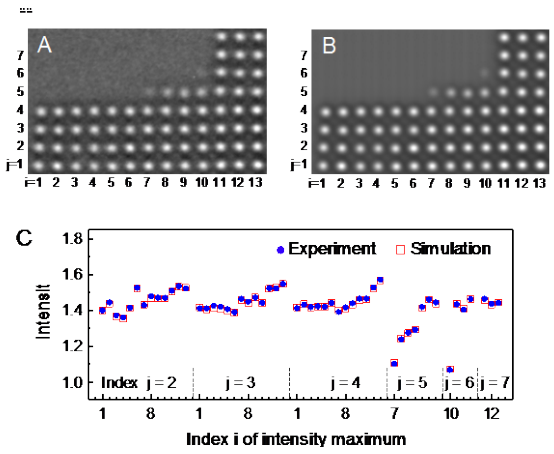

FIG. 1 A. Experimental image. B. Best-fitting simulated image displayed on the same intensity scale. The individual intensity maxima are indexed according to their positions (i, j). C. Quantitative comparison of experimental (full circles) and simulated (open squares) peak intensities, normalized with respect to the mean intensity of the image. The peak intensities are extracted from small areas of 100 image pixels by fitting a Gaussian peak function to local intensity distributions around the maxima.

In order to exploit even very weak contrast details and to enable quantitative determination of the atomic structure underlying the image, an iterative fitting procedure is employed. This iterative fitting procedure is applied to the image in Fig. 1A and is executed in two steps. In the first step, an ideally flat MgO crystal is assumed. All globally effective parameters are refined, such as the mean specimen thickness, the specimen misorientation, the effective absorption constant and optical aberrations of the microscope. In the second step of the fitting procedure, the local properties of the sample are further refined. This refinement includes not only the *x*- and *y*-coordinates and the occupancies of the individual atomic columns, but in particular also their *z*-positions. At the same time, the globally effective parameters that were estimated in the first step are also further refined.

Figure 1B shows the best-fitting image simulated on the basis of the refined structure model. A quantitative illustration of the quality of the match achieved between the experimental and simulated peak intensity values is given in Fig. 1C. Image simulation demonstrated that the addition or removal of a single Mg or O atom from an atomic column can be detected, since this action causes an average change in the absolute peak intensity value of 0.052, which is much larger than the residual fit discrepancy σ_f = 0.0053 (root-mean-square value, rms) and is also larger than the vacuum noise variation σ_n = 0.013 (rms). It is important that the signal resulting from the addition or removal of a single atom is four times higher than the experimental noise level, as this means that the detection sensitivity can even be extended formally towards half-occupied lattice sites. For this reason, the possibility of a formal occupancy of 50% at the surface sites is permitted in our refinement procedure.

Figure 2 shows the refined atomic model as a main outcome of the 3D shape reconstruction. The decisive progress made here is that the morphology of the top and bottom surfaces can now be resolved separately and displayed with atomic precision, even including the light oxygen atoms. The surface atoms that are displayed in gray and cyan denote formally half-occupied Mg and O sites, respectively.

It is of crucial importance to assess the correctness of the final 3D structure model quantitatively. Such an assessment step forms the third building block of our reconstruction procedure. The strategy of simply taking the best-fitting simulation as an indicator of the correct solution could potentially fail due to uniqueness problems, whereby two different column configurations could produce the same or nearly the same image contrast, which could no longer be identified uniquely in the presence of noise. In order to exclude such potential sources of error, we developed a statistical analysis procedure based on the Monte Carlo principle [2]. A quantitative reliability measure for the chosen best-fit strategy can be obtained by simulating thousands of column recognition attempts in the presence of noise and bookkeeping the number of correct and incorrect recognitions.

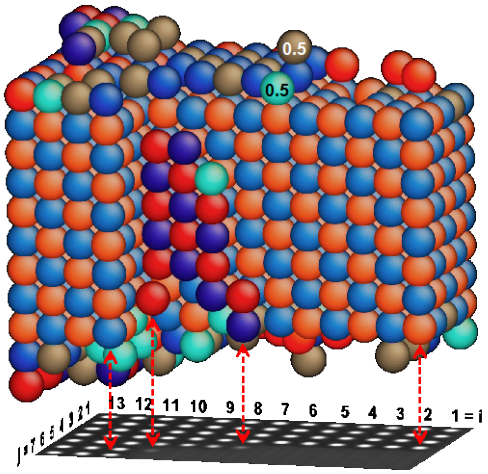

FIG. 2 Atomically resolved view of the best-fitting 3D atomic arrangement for the sample region shown in Fig. 1 A. Red spheres indicate fully occupied Mg sites and blue spheres fully occupied O sites. Increased color saturation is used to highlight surface atoms. In the surface layers, grey spheres indicate formally half-occupied Mg sites, while cyan spheres indicate formally half-occupied O sites.

A possible explanation for finding formally half-occupied lattice sites at the crystal surfaces can be proposed by considering two different scenarios. In the first scenario, we assume that Mg and O atoms are mobilized by electron irradiation and occupy surface sites only during approximately 50% of the 0.5 s exposure time. In the second scenario, we assume that weakly scattering C atoms, instead of regular lattice Mg atoms, reside at the partially-occupied surface sites. Both the dynamic surface migration scenario and the static carbon adsorption scenario result in similar improvements to the fit between simulations and experiment.

In this work, we have successfully revealed the 3D shape of a nanoscale crystal from only one single experimental high-resolution TEM image. We have demonstrated that the surfaces of the crystal, in particular its top and bottom surfaces, can be analysed separately with single-atom precision, including weakly scattering chemical species such as oxygen. The sensitivity achieved is high enough to detect the presence of impurity atoms adsorbed on the crystal surfaces. The present single-image approach can be highly advantageous, when dealing with radiation-sensitive crystals, for which it is often impossible to acquire more than a single image before the atomic structure has changed. It therefore offers broad application potential for atomically-resolved 3D studies of nanoscale materials.

[1] H. Gleiter, Acta Materialia **48**, 1 **(**2000**).**

[2] C. L. Jia et al , Nature Mater. **13**, 1044 (2014).

[3] A. Thust, Phys. Rev. Lett. **102**, 220801 (2009).

[4] C. L. Jia et al. Microsc. Microanal. **19**, 310 (2013).

Experimental Demonstration of Graphene-Enhanced Infrared Near-Field Optical Imaging

P. Li, T. Wang, H. Böckmann, and T. Taubner

I. Institute of Physics A, RWTH Aachen University, Germany

Graphene is a promising two-dimensional platform for widespread nanophotonic applications. Recent theories have predicted that graphene can also enhance evanescent fields for sub-diffraction-limited imaging. Here, for the first time we experimentally demonstrate graphene-enhanced near-field imaging. We show that a monolayer graphene offers a 7-fold enhancement of evanescent information, improving conventional infrared near-field microscopy to resolve buried structures at a 500-nm depth with λ/11-resolution.

The spatial resolution of conventional optical microscopy is limited by diffraction to about a half of the illumination wavelength because of the fast decay of evanescent information. To overcome this fundamental limit, scanning near-field optical microscopy (SNOM) uses a near-field probe, a tiny hole in the aperture-type [1] or a sharp tip apex [2] in the scattering version (s-SNOM), to pick up evanescent information before it is decayed, which allows the resolution down to 10-nm scale. However, this mechanism also implies that the SNOM probe needs to be close to the investigated object. For imaging deeply buried structures, evanescent fields decay exponentially before being picked up by the probe, thus the SNOM is unable to achieve a useful resolution.

Graphene provides a more feasible solution to improve the performance of near-field subsurface imaging. When a monolayer graphene is transferred onto the top of the sample, it is also able to support surface plasmon polaritons with ultra-small plasmon wavelengths [3,4]. These subdiffractive waves can go below the sample surface (involving the vertical decay length) to enhance and probe the evanescent information of the subsurface and sub-diffraction-limited object.

In this case, the resolution of the combined imaging system is not limited by the free-space wavelength, but mainly by the polariton wavelength λ_p of the graphene plasmon. As pointed out in our previous theory [5], the graphene offers a weaker enhancement of evanescent fields compared to that in the superlens. The superlens is a slab of a material with negative permittivity [6-8], which can support surface polariton modes with infinitely small λ_p at the resonant condition of $\varepsilon_{lens} = -\varepsilon_d$, where ε_{lens} and ε_d are dielectric permittivities of the superlens and the surrounding dielectric, respectively. We show in ref. [5] that the graphene superlens does not fulfill this resonant condition, leading to a weaker enhancement of evanescent fields. Here we experimentally verify that the enhancement provided by monolayer graphene is sufficient enough to improve the resolution of near-field subsurface microscopy [9]. Since graphene can be easily transferred onto the sample of interest, this novel method could have great application prospects.

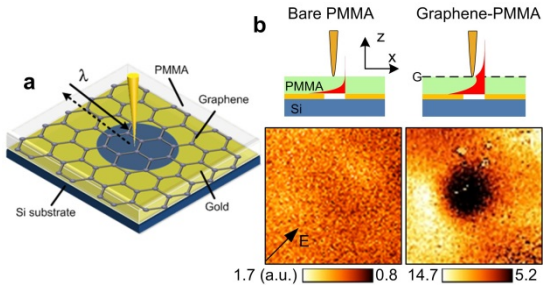

FIG. 1: (a) Sketch of the experiments. A 1.5-μm-diameter hole covered by monolayer graphene and a 500-nm-thick PMMA layer is imaged by the s-SNOM. (b) Infrared near-field amplitude images for the cases covered with a bare PMMA layer (left panel), graphene-PMMA (right panel). Black arrow indicates the polarization direction of the illumination light. Sizes of all images are 4 μm × 4 μm. Red plots in each sketch show the magnitude distribution of evanescent fields along the z-direction.

Our near-field imaging experiments are sketched in Fig. 1a. A 1.5-μm-diameter hole is prepared in an Au layer (40-nm-thick, on Si substrate). Monolayer graphene attached a 500-nm-thick PMMA (Poly(methyl methacrylate)) layer is transferred to cover the hole. For comparison, a control experiment is conducted where the hole is only covered by a 500-nm-thick PMMA layer. Near-field amplitude images taken at 11.3 μm are shown in Fig. 1b. The deeply buried hole can be hardly seen in the case without the graphene. On the other hand, it is well resolved in the graphene-involved case, indicating that graphene introduces an obvious enhancement of evanescent information.

To understand this phenomenon, in Fig. 2 we calculate the transmittance of the PMMA-graphene system as a function of in-plane (x-axis) momenta k_x and the wavelength λ. This transmission plot describes the complete electrodynamics of the

PMMA-graphene system, not only in the near field, but also in the far field. This is because the transmission properties of all the in-plane components, both propagating ($k_x < k_0$, k_0 being

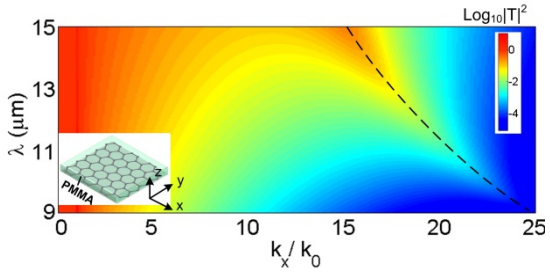

FIG. 2: The transmittance of the graphene-PMMA system (sketched in the insert) as a function of k_x and λ. Black dashed line indicates the position of the plasmon mode.

the wavenumber in free space) and evanescent waves ($k_x > k_0$), can be evaluated in the plot. Two transmission peaks are found in this dispersion plot. The one around $k_x = k_0$ indicates the light line in the air which relates to the total internal reflection. The other transmission peak (indicated by the black dashed line) represents the graphene plasmon mode. If the in-plane components match the graphene plasmon ($k_x = k_p$, k_p being graphene plasmon momenta), it leads to the maximum transmission peak of high-k_x components found in transmission. This mode shows a curved wavelength-dependent resonance behavior. This dispersion characteristic is different from that of the superlens, which usually has a flat dispersion for nearly all the high-k_x components at the superlensing wavelength (more detailed discussions can be found our previous theory work [5]).

In order to quantify the graphene enhancement of evanescent fields, we perform near-field imaging of a graphene-covered Au subwavelength grating. Fourier transforms of line scans taken from the amplitude imaging of s-SNOM are shown in Fig. 3. Comparing the cases with and without graphene, the near-field graphene enhancement is clearly presented in this figure. 7-fold for the third order ($k_x = 11.3k_0$), respectively.

In summary, we experimentally demonstrated that monolayer graphene can significantly enhance evanescent fields for improving the subsurface imaging capability in near-field microscopy. As a next step, the extensions to a multilayered graphene configuration will not only improve the resolution to the nanoscale, but can also realize new sub-diffraction-limit imaging devices like far-field graphene hyperlenses and near-field graphene lenses.

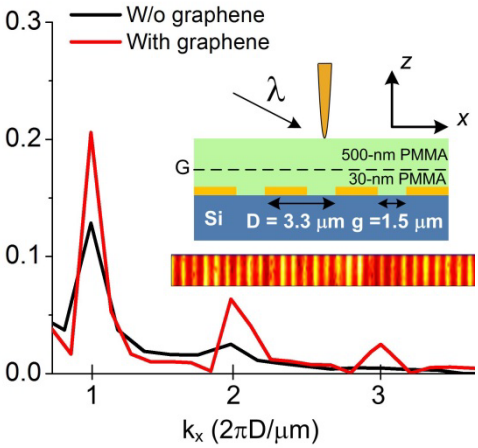

FIG. 3: Near-field enhancement of monolayer graphene on an Au grating. The insert shows the set-up of the experiments. An Au grating is prepared on a Si substrate. A 30-nm-thick PMMA layer is coated as a spacer layer between the graphene and the grating. The s-SNOM tip scans across the 500-nm-thick PMMA layer. Fourier transform (red line) of line scans is taken from the amplitude image (at λ = 11.3 μm, shown below the sketch), normalized to the zero-frequency components. High spatial-frequency components, up to the grating's third order harmonic ($k_x = 11.3k_0$), are resolved by the graphene-enhanced s-SNOM system. The control case without the graphene (the grating covered with a bare 500-nm-PMMA film, black line) is shown for comparison.

Further experiments by gate-tuning or chemical doping will yield a frequency-tunable effect to cover a broader wavelength range for infrared spectroscopic applications like vibration absorption spectroscopy and nanoscale material identification. Moreover, the presented imaging mechanism is not only restricted to the use of graphene, but also suitable for other graphene-like two-dimensional materials like transition metal dichalcogenides and hexagonal boron nitride [10].

[1] A. Lewis et al., Nat. Biotechnol. **21**, 1278 (2003)
[2] R. Hillenbrand T. Taubner, F. Keilmann, Nature **418**, 159 (2002)
[3] J. Chen et. al., Nature **487**, 77 (2012)
[4] Z. Fei et. al., Nature **487**, 82 (2012)
[5] P. Li, T. Taubner, ACS Nano **6**, 10107 (2012)
[6] J. B. Pendry, Phys. Rev. Lett. **85**, 3966 (2000)
[7] N. Fang et al., Science **308**, 534 (2005)
[8] T. Taubner et al., Science **313**, 159 (2006)
[9] P. Li et. al., Nano Lett. **14**, 4400 (2014)
[10] P. Li et al. Nature Communications, **6** (2015) doi:10.1038/ncomms8507

Cylindrical Imaging System Based on a Mechanical Flexible CMOS Image Sensor

J. Häfner and W. Mokwa

Institute of Materials in Electrical Engineering I, RWTH Aachen University, Germany

Based on the desire for increasingly compact and powerful electronic devices not only the feature sizes but also the chip thicknesses are reduced. This allows for the reduction of the device area by stacking of multiple ICs on top of each other [1]. Furthermore, chip thinning is a prerequisite for the integration of ICs in low profile electronic products like smart cards or smart labels [2]. In addition to the obvious space savings thin silicon offers entirely new applications. The normally brittle material shows a remarkable mechanical flexibility when its thickness is reduced to below 30 µm. The use of curved silicon based focal plane arrays for the compensation of the field of curvature that is inherent in simple lens optics is subject of recent studies [3, 4]. However, the mechanical flexibility of thinned CMOS image sensors enables totally new image acquisition systems that could be used in endoscopy, for example. This is achieved by mounting the flexible sensor IC on a cylindrical surface (Fig. 1). Classical single aperture optics are not suitable so a multi aperture optic similar to the compound eyes of insects is employed.

The image sensor is a commercially available CMOS sensor with 1280x960 active pixels with a pixel size of 3.75 µm and a fully digital interface. The die size is approximately 8 mm x 8 mm. For the thinning process the sensor dice are attached with their front sides to a glass carrier using a cyanoacrylate adhesive. Dummy dice are placed next to the sensor dice to protect the edges from chipping.

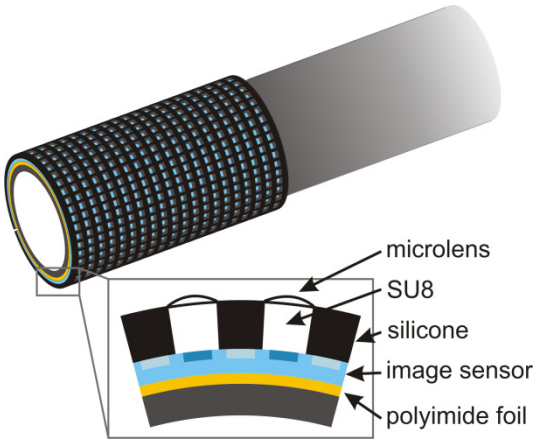

FIG. 1: Concept of a cylindrical bent image sensor incorporating a compound eye optic

Thinning is achieved by mechanical lapping, reactive ion etching and a final chemical mechanical polishing step leading to a chip thickness of approximately 25 µm. After the thinning process the chips are detached from the carrier substrate by dissolving the adhesive in acetone. Electrical connection and mechanical support of the sensor is achieved by embedding the thinned chip in a polyimide foil. PI-2611 (HD MicroSystems) is used as the precursor. Layers of a final thickness between 3 µm and 8 µm can be achieved by spin coating, photolithographic patterning and curing in an inert gas oven. The process, which is carried out on a 4” silicon wafer, is depicted in Fig. 2.

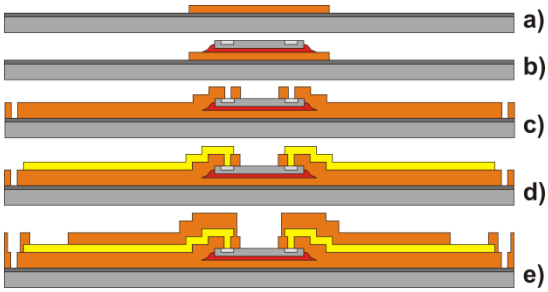

FIG. 2: Embedding of a thinned CMOS image sensor in a polyimide foil. a) first PI layer on aluminum sacrificial layer, b) die attach of image sensor, c) application of second PI layer, d) electroplating of gold conductors, e) application of third PI layer

Firstly a base layer of polyimide is created on top of a sacrificial layer of aluminum (Fig. 2a). Secondly the thin chip is glued on top of the base layer (Fig. 2b) using Cyclotene 3022-46 (Dow Chemical Company), a benzocyclobutene (BCB) based polymer that, in contrast to polyimide, does not produce any volatile byproducts during cure. These byproducts are trapped under the silicon chip and lead to voids in the adhesive layer and severe buckling of the chip. Additionally, BCB withstands the high temperatures used for curing the following polyimide layers. Thirdly the second layer of PI-2611 is spin-coated, patterned and cured (Fig. 2c). Electrical connection is provided by electroplating gold conductors on top of an e-beam evaporated seed layer of chromium-gold (Fig. 2d). Before thinning the aluminum pads of the sensor IC had been treated with electroless nickel-gold to provide an oxide-free surface and thus a good electrical contact. Lastly, the conductors are isolated by a third layer of polyimide (Fig. 2e). The

chip-in-foil is separated from the carrying wafer by etching the sacrificial layer in hydrochloric acid resulting in a very flat and bendable package shown in Fig. 3.

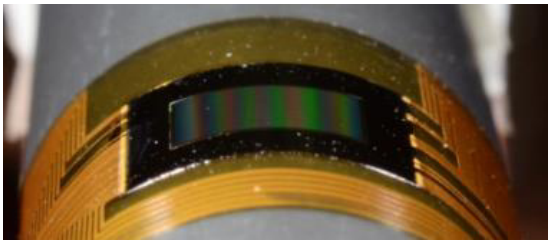

FIG. 3: Functional image sensor (thickness: 25 µm) integrated in polyimide foil. It is bend around a cylinder (radius: 7 mm) to demonstrate its flexibility.

For an imaging system it is crucial that every photodetector samples only a small and distinct solid angle. In the presented imaging system this is achieved by using a microlens as a focusing element for each photodiode (Fig 4). The combination of the photodetector and its associated optical system is called an ommatidium [5]. Light not hitting the lens along its optical axis is focused away from the photodiode and consequently not detected. The optical layers are created on top of the sensor IC after encapsulation in polyimide but before etching the sacrificial layer. The transparent light guiding pillars are made of the mechanically and chemically stable negative photoresist SU-8 by spin coating and photolithographic patterning. The gaps between the pillars are filled with a carbon black filled silicone. The carbon black reduces optical crosstalk between adjacent ommatidia and the low Young's modulus of silicone provides for the necessary mechanical flexibility.

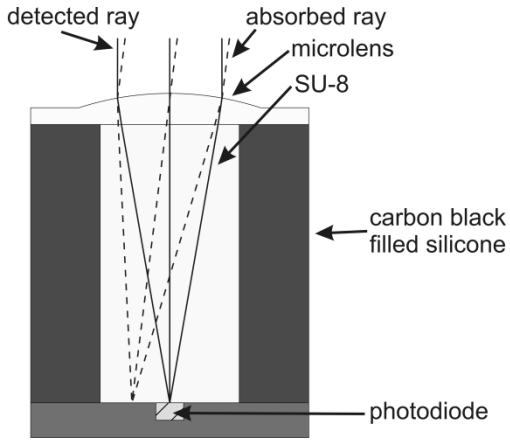

FIG. 4: Working principle of an artificial ommatidium.

The microlenses are fabricated by imprint lithography. A positive mold is made by patterning small discs in the photoresist AZ9260 (AZ Electronic Materials) which is subsequently molten so that spherical caps are formed because of surface tension (Fig. 5a). The influence of design parameters on the microlens radius and the reproducibility of the reflow process have been investigated.

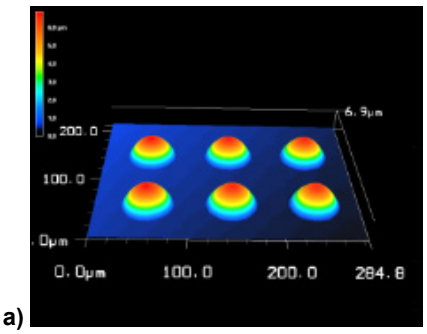

a)

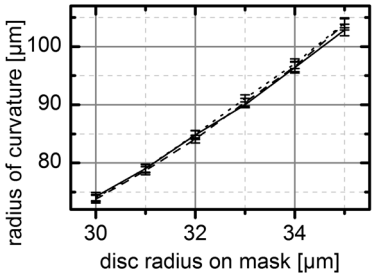

b)

FIG. 5: Microlenses made by reflow of photoresist. a) confocal laser scanning microscope image b) reproducibility of reflow process

Fig. 5b shows the dependence of the lenses' radius of curvature on the radius of the discs on the lithography mask for three different wafers. The standard deviation of the radius of curvature was observed to be below 1.1 µm. Molding is carried out in a mask aligner MA6/BA6 with nanoimprint lithography option (Süss Microtec AG). The gap between a glass substrate and the positive mold is filled with the hybrid polymer OrmoStamp (micro resist technology GmbH) and polymerization is initiated by UV radiation to form a negative mold. This mold is then used in the same fashion to produce micro lenses made of OrmoComp (micro resist technology GmbH) on top of the SU-8 pillars.

This work was supported by a research grant provided by the German Research Foundation (DFG) under contract No. MO 781/9-2.

[1] S. K. Pienimaa, J. Valtanen, R. Heikkila, and E. Ristolainen, 51st Electronic Components and Technology Conference, p. 361 (2001)

[2] M. Feil, C. Adler, D. Hemmetzberger, M. Konig, and K. Bock, 54th Electronic Components and Technology Conference, p. 35 (2004)

[3] K. Itonaga, T. Arimura, K. Matsumoto et al., 2014 IEEE Symposium on VLSI Technology, p. 1 (2014)

[4] O. Iwert, D. Ouellette, M. Lesser, and B. Delabre, SPIE Astronomical Telescopes + Instrumentation, p. 84531W. (2012)

[5] J. Duparré, P. Dannberg, P. Schreiber, A. Bräuer, and A. Tünnermann, Appl. Opt. **43**, 22, 4303, (2004)

Plasma oxidation of thin metal layers on GaN-based heterostructures

H. Hahn[1], B. Pécz[2], A. Kovács[3], M. Heuken[1,4], H. Kalisch[1], and A. Vescan[1]

[1] GaN Device Technology, RWTH Aachen University, Germany
[3] MTA TTK MFA, Budapest, Hungary
[4] Ernst Ruska-Centrum and Peter Grünberg Institut-5, Forschungszentrum Jülich, Germany
[5] AIXTRON SE, Herzogenrath, Germany

Devices on the basis of group III-nitride heterostructures are currently considered to replace Si-based IGBTs and MOSFETs for power-switching applications. Since enhancement mode behaviour is a must, gate current suppression under forward-bias is required in such devices. Consequently, the insertion of an oxide between gate contact and semiconductor plays a pivotal role. To maintain e-mode behaviour whilst reducing gate leakage, the plasma oxidation of thin metal layers has appeared to be an appropriate method. In this study, plasma-oxidised metal layers on top of group III-nitrides heterostructure are investigated in terms of structural properties. Polycrystalline appearance together with smooth interfaces is observed, and the incorporation of oxygen is identified only in the gate metal.

GaN-based devices are currently seen as promising candidates for the use in circuits for power-switching applications [1]. Among the prerequisites for a successful utilisation of such devices are low leakage currents. With enhancement mode (e-mode) being a second prerequisite [1], this can be fulfilled most appropriately by using an oxide in between the commonly used gate metal and the semiconductor. However, in GaN devices, an oxide very often leads to a negative shift in threshold voltage (V_{th}) [2], rendering the device from e-mode back to depletion mode (d-mode). To mitigate this effect, plasma-oxidation has recently been found as a viable method [3,4]. Although the reported results are promising, the data has been limited to electrical characterisation. Hence, structural analysis of the plasma-oxidised layers is in the focus here. Electrical characterisation of the discussed layers is available in [5].

The heterostructures used in this work were grown on a 6" Si substrate in an AIXTRON SE planetary reactor. On top of a GaN buffer, a thin AlN spacer layer and a 20 nm thick $Al_{0.26}Ga_{0.74}N$ barrier layer were deposited.

In this study, two samples are discussed for which the cross sections are shown in Fig. 1. The samples were first fully covered with either 4 nm Al or 3 nm Zr. These layers were subsequently oxidised in an inductively-coupled plasma reactive ion etch (ICP-RIE) tool. This was ensured by a pure oxygen plasma (30 sccm O flow rate) for 10 min under high pressure (13.3 Pa) with a DC bias of -55 V and -90 V for the Al and Zr sample, respectively. Thereafter, a Ni/Au electrode was deposited on top of the plasma-oxidised layers, and the full stacks were finally annealed for 10 min at 600 °C.

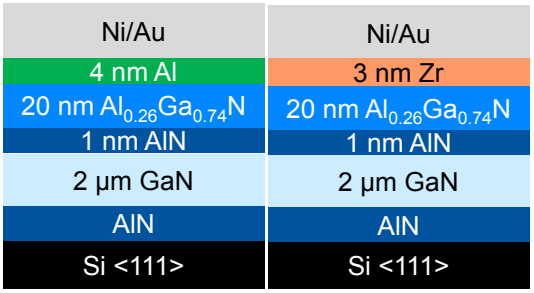

FIG. 1: Final layer stack of the epitaxially grown structure together with the plasma-oxidised layer stack [4 nm Al (left), 3 nm Zr (right)] and ohmic as well as gate contact.

The characterisation of the stack was performed by transmission electron microscopy (TEM) and energy dispersive X-ray spectroscopy (EDX). For TEM analysis, the specimens were prepared by mechanical polishing and Ar ion milling.

The samples with plasma-oxidised Al and Zr layer were first analysed by TEM. A TEM micrograph of the sample with Al is shown in Fig. 2 a). The AlGaN barrier of the heterostructure is visible in the lower part of the image. Above, the oxidised Al layer (marked with AlO_x) is clearly visible. The AlOx layer appears to be polycrystalline. A quite homogeneous interface to the AlGaN barrier is also observed. An interface roughness of only a single atomic layer is present. The upper interface is slightly less well defined (two atomic steps). The thickness of the AlO_x layer is extracted to be 5.5 nm.

A TEM micrograph of the sample with the thin plasma-oxidised Zr film is presented in Fig. 2 b). Again, the oxidised layer appears to be polycrystalline. However, at the interface to the barrier, a very thin layer is detected which is poorly ordered and possibly amorphous. Furthermore, the amorphous parts appear to be present in an island-like structure.

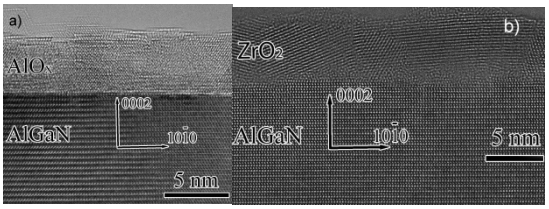

FIG. 2: Aberration-corrected high-resolution TEM micrograph of the sample with the plasma-oxidsed (a) Al and (b) Zr layer [5].

In between these islands, polycrystalline parts are also visible. As a result, the interface of the ZrO_2 layer to AlGaN is not as sharp as in the case of AlO_x. The total thickness of the layer is extracted to be 6.0 nm.

To evaluate the penetration depth of oxygen into the barrier and also secondary effects, EDX analysis was performed on both samples. Exemplarily, the result for the sample with the plasma-oxidised Zr layer is shown in Fig. 3. In Fig. 3 a), a darc field scanning TEM (STEM) micrograph is shown. Apparently, the Au layer is beneath the Ni layer. This is related to the TEM preparation and can be excluded for samples which were prepared for full device characterisation [5]. In Figs. 3 b) and c), a clear distinction between Au film and Ni film is visible. Hence, no intermixing occurred. As visible in Fig. 3 d), oxygen is strongly present both in the Zr layer (thin layer) as well as in the Ni layer. Hence, during thermal annealing, part of the oxygen moved from the Zr layer into the Ni layer, leading to a formation of NiO. Moreover, oxygen does not move into the barrier, as can be seen from the lowest part of Fig. 3 d). The few dots visible are related to a background impurity concentration in MOCVD layers [6].

C-V characteristics of fully processed samples (details in [5]) are shown in Fig. 4. Compared to the Schottky-gated reference (no plasma-oxidised layer), both the sample with Al and Zr show a

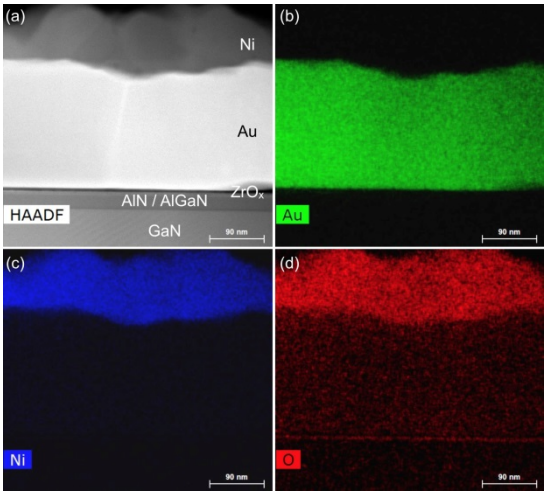

FIG. 3: a) High-angle annular dark field (HAADF) scanning TEM (STEM) micrograph of sample Zr and elemental maps for b) Au, c) Ni, and d) O extracted from EDX analysis [5].

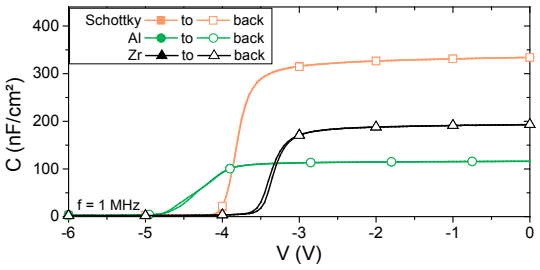

FIG. 4: C-V curves of Schottky-gate reference and the two samples with plasma-oxidised metal layers. After [5].

largely reduced on-state capacitance. This large reduction is partly related to the oxidised Ni which was observed in Fig. 3. Most importantly, for sample Zr, a positive shift in V_{th} (0.5 V) compared to the Schottky-gated reference is obtained. This positive shift is further without any significant hysteresis. Hence, plasma oxidation of Zr presents a viable approach to allow for fabrication gate-insulated e-mode devices.

In summary, plasma-oxidised metal layers on group III-nitride heterostructures have been evaluated. Polycrystalline appearance has been found for both the sample with Al layer and the sample with Zr layer. For both samples, sharp interfaces have been identified. It has further been found that during annealing oxygen diffuses into the Ni gate electrode and leads to its oxidation. Apart from a background impurity concentration, the presence of oxygen in the barrier can be excluded.

The Hungarian National Scientific Research Fund (OTKA) supported this work through Grant No. K108869. The authors acknowledge financial support from the European Union under the Seventh Framework Program under a contract for an Integrated Infrastructure Initiative. Reference 312483 – ESTEEM2.Financial support by the DFG is acknowledged.

[1] N. Ikeda, Y. Niiyama, H. Kambayashi, Y. Sato, T. Nomura, S. Kato and S. Yoshida, Proc. IEEE, **98**, 1151-1161 (2010).

[2] S. Ganguly, J. Verma, G. Li, T. Zimmermann, H. Xing, and D. Jena, Appl. Phys. Lett., **99**, 193504 (2011).

[3] H. Hahn, A. Alam, M., Heuken, H. Kalisch, and A. Vescan., Semicond. Sci. Technol., **27**, 062001 (2012).

[4] H. Hahn, H. Behmenburg, N. Ketteniss, M. Heuken, H. Kalisch, and A. Vescan, Phys. Status Solidi C, **10**, 840-843 (2013).

[5] H. Hahn, B. Pécz, A. Kovács, M. Heuken, H. Kalisch, and A. Vescan, submitted to J. Appl. Phys.

[6] D. D. Koleske, A. E. Wickenden, R. L. Henry and M.E. Twigg, J. Cryst. Growth, **242**, 55-69 (2002).

An Explosive Graphene-like Material from Copper and Nitrogen: β-CuN_3

X. Liu, J. George, S. Maintz, and R. Dronskowski

Institute of Inorganic Chemistry, RWTH Aachen University, Germany

The highly energetic phase CuN_3 has been around for many decades but there is a so far unknown ground-state polymorph, dubbed β-CuN_3, which crystallizes in the orthorhombic space group *Cmcm* and adopts a layered structure resembling graphite with layers similar to graphene. Within the heterographene layers, one finds hexagonal rings if one considers the complex azide anion as one structural unit. Copper and nitrogen atoms are covalently bonded with Cu–N between 1.91 and 2.00 Å, and the azide group is linear with N–N = 1.14 and 1.20 Å. Both density-functional calculations and experimental thermochemistry clearly show that the new polymorph is more stable than the previously reported one. In addition, the new copper azide is the thermochemical ground-state according to the calculated phonon density of states. As expected for such a material, β-CuN_3 exhibits negative thermal expansion within the heterographene layers.

Nitrogen-rich materials such as azides are known to the wide public as important energetic materials [1,2]. For example, there is the well-known copper(I) azide, α-CuN_3, which is even more sensitive to heat and impact than the notorious lead azide, another classic explosive stuff. Probably because of its high sensitivity copper(I) azide was never used as an energetic material but there is an early crystal-structure report shortly after WW II [3]; since then, more experiments on copper azide have been avoided like the plague. With respect to its outstanding crystal structure, α-CuN_3 is a beautiful example of a three-dimensional network between monovalent copper and azide groups oriented along the body diagonal in a tetragonal cell. The copper atoms experience a distorted planar coordination by four azide units, and vice versa, with Cu–N between 2.23 and 2.30 Å and a linearly shaped azide ion with N–N = 1.17 Å. Such interatomic distances can be easily transformed (using a hand-held calculator) into an empirical bond-valence sum for the copper atom which arrives at a value of 0.7, seemingly a bit too small for monovalent copper. Despite this discrepancy, this phase has been regarded as the ground state of CuN_3 for more than half a century.

Nonetheless, there is another phase with the composition CuN_3, and just a tiny but nonetheless important synthetic improvement is needed to obtain it in phase-pure form [3]. First of all, caution is strongly advised in all experiments. The bold chemist first reduces Cu^{2+} to Cu^{+} using Na_2SO_3 and then adds NaN_3; filtering and washing leads to the well-known α-CuN_3 which already converts into another crystal structure by staying in the mother solution for a few days. The direct synthesis of the new β-CuN_3 proceeds via a brown, somewhat mysterious precipitate that results from mixing a Cu(II) salt and NaN_3 solution; upon adding Na_2SO_3, one finds to a mixture of α-and β-CuN_3 which slowly but steadily transforms into phase-pure β-CuN_3, easily distinguishable from α-CuN_3 by means of X-ray powder diffraction (XRD) due to strongly differing Bragg reflections.

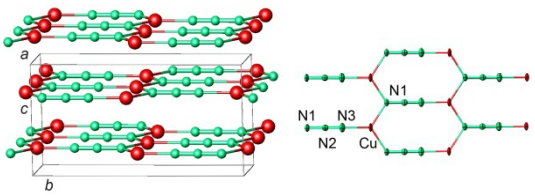

FIG. 1: The crystal of β-CuN_3 adopting a graphite-like layered structure with an inter-layer distance of 2.78 Å (left) and the Cu–N coordinations within the layer drawn with thermal ellipsoids at the 90% level (right). Reproduced from Ref. [4]. © 2015 Wiley-VCH Verlag GmbH & Co. KGaA, Weinheim.

A single-crystal X-ray study of β-CuN_3 yields the orthorhombic space group *Cmcm* with *a* = 3.4, *b* = 10.7, *c* = 5.6 Å and *V* = 199 $Å^3$. The structure as shown in Fig. 1 is composed of infinite heterographene-like layers made from monovalent Cu and azide anions arranged in the form of perfectly planar 10-membered hexagons. These layers are stacked along *c* according to an *ABAB* pattern such that Cu and N_3^- ions from alternating planes align with each other, as seen before for the carbon ground-state allotrope graphite. The distance between the layers is rather short, namely 2.78 Å; in turn, the density of β-CuN_3 comes out about 8% larger than the one of α-CuN_3. Because of the proximity to graphite or graphene, one finds a triangle-like coordination of Cu(I) by the azide units, with three Cu–N bonds between 1.91 and 2.00 Å. Indeed, such short bonds indicate a stronger covalent bonding, and Cu(I) now has a larger bond-valence sum of 1.1, just as expected. Also, the N_3^- group is still linear but differs in the N–N bonds which are 1.14 and 1.20 Å.

Electronic-structure theory of the density-functional type at the PBE+D3/PAW level of theory reproduces the structural details pretty well, with a maximum deviation of about 1–2.5 % for the individual bonds. In addition, the theoretical phonon densities of states (PDOS) exhibit many

imaginary modes for the well-known α but not for the β phase. Thermochemically speaking, β-CuN_3 is hence theoretically identified as the ground-state phase. Why, then, has α-CuN_3 been ever isolated in crystalline form? We re-iterate that electronic-structure theory shows that the α → β transformation occurs at any temperature. Also, it is somewhat unexpected that the HSE06 functional yields a narrower band gap of 2.4 eV for the more stable β-CuN_3 instead of 3.4 eV for α-CuN_3. Nonetheless, theory is in harmony with experiment since β-CuN_3 crystals appear as slightly grey while those of α-CuN_3 are colorless. Thus, both theory and experiment indicate that the more stable polymorph has the smaller band gap.

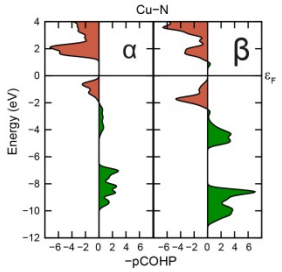

FIG. 2: Projected COHP curves of the shortest Cu–N interactions in α- and β-CuN_3 based on the PBE functional. Reproduced from Ref. [4]. © 2015 Wiley-VCH Verlag GmbH & Co. KGaA, Weinheim.

Chemical-bonding analysis, now so easily done using the projected Crystal Orbital Hamilton Population (pCOHP) technique [5,6], shows the reason for the different stabilities of α- and β-CuN_3. Everything boils down to the nearest Cu–N bonds in both compounds (Fig. 2), namely the four shortest Cu–N bonds in α-CuN_3 and the three shortest Cu–N bonds in β-CuN_3. It is not surprising at all that both explosive phases exhibit antibonding Cu–N interactions below the Fermi level, characteristic for an unfortunate bonding situation. Because of the shorter Cu–N bonds in β-CuN_3, however, its electronic dispersion is wider such that the shorter bonds are also more covalent, as guessed by any trained chemist. Numerical integration of the band-structure energy also shows that the Cu–N bonds in β-CuN_3 are more than twice as strong than in α-CuN_3, such that the classic bond-valence argument is fully corroborated. We believe that both the imaginary phonon frequencies and the structural instability of α-CuN_3 is a consequence of the weaker Cu–N interactions.

Differential scanning calorimetric (DSC) measurements were utilized to determine the enthalpy difference between α- and β-CuN_3 although thermochemical experiments on explosives are anything but trivial. As expected, both compounds start to decompose very energetically to Cu metal and nitrogen gas around 150 °C, and the excess enthalpy is larger by 35 kJ mol^{-1} for α-CuN_3 in comparison to β-CuN_3. Indeed, the α phase is less stable.

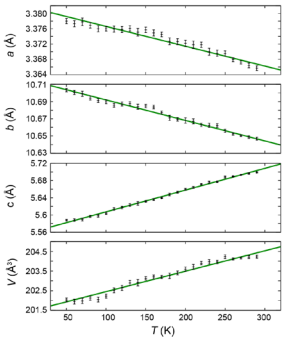

FIG. 3: Course of the temperature-dependent lattice parameters and volume of β-CuN_3 measured by powder XRD. Reproduced from Ref. [4]. © 2015 Wiley-VCH Verlag GmbH & Co. KGaA, Weinheim.

Because of the structural proximity to graphite and graphene, the thermal-expansion coefficients were determined based on XRD data between 50–290 K. Only the lattice parameter *c* increases upon heating while *a* and *b* shrink almost linearly (Fig. 3); the volume, however, expands just a bit. The resulting thermal coefficient along *c*, for example, is more than twice as large if compared to the structurally closest graphite, and the weak stacking interaction is reflected in the expansion of *c* upon heating. On the other side, β-CuN_3 exhibits a negative thermal expansion (NTE) solely within *ab*, namely where the covalent and rigid N–N bonds are aligned. This also resembles the behavior of layered structures such as graphite and boron nitride but it is clearly more pronounced than in graphite.

In summary, phase-pure β-CuN_3 was synthesized, and its fascinating crystal structure, energetics and NTE behavior were experimentally determined. Theoretical investigations of its thermochemistry and its electronic and vibrational properties manifest that β-CuN_3 is the ground-state of copper(I) azide [4]. One question remains, however: will our physicist friends have enough courage to study its heterographene properties?

[1] T. M. Klapötke, N. Mehta, Propellants Explos. Pyrotech. **39**, 7 (2014)

[2] G. Steinhauser, T. M. Klapötke, Angew. Chem. Int. Ed. **47**, 3330 (2008).

[3] H. Wilsdorf, Acta Cryst. **1**, 115 (1948).

[4] X. Liu, J. George, S. Maintz, R. Dronskowski, Angew. Chem. Int. Ed. **54**, 1954 (2015).

[5] R. Dronskowski, P. E. Blöchl, J. Phys. Chem. **97**, 8617 (1993)

[6] S. Maintz, V. L. Deringer, A. L. Tchougréeff, R. Dronskowski, J. Comput. Chem. **34**, 2557 (2013); see also www.cohp.de

Coexistence of Superconductivity and Ferromagnetism in P-doped $EuFe_2As_2$

S. Nandi[1,2], W. T. Jin[1,2], Y. Xiao[1], Y. Su[2], and Th. Brückel[1,2]

[1] Jülich Centre for Neutron Science-2 and Peter Grünberg Institute-4, Forschungszentrum Jülich, Germany
[2] Jülich Centre for Neutron Science at Maier-Leibniz-Zentrum, Garching, Germany

The discovery of iron-based superconductors has stimulated tremendous research interests in unconventional high-T_c superconductivity. Among various parent compounds of iron pnictide superconductors, $EuFe_2As_2$ stands out due to the presence of both spin density wave of Fe and antiferromagnetic ordering of the localized Eu^{2+} moments. Superconductivity can be achieved in $EuFe_2As_2$ system by substituting As with P. Combining magnetic and element-specific x-ray resonant magnetic scattering measurements, we conclude that the long-range ferromagnetic order of the Eu^{2+} moments aligned primarily along the *c*-axis coexists with the bulk superconductivity in P-doped $EuFe_2As_2$. A spontaneous vortex state is proposed to explain the coexistence of superconductivity and ferromagnetism in P-doped $EuFe_2As_2$.

Superconductivity and magnetism are two antagonistic phenomena since the superconducting state expels external magnetic flux. Nevertheless, superconductivity in the pnictides and cuprates is always found in close proximity to an antiferromagnetic order and the superconducting pairing is believed to be mediated by the antiferromagnetic spin fluctuations [1]. For a magnetic superconductor with rare-earth moments, several theoretical studies claim that the superconductivity can coexist with several forms of the magnetic states [2], namely, (a) "cryptoferromagnetism" (which is a ferromagnetic state with small domains, smaller than the superconducting coherence length), (b) transverse amplitude modulated collinear antiferromagnetic structure, (c) spiral antiferromagnetic structure, or (d) with a spontaneous vortex state of the magnetic moments. A spontaneous vortex state or a self-induced vortex state is a new state of matter in which the two competing orders, super-conductivity and ferromagnetism, coexist due to the lower free energy of the combined states compared to the individual ones. The pure ferromagnetic state is least preferred. These results clearly show the importance of the alignment for the rare-earth moments in the superconducting samples.

Regarding to the $EuFe_2(As_{1-x}P_x)_2$ system, direct microscopic evidence for the coexistence of superconductivity and ferromagnetism is still lacking. Here, we report on the first element-specific x-ray resonant magnetic scattering studies of the superconducting $EuFe_2(As_{1-x}P_x)_2$ to explore the details of the magnetic structure of the Eu^{2+} moments. Our scattering experiments show that the Eu^{2+} moments order ferromagnetically along the *c*-axis and the ferromagnetic order of the Eu^{2+} moments coexist with the bulk superconductivity [3].

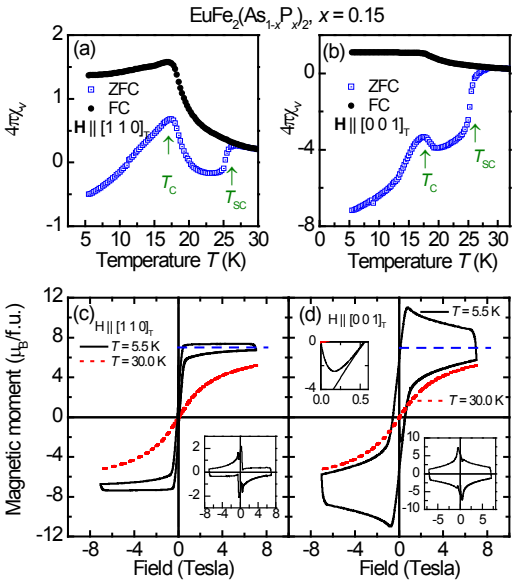

FIG. 1: A and B. Temperature dependencies of the magnetic susceptibility measured on heating of the zero-field cooled and field cooled sample at an applied magnetic field of 1 mT along the crystallographic [1 1 0]$_T$ and [0 0 1]$_T$ directions, respectively. C and D. M-H curves for magnetic fields parallel and perpendicular to the c-axis at T = 5 K and 30 K. Horizontal dashed lines in both figures denote a fully saturated moment of Eu^{2+}. Lower insets for both figures show the hysteresis curves after subtraction of the ferromagnetic contribution. The upper inset of Fig. 1D shows details of the M-H dependence in the low-field region.

Fig. 1 shows magnetic susceptibility and isothermal magnetization of the $EuFe_2(As_{0.85}P_{0.15})_2$ sample, respectively, measured for magnetic fields parallel and perpendicular to the *c*-axis. Zero-field cooled magnetization becomes negative for both field directions at T_{SC} = 25 K, signifying a superconducting transition at this temperature. Upon cooling towards the onset of Eu^{2+} ordering at T_C=19K, the superconducting signal is first weakened, before it becomes more pronounced at temperatures below T_C. Superconductivity wins over the Eu^{2+} magnetism if temperature is lowered further. The diamagnetic volume susceptibility for the magnetic field parallel to the [1 1 0] direction (in this direction demagnetization correction is small) is greater than -0.5 indicating bulk superconductivity. Effective diamagnetic

susceptibility close to -1 for the zero-field cooled curve provides an upper limit of superconducting volume fraction of 100%. Fig. 1C and Fig. 1D show hysteresis loops at T = 5 and 30 K for the two field directions. The observed hysteresis curves look different than a type II nonmagnetic superconductor. However, a jump in magnetization, which is typical for a type-II superconductor, is clearly observed at 7 T magnetic field between the field increasing and decreasing cycles.

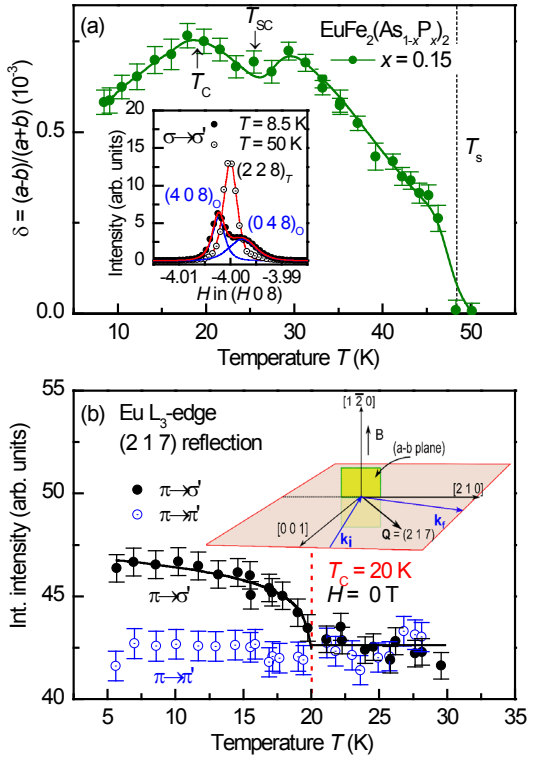

FIG. 2: A. Temperature dependence of the orthorhombic distortion for the $EuFe_2(As_{0.85}P_{0.15})_2$ sample. The inset shows $(\xi\ \xi\ 0)_T$ scans through the $(2\ 2\ 8)_T$ position above and below the structural phase transition. The lines represent fits to the data using either one (red) or two (blue) Lorentzian squared peaks. B. Temperature dependence of the (2 1 7) reflection in both the π→σ' and π→π' scattering geometries at zero field. The schematic shows the used scattering geometry. The inset to Fig. 2A shows a subset of $(\xi\ \xi\ 0)_T$ scans through the $(2\ 2\ 8)_T$ reflection for the 15% doped sample as the sample was cooled through T_S = 49 K. the splitting of the $(2\ 2\ 8)_T$ Bragg reflection into orthorhombic $(4\ 0\ 8)_O$ and $(0\ 4\ 8)_O$ Bragg reflections below T_S is consistent with the structural transition, from space group I4/mmm to Fmmm, with a distortion along the [1 1 0] direction. As the sample is cooled further, the orthorhombic splitting (δ) increases down to T = 30 K as can be seen from Fig. 2A. Near T_{SC}, δ shows a local minimum due to the competition between superconductivity and ferromagnetism.

Below T_C = 20 K, a magnetic signal was observed when the x-ray energy was tuned through the Eu L_3 edge at reciprocal lattice points identical to those of the charge reflections, indicating the onset of the Eu^{2+} magnetic order at the magnetic propagation vector τ = (0 0 0). Fig. 2B depicts the temperature evolution of the (2 1 7) reflection measured at the Eu L_3 edge at resonance energy 6.973 keV. A variation of the magnetic intensity with temperature was only observed in the π→σ' scattering channel, whereas the π→π' scattering channel shows no discernible temperature dependence. The transition temperature is similar to that observed in the parent $EuFe_2As_2$ compound and consistent with the results presented in Fig. 1. For the crystallographic space group *Fmmm* with τ = (0 0 0), only ferromagnetic structures with magnetic moments along the three crystallographic directions *a, b*, *c* are allowed by symmetry. For the π→σ' scattering geometry, the magnetic signal is sensitive to the component of the ordered moment in the scattering plane, i.e., *a/b* and *c* components. For the π→π' scattering geometry, the magnetic signal is sensitive to the component of the ordered moment perpendicular to the scattering plane, i.e., only *a/b* components. Since, no magnetic signal was observed in the π→π' scattering channel at zero field, we conclude that the magnetic moments are aligned primarily along the *c*-axis.

The most important result of the present study is the observation of strong ferromagnetic order of the Eu^{2+} moments coexisting with bulk superconductivity. In the Fe-As based superconductors, it is believed that the superconducting carriers are in the Fe-As layers. To a first approximation, the dipole field due to the Eu^{2+} moments at the Fe-As layers is less than 1 T, which is much less than the superconducting upper critical field H_{C1} but higher than the lower critical field H_{C2}. Since the internal field is between H_{C1} and H_{C2}, it is most likely that the $EuFe_2(As_{1-x}P_x)_2$ is in a spontaneous vortex state.

In summary, the magnetic structure of the Eu moments in superconducting $EuFe_2(As_{0.85}P_{0.15})_2$ has been determined using element specific x-ray resonant magnetic scattering. Combining magnetic and scattering measurements we conclude that the long-range ferromagnetic order of the Eu^{2+} moments aligned primarily along the *c*-axis coexists with the bulk superconductivity. According to our extensive investigations on the $EuFe_2As_2$ system, the coexistence of superconductivity and ferromagnetism seems a common feature for $EuFe_2As_2$ superconductors with different doping elements [4-6]. Additional measurement such as small angle neutron scattering is needed to confirm the existence of a spontaneous vortex state.

This work was supported by a research grant provided by Forschungszentrum Jülich.

[1] D. C. Johnston, Adv. Phys. **59**, 803(2010).

[2] P. W. Anderson et al., Phys. Rev. **116**, 898(1959).

[3] S. Nandi et al., Phys. Rev. B **89**, 014512(2014).

[4] W. T. Jin et al., Phys. Rev. B **88**, 214516(2013).

[5] S. Nandi et al., Phys. Rev. B **90**, 094407(2014).

[6] W. T. Jin et al., Phys. Rev. B **91**, 064506(2015).

Generation of circularly polarized radiation from a compact plasma-based EUV light source for tabletop X-ray magnetic circular dichroism studies

D. Wilson[1,2], D. Rudolf[1,2], C. Weier[3], R. Adam[3], G. Winkler[4], R. Frömter[4], S. Danylyuk[5], K. Bergmann[6], D. Grützmacher[2], C. M. Schneider[3], and L. Juschkin[1,2]

[1] Experimental Physics of EUV, RWTH Aachen University, Germany
[2] Peter Grünberg Institut-9, Forschungszentrum Jülich, Germany
[3] Peter Grünberg Institut-6, Forschungszentrum Jülich, Germany
[4] Institut für Angewandte Physik, Universität Hamburg, Germany
[5] Chair for Technology of Optical Systems, RWTH Aachen University, Germany
[6] Fraunhofer Institute for Laser Technology, Aachen, Germany

Generation of circularly polarized light in the extreme ultraviolet (EUV) spectral region (about 25 eV-250 eV) is highly desirable for applications in spectroscopy and microscopy but very challenging to achieve in a small-scale laboratory. In this spectral range, the 3p absorption edges of Fe (54 eV), Co (60 eV) and Ni (67 eV) offer a high magnetic contrast often employed for magneto-optical and electron spectroscopies as well as for magnetic imaging. We simulated and designed an instrument capable of generating both linearly and circularly polarized EUV radiation and performed polarimetric measurements of the degree of linear and circular polarization. Furthermore, for the first time, we demonstrate measurements of the X-ray magnetic circular dichroism (XMCD) at the Co 3p absorption edge with a plasma-based EUV light source.

Magneto-optical polarization spectroscopy with polarized EUV and soft X-ray radiation provides valuable information about magneto-optical constants and enables studies of element- and layer-selective magnetization [1]. For magneto-optical spectroscopy, both linearly and circularly polarized light is required. In particular, X-ray magnetic circular dichroism (XMCD) is frequently used for magneto-optical and photoemission spectroscopy at the 2p (700 eV–860 eV) and 3p (50 eV–70 eV) absorption edges of Fe, Co, and Ni [1,2].

A straightforward concept for conversion of linearly- to circularly polarized EUV light is to exploit the phase shift between the s– and p-components of light-waves upon reflection from a flat surface. For that purpose, a phase shift of ±90° between the s- and p-components and identical reflectivity for the s- and p-components are required [3]. Laboratory-based instruments for generation of circularly polarized EUV light employ up to four mirrors [3]. Due to the low overall reflectivity (few percent) an intense EUV light source is required to obtain a reasonable photon flux after the polarization conversion.

In our work, we employed an intense gas-discharge plasma-based EUV light source [4] and optimized it for operation above 50 eV photon energy. To linearly polarize the initially unpolarized EUV light and to simultaneously select emission lines around the 3p absorption edge of Co (60 eV), we designed a multilayer Bragg mirror linear polarizer operating close to the Brewster angle [5]. A spectrum behind the Bragg mirror linear polarizer for nitrogen and oxygen gas is shown in Fig. 1 (a). Behind the linear polarizer, we placed a broadband triple-reflection polarizer (consisting of three subsequent mirrors), which covers the 3p absorption edges of Fe, Co and Ni between 50 eV and 70 eV. For a 20 nm Mo layer on a Si substrate, we found the triple-reflection at $20° - 40° - 20°$ grazing incidence to give the highest degree of circular polarization $|p_C|$ of > 0.99 at 60.5 eV. The degree of circular polarization p_C depends on the rotation angle φ_{CP} of the circular polarizer around the beam axis and amounts to $p_C = +1$ (right circular) for a rotational angle of the triple reflection polarizer $\varphi_{CP} \approx 70°$ $(250°)$ and to $p_C = -1$ (left circular) for $\varphi_{CP} \approx 110°$ $(290°)$ at the 3p absorption edges of Fe, Co and Ni. A representative measurement for $\varphi_{CP} = 30°, 70°$ and $330°$ is displayed in Fig. 1 (b). Here, φ_A denotes the analyzer rotation angle around the beam axis. The periodic voltage modulations present for $\varphi_{CP} = 30°$ and $\varphi_{CP} = 330°$ disappear for $\varphi_{CP} = 70°$, *i.e.*, the photodiode signal does not depend on the analyzer angle φ_A. For this rotation angle of the circular polarizer, we efficiently convert linearly to circularly polarized light at 60.5 eV as expected from simulations [5]. From measurements at six different angles φ_{CP}, we derived a maximum value of $p_C = 0.81 \pm 0.15$ for $\varphi_{CP} = 70°$.

As a suitable test sample for our XMCD measurements at the Co 3p absorption edge we

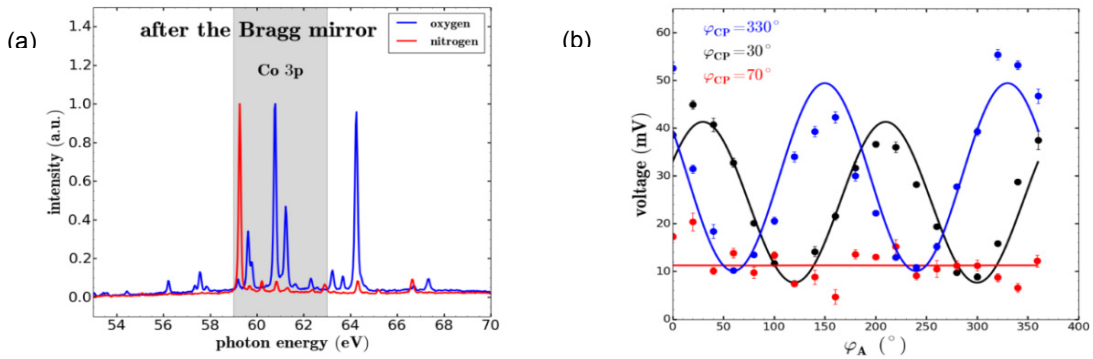

FIG 1. (a) Spectra of highly ionized nitrogen and oxygen plasmas measured directly after the Bragg-mirror linear polarizer for 60.5 eV comprising [Si(9.09 nm)/B_4C(6.06 nm)]$_{50x}$ layers. (b) Measurement of the degree of circular polarization (dots) with emission lines from oxygen around 60.5 eV behind the triple reflection circular polarizer. Solid lines represent fits. The photodiode voltage is shown as a function of the analyzer rotating angle $\boldsymbol{\varphi_A}$ (dots) for different rotation angles $\boldsymbol{\varphi_{CP}}$ of the circular polarizer. For $\boldsymbol{\varphi_{CP} = 70°}$ (red dots), the signal is independent of $\boldsymbol{\varphi_A}$ confirming that the degree of circular polarization is at maximum.

chose [Co (0.8 nm)/Pt (1.4 nm)]$_{16x}$ layers exhibiting a large perpendicular uniaxial anisotropy (see the magnetic hysteresis in the inset of Fig. 2) [6].

We first set the circular polarizer to $\varphi_{CP} = 70°$ ($p_C = +1$), alternately applied ± 320 mT magnetic field and then recorded the transmitted signal $I^{\pm}(\pm 320\,\mathrm{mT})$ on an EUV-sensitive CCD camera for both magnetic fields. The difference of the transmitted intensity averaged over 50 measurements for each magnetic field (10 s or 200 pulses per measurement), is shown in Fig. 2. For the background-corrected XMCD asymmetry A_{XMCD} calculated according to equation

$$A_{XMCD} = \frac{I^{+}(+320\,\mathrm{mT}) - I^{-}(-320\,\mathrm{mT})}{I^{+}(+320\,\mathrm{mT}) + I^{-}(-320\,\mathrm{mT})}, \qquad (1)$$

we obtained $A_{XMCD} = +(2.7 \pm 0.1)\%$. After that, we changed the rotation angle of the circular polarizer to $\varphi_{CP} = 110°$ ($p_C = -1$) and repeated the above described measurement procedure. As expected for the XMCD effect, the difference signal and thus the asymmetry (we measured $A_{XMCD} = -(2.8 \pm 0.1)\%$) keeps the same magnitude as for the other magnetic field direction but changes its sign.

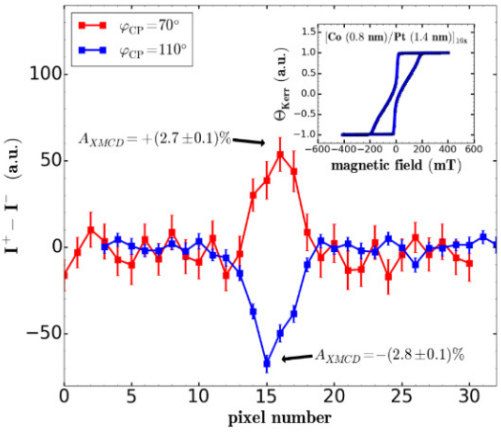

FIG 2. XMCD difference signal $I^{+}(+320\,mT) - I^{-}(-320\,mT)$ as recorded by the CCD camera for $\varphi_{CP} = 70°$ ($p_C = +1$) and $\varphi_{CP} = 110°$ ($p_C = -1$). We note that the graph displays a beam profile including all oxygen spectral lines reflected by the Bragg mirror linear polarizer (Fig. 1 (a)). For the background-corrected XMCD asymmetry, we obtained $A_{XMCD} = +(2.7 \pm 0.1)\%$ and $A_{XMCD} = -(2.8 \pm 0.1)\%$ for different helicities. The inset shows the magnetization curve (Kerr rotation Θ_{Kerr}) of a [Co (0.8 nm) /Pt (1.4 nm)]$_{16x}$ multilayer measured by polar magneto-optical Kerr effect (P-MOKE) with visible light (350 nm wavelength). Using our magnetic yoke with a maximum field of 320 mT the sample can be magnetized to saturation.

In summary, we simulated, designed, and characterized an instrument for generation of circularly polarized EUV light at the 3p absorption edges of Fe, Co, and Ni (50 eV-70 eV) employing a compact gas-discharge plasma-based EUV light source. For the first time in a laboratory-based experiment with a plasma-based EUV light source, we successfully measured the XMCD effect at the Co 3p absorption edge (60.5 eV) [5]. Our work paves the way for element-selective microscopy of ferromagnetic domains in a small-scale laboratory.

We acknowledge financial support by JARA-FIT Seed Funds through the Excellence Initiative.

[1] H.-Ch. Mertins, S. Valencia, A. Gaupp, W. Gudat, P. M. Oppeneer, and C. M. Schneider, Appl. Phys. A **80**, 1011 (2005).

[2] L. Baumgarten, C.M. Schneider, H. Petersen, F. Schäfers, and J. Kirschner, Phys. Rev. Lett. **65**, 492 (1990).

[3] B. Vodungbo, A. Barszczak Sardinha, J. Gautier, G. Lambert, C. Valentin, M. Lozano, G. Iaquaniello, F. Delmotte, S. Sebban, J. Lüning, and P. Zeitoun, Opt. Express **19(5)**, 4346 (2011).

[4] M. Benk and K. Bergmann, J. Micro/Nanolith. MEMS MOEMS **11(2)**, 021106 (2012).

[5] D. Wilson, D. Rudolf, C. Weier, R. Adam, G. Winkler, R. Frömter, S. Danylyuk, K. Bergmann, D. Grützmacher, C. M. Schneider, and L. Juschkin, Rev. Sci. Instrum. **85**, 103110 (2014).

[6] D. Stickler, R. Frömter, H. Stillrich, C. Menk, H. P. Oepen, C. Gutt, S. Streit-Nierobisch, L.-M. Stadler, G. Grübel, C. Tieg, and F. Yakhou-Harris, Phys. Rev. B **84**, 104412(2011).

Hybrid P3HT/Silicon Solar Cells with Power Conversion Efficiency up to 6.5%

M. Weingarten, T. Zweipfennig, A. Vescan, and H. Kalisch

GaN-Bauelementtechnologie, RWTH Aachen University, Germany

Due to their promising features (e.g. easy fabrication in a low-temperature process) hybrid organic/silicon heterostructures have become of great interest for photovoltaic application. This work is focused on hybrid devices based on a flat heterojunction between the polymer poly(3-hexylthiophene-2,5-diyl) (P3HT) and monocrystalline n-doped silicon. Devices with different P3HT thicknesses were processed by spin-casting and compared with an Au/n-Si Schottky diode reference without P3HT. Under illumination, the hybrid devices show a significant increase of open-circuit voltage (V_{OC}) compared to the Schottky diode reference. This indicates that the reverse current into the gold contact is effectively reduced by the P3HT interlayer. On the other hand, the short-circuit current density (J_{SC}) starts to decrease with increasing P3HT thickness indicating a less efficient charge generation in P3HT compared to silicon. For the best performing hybrid devices, power conversion efficiencies (PCE) up to 6.5% are achieved, which is more than twice the PCE of the Schottky reference.

In the field of photovoltaic applications, organic semiconductors (OS) have attracted much interest due to their versatility and low-cost production potential. However, until now they cannot compete with the established crystalline silicon (c-Si) technology, which however is rather expensive due to the high-temperature diffusion process of the p-n junction [1,2]. In this context, hybrid organic/silicon solar cells are an emerging approach, aiming to combine the advantages of both material classes. In these devices, the OS is deposited by a low-temperature process (e.g. spin-casting) on top of an n-doped silicon wafer. The energy barrier at the hybrid interface between the conduction band (CB) of silicon and the lowest unoccupied molecular orbital (LUMO) of the OS blocks the electrons from diffusing into the gold contact and thereby reduces the dark current. This structure is employed to replace the high-temperature p-n junction of a conventional c-Si solar cell [3]. On the other hand, the OS may also contribute to the photocurrent generation leading to a more efficient utilization of the solar spectrum and hence an increased J_{SC} [4].

As OS, the polymer P3HT is used, which was obtained from Sigma Aldrich with a molecular weight of M_n ~ 54000 - 75000. The phosphorous-doped Si wafers with a specific resistivity of 10 – 20 Ωcm were purchased from Siegert Wafer. P3HT was spin-cast from toluene solution onto cleaned Si wafers under ambient conditions. The semitransparent gold top contact (15 nm thickness, 50 – 60% transmittance) and the aluminum backside contact were deposited by electron beam evaporation. Figure 1 shows the device layout and the corresponding energy level diagram of the hybrid P3HT/Si solar cells processed in this work.

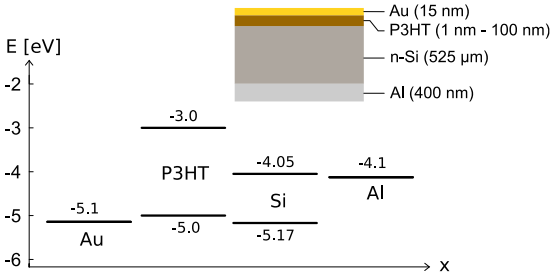

FIG. 1: Device layout (inset) and corresponding energy level diagram [5-7] of the processed hybrid P3HT/silicon solar cells.

In hybrid devices, photocurrent generation is fundamentally different for photons absorbed in the inorganic and in the organic part of the solar cell. A schematic of the different mechanisms is shown in figure 2.

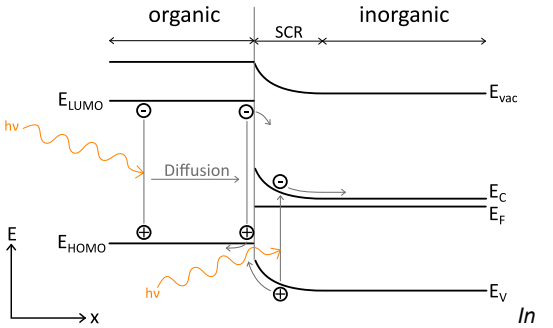

FIG. 2: Schematic drawing of the different charge carrier pair generation mechanisms in hybrid organic/inorganic solar cells.

In inorganic silicon, the photon generates weakly bound excitons, which dissociate at room temperature (RT) and are separated by the electric field of the space charge region (SCR). In contrast, photons absorbed in organic P3HT generate strongly bound excitons which have to diffuse to the organic/inorganic interface to dissociate. Efficient dissociation is possible if the energy difference between the LUMO of P3HT and the CB of silicon is sufficiently large to overcome the exciton binding energy of about 0.6 eV in P3HT [8]. In addition, the magnitude of this energy difference directly affects the electron blocking

properties of the hybrid interface and thereby V_{OC} of the solar cell [9].

Hybrid solar cells with different P3HT thicknesses as well as a Schottky diode reference were processed and characterized by illuminated (AM1.5) current density-voltage (J-V) measurements. The corresponding J-V and PCE characteristics are shown in figure 3.

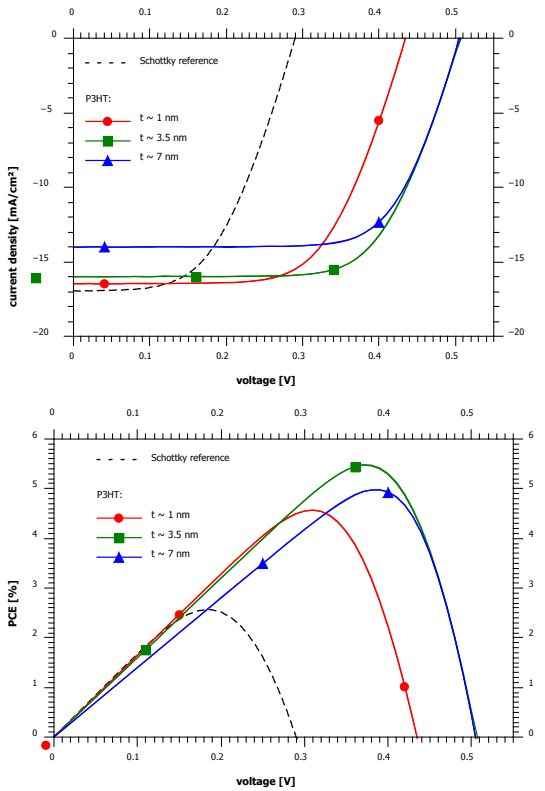

FIG. 3: Illuminated J-V (top) and PCE (bottom) characteristics of hybrid devices with different P3HT thicknesses t and the Schottky diode reference.

For the devices with a thicker P3HT layer, a significant increase of V_{OC} (0.29 V → 0.59 V) compared to the Schottky reference can be identified. This is related to the efficient electron blocking at the hybrid P3HT/Si interface. The lower V_{OC} of the device with 1 nm P3HT can be attributed to a not completely closed film. On the other hand, the J_{SC} of the hybrid solar cells decreases with increasing P3HT thickness. This indicates a less efficient photocurrent generation for photons absorbed in P3HT compared to those absorbed in silicon. Nevertheless, the PCE of all hybrid devices is significantly improved compared to the Schottky reference. For the best performing device with a P3HT thickness of 3.5 nm, a PCE of 5.5% (V_{OC} = 0.50 V, J_{SC} = 16.0 mA/cm², FF = 69%) is achieved. This is more than twice the PCE of the reference device without P3HT (2.6%).

The performance of the hybrid solar cell was further improved by a thermal annealing step. The device with 3.5 nm P3HT was placed on a heating plate at 130 °C for 10 min. under ambient conditions. After cooling down to RT, the solar cell was characterized again. The results are shown in figure 4.

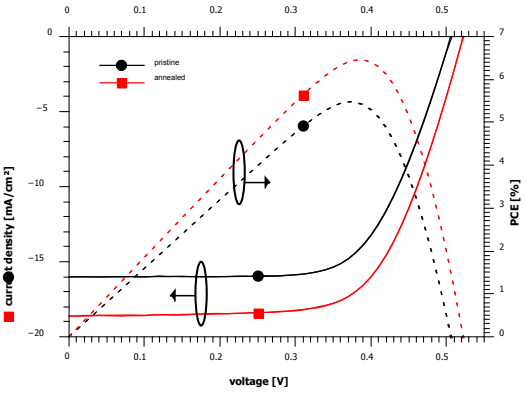

FIG. 4: Illuminated J-V and PCE characteristics of the pristine and annealed hybrid solar cell with 3.5 nm P3HT.

By annealing, J_{SC} of the device is increased by ~ 15% to 18.6 mA/cm² and V_{OC} is slightly increased to 0.52 V. Consequently, the PCE is increased by ~ 18% to 6.5% which is more than 2.5-fold the PCE of the Schottky reference without P3HT. Unlike in all-organic solar cells, the increased J_{SC} cannot be related to an improved mixing of donor and acceptor material, since the hybrid devices are based on a flat heterojunction. In addition, no change in device performance was detected for the Schottky reference. Therefore, we attribute the increased J_{SC} to an improvement of hole transport in P3HT or hole extraction at the P3HT/Au interface.

Regarding the limited transmittance of the top gold contact of 50 – 60%, even higher PCE should be achievable by using more transparent contact materials, e.g. a combination of the conductive polymer poly (3,4-ethylenedioxythiophene)-poly(styrenesulfonate) (PEDOT:PSS) with a thin metal grid.

[1] NREL research cell efficiency records, http://www.nrel.gov/ncpv/.

[2] N. Espinosa, M. Hösel, D. Angmo, F.C. Krebs, Energy Environ. Sci. **5**, 5117 (2012).

[3] S. Avashti, Crystalline-Silicon/Organic Heterojunctions for Solar Photovoltaics, Disseration (2011).

[4] M. Slawinski, M. Weingarten, S. Axmann, F. Urbain, D. Fahle, M. Heuken, A. Vescan, H. Kalisch, Appl. Phys. Lett. **103**, 153305 (2013).

[5] H.B. Michaelson, J. Appl. Phys. **48**, 4729 (1977).

[6] P3HT data sheet from Sigma Aldrich.

[7] S. Kasap, P. Capper, Springer handbook of electronic and photonic materials, (Springer Science & Business Media, 2007).

[8] C. Deibel, D. Mack, J. Gorenflot, A. Schöll, S. Krause, F. Reinert, V. Dyakonov, Physical Review B **81**, 085292 (2010).

[9] 5.S. Avasthi, S. Lee, Y.L. Loo, J.C. Sturm, Advanced Materials **23**, 5762 (2011).

A Direct Band Gap GeSn Laser on Si

S. Wirths, N. von den Driesch, D. Stange, S. Mantl, D. Grützmacher, and D. Buca

Peter Grünberg Institut-9, Forschungszentrum Jülich, Germany

Temperature dependent photoluminescence spectroscopy reveals that partially strain-relaxed $Ge_{0.87}Sn_{0.13}$ exhibits a fundamental direct band gap. We demonstrate lasing for different GeSn compositions in the wavelength range of 2.0 – 2.6 µm under optical pumping up to a temperature of 90 K.

Silicon photonics is the key to overcome current limits in bandwidth and energy consumption associated with metal interconnects on complementary metal-oxide-semiconductor (CMOS) chips [1]. However, despite the progress in the development of the various optical components, such as waveguides, modulators or detectors in a Si-compatible fashion [2], an integrated light source is still missing.

Recently, Ge has gained a lot of attention as material for on-chip lasing due to its CMOS compatibility and its electronic band structure, where the indirect L-valleys lie only approx. 140 meV below the direct Γ-valley. The substitutional incorporation of Sn atoms into the Ge lattice reduces the Γ-valley faster than the indirect valley leading to a transition into a fundamental direct bandgap material. The transition takes place for cubic crystals at a Sn content in the range of 10%. However, epitaxial growth of GeSn layers on Ge or Si substrates leads to large compressive strain in the GeSn alloys that shifts the direct bandgap transition to considerably higher Sn concentrations.

Here we provide direct evidence for the existence of a direct band gap in $Ge_{0.87}Sn_{0.13}$ with a compressive strain of -0.7% on the base of temperature dependent photo-luminescence (PL) measurements. On waveguide structures fabricated on thick GeSn layers, optical gain and unambiguous lasing action has been confirmed under optical pumping up to 90 K [3].

The investigated GeSn layers were grown on Ge virtual substrates using an Aixtron industry-compatible reduced pressure CVD reactor with Ge_2H_6 and $SnCl_4$ as precursors [4]. We studied the PL emission of GeSn alloys with Sn contents ranging from 8% to 13% where the indirect to direct transition is expected to occur. The residual compressive strain in the layers is between -0.4% and -0.7%. Fig. 1 shows the temperature-dependent integrated PL intensity normalized to their emission intensity at 300 K for a set of samples with thicknesses between 200 to 300 nm. Whereas for a $Ge_{0.92}Sn_{0.08}$ sample the direct gap emission vanishes upon cooling (as expected for an indirect semiconductor), the integrated intensity for $Ge_{0.87}Sn_{0.13}$ increases by a factor of 60 by decreasing the temperature to 20 K. This change in emission intensity function of temperature is determined by the alignment of Γ- and L-valleys in the conduction band ΔE, as well as by the increase in carrier lifetime and, hence, in carrier density. Therefore, we calculated the emission intensities with a joint density of states (JDOS) model in a recursive approach, where we assume an identical change in carrier lifetimes for all samples and use the conduction band offset ΔE as the main fitting parameter. The lines in Fig. 1 show the best fits of the experimental results by the JDOS model with the band offsets for the $Ge_{1-x}Sn_x$ alloys with Sn content x and strain (in brackets): 8% (-0.7%), 10% (-0.5%), 11% (-0.4%), and 13% (-0.7%) and ΔE = -80, -10, -5, and 25 meV, respectively. The alloy with x = 13% presents a true fundamental direct bandgap group IV semiconductor with the minimum of the Γ-valley 25 meV below the usually occupied conduction band minimum of the 4 L-valleys.

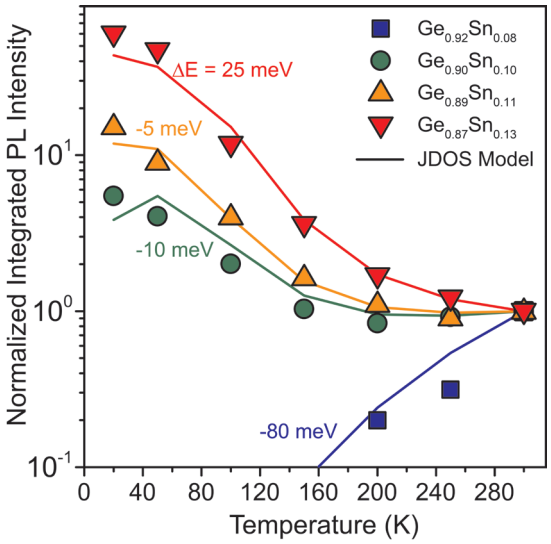

FIG. 1: Integrated PL signal for GeSn alloys with varying Sn content normalized to unity at 300 K. The solid curves show JDOS model fit with the conduction band offset between Γ- and L-valleys as fitting parameter. $Ge_{0.87}Sn_{0.13}$ is found as a direct bandgap semiconductor.

Due to the small difference in refractive index between GeSn and Ge, thick layers are required to ensure sufficient overlap between a guided cavity mode and the GeSn gain material. Hence, a 560 nm thick layer of $Ge_{0.87}Sn_{0.13}$ was grown on Ge, offering 60% mode overlap for the fundamental TE mode. Modal gain values were extracted at 20 K under varying excitation intensities in a 5 µm wide and several mm long Fabry-Perot (FP) cavity via the variable-stripe-length method (VSL). We found a linear dependence of the modal gain on

excitation density with a differential gain of ≈ 0.40 cm/kW and a corresponding threshold density of 325 kW/cm^2.

Fig. 2 right inset shows the emission at 20 K from a 5 µm wide and 2 mm long cavity collected from the facet while pumping over the whole cavity length. The spectra were multiplied by 200 for excitations below 310 kW/cm^2 and offset for clarity. While below 324 kW/cm^2 the emission is broad and weak, the situation changes drastically for excitation densities starting from 324 kW/cm^2. At this threshold density, which agrees very well with the threshold obtained by the VSL method, there is a distinct increase in output intensity (c.f. Fig. 2) accompanied by a clear decrease in emission width (c.f. left inset). Furthermore, the FP modes of 250 µm and 500 µm long cavities have been resolved as an additional proof of lasing action. At an excitation density of 1000 kW/cm^2, lasing could be observed up to 90 K.

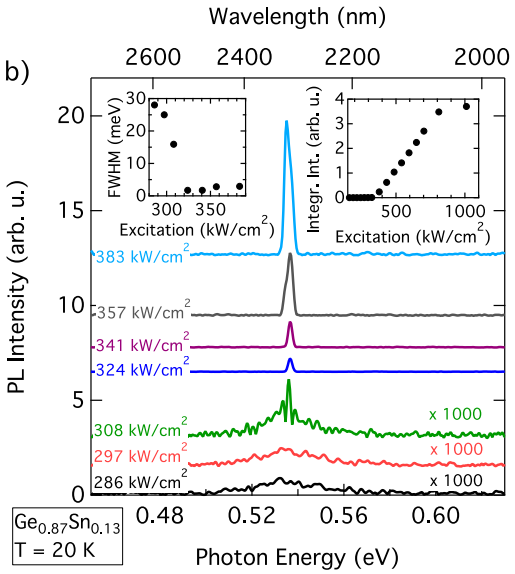

FIG. 2: Emission spectra measured from a 5 µm wide and 2 mm long $Ge_{0.87}Sn_{0.13}$ Fabry-Perot waveguide under optical pumping at 20 K. The spectra show a clear threshold behavior with respect to output intensity (c.f. right inset) and linewidth narrowing (c.f. left inset).

Lasing was demonstrated for different Sn content alloys where the compressive strain was reduced by growing thick, strained relaxed GeSn layers. Fig. 3 shows lasing emission at 20 K from GeSn waveguides with Sn contents from 8% to 14%, showing the potential of GeSn technology for covering the complete short wave infrared range between 2µm to 2.6 µm.

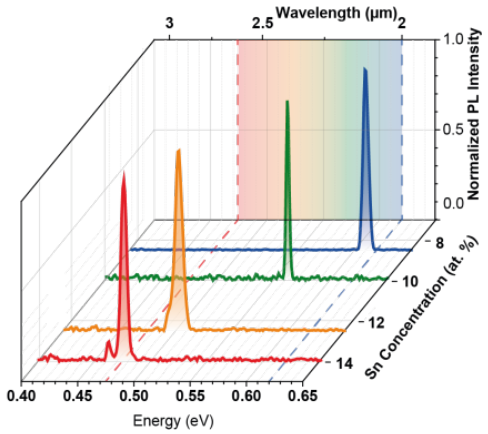

FIG. 3: Emission spectra measured from GeSn Fabry-Perot waveguides under optical pumping at 20 K. The laser emission can be tuned via the Sn content in the alloy.

To decrease the threshold and to enable lasing up to higher temperatures, optimizations of the design regarding surface passivation, n-type doping, and optical mode confinement or carrier injection are future steps for improvements.

In conclusion, we have achieved the first group IV semiconductor with a fundamental direct band gap which exhibits modal gain. Furthermore, we show the proof of lasing at low temperature for a different direct band gap GeSn alloys.

This work was done in collaboration with R. Geiger and Hans Sigg, Laboratory for Micro- and Nanotechnology, Paul Scherrer Institute, Switzerland, J-M- Hartmann, CEA-LETI, France and Z. Ikonic, Institute of Microwaves and Photonics from the University of Leeds, UK.

This research received funding for CVD growth investigations from the European Community's Seventh Framework Programme (grant agreement no. 619509; project E2SWITCH) and the BMBF project UltraLowPow (16ES0060 K).

[1] M. Paniccia and S. Koehl, IEEE Spectrum **42**, 30 (2005).

[2] P. Chaisakul et al. Nat. Photon. **8**, 482 (2014).

[3] S. Wirths, R. Geiger et al., Nat Photon.(2015)

[4] S. Wirths et al. Appl. Phys. Lett. **103**, 192110 (2013).

[5] A. Ghetmiri et al. Appl. Phys. Lett. **105**, 151109 (2014).

Experimental demonstration of planar SiGe TFETs with counter doped pocket

S. Blaeser, S. Richter, S. Wirths, S. Trellenkamp, D. Buca, Q.-T. Zhao and S. Mantl

Peter Grünberg Institut-9 , Forschungszentrum Jülich, Germany

Tunneling field-effect transistors (TFETs) have been suggested as a promising concept for steep slope devices in order to reduce power consumption, but still suffer from low on-currents I_{on} compared to state of the art metal-oxide-semiconductor field-effect transistors (MOSFETs). One approach to encounter this issue is the introduction of small band gap materials like strained SiGe, Ge or (Si)GeSn which results in an enhanced BTBT probability and thus, increased on-current I_{on} while maintaining silicon process compatibility. In this work, we present planar TFETs with compressively strained $Si_{0.45}Ge_{0.55}$ on Si which benefit from a smaller band gap and in parallel, exploit the concept of line tunneling aligned with the gate electric field by introducing a selective and self-adjusted silicidation at the source tunnel junction to enlarge the tunneling area [1]. Additionally, a counter doped pocket at the source tunnel junction is formed in order to further enhance the BTBT probability by sharpening the effective doping profile and thus, the resulting on-current I_{on} [2].

The planar TFETs were fabricated on 5 nm $Si_{0.45}Ge_{0.55}$ pseudomorphically grown on a 15 nm silicon on insulator (SOI) substrate with a 5 nm Si cap [3]. After mesa etching a high-k/metal gate stack consisting of 4 nm HfO_2 and 40 nm TiN was deposited by atomic layer deposition (ALD) and atomic vapor deposition (AVD) respectively. The gate stack was patterned by reactive ion etching (RIE) and selective wet chemical etching. Boron ions were implanted at a tilt angle of 45° and 135° respectively in order to form a p-doped drain and p-doped pocket directly underneath the gate. Dopant activation of drain and pocket was carried out at a low temperature of 500 °C isn order to sustain the compressive biaxial strain in the SiGe layer. Afterwards, the SiGe layer at the source side was etched by RIE, followed by metal deposition of 6 nm Co and 10 nm Ti. Thereby, the Ti cap served to prevent the Co layer from oxidizing during the following silicidation carried out at 500 °C in forming gas to form CoSi. The use of Co instead of Ni enables the Co to encroach under the gate along the SOI substrate without reaction to the SiGe and thus to increase the tunneling area [4]. Finally, Phosphorus ions were implanted at a tilt angle of 135° into the CoSi/Ti stack, followed by an anneal at 500 °C to drive out the dopants from the CoSi into the SiGe layer and thus form a n^+-p tunnel junction with sharp doping profile and high doping level directly underneath the gate. Fig. 1 shows a schematic of the device with a scanning electron microscope (SEM) image as inset.

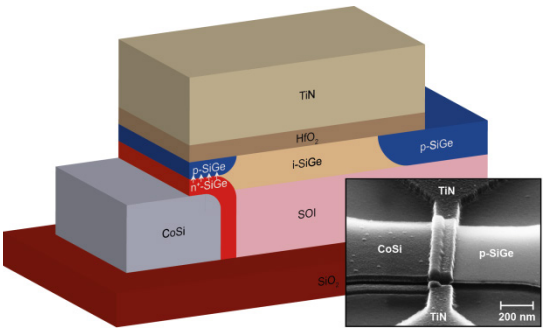

FIG. 1: Schematic of a planar TFET with compressively strained $Si_{0.45}Ge_{0.55}$ on Si. The n^+-p tunnel junction at the source is coloured in red and blue respectively. The inset shows a SEM image of a processed device.

In order to investigate the influence of the counter doped pocket on the device performance, reference samples without pocket implantation have been fabricated in parallel to devices with pocket implantation. The resulting transfer characteristics of the p-type devices without and with counter doped pocket and two different source doping levels are shown in Fig. 2 a). The transfer characteristics reveal a by one order of magnitude increased on-current I_{on} by introducing a counter doped pocket. Also, the off-current I_{off} decreases due to the n^+-p tunnel junction formation, resulting in an overall improved I_{on}/I_{off} ratio as well as in a reduced SS of ~100 mV/dec with counter doped pocket compared to ~200 mV/dec without it. Increasing the implantation dose for the source doping from $2x10^{15}$ cm^{-2} to $5x10^{15}$ cm^{-2} improves the on-current I_{on} by half an order of magnitude as well. Additionally, the ambipolar switching of the planar TFET with counter doped pocket is more suppressed compared to the case without counter doped pocket. The resulting output characteristics for the planar TFET with counter doped pocket and a source doping of $5x10^{15}$ cm^{-2} are shown in Fig. 2 b). They exhibit a good saturation as well as a linear onset of the drain current I_d. In this regard, a linear onset of the drain current I_d compared to a superlinear onset is an indication for a sufficiently high doping level at the source tunnel junction.

In addition, TCAD simulations with Sentaurus Device have been performed in order to analyse the device characteristics discussed above [5]. Fig.

3 shows the hole band-to-band (hBTB) generation rate of a planar TFET (a) without and (b) with counter doped pocket at a doping concentration of $5x10^{19}$ cm^{-3}. The corresponding (c) band structure

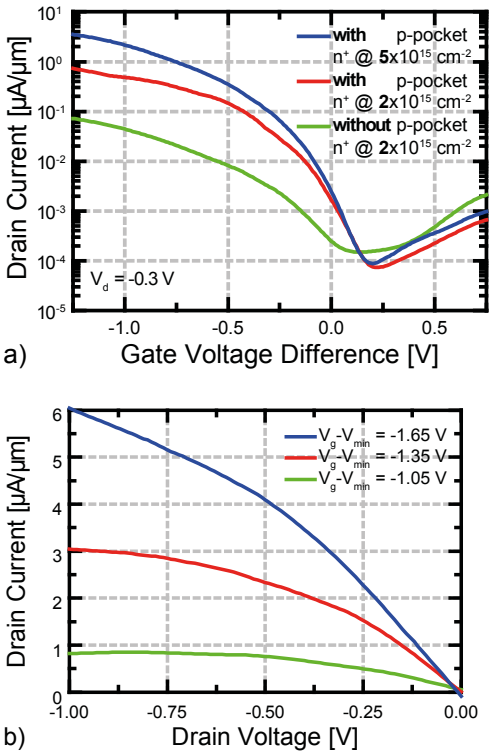

FIG. 2: (a) Measured transfer characteristics of a planar TFET without and with counter doped pocket for two different source doping levels. (b) Measured output characteristics of a planar TFET with counter doped pocket which reveal a good saturation as well as a linear onset of the drain current I_d.

for each device in direction perpendicular to the gate along a cutline is also depicted. The bending of both the conduction and the valence band in direction perpendicular to the gate defines the hBTB generation rate and consequently, the on-current I_{on} of the device. For the case of the planar TFET with counter doped pocket this bending is stronger compared to the reference device which results in a shorter tunneling length and in a one order of magnitude higher hBTB generation. Hence, the counter doped pocket helps to sharpen the doping profile of the source and enables line tunneling aligned with the gate electric field to a region directly underneath the gate.

In summary, planar TFETs using compressively strained $Si_{0.45}Ge_{0.55}$ on Si and a counter doped pocket at the source tunnel junction were fabricated, electrically characterised and analysed by TCAD simulations. The counter doped pocket in combination with a selective and self-adjusted silicidation enables line tunneling aligned with the gate electric field which results in an enhanced BTBT probability and higher on-current I_{on}.

This work is partially supported by the BMBF project UltraLowPow (16ES0060K) and the European project E2SWITCH.

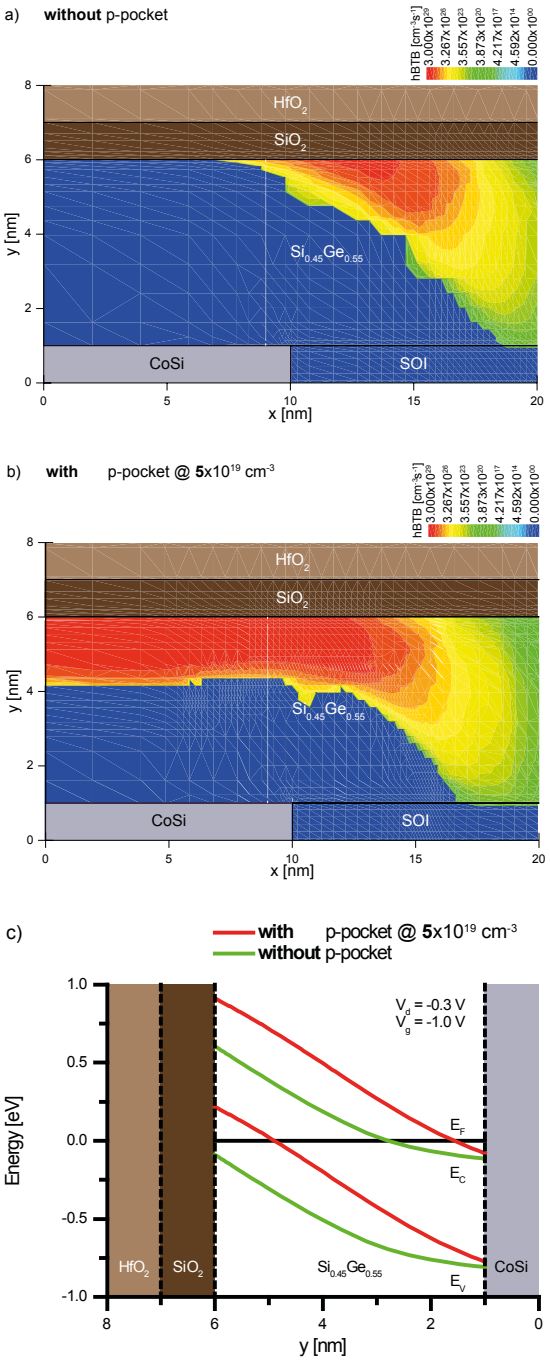

FIG. 3: Contour plot for a planar TFET (a) without and (b) with counter doped pocket showing hBTB generation at the source tunnel junction. The corresponding (c) band structure for both cases in direction perpendicular to the gate along a cutline indicated in each contour plotis also depicted.

[1] W. G. Vandenberghe et al., *SISPAD 2008*, pp. 137-140 (2008).

[2] K.-H. Kao et al., *IEEE Transactions on Electron Devices*, **59**, no. 8, pp. 2070-2077 (2012).

[3] S. Wirths et al., *Solid-State Electronics*, **83**, pp. 2-9 (2013).

[4] B. I. Boyanov et al., *J. Appl. Phys.*, **84**, no. 8, p. 4285, 1998.

[5] Synopsys, "Sentaurus™ Device User Guide," Version J-2014.09, September 2014.

Angle dependent magneto transport in GaAs/InAs core/shell nanowires

F. Haas, P. Zellekens, T. Wenz, D. Grützmacher, H. Lüth, and Th. Schäpers

Peter Grünberg Institut – 9, Forschungszentrum Jülich; Germany

GaAs/InAs core/shell nanowires (NWs) were measured at low temperatures in strong external magnetic fields at different angles to investigate the influence of flux pick up through the NWs. Due to their unique type-I band alignment in combination with their low dimensionality and geometry, GaAs/InAs core/shell NWs allow the observation of the transition from flux periodic Aharonov-Bohm type oscillations, when their axis is aligned parallel to the magnetic field, to universal conductance fluctuations (UCF) in a perpendicular oriented magnetic field. This gives rise to a new understanding of mesoscopic transport in NWs and the possibilities band design offers using the nanowire geometry.

GaAs/InAs core/shell NWs consist of a high bandgap GaAs core nanowire surrounded by a low bandgap InAs shell. Although the two materials GaAs and InAs are highly lattice mismatched, the nanowire geometry allows their epitaxial combination in a layered core/shell system. The two materials form a type-I band alignment, where the InAs shell bandgap is aligned almost centred within the GaAs bandgap of the core, which creates a radial quantum well in the InAs shell. Due to the existence of donor type surface states at the InAs surface, the InAs conduction band is filled with electrons. The GaAs/InAs core/shell NWs therefore form intrinsically conductive nanotubes with ring-like geometry [1].

The NWs investigated in this report were grown using a catalyst free approach using molecular beam epitaxy, first growing the GaAs core which is then subsequently epitaxially overgrown with InAs. The core inhibits zinc blende crystal structure with many stacking faults and rotational twins. Due to the large lattice mismatch, misfit dislocations are present at the GaAs/InAs interface [2]. An example of such a GaAs/InAs core/shell nanowire can be seen in the inset of fig. 1. Afterwards, the NWs were mechanically transferred to a pre-patterned substrate and contacted by Ti/Au leads using electron beam lithography and lift off. Magneto transport measurements were carried out in a He^3 cryostat at temperatures around 300 mK with a rotatable sample holder, which tilts the plane of the nanowire axis versus the external magnetic field by an angle $\theta = -10° \ldots 100°$.

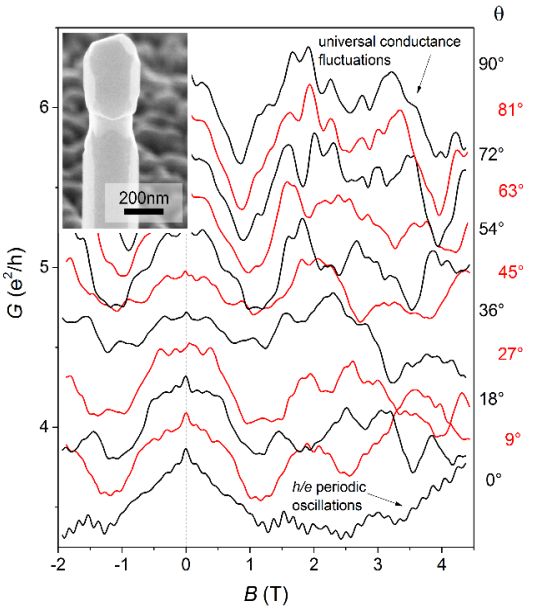

FIG. 1: Magneto conductance of a GaAs/InAs core/shell nanowire (inset shows an example nanowire) at different magnetic field alignments. The conductance of the nanowire transitions from Aharonov-Bohm type oscillations at low angles to universal conductance fluctuations at large tilt angles.

Fig. 1 shows the magneto conductance traces of a GaAs/InAs core/shell nanowire at different magnetic field directions. Most notable is the presence of very periodic oscillations at low tilt angles. The periodicity ΔB of the conductance G follows the equation $\Delta B\, A = h/e$, where A is the area enclosed by the electrons within the InAs shell and h/e is the magnetic flux quantum. These Aharonov-Bohm type oscillations are caused by electron transport through angular momentum states, which are the solution of the Schrödinger equation for an electron on a ring within an external magnetic field [3]. These states exist in the ring-like InAs shell and can be mapped by transport up to tilt angles of about $\theta = 30°$. Fig. 2 shows the Fourier transformation of the traces and the clearly separated frequency components of these states next to the components from the background. With increasing tilt, the centre of the frequency drops to lower frequencies and then disappears, caused by the reduced projection of the flux through the InAs ring.

The slowly varying underlying background fluctuation of the conductance is caused by localisation of electrons within scattering loops in the InAs shell. As transport is diffusive yet phase coherent, magnetic flux is also picked up by the electrons in these loops, which each contribute with a flux periodicity dependent on their enclosed area. These are the so called universal conductance fluctuations (UCF). Thus, as the electrons are confined only within the InAs shell, the area of these scattering loops is significantly smaller than the nanowire cross section, relevant for the Aharonov-Bohm type oscillations. Therefore, localisation effects only contribute with large periodicities to the observed magneto transport at low tilt angles.

This observation changes with increasing tilt, as additional scattering loops with loop areas parallel to the nanowire sidewalls can also pick up magnetic flux. As the nanowire is tilted more and more in the magnetic field, additional scattering loops can contribute to the observed magneto conductance. These loops have areas with bigger magnetic field projections than for alignment in a parallel oriented field and therefore contribute with larger frequencies to the Fourier spectrum. This transition is highlighted via a dotted trend line in Fig. 2.

In fig. 1 this effect can be seen as a stabilisation of the UCF with increasing tilt, as certain peaks and dips are reproduced with every measurement. Their positions in the trace move to lower magnetic field as less magnetic field is needed to pick up a magnetic flux quantum in a scattering loop in the sidewall, when the field is aligned perpendicular to the nanowire axis. Additional measurements on different NWs have confirmed this behaviour.

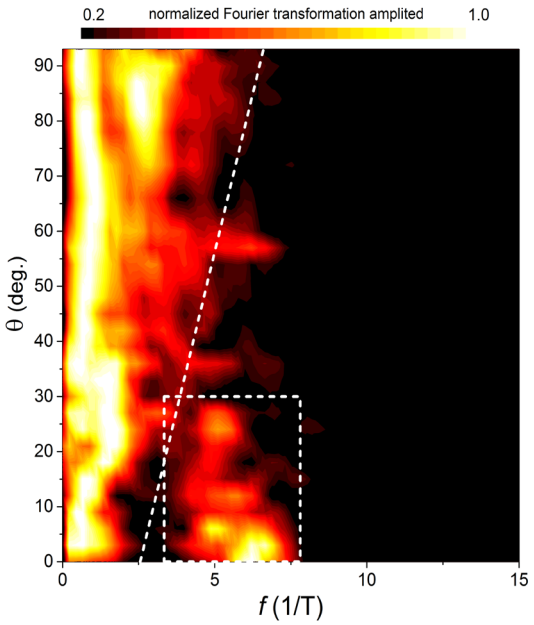

FIG. 2: Fourier transformation of the magneto conductance traces of fig. 1. At low angles flux periodic Aharonov-Bohm type oscillations (dotted box) are clearly separated from the low frequency background fluctuations. At large tilt angles UCF dominate the spectrum with increasing frequency components for increasing tilt (dotted trend line).

The ring-like geometry formed by the band alignment of the GaAs/InAs core/shell NWs is therefore an ideal system for studying low temperature transport, as mesoscopic quantum interference effects are directly visible in the conductance of the NWs.

[1] T. Rosdahl, A. Manolescu & V. Gudmundsson Phys. Rev. B **90**, 035421 (2014)

[2] T. Rieger, M. Luysberg, M. Lepsa et al., Nano Letters **12,** 5559 (2012)

[3] C. Blömers, T. Rieger, P. Zellekens, F. Haas et al., Nanotechnology **24**, 035203 (2013)

Microwire arrays for particle actuation and thermal lesion of cellular networks

P. Rinklin, T. K. M. Dang, H.-J. Krause, A. Offenhäusser, and B. Wolfrum

Institute of Complex Systems and Peter Grünberg Institut-8, Forschungszentrum Jülich, Germany

We present the use of microwire arrays for the actuation of particles and the introduction of lesions into cellular networks. Crossbar arrays of wide (10 µm) wires are used to magnetically actuate individual 1 µm particles. Subsequently, the positional data obtained from video analysis is used to recalculate the force acting on the particle. The experiments are repeated in solutions of dynamic viscosities of 1, 1.5, and 2 mPa s. Furthermore, arrays of thin (2 µm) wires are used to thermally induce lesions in networks of cardiomyocyte-like HL-1 cells. An analysis of Ca^{2+} imaging data yields insight into the signal propagation in the network after lesion. The effect of differing electrical power applied to the wires is demonstrated.

The development of miniaturized experimental platforms, so-called *lab-on-a-chip* or *micro total analysis systems* (µTAS), is a vivid interdisciplinary field of research. Driven by seminal works form the groups of G.M. Whitesides, A. Manz, C.M. Lieber, and others, this field aims to reduce reagent and time consumption by implementing classical wet-lab experiments into chip-based tools [1–3]. Reducing the effective cost of an experiment, the micro- and nanotechnological approaches inherent to these systems can also open up new experimental approaches. Recent examples include massively parallelized mechanical modulation of cell behavior [4], platforms for subcellularly resolved extracellular recordings [5], parallelized recording of single vesicle release events [6], or parallelized mechanical actuation of particles and cells [7,8].

Employing a similar technological chip-based approach, we have recently shown that microwire arrays are efficient tools for particle actuation and thermal stimulation of cells [9–11]. Here, we demonstrate applications of these two concepts. Firstly, we show that single particle actuation and tracking techniques can be used to calculate the forces acting on particles in media of differing viscosity. Secondly, we demonstrate the use of microwire arrays as a tool to thermally induce lesions of variable width in cellular networks.

Fig. 1 shows the application of microwire crossbar arrays for the calculation of forces acting on individual beads during the actuation in media of different viscosities. In these experiments, an individual particle is deployed into a magnetic trap generated by the wire array as described

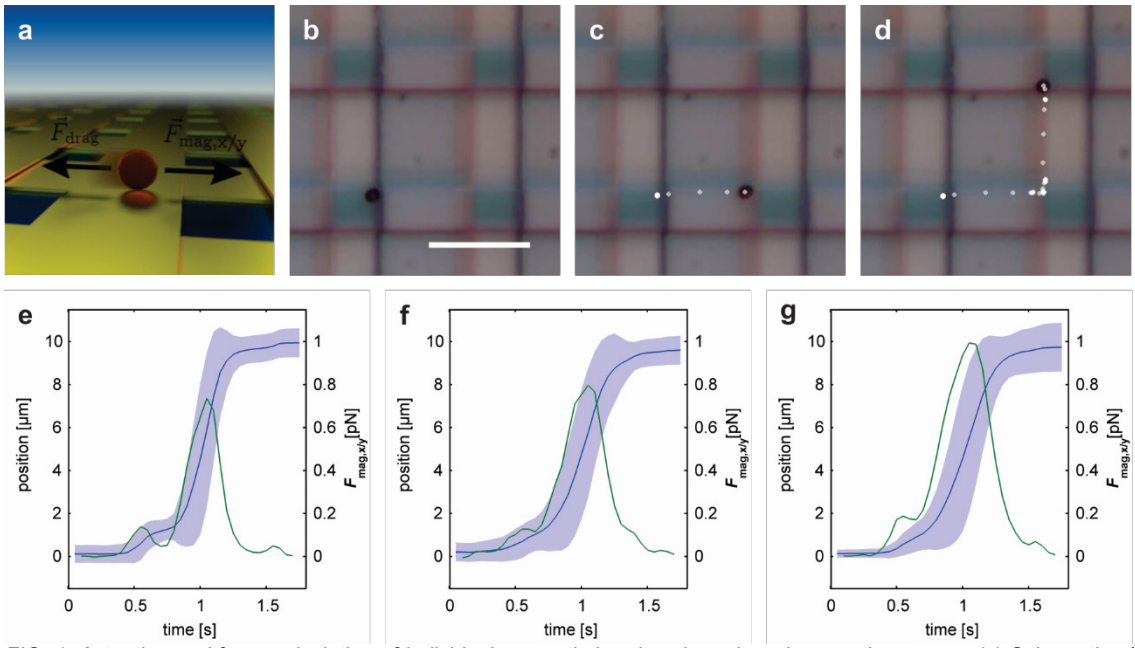

FIG. 1: Actuation and force calculation of individual magnetic beads using microwire crossbar arrays. (a) Schematic of the experiment. During the actuation by the microwire array (shown in yellow), the magnetic force in the x/y-plane and the drag force are assumed to be balanced. (b)-(d) Image sequence from an exemplary actuation experiment (scale bar: 10 µm). The particle's position can be extracted digitally (white markers). (e)-(g) Using the positional data, the force acting on the particle can be calculated. The plots show data from experiments of media wit a viscosity of 1 mPa s (n=112), 1.5 mPa s (n=112), and 2 mPa s (n=88; left to right, respectively).

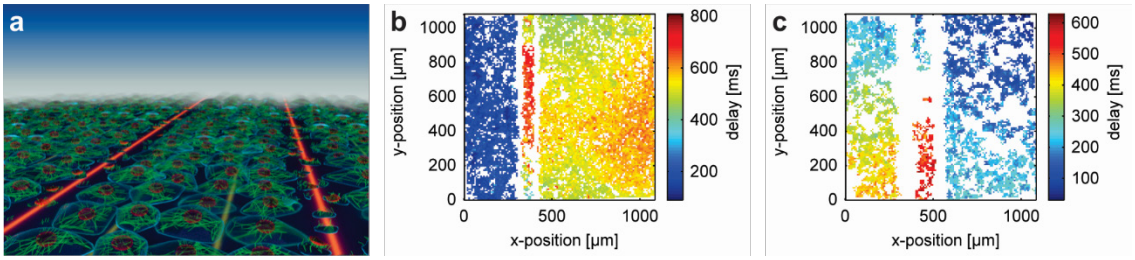

FIG. 2: Thermal introduction of lesions into cell networks. (a) Schematic of the experiments. Layers of cardiomyocyte-like HL-1 cells are cultured on the microwire array. Supplying individual wires with electrical power leads to resistive heating (indicated in orange) and consequent cell death. (b) Ca^{2+} signal delay in a cell layer after the application of a lesion pattern. Two wires located at x-positions of approx. 320 and 410 µm were supplied with 2 W. As a result, the cells directly above the wires cease activity as indicated by the white (i.e. inactive) regions. (c) Ca^{2+} signal delay after the application of 4 W to two wires located at x-positions of approx. 350 and 530 µm. As a result of the increased heating, the inactive regions become broader.

elsewhere [10]. During the actuation, the magnetic force in the x/y-plane (i.e. coplanar to the chip's surface) is assumed to be in balance with the viscous drag force (compare FIG. 1a). FIG. 1b-d show an exemplary image sequence recorded during the actuation of a 1 µm magnetic particle. An analysis of the positional data obtained via digital image analysis can be used to recalculate the actuation force as shown in FIG. 1e-g. The plots represent the positional data (mean ± standard deviation) and forces obtained from measurements in media of three different viscosities (e: 1 mPa s (n = 112), f: 1.5 mPa s (n = 112), g: 2 mPa s (n = 88)).

FIG. 2 shows the use of microwire arrays as a means to thermally introduce lesions to cellular networks cultured on the chip. In this case, arrays of thin wires (approx. 2 µm) are used. Supplying the wires with electrical power will result in resistive heating of the wire and its immediate surrounding (compare FIG. 2a.). For sufficiently high electrical power, this localized heating can be used to section layers of cells cultivated on the chip as shown schematically in FIG. 2a. In the experiments, the cardiomyocyte-like HL-1 cell line was used. This cell line spontaneously generates periodic Ca^{2+} waves that travel through the cell layer. Using fluorescent imaging techniques, the propagation of these waves can be visualized as seen in FIG. b and c. The plots show Ca^{2+} imaging data recorded after the application of different lesion patterns. In the case of FIG. 2b, two wires with a distance of 90 µm were supplied with a power of 2 W. The resulting temperature field leads to the selective inactivation of the cells directly above the wires (as indicated by the two white vertical regions). In between the active wires, the cell layer remains active. FIG. 2c displays a similar plot recorded after applying 4 W of electrical power to two wires positioned 180 µm apart. Similar to FIG. 2b, the vertical lines indicate cell death directly over the active wires. Due to the increase in electrical power, however, these regions are significantly broader. As before, the cells in between the two wires remain active.

In summary, we have shown the application of microwire arrays in two examples within the context of lab-on-a-chip platforms. On the one hand, the arrays pose a flexible and efficient platform for particle actuation. Supplying the wires with appropriate current patterns allows precise control over individual microbeads. Positional data obtained from videos of the experiments can be used to recalculate the forces acting on the particle giving insight on viscous drags exerted by the media. On the other hand, using the microwires as resistive heating elements allows the generation of highly localized temperature fields. These fields can then be used to induce lesions in cellular networks and study network properties such as signal propagation.

This work was supported by the Helmholtz Young Investigator program.

[1] G. M. Whitesides, Nature **442**, 368 (2006).

[2] J. West, M. Becker, S. Tombrink, and A. Manz, Anal. Chem. **80**, 4403 (2008).

[3] X. Duan and C. M. Lieber, Nano Res. **8**, 1 (2015).

[4] P. Tseng, J. W. Judy, and D. Di Carlo, Nat. Methods **9**, 1113 (2012).

[5] D. J. Bakkum, U. Frey, M. Radivojevic, T. L. Russell, J. Müller, M. Fiscella, H. Takahashi, and A. Hierlemann, Nat. Commun. **4**, 2181 (2013).

[6] A. Yakushenko, E. Kätelhön, and B. Wolfrum, Anal. Chem. **85**, 5483 (2013).

[7] C. S. Lee, H. Lee, and R. M. Westervelt, Appl. Phys. Lett. **79**, 3308 (2001).

[8] H. Lee, A. M. Purdon, and R. M. Westervelt, Appl. Phys. Lett. **85**, 1063 (2004).

[9] P. Rinklin, H.-J. Krause, and B. Wolfrum, Phys. Status Solidi **209**, 871 (2012).

[10] P. Rinklin, H.-J. Krause, and B. Wolfrum, Appl. Phys. Lett. **100**, 014107 (2012).

[11] P. Rinklin, D. Afanasenkau, S. Wiegand, A. Offenhäusser, and B. Wolfrum, Lab Chip **15**, 237 (2015).

Influence of Nanotopography on Neuron Adhesion

P. Li[1], Q. Tran[1], U. Simon[2], A. Offenhäusser[1], and D. Mayer[1]

[1] Peter Grünberg Institut-8, Forschungszentrum Jülich, Germany
[2] Institute of Inorganic Chemistry, RWTH Aachen University, Germany

Silicon wafers decorated with positively charged, aminoalkyl thiol-terminated gold nanoparticles (AuNPs) are used as model surface to investigate of competitive role of two adhesion cues namely nanotopographies and density of binding ligands on the adhesion of neurons. The density as well as the size of nanoparticles is varied in the range from 0 to 800AuNP/µm² and 10nm to 50nm, respectively. The cells bind to the amino-functionalized particles via negatively charged moieties of the cell membrane associated glycocalyx. The viability of primary rat cortical neurons and their maturation is investigated as a function of the three-dimensional topography of the sample surface. This study reveals that the enhancement of neuron viability obtained for increasing particle sizes can be attributed to a larger number of ligands bound to big particles due to the increased geometrical 3D surface area.

Adhesion of neurons on solid surfaces is required for the investigation of fundamental aspects of neurobiology, for tissue engineering, and for numerous bioelectronic applications. Mainly three cues of solid surfaces are influencing adhesion of neurons: the chemical composition of the surface, the compliance, and the topography of the sample surface. In particular, the effect of the topography on cell properties like shape, viability, motility, and projection outgrowth has been intensively studied during the last decades. However, most of these investigations have been focused on topographies in the micrometer or large nanometer range. This study aims to elucidate the role of nanotopographies on cell viability and maturation in the sub-50nm range. It is demonstrated that the topographical influence on neuron adhesion has a chemical origin.

Gold nanoparticles with sizes between 10nm and 50nm are deposited on a planar SiO_2 surface. The AuNPs are tethered to the surface with random packing from colloidal solution by electrostatic interactions between charged particles and the oppositely charged solid surface.[1,2] The density of particles on the surface can be tuned via the particle concentration in solution. The AuNPs are functionalized by 11-amino-1-undecanethiol (AUT), a molecule that possesses a positively charged terminal group under neuron culture conditions. The amino-functionalized gold nanoparticle (AF-AuNP) can be considered as cationic anchor spots for glycosylated plasma membrane proteins. In neurons, the polysialation of neural cell adhesion molecule (NCAM) facilitates cell migration and plasticity by regulating the repulsion between adjacent cells.[3] We exploited the electrostatic interactions between the negatively charged glycocalyx and particle associated cationic molecules to immobilize neurons on solid surfaces, Fig.1 top. The presence of a positive net charge on amino-functionalized nanoparticle SiO_2-samples has been confirmed by streaming potential measurements.[4] The AuNP can be considered equivalent to cationic polyamino acids like poly(lysines), which are widely used to promote cell adhesion. However, the confinement of the amino-groups to the particles facilitates the control over density and local distribution of adhesion cues on the surface. Samples homogeneously modified with poly-D-lysine (PDL) are used as control to evaluate the maturation of the neurons. The surrounding background of the AF-AuNP was modified with protein repellant polyethylene glycol silane molecules (PEG) to prevent unspecific interactions between cells and the sample surface.

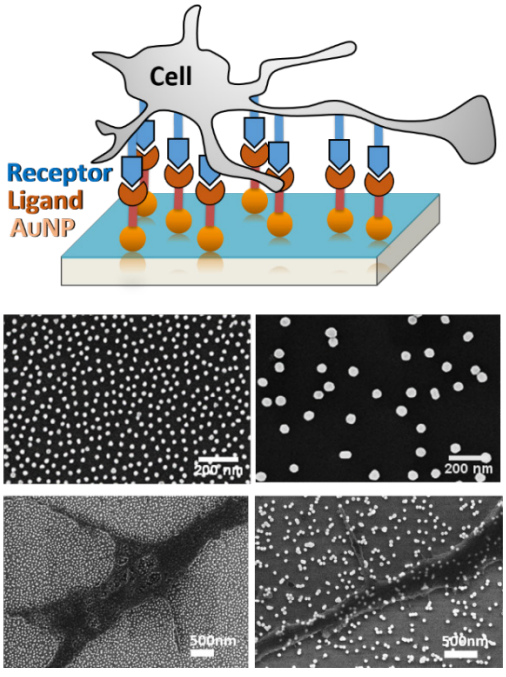

FIG. 1: Top: Scheme of SiO_2 surface modified with adhesion ligand decorated gold nanoparticles. Middle: SEM images of 20nm (left) and 50nm (right) gold nanoparticles. Bottom: SEM images of neurites from rat cortical neurons seeded at 3div on modified SiO2 surfaces decorated with 20nm (left) and 50nm (right) gold nanoparticles.

As the density of surface associated particles can be tuned over large ranges, we are able to control

the density of binding cues on the surface. In addition, the particle size is varied, which allows to separately investigate the influence of ligand density and surface topography on neuron adhesion. Fig.1 middle shows two exemplary samples with similar ligand coverage (approx. 16%) but different ligand distribution due to different particle sizes. The impact of ligand density, distribution, and topography on neuron viability is discussed in the following.

For all particle sizes, it is observed that the particle density has a significant impact on the viability of the neurons seeded on these surfaces, Fig.2 top. At the lowest densities, only few vital neurons are observed on the sample after 3 days in culture due to the small number of particle associated binding cues. However, the relative live cell density steeply increases with the density of large particles, while the viability remains poor for 10nm AuNPs. The unequal capability of the differently sized particles to support neuron survival at the surface suggests a strong topographical influence also in the sub-50nm range.

However, it should be taken into account that particles of different sizes possess different capabilities to bind adhesion ligands. The particle density reflects a 2-dimensional distribution of adhesion sites on the sample surface and neglects the 3-dimensional shape of the particles. However, the surface area of a 50nm particle is 25 times larger than the surface area of a 10nm particle and thus capable to bind more adhesion ligands. Assuming a surface coverage of 5.5 AUT/nm^2 on the particle surface, it is possible to determine the density of adhesion ligands on the sample surface. Plotting the relative live cell density versus the ligand density provides now a topography independent presentation of the neuron viability on different AuNPs decorated surfaces, Fig.2 bottom. From this presentation, it can be derived that the cell viability increases with the ligand density similarly for all particle sizes and saturates at about 1.5*10^6 ligands/µm². Under these saturation conditions, neurons exhibit a matured development with long branched as well as short neurites. The viability is similar or even better than for PDL-control samples.

From the density of AUT molecules, the surface charge density of the sample surface can be estimated. Considering only the AF-AuNP associated ligands, a surface charge density of 24×10^{-2} C/m^2 is obtained. This value is about one order of magnitude larger than the surface charge density of 15×10^{-3} C/m^2 determined for HEK293 cells.[6] The difference between sample associated positive charges and negative cell surface charges suggests that an excess of positive charges is required at the sample surface to support the neuron adhesion. However, it cannot be excluded that the surface charge density of HEK cells and neurons differ significantly.

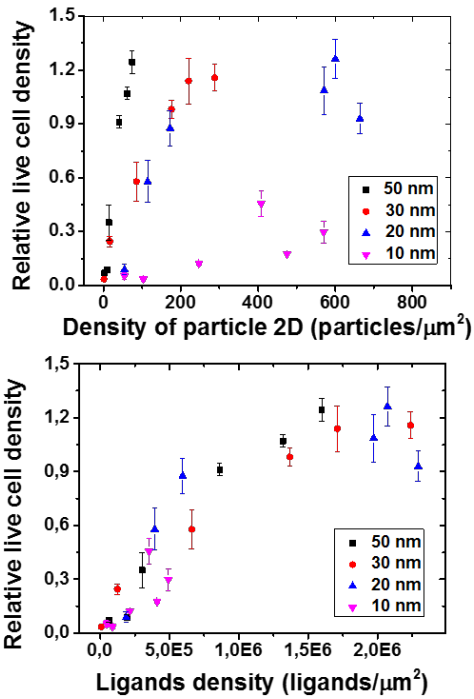

FIG. 2: Top: Dependence of the relative live cell density of primary rat cortical neurons on the size and density of AuNP. Bottom: Same relative live cell density as top but this time plotted versus ligand density.

In summary, we found that both, increasing density and increasing size of amino-functionalized nanoparticles enhance the adhesion of neurons. However, the enhancing properties associated to the particle size are evidently based on a geometrical increase of the 3-dimensional particle surface. A transformation of the particle density into the ligand density reveals that the topographical enhancement is caused by the capability of large particles to bind more ligands. Thus, the observed topographical enhancement of neuron adhesion on 3-dimensional surfaces has a chemical origin in the sub-50nm range. Furthermore, the results demonstrate that the ligand density determines neuron viability, whereas the distribution of ligands over the surface is of minor importance.

This work was supported by a Seed Fund research grant provided by JARA-FIT.

[1] S. Gilles, C. Kaulen, M. Pabst, U. Simon, A. Offenhäusser, D. Mayer, Nanotechnology, **22**, 295301 (2011).

[2] S. Gilles, S. Winter, K. E. Michael, S. H. Meffert, P. Li, K. Greben, U. Simon, A. Offenhäusser, D. Mayer, Small, **8**, 3357 (2012).

[3] C. Johnson, I. Fujimoto, U. Rutishauser D. Leckband, J. Biol. Chem. **280**,137 (2005).

[4] K. Greben, P. Li, D. Mayer, A. Offenhausser, R. Wördenweber, J. Phys. Chem. B, **119**, 5988 (2015).

[5] P. Li, K. Greben, R. Wördenweber, U. Simon, A. Offenhäusser, D. Mayer, RSC Advances, **5**, 39252 (2015).

[6] P.C. Zhang, A.M. Keleshian, F Sachs, Y. Xiong and Y. Xia, Nature **413**, 428 (2001).

Detection and Origin of Temporal Structure in Cortical Activity

S. Grün[1,2,3], M. Denker[1], M. Helias[1,4], J. Ito[1], T. Tetzlaff[1], and M. Diesmann[1,4,5]

[1] Institute of Neuroscience and Medicine-6 and Institute for Advanced Simulation-6, Forschungszentrum Jülich, Germany
[2] Theoretical Systems Neurobiology, RWTH Aachen University, Aachen, Germany
[3] RIKEN Brain Science Institute, Wako-shi, Saitama, Japan
[4] Department of Physics, Faculty 1, RWTH Aachen University, Germany
[5] Department of Psychiatry, Psychotherapy and Psychosomatics, Medical Faculty, RWTH Aachen University, Germany

A promising approach to characterize the origins of oscillatory synchronization in recordings of neural activity is to investigate its emergence during early development. To support the analysis of such data, we provided a first robust and unbiased classification of the different types of discontinuous oscillatory activity patterns leading up to rhythms observed in adult animals. We found that delta band (0.5 – 4 Hz) oscillation in local field potential (LFP) activity in the whisker barrel cortex of awake mice is phase locked to respiration. Furthermore, LFP oscillations in the gamma frequency band (30–80 Hz) are amplitude modulated in phase with the respiratory rhythm. With the help of theoretical tools from statistical physics, we were able to disentangle, how recurrent connectivity and external inputs each contribute to the synchronous activation of neurons in cortical networks.

Flexible communication within the brain, which relies on oscillatory activity, is not confined to adult neuronal networks. Experimental evidence has documented the presence of discontinuous patterns of oscillatory activity already during early development (see Figure 1). Indeed, understanding the development of these early cortical rhythms may provide valuable insights as to which components of the early network shape the dynamic features seen in adult activity. The highly variable spatial and time-frequency organization of early oscillatory activity has been related to region specificity. However, it might be equally due to the absence of unitary criteria for classifying the early activity patterns, since they have been mainly characterized by visual inspection. Therefore, before these patterns can be reproducibly quantified, robust and unbiased methods for categorizing these discontinuous oscillations are needed for increasingly complex data sets from different labs. In [1], we introduced an unsupervised detection and classification algorithm for the discontinuous activity patterns of rodents during early development based on a multi-dimensional clustering of extracted features of individual oscillatory events. Results were validated on manually characterized neonatal spindle bursts (SB), which ubiquitously entrain neocortical areas of rats and mice, and prelimbic nested gamma spindle bursts (NG). Moreover, the algorithm led to satisfactory results for oscillatory events that, due to increased similarity of their features, were more difficult to classify, e.g., during the pre-juvenile developmental period. In a first application of the method, we showed that this algorithm allows the comparison of neonatal and pre-juvenile oscillatory patterns in their spatial and temporal organization. Thus, in line with our efforts to strengthen reproducibility in neuronal data analysis, our work represents a first step for the robust, unbiased elucidation of activity patterns during development.

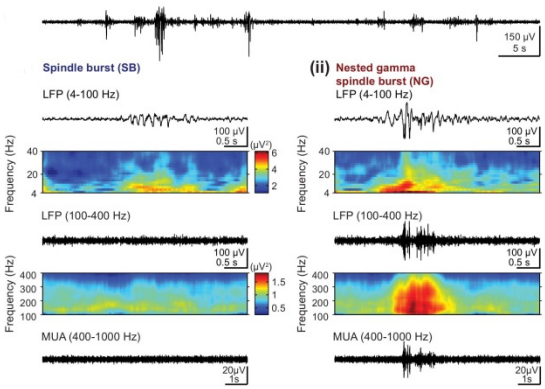

FIG. 1: Patterns of network activity and their frequency components in the developing prelimbic cortex of rats. Top: Extracellular LFP recording (4–100 Hz) of the discontinuous oscillatory activity in the PFC of a P8 rat. Bottom: Examples of characteristic SB (left) and NG (right) displayed after band-pass (upper graph: 4–100 Hz, middle graph: 100–400 Hz, lower graph: MUA activity 400–1000Hz) filtering and accompanied by the wavelet spectra of the LFP at identical time scales.

Local field potential (LFP) in mammalian brains show prominent oscillations in a broad range of frequencies from slow (1-8 Hz) delta/theta band to gamma band (40-100 Hz) and higher frequencies. There is increasing evidence that amplitude modulations in the gamma frequency band locked to the phase of the delta/theta rhythm reflect cognitive processes. In our recent work [2] we found that delta frequency LFP oscillations in the whisker barrel cortex of mice are locked to respiratory rhythm (Fig. 2A, B). Furthermore, LFP oscillations occurring in parallel in the gamma

frequency band (64-128 Hz) were amplitude-modulated in phase with the respiration frequency (Fig.2C, D). We confirmed in tracheotomized mice, where the airflow through the nose canal was modulated independently from the voluntary respiration, that this LFP-respiration correlation was not an artifact due to the body motion by breathing but directly related to the rhythm of the airflow per se. We also found in bulbectomized mice, where the olfactory bulb was removed, that the coherence between respiration and barrel cortex LFP oscillations was considerably weakened. Our findings indicate that respiratory activity in mice directly modulates delta/theta band LFP oscillations in the whisker barrel cortex through respiration-locked olfactory bulb activity and indirectly, through phase-amplitude coupling, gamma band power.

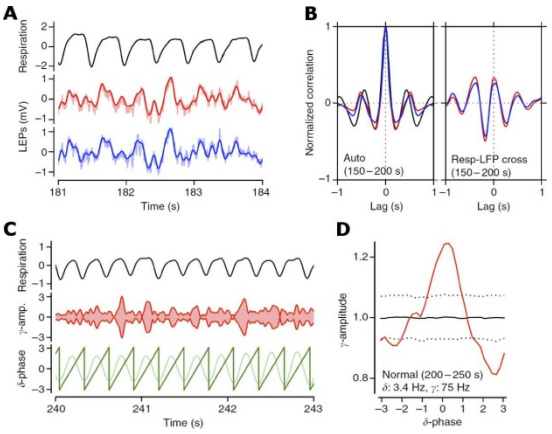

FIG. 2: Respiration-locked LFP oscillations in barrel cortex. A. Respiration (top) and LFP (bottom two) traces during normal breathing. Solid curves are the signals after band-pass filtering in 0.5-10 Hz. Raw LFP signals are plotted with shaded colors. B. Auto-correlation of the respiration and the LFP signals (left) and cross-correlation between the respiration signal and each of the LFP signals (right) during normal breathing. C. Respiratory activity (top trace), amplitude of gamma band oscillations (middle trace) and delta oscillations (light green bottom trace) and its phase (dark green bottom trace) in an intact mouse. D. Gamma oscillation amplitude as a function of delta phase (red). The solid and dotted black lines indicate the mean and the 2.5 and 97.5 percentile boundaries of the surrogate amplitude distribution.

The co-occurrence of action potentials in pairs of neurons within short time intervals has been known for a long time: It is a natural consequence of the network connectivity and shared inputs to pairs of neurons. Synchronous activity locked to the behavior of an animal argues for a functional role of this correlated activity. It is therefore of fundamental importance to understand the mechanisms that shape the correlated activity. Recently, the recurrent connectivity of cortical networks was shown responsible for the observed low correlations under baseline conditions. Two different explanations were given: One argues that excitatory and inhibitory population activities closely follow the external input to the network (fast tracking), so that their recurrent effects on a pair of cells mutually cancel. Another explanation showed that the negative feedback that suppresses fluctuations in the population activity is equivalent to small correlations. In a biological neuronal network one expects both, external inputs and recurrence, to shape correlated activity. In our recent work [3] we extended the theory of correlations to include both contributions to explain their qualitative differences (see Figure 3): the study shows that the arguments of fast tracking and recurrent feedback are not equivalent, only the latter correctly predicts the cell-type specific correlations observed in networks of finite numbers of neurons.

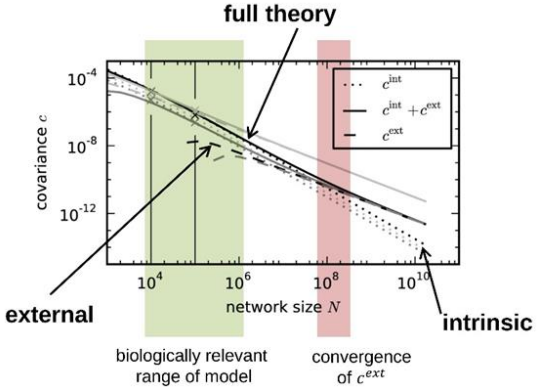

FIG. 3: Comparison of external (cext) and intrinsic (cint) sources to correlations in recurrent neuronal networks shows that at realistic network sizes, the intrinsic connectivity dominates over external input. This corrects a previous and contrary claim, derived from a theory valid only for infinite-sized networks.

We show that at realistic network sizes, the structure of correlations is mainly determined by the local recurrent connectivity and external input only provides a common additive component. This insight corrects the previously published contrary claim that correlated activity in networks is mainly shaped by external inputs into the network.

This work was supported by DFG grant GR 1753/ 4-1 Priority Program SPP 1665, the Helmholtz Alliance on Systems Biology and Portfolio Supercomputing and Modeling for the Human Brain (SMHB) to S. Grün and the young investigator's group VH-NG-1028 "Theory of multi-scale neuronal networks" led by M. Helias.

[1] N.B. Cichon, M. Denker, S. Grün, I.L. Hanganu-Opatz Unsupervised classification of neocortical activity patterns in neonatal and pre-juvenile rodents. Front. Neural Circuits **27** (8):50 (2014)

[2] J. Ito, S. Roy, Y. Liu, Y. Cao, M. Fletcher, L. Lu, J.D. Boughter, S. Grün, D.H. Heck Whisker barrel cortex delta oscillations and gamma power in the awake mouse are linked to respiration. Nat Commun **5**: 3572 (2014)

[3] Helias M, Tetzlaff T, Diesmann M The Correlation Structure of Local Neuronal Networks Intrinsically Results from Recurrent Dynamics. PLoS Comput Biol **10** (1): e1003428 (2014)

Reduction of skin effect losses in multi-level-T-gate structure

M. Mikulics[1], H. Hardtdegen[1], Y. C. Arango[1], A. Fox[1], M. Marso[2], and D. Grützmacher[1]

[1] Peter Grünberg Institut-9, Forschungszentrum Jülich, Germany
[2] Université du Luxembourg, Luxembourg

We developed a novel T-gate technology based on selective wet etching yielding ~100 nm wide T-gate structures used for fabrication of High Electron Mobility Transistors (HEMT). Major advantages of our process are the use of only a standard photolithographic process and the ability to generate T-gate stacks. HEMTs with a multi-level-T-gate (MLTG) structure exhibit up to 40% improvement of the f_{max} (~120 GHz) value compared to a single T-gate device. This indicates a significant reduction of skin effect losses in the MLTG structure compared to its standard T-gate counterpart. This novel technology is a strategic key towards sub-THz operated optoelectronic integrated circuits.

During the last three decades the fabrication and performance of transistors operating in the GHz frequency range have progressed rapidly by introducing new material systems, novel technological processes, or new device geometries with reduced gate dimensions. The transistor scaling process has the drawback that the parasitic gate resistance increases linearly with decreasing gate length L_g. A small gate length is crucial for the transistor speed; however, the increase of gate resistance degrades the external device properties, especially the power gain. Therefore, the parasitic gate resistance must be kept as low as possible with decreasing L_g. One solution for the contradictory requirements is to use T-shaped gates allowing the fabrication of gates with small L_g (corresponding to the base of the T) with a low value of R_g, due to the large top of the T. The larger the head the lower the resistance. The major research effort to provide these T-shaped gates concentrates on structures fabricated by electron beam lithography, deep UV lithography or nano-imprint techniques. Especially the fabrication of T-shaped gates by e-beam lithography is commonly used in high frequency device technology. Nevertheless, yield and uniformity of T-gate fabrication are often affected by the nanoscale lithography and other technological steps required for their realization.

In this work, we present an alternative T-gate structure fabrication technology with the advantages of using only photolithography and with significantly increased electrode surface [1,2]. The total cross-section of our developed multi-level-T-gate (MLTG) contributes to the current transport and is about 2-times higher than for a standard T-gate design (Fig. 1-top), resulting in halving the gate resistance [1].

Our MLTG layout is expected to provide a significant improvement in the high-frequency performance of HEMT (high electron mobility transistor) devices in comparison with conventional T-gate electrodes. Simulations of the resistance-frequency dependence for both T-gate layouts, were performed with the COMSOL 4.2 Multiphysics (AC/DC module) software. The results reveal a pronounced frequency dependence already below 10 GHz. From 50 GHz the MLTG shows a decrease of the gate resistance compared to the conventional T-gate [2]. At 200 GHz the decrease is already 25%. The effect of surface roughness should even increase the influence of the MLTG. Figure 1-bottom shows the current distribution of both layouts at 300 GHz [2]. The current density in the Ni layers with high permeability is very strongly suppressed.

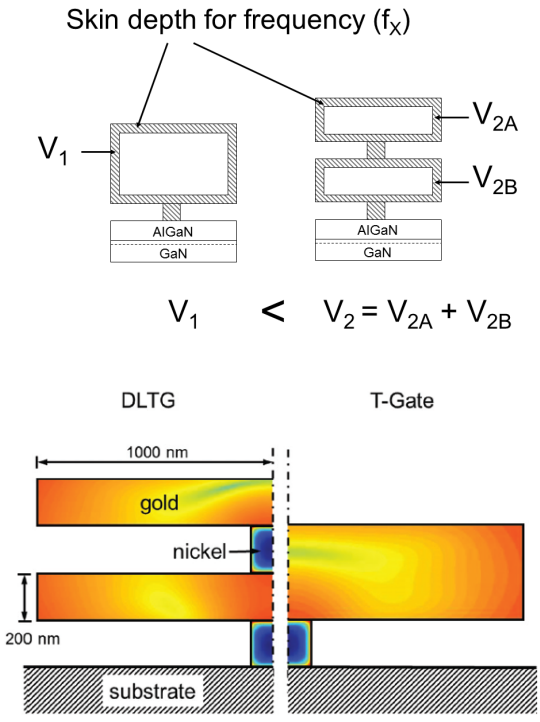

FIG. 1: Principle of multi-(double)-level-T-gate compared to conventional T-gate, showing double cross-section for current transport (top) and a simulation of the current distribution at 300 GHz (bottom) [2].

For the realization of this enhanced multi-level-T-gate shape we developed a technological procedure based on selective wet chemical etching of the Ni films while keeping the Au layers intact. The implementation of these MLTG structures in a HEMT device was performed using a standard AlGaN/GaN HEMT technology.

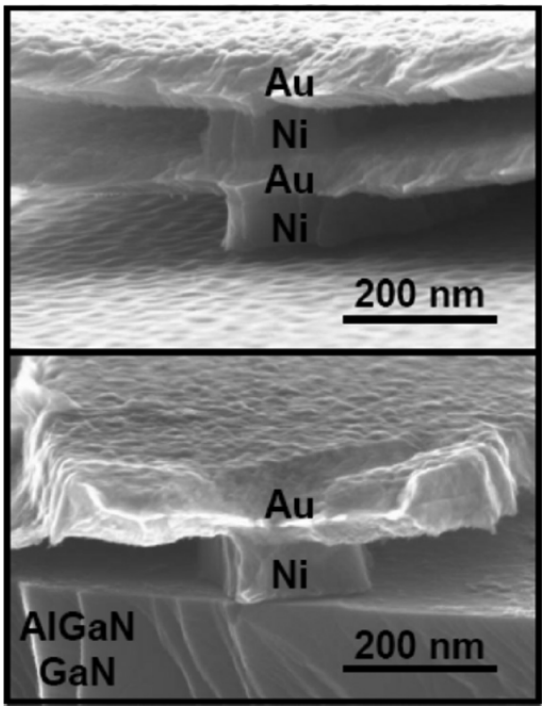

FIG. 2: Scanning electron micrograph of a double-level-T-gate contact (top) and T-gate (bottom) fabricated on AlGaN/GaN/sapphire material.

The fabricated HEMT devices were first tested by DC measurements, showing nearly a two times higher maximum drain current (0.7 A/mm) for the double-level-T-gate structure compared to the unetched counterpart with L_g = 2 µm (0.4 A/mm). Similarly, the extrinsic transconductance exhibits a value of 175 mS/mm for the 200 nm gate length device compared to 125 mS/mm for the 2 µm gate length transistor. The reduction of the gate electrode length due to the recess etching is also demonstrated by the decrease of the threshold voltage from -3 V to -4.6 V for the 200 nm gate HEMT [2].

High frequency S-parameter measurements reveal an increase of the cutoff frequency from 6 GHz for the 2 µm device to 60 GHz for the same device after etching the 200 nm double-level-T-gate structure (Fig. 3). The cutoff frequency exhibits a $1/L_g$ dependence without any indication of saturation for short gate lengths. The same figure shows that the DC gate current I_g decreases with decreasing L_g contributing to the improvement of device performance. The behavior is similar for DLTG and T-gate devices.

Figure 4 presents a comparison of current gain and unilateral power gain (GU) of HEMTs with T-gate and double-level-T-gate structure (both with 200 nm gate width). While the performance of both

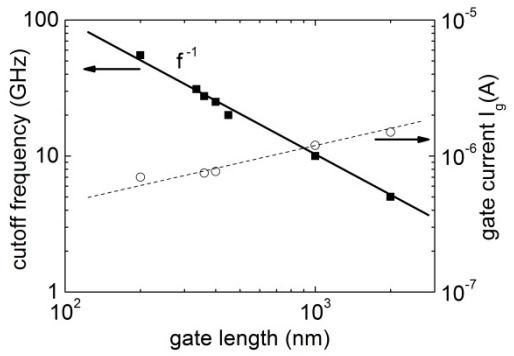

FIG. 3: Cutoff frequency and DC gate current vs. gate length of DLTG devices.

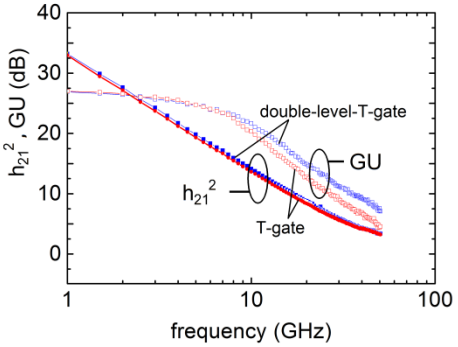

FIG. 4: Comparison of the current gain and unilateral power gain on HEMTs with T-gate structure and double-level-T-gate structure. The gate length is 200 nm.

transistors is identical for the current gain (the current gain is nearly independent on gate resistance), the HEMT device with the DLTG electrode structure exhibits improved power gain at high frequencies compared to the T-gate counterpart. The f_{max} value of the DLTG device is 120 GHz increased by ~ 40% compared to 85 GHz for the T-gate transistor.

In conclusion, we developed a multi-level-T-gate technique for the fabrication of submicron gate lengths based on wet chemical etching that uses only standard photo-lithographical processes (no e-beam lithography). HEMTs with a double-level-T-gate (DLTG) structure exhibit a 40% improvement of the f_{max} value, compared to their conventional T-gate counterparts. Our technology demonstrates that the application of T-gate stacks has a strong potential to decrease skin effect losses in gate structures, leading to a substantial improvement of the high-frequency performance of HEMTs.

Y.C. Arango thanks the Alexander von Humboldt Foundation for her research fellowship.

[1] M. Mikulics, D. Grützmacher, H. Hardtdegen, Patent PCT/DE2014/000149.

[2] M. Mikulics, H. Hardtdegen, Y.C. Arango, R. Adam, A. Fox, D. Grützmacher, D. Gregušová, S. Stanček, J. Novák, P. Kordoš, Z. Sofer, L. Juul, and M. Marso, APL **105**, 232102 (2014)

Hierarchical Manipulation of Block Copolymer Self-assembled Patterns via Topographical guidance

S. Park[1], A. Böker[1,2], and L. Tsarkova[1]

[1] DWI-Leibniz-Institut für Interaktiven Materialien, Aachen, Germany
[2] Fraunhofer-Institut für Angewandte Polymerforschung-IAP, Potsdam, Germany

We report an approach towards fabrication of complex topographic and chemical patterns by equilibrating thin films of block copolymers on 3D corrugated substrates produced by lithography-free technique. Cylinder- and lamella forming block copolymers can be quided into sequenced versatile nanostructures depending on the film thickness, solvent concentration in the film and the geometry of the topographic features. The approach exploits thickness- and swelling-responsive morphological behavior, and demonstrates novel possibilities of topography-guided registration of nanopatterns by fine manipulation of the microphase separation in thin films.

The spontaneous formation of highly ordered functional surfaces and patterns via directed self-assembly of block copolymers under application of external fields is a fascinating research area driven by emerging nanotechnological applications in lithogrpagy, data storage media, electronic circuits, templates for nanodots fabrication. Block copolymers are comprised of two or more immiscible blocks, so that the representative microphase separated structures in bulk are determined by the relative length of the blocks and mutual interaction between the components. In thin films the phase behavior is dictated by additional driving forces such as polymer-substrate interactions, film thicknesses, as well as by processing conditions. For lamella-forming systems, any cross section parallel to a lamella exhibits the same symmetry, while thickness-dependent morphological behavior results in mixed patterns of featureless in-plane lamella ($L_{\perp}$) and of striped patterns with perpendicular-oriented lamella ($L_{\parallel}$). Asymmetric cylinder-forming AB diblock copolymers are known to exhibit structural polymorphisms in confined geometries.

Here we report novel complex structural features of asymmetric and symmetric diblock copolymers in thin films annealed on 3D structured substrates. Ceramic topographic substrates have been fabricated by non-lithogralhic replication procedure.Thin films from cylinder-forming polystyrene-*b*-polybutadiene (PS-*b*-PB) and lamella-forming polystyrene-*b*-poly(2-vivylpiridine) (PS-*b*-P2VP) diblock copolymers have been deposited by spincoating or by floating procedures for comparison, and have been annealed under controlled atmosphere of solvent vapor or by thermal treatment above the temperature of the glass transition on squared and wrinkled topographic SiCN ceramic substrates. The structures have been compared with that in films on flat silicon wafers under similar processing conditions.

Figure 1a illustrates the production of 3D SiCN ceramic substrates by facile replication process using a wrinkled polydimethylsiloxane (PDMS) master as described earlier [1]. In the second step, the pre-patterned SiCN substrate is covered with a soft curable layer of ceramic precursor poly(vinylsilazane) (PVSZ) which is then molded with the PDMS corrugated master rotated in 90° with respect to the initial corrugations. Subsequent photopolymerization and pyrolysis result in squared corrugated pattern with an averaged period λ of ca 1250 nm and the amplitude of corrugations in the range of ~ 30 nm. Such 3D patterns can be produces almost defect-free on macroscopically large areas, as seen in the scanning force microscopy (SFM) topography image in Figure 1b.

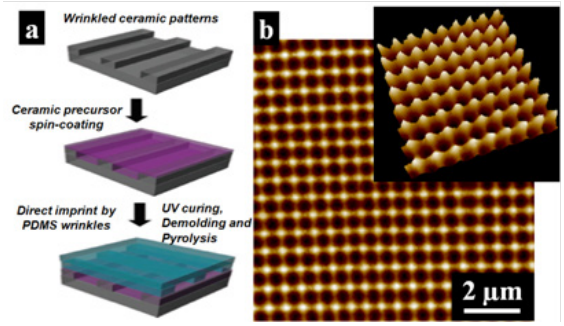

FIG. 1: (a) Schematic illustration of the fabricating fabrication of three-dimensionally patterned SiCN ceramic substrates. (b) SFM topography image of the squared patterned substrate. The corrugations amplitude is ~ 30 nm, and the wavelength of the corrugations is ~1250 ± 50 nm.

Figure 2 presents topography and phase images of 54 nm thick (about one and a half lamella spacing L_0) PS-*b*-P2VP films on corrugated substrates. The samples have been equilibrated in chloroform vapors, first 40 min at a degree of swelling α of 1.4 and then 80 min at α ~ 1.5.

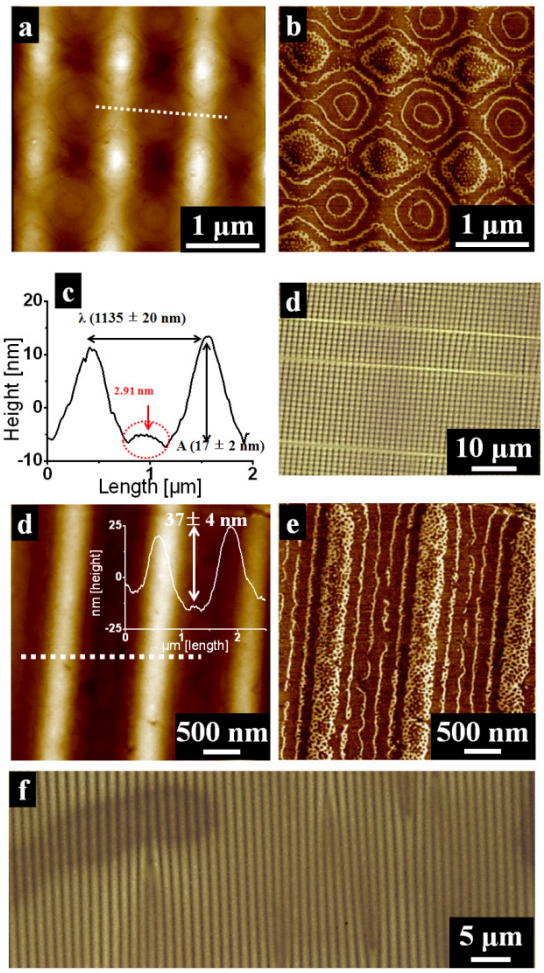

FIG. 2: SFM topography (a, d) and phase (b, e) images of 54 nm thick (lamella-forming PS-b-P2VP films prepared by spin-coating and subsequently annealed on 3D SiCN ceramic squared substrates (a, b) and on wrinkled SiCN ceramic substrates (d, e) under saturated chloroform vapor pressure. (c) Cross-sectional height profile along the indicated white dashed lines in (a). Optical images of the film on the 3D SiCN ceramic squared (d) and wrinkled substrates (f). Insets in (d) show cross-sectional height profiles along the indicated white dashed lines.

Similar processing conditions on flat substrates (not shown here) result in quantized film thickness corresponding to coexisting terraces of $L_{\perp}$ and $L_{\parallel}$ lamella. On corrugated substrates the formation of terraces (surface relief structures) is suppressed [2]. As seen in Figure 2b and e, the microphase separation follows the topographic pattern in that the sequenced patterns of in-plane oriented lamella $L_{\parallel}$ (featureless areas) and vertically oriented lamella $L_{\perp}$(stripes) can be linked to the topography of the substrate.

Figure 3 a,b presents films of PS-*b*-PB block copolymer prepared by floating procedure which includes a transfer of the spin-coated films via floating from mica to a water surface and then deposition onto the SiCN ceramic substrate. The phase image in Figure 2b shows a disordered structure which is a typical pattern after spin-coating. As shown in Figure 2c, upon thermal annealing the amplitude of the topographic features is reduced due to the polymer flow into the depressions, while the structures developed into distinct morphologies which follow the thickness-dependent phase behavior (Figure 2d): white stripes (PS cylinders $C_{\parallel}$) are confined to protruding patterns, while in-plane lamellae phase ($L_{\parallel}$) is generated in trenches of the substrate. The two main morphologies ($C_{\parallel}$, $L_{\parallel}$) are separated by narrow region of perforated lamellae (PL) in a circle boundary.

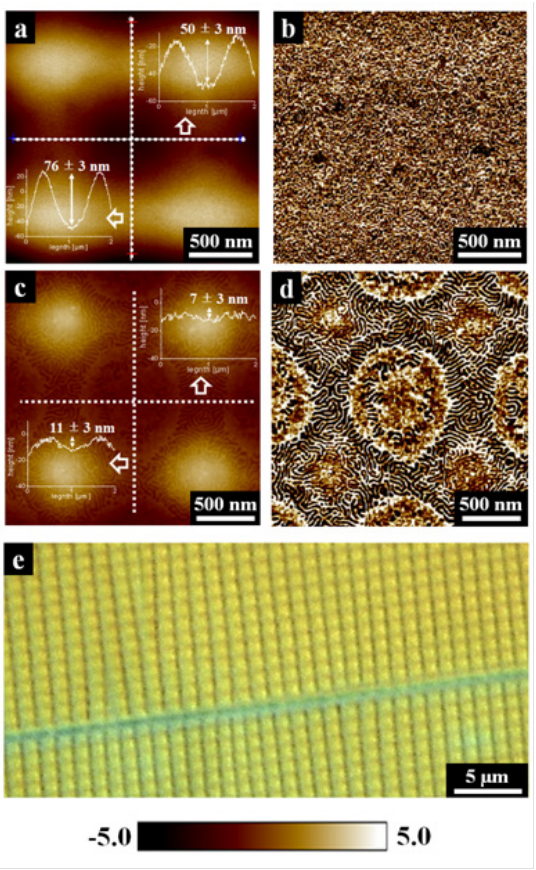

FIG. 3: SFM topography (a, c) and phase (b, d) images of a 24 nm thick PS-b-PB film (initial thickness after spin-coating on mica substrate): after deposition via floating onto the 3D SiCN ceramic substrate (a, b) and after thermal annealing at 120 °C for 18 h (c, d). (d) Optical microscopy image of the film. Insets in (a) and (c) show cross-sectional height profiles along the indicated white dashed lines.

By systematically varying film thickness, polymer deposition method, solvent concentration in the film during vapor annealing we demonstrate a fine tunability of the resulting hierarchical patterns which combine the topographic features and nanoscale chemical patterning, using low-cost pre-patterning method and guided self-assembly of polymer building blocks.

[1] Park, S.; Böker, A. J. Mater. Chem. **21**, 11734 (2011).

[2] Park, S.; Tsarkova, L.; Hiltl, S.; Roitsch, S.; Mayer, J.; Böker, A., Macromolecules **45**, 2494, (2012).

[3] Park, S.; Böker, A., Tsarkova, L., submitted (2015).

Impact of Interconnect Parasitics in Reconfigurable Nanoelectronic Logic Circuits

A. Heittmann, Q. Wang, and T.G. Noll

Electrical Engineering and Computer Systems, RWTH Aachen University, Germany

In reconfigurable logic circuits the interconnect plays a dominant role in the formation of arbitrary logic functions. By the scaling of nanoelectronic devices down to several nanometers it is expected that the performance of reconfigurable logic circuits gets increasingly impacted by the interconnect parasitics formed by resistances, capacitances, and inductances. Derived from a particular design style using nanoelectronic resistive switches (RS) as programmable elements an interconnect model focused on parasitics was developed which allows for the characterization of delay, power consumption, and area occupation of nanoelectronic circuits realized by resistive switches.

Fundamentally, resistive switches are two-terminal devices whose resistance can be programmed by a specific voltage pattern applied to the device [1]. Dependent on the applied stimulus the state of the resistive switch is considered to be either high-ohmic (high resistive state, HRS) or low-ohmic (low resistive state, LRS). Ideally, after programming the state of the RS appears to be non-volatile, but it also can be reprogrammed which designates RSs mainly as non-volatile memory elements as well as for the realization of reconfigurable interconnect.

In the case that a RS is in a LRS both RS the device electrodes appear to be connected while in the HRS both electrodes are more or less isolated from each other. If the HRS is large enough point-to-point connection can be established by switching particular RS cells between crossing wires into the LRS. Any point-to-point connection allows for merging of N digital signals into a mix signal which represents the number of input signals in digital high-state relative to the total number of independent inputs. By thresholding of the mix signal by an active amplifier circuit *N*-input AND gates (and equivalently *N*-input NAND gates) will be obtained which can be used to realize complex Boolean functions. As the ability of an amplifier to reliably discriminate individual levels of the mix signal diminishes considerably for large numbers of *N*, threshold gates with low *N* are considered in the following. Here, the particular focus is set on *N*=2. These threshold gates show maximum reliability. Fig.1a depicts the basic architecture of a reconfigurable circuit. Several word lines (WLs) running horizontally can connect to vertical bit lines (BLs) via RSs. Bit lines are considered as input signals for the amplifiers while word lines represent the corresponding output signals. The mixing operation occurs on the bit lines by summing up *N* currents resulting from Kirchoff's circuit law at crosspoints comprising a LRS.

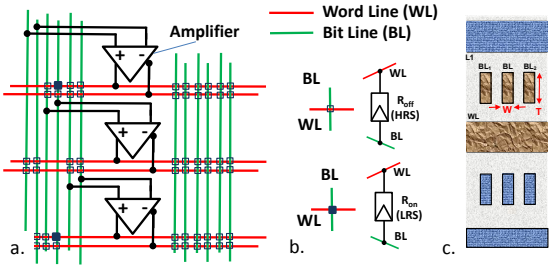

FIG. 1: Regular array of amplifiers with interconnect structure (a), connection of BL and WL by RS in LRS (b), 3D interconnect stack (c).

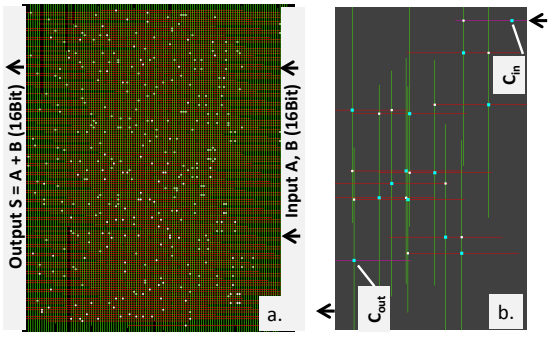

FIG. 2: Layout of a 16Bit Brent-Kung adder realized by RS connections (white dots) (a), multi-stage logic path (carry C_{in} to carry C_{out}) composed of interconnected WL (red) and BL (green) segments (b).

In order to characterize the impact of interconnect parasitics on the circuit performance reasonable wiring dimensions have to be anticipated than allows for the realization of several useful functions. In particular, the number of required (potential) connections per bit line (word line) is of interest. For that purpose, parallel prefix adder circuits (Brent-Kung [2], Han-Carlson [3], Kogge-Stone [4]) with different complexities were considered exemplarily. First, these circuits were transformed into a standard And-Inverter-Graph (AIG). After transformation, the AIG-representation

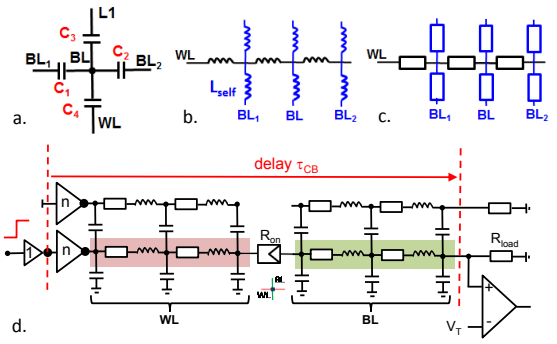

FIG. 3: Modeling of interconnect parasitics by coupling capacitances (a), self-inductances (b), and series resistance (c). Equivalent circuit of connected segments (d).

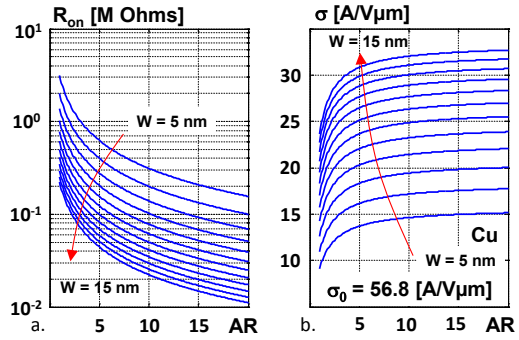

FIG. 4: Minimum On-resistance (LRS) (a) and series resistance per cell (b) over aspect ratio AR = T/W and different wire widths W.

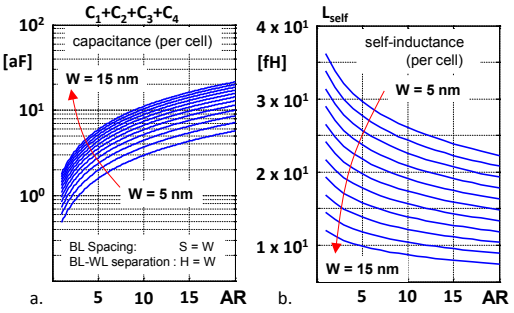

FIG. 5: Total cell capacitance (a) and self-inductance (b) over AR and different W.

was physically mapped on an array structure using a simulated annealing approach, cf. Fig. 2. By elaboration of various design alternatives and parameterizations it turned out that the successful realization of adder circuits (8 bit word size up to 16 bit word size) at least 128 connections per bit line (word line) have to be provided. By considering a minimal area occupation of $4F^2$ (F: lithographic resolution) per connection realized in a typical interconnect stack (cf. Fig. 1c) equivalent circuit elements for capacitance, inductance, and resistance (cf. Fig. 3a-c) were obtained by solving of Laplace's equation, equations for partial inductances, and the Fuchs-Sondheimer equation.

Additionally, in order to account for different possible LRSs (R_{on}) of the connection points the current carrying capacity of the bit lines and word lines had to be parameterized in order to reduce the risk of electromigration. This particular issue was covered by increasing the wire thickness *T*. By independent variation of *T* and the wire width *W* the equivalent circuit representing the connection between a WL and a BL (cf. Fig. 3d) was parameterized (cf. Fig. 4 and Fig. 5) and dynamically simulated. Especially for the delay (cf. Fig. 3d and Fig. 6a) it turned out the impact of inductance (self-inductance and mutual inductance) can be neglected while a technology-specific delay optimum exists for the unusual case of *T/W>>2* which mainly can be explained by the possibility to use RSs with very small R_{on} here (cf. Fig. 4a).

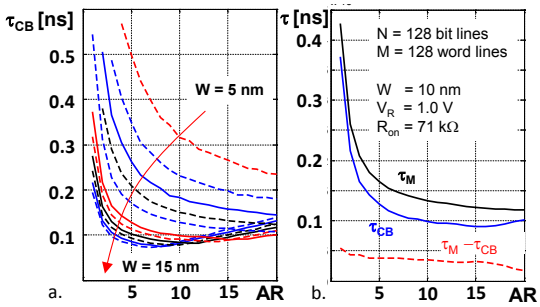

FIG. 6: Interconnect delay (a) and delay margin (b) over AR and different W.

The results clearly show that for future reconfigurable logic circuits wires with high aspect ratio may establish a preferred solution in order to minimize delays due to the interconnect.

[1] D.Strukov, G.Snider, D.Steward, R.Williams, "The Missing Memristor Found", Nature **53**, 80 (2008).

[2] R.P.Brent, H.T. Kung, "A Regular Layout for Parallel Adders", IEEE Trans. Comput., **C-31**, 260-264, (1982)

[3] T.Han, D.A. Carlson, "Fast area-efficient VLSI adders", Proc. 8th IEEE Symp. Comput.Arithmet., 49-56 (1987)

[4] P.M. Kogge, H.S. Stone, "A parallel algorithm for the efficient solution of a general class of recurrent equations", IEEE Trans. Comput., **C-22**, 8, 786-793 (1973)

Publications

Acres R. G., Feyer V., Tsud N., Cadino E., and Prince K. C.
Mechanisms of Aggregation of Cysteine Functionalized Gold Nanoparticles
Journal of Physical Chemistry C **118**, 10481 (2014)

Ahmed T., Albers R. C., Balatsky A. V., Friedrich C., and Zhu J.-X.
GW quasiparticle calculations with spin-orbit coupling for the light actinides
Physical Review B **89**, 035104 (2014)

Akhtari-Zavareh A., Carignan L. P., Yelon A., Ménard D., Kasama T., Herring R., Dunin-Borkowski R., McCartney M. R., and Kavanagh K. L.
Off-axis electron holography of ferromagnetic multilayer nanowires
Journal of Applied Physics **116**, 023902 (2014)

Akola J., Atodiresei N., Kalikka J., Larrucea J., and Jones R. O.
Structure and dynamics in liquid bismuth and Bi_n clusters: A density functional study
The Journal of Chemical Physics **141**, 194503 (2014)

Akola J., Jóvári P., Kaban I., Voleská I., Kolář J., Wágner T., and Jones R. O.
Structure, electronic, and vibrational properties of amorphous AsS_2 and $AgAsS_2$: Experimentally constrained density functional study
Physical Review B **89**, 064202 (2014)

Alekseev P. A., Nemkovski K. S., Kozlenko D. P., Menushenkov A. P., Yaroslavtsev A. A., Gribanov A. V., Clementyev E. S., Pantalei C., Klobes B., and Hermann R. P.
Coexistence of long range magnetic order and intervalent state of Eu in $EuCu_2(Si_xGe_{1-x})_2$: Evidence from neutron diffraction and spectroscopic studies
JETP Letters **99**, 164 (2014)

Alekseev P. A., Nemkovskiy K., Mignot J.-M., Clementyev E. S., Ivanov A. S., Rols S., Bewley R. I., Filipov V. B., and Shitsevalova N. Y.
Possible undercompensation effect in the Kondo insulator $(Yb,Tm)B_{12}$
Physical Review B **89**, 115121 (2014)

Altarev I., Babcock E., Gutsmiedl E., Knappe-Grüneberg S., Kuchler F., Lauer T., Link P., Lins T., Marino M., McAndrew J., Niessen B., Paul S., Beck D., Petzoldt G., Schläpfer U., Schnabel A., Sharma S., Singh J., Stoepler R., Stuiber S., Sturm M., Taubenheim B., Trahms L., Burghoff M., Voigt J., Zechlau T., Chesnevskaya S., Chupp T., Degenkolb S., Fan I., Fierlinger P., and Frei A.
A magnetically shielded room with ultra low residual field and gradient
Review of Scientific Instruments **85**, 075106 (2014)

Andreev I. V., Tchougreeff A. L., Kogerler P., and Rai R. C.
Magneto-optical Response of 3*d*-Decorated Polyoxomolybdates with ε-Keggin Structure
Inorganic Chemistry **53**, 2892 (2014)

Aoki Y., Wiemann C., Feyer V., Kim H. S., Schneider C. M., Ill-Yoo H., and Martin M.
Bulk mixed ion electron conduction in amorphous gallium oxide causes memristive behaviour
Nature Communications **5**, 3473 (2014)

Aslam N., Longo V., Keuning W., Roozeboom F., Kessels W. M. M., Waser R., and Hoffmann-Eifert S.
Influence of stoichiometry on the performance of MIM capacitors from plasma-assisted ALD $Sr_xTi_yO_z$ films
Physica Status Solidi A **211**, 389 (2014)

Aslam N., Longo V., Rodenbucher C., Roozeboom F., Kessels W. M. M., Szot K., Waser R., and Hoffmann-Eifert S.
Impact of composition and crystallization behavior of atomic layer deposited strontium titanate films on the resistive switching of Pt/STO/TiN devices
Journal of Applied Physics **116**, 064503 (2014)

Atodiresei N., Caciuc V., and Lazić P.
A Short Review on the Magnetic Effects Occurring at Organic Ferromagnetic Interfaces Formed between Benzene-Like Molecules and Graphene with Ferromagnetic Surfaces
Zeitschrift für Naturforschung A **69a**, 360 (2014)

Atodiresei N. and Raman K. V.
Interface-assisted spintronics: Tailoring at the molecular scale
MRS Bulletin **39**, 596 (2014)

Azpiroz J. I., Eiguren A., Bergara A., Pettini G., and Modugno M.
Breakdown of the Peierls substitution for the Haldane model with ultracold atoms
Physical Review A **90**, 033609 (2014)

Babajani N., Kaulen C., Homberger M., Mennicken M., Waser R., Simon U., and Karthauser S.
Directed Immobilization of Janus-AuNP in Heterometallic Nanogaps: a Key Step Toward Integration of Functional Molecular Units in Nanoelectronics
Journal of Physical Chemistry C **118**, 27142 (2014)

Babichev A. V., Gasumyants V. E., Egorov A. Y., Vitusevich S., and Tchernycheva M.
Contact properties to CVD-graphene on GaAs substrates for optoelectronic applications
Nanotechnology **25**, 335707 (2014)

Bäcker M., Kramer F., Huck C., Poghossian A., Bratov A., Abramova N., and Schöning M. J.
Planar and 3D interdigitated electrodes for biosensing applications: The impact of a dielectric barrier on the sensor properties
Physica status solidi A **211**, 1357 (2014)

Baldizzone C., Mezzavilla S., Carvalho H. W. P., Meier J. C., Schuppert A. K., Heggen M., Galeano C., Grunwaldt J. D., Schüth F., and Mayrhofer K. J. J.
Confined-space alloying of Nanoparticles for the synthesis of efficient fuel cell catalysts
Angewandte Chemie: International Edition **53**, 1 (2014)

Bandodkar A. J., Molinnus D., Mirza O., Guinovart T., Windmiller J. R., Valdés-Ramírez G., Andrade F. J., Schöning M. J., and Wang J.
Epidermal tattoo potentiometric sodium sensors with wireless signal transduction for continuous non-invasive sweat monitoring
Biosensors and Bioelectronics **54**, 603 (2014)

Barzanjeh S., DiVincenzo D., and Terhal B. M.
Dispersive Qubit Measurement by Interferometry with Parametric Amplifiers
Physical Review B **90**, 134515 (2014)

Battista F., Haupt F., and Splettstoesser J.
Correlations between charge and energy current in ac-driven coherent conductors
Journal of Physics: Conference Series **568**, 052008 (2014)

Battista F., Haupt F., and Splettstoesser J.
Energy and power fluctuations in ac-driven coherent conductors
Physical Review B **90**, 085418 (2014)

Baum M., Leist J., Finger T., Schmalzl K., Hiess A., Regnault L. P., Becker P., Bohatý L., Eckold G., and Braden M.
Kinetics of the multiferroic switching in $MnWO_4$
Physical Review B **89**, 144406 (2014)

Beattie N. S., Zoppi G., See P., Farrer I., Duchamp M., Morrison D. J., Miles R. W., and Ritchie D. A.
Analysis of As/GaAs quantum dot solar cells using Suns-Voc measurements
Solar Energy Materials & Solar Cells **130**, 241 (2014)

Beleggia M., Kasama T., Larson D. J., Kelly T. F., Dunin-Borkowski R., and Pozzi G.
Towards quantitative off-axis electron holographic mapping of the electric field around the tip of a sharp biased metallic needle
Journal of Applied Physics **116**, 024305 (2014)

Bensmann S., Gaussmann F., Lewin M., Wuppen J., Nyga S., Janzen C., Jungbluth B., and Taubner T.
Near-field imaging and spectroscopy of locally strained GaN using an IR broadband laser
Optic Express **22**, 22369 (2014)

Bessas D., Merkel D. G., Chumakov A. I., Ruffer R., Hermann R. P., Sergueev I., Mahmoud A., Klobes B., McGuire M. A., Sougrati M. T., and Stievano L.
Nuclear Forward Scattering of Synchrotron Radiation by Ru-99
Physical Review Letters **113**, 147601 (2014)

Bessas D., Simon R. E., Friese K., Koza M., and Hermann R. P.
Lattice dynamics in intermetallic Mg_2Ge and Mg_2Si
Journal of Physics: Condensed Matter **26**, 485401 (2014)

Black-Schaffer A. M. and Honerkamp C.
Chiral d-wave superconductivity in doped graphene
Journal of Physics: Condensed Matter **26**, 423201(2014)

Bocquet F., Bisson R., Themlin J.-M., Layet J.-M., and Angot T.
Deuterium adsorption on (and desorption from) SiC(0 0 0 1)-(3 × 3), (√3×√3) *R*30°, (6√3×6√3) *R*30° and quasi-free-standing graphene obtained by hydrogen intercalation
Journal of Physics D: Applied Physics **47**, 094014 (2014)

Boothroyd C. B., Moreno M. S., Duchamp M., KovACS A., Monge N., Morales G. M., Barbero C. A., and Dunin-Borkowski R.
Atomic resolution imaging and spectroscopy of barium atoms and functional groups on graphene oxide
Ultramicroscopy **145**, 66 (2014)

Botezat O., van Leusen J., Baca S. G., Hermann R., Kravtsov V. C., Filippova I. G., Hauser J., Speldrich M., Krämer K. W., Liu S.-X., Decurtins S., and Kögerler P.
Interpenetrated (8,3)-c and (10,3)-b Metal–Organic Frameworks Based on $\{Fe^{III}_3\}$ and $\{Fe^{III}_2Co^{II}\}$ Pivalate Spin Clusters
Crystal Growth & Design **14**, 4721 (2014)

Bouhassoune M., Zimmermann B., Mavropoulos P., Wortmann D., Dederichs P. H., Blügel S., and Lounis S.
Quantum well states and amplified spin-dependent Friedel oscillations in thin films
Nature Communications **5**, 5558 (2014)

Boussinot G. and Brener E.
Achieving realistic interface kinetics in phase-field models with a diffusional contrast
Physical Review E **89**, 060402 (2014)

Braakman F. R., Danon J., Schreiber L. R., Wegscheider W., and Vandersypen L. M. K.
Dynamics of spin-flip photon-assisted tunneling
Physical Review B **89**, 075417 (2014)

Brand J., Stunault A., Wurmehl S., Harnagea L., Büchner B., Meven M., and Braden M.
Spin susceptibility in superconducting LiFeAs studied by polarized neutron diffraction
Physical Review B **89**, 045141 (2014)

Brede J., Atodiresei N., Caciuc V., Bazarnik M., Al-Zubi A., Blügel S., and Wiesendanger R.
Long-range magnetic coupling between nanoscale organic–metal hybrids mediated by a nanoskyrmion lattice
Nature Nanotechnology **9**, 1018 (2014)

Breinlich C., Buchholz M., Moors M., Le Moal S., Becker C., and Wandelt K.
Scanning Tunneling Microscopy Investigation of Ultrathin Titanium Oxide Films Grown on $Pt_3Ti(111)$
The Journal of Physical Chemistry C **118**, 6186 (2014)

Breuckmann N. P. and Terhal B. M.
Space-time circuit-to-Hamiltonian construction and its applications
Journal of Physics A: Mathematical and Theoretical **47**, 195304 (2014)

Brisbois M., Krins N., Hermann R. P., Schrijnemakers A., Cloots R., Vertruyen B., and Boschini F.
Spray-drying synthesis of Na_2FePO_4F/carbon powders for lithium-ion batteries
Materials Letters **130**, 263 (2014)

Brok E., Sales M., Lefmann K., Kuhn L. T., Roessli B., Robinson P., McEnroe S. A., Harrison R. J., and Schmidt W.
Experimental evidence for lamellar magnetism in hemo-ilmenite by polarized neutron scattering
Physical Review B **89**, 054430 (2014)

Buchkremer A., Linn M. J., Timper J. U., Eckert T., Mayer J., Richtering W., von Plessen G., and Simon U.
Synthesis and Internal Structure of Finite-Size DNA-Gold Nanoparticle Assemblies
The Journal of Physical Chemistry C **118**, 7174 (2014)

Bürgler D., Muto S., Rusz J., Tatsumi K., Adam R., Arai S., Kocevski V., Oppeneer P. M., and Schneider C. M.
Quantitative Characterization of Magnetic Materials Based on ElectronMagnetic Circular Dichroism with Nanometric Resolution Using the JEM-1000KRS Ultra-High Voltage STEM
JEOL News **49**, 49 (2014)

Cai B., Schwarzkopf J., Hollmann E., Schmidbauer M., Abdel-Hamed M. O., and Wordenweber R.
Anisotropic ferroelectric properties of anisotropically strained epitaxial $NaNbO_3$ films
Journal of Applied Physics **115** 224103 (2014)

Caspers C., Gloskovskii A., Drube W., Schneider C. M., and Müller M.
“Conductive” yttria-stabilized zirconia as an epitaxial template for oxide heterostructures
Journal of Applied Physics **115**, 17C111 (2014)

Catelani G.
Parity switching and decoherence by quasiparticles in single-junction transmons
Physical Review B **89**, 094522 (2014)

Cerfontaine P., Botzem T., DiVincenzo D., and Bluhm H.
High-Fidelity Single-Qubit Gates for Two-Electron Spin Qubits in GaAs
Physical Review Letters **113**, 150501 (2014)

Čermák P., Javorský P., Kratochvílová M., Pajskr K., Klicpera M., Ouladdiaf B., Lemée-Cailleau M.-H., Rodriguez-Carvajal J., and Boehm M.
Magnetic structures of non-cerium analogues of heavy-fermion Ce_2RhIn_8: The case of Nd_2RhIn_8, Dy_2RhIn_8, and Er_2RhIn_8
Physical Review B **89**, 184409 (2014)

Chang K., Zhang Y., Wang Y., Zeng J., Xu X., Qiu Y., Krause H.-J., Xie X., and Offenhäusser A.
A simple SQUID system with one operational amplifier as readout electronics
Superconductor Science and Technology **27**, 115004 (2014)

Chang S. L. Y., Singh A., Hocking R. K., Dwyer C., and Spiccia L.
Nanoscale structural disorder in manganese oxide particles embedded in Nafion
Journal of Materials Chemistry A **2**, 3730 (2014)

Chen Y. G., Francescato Y., Caldwell J. D., Giannini V., Mass T. W. W., Glembocki O. J., Bezares F. J., Taubner T., Kasica R., Hong M. H., and Maier S. A.
Spectral Tuning of Localized Surface Phonon Polariton Resonators for Low-Loss Mid-IR Applications
ACS Photonics **1**, 718 (2014)

Cherpak N. T., Lavrinovich A. A., Gubin A. I., and Vitusevich S.
Direct-current-assisted microwave quenching of $YBa_2Cu_3O_{7-\delta}$ coplanar waveguide to a highly dissipative state
Applied Physics Letters **105**, 022601 (2014)

Chumakov A. I., Monaco G., Carini Jr. G., Carini G., D’Angelo G., Gilioli E., Tripodo G., Zanatta M., Winkler B., Milman V., Refson K., Dove M. T., Fontana A., Dubrovinskaia N., Dubrovinsky L., Keding R., Yue Y. Z., Hermann R., Bosak A., Bessas D., Wehinger B., Crichton W. A., Krisch M., Rüffer R., and Baldi G.
Role of Disorder in the Thermodynamics and Atomic Dynamics of Glasses
Physical Review Letters **112**, 025502 (2014)

Classen L., Scherer M. M., and Honerkamp C.
Instabilities on graphene's honeycomb lattice with electron-phonon interactions
Physical Review B **90**, 035122 (2014)

Claudio T., Bessas D., Birke C. S., Kieslich G., Panthöfer M., Sergueev I., Tremel W., and Hermann R.
Enhanced Debye level in nano $Zn_{1+x}Sb$, $FeSb_2$, and NiSb: Nuclear inelastic spectroscopy on ^{121}Sb
Physica Status Solidi B **251**, 919 (2014)

Claudio T., Stein N., Stroppa D. G., Klobes B., Koza M. M., Kudejova P., Petermann N., Wiggers H., Schierning G., and Hermann R.
Nanocrystalline silicon: lattice dynamics and enhanced thermoelectric properties
Physical Chemistry, Chemical Physics **16**, 25701 (2014)

Couto N. J. G., Costanzo D., Engels S., Ki D. K., Watanabe K., Taniguchi T., Stampfer C., Guinea F., and Morpurgo A. F.
Random Strain Fluctuations as Dominant Disorder Source for High-Quality On-Substrate Graphene Devices
Physical Review X **4**, 041019 (2014)

Cui C., Gan L., Neumann M., Heggen M., and Strasser P.
Carbon Monoxide-Assisted Size-Confinement of Bimetallic Alloy Nanoparticles
Journal oft he American Chemical Society **136**, 4813 (2014)

Czaja P., Freimuth F., Weischenberg J., Blügel S., and Mokrousov Y.
Anomalous Hall effect in ferromagnets with Gaussian disorder
Physical Review B **89**, 014411 (2014)

Czeschik A., Offenhausser A., and Wolfrum B.
Fabrication of MEA-based nanocavity sensor arrays for extracellular recording of action potentials
Physica Status Solidi A **211**, 1462 (2014)

Dadda J., Müller E., Perlt S., Höche T., Hermann R., and Neubrand A.
Evolution of phase segregation and eutectic structures in $AgPb_{18}SbTe_{20}$
Physica Status Solidi A **211**, 1276 (2014)

Dammers J., ChocholACS H., Eich E., Boers F., Faley M., Dunin-Borkowski R., and Shah N. J.
Source localization of brain activity using helium free interferometer
Applied Physics Letters **104**, 213705 (2014)

Dang H. T., Ai X. Y., Millis A. J., and Marianetti C. A.
Density functional plus dynamical mean-field theory of the metal-insulator transition in early transition-metal oxides
Physical Review B **90**, 125114 (2014)

Danilchenko B. A., Tripachko N. A., Belyaev A. E., Vitusevich S., Hardtdegen H., and Lüth H.
High-field quasi-ballistic transport in AlGaN/GaN heterostructures.
Applied Physics Letters **104**, 072105 (2014)

Dauber J., Terres B., Volk C., Trellenkamp S., and Stampfer C.
Reducing disorder in graphene nanoribbons by chemical edge modification
Applied Physics Letters **104**, 083105 (2014)

Dauth M., Wiessner M., Feyer V., Schöll A., Puschnig P., Reinert F., and Kümmel S.
Angle resolved photoemission from organic semiconductors: orbital imaging beyond the molecular orbital interpretation
New Journal of Physics **16**, 103005 (2014)

de la Pena D. S., Scherer M. M., and Honerkamp C.
Electronic instabilities of the AA-honeycomb bilayer
Annalen der Physik **526**, 366 (2014)

De Souza R. A., Gunkel F., Hoffmann-Eifert S., and Dittmann R.
Finite-size versus interface-proximity effects in thin-film epitaxial $SrTiO_3$
Physical Review B **89**, 241401(R) (2014)

De Souza R. A., Voisin C., Schraknepper H., Teusner M., Kessel M., Dufour P., Tenailleau C., and Guillemet-Fritsch S.
Complex diffusion behavior of oxygen in nanocrystalline $BaTiO_3$ ceramics
Physical Chemistry Chemical Physics **16**, 2568 (2014)

Deák A., Simon E., Balogh L., Szunyogh L., dos Santos Dias M., and Staunton J. B.
Metallic magnetism at finite temperatures studied by relativistic disordered moment description: Theory and applications
Physical Review B **89**, 224401 (2014)

Decker R., Bazarnik M., Atodiresei N., Caciuc V., Blügel S., and Wiesendanger R.
Local tunnel magnetoresistance of an iron intercalated graphene-based heterostructure
Journal of Physics: Condensed Matter **26**, 394004 (2014)

Deringer V. L. and Dronskowski R.
Ab initio study of molecular and atomic oxygen on GeTe(111) surfaces
Journal of Applied Physics **116**, 173703 (2014)

Deringer V. L. and Dronskowski R.
Pauling's third rule beyond the bulk: chemical bonding at quartz-type GeO_2 surfaces
Chemical Science **5**, 894 (2014)

Deringer V. L., Stoffel R. P., and Dronskowski R.
Vibrational and thermodynamic properties of GeSe in the quasiharmonic approximation
Physical Review B **89**, 094303 (2014)

Deringer V. L., Stoffel R. P., and Dronskowski R.
Thermochemical Ranking and Dynamic Stability of TeO_2 Polymorphs from Ab Initio Theory
Crystal Growth & Design **14**, 871 (2014)

Deringer V. L., Zhang W., Lumeij M., Maintz S., Wuttig M., Mazzarello R., and Dronskowski R.
Bonding Nature of Local Structural Motifs in Amorphous GeTe
Angewandte Chemie International Edition **53**, 10817 (2014)

Ding K., Aeberhard U., Lambertz A., Smirnov V., Holländer B., Finger F., and Rau U.
Impact of doped microcrystalline silicon oxide layers on crystalline silicon surface passivation
Canadian Journal of Physics **92**, 758 (2014)

Disch S., Hermann R. P., Wetterskog E., Podlesnyak A. A., An K., Hyeon T., Salazar-Alvarez G., Bergstrom L., and Bruckel T.
Spin excitations in cubic maghemite nanoparticles studied by time-of-flight neutron spectroscopy
Physical Review B **89**, 064402 (2014)

Divin Y. and Pandya H. K. B.
Feasibility of ECE measurements using Hilbert-transform spectral analysis
Fusion science and technology **65**, 399 (2014)

Divin Y., Snezhko A., Lyatti M., Poppe U., and Pavlovskiy V.
Terahertz Applications of Hilbert-Transform Spectral Analysis
IEEE Transactions on Applied Superconductivity **24**, 1500807 (2014)

Drees Y., Li Z. W., Piovano A., Castellan J. P., Komarek A. C., Ricci A., Rotter M., Schmidt W., Lamago D., Sobolev O., Rütt U., Gutowski O., and Sprung M.
Hour-glass magnetic excitations induced by nanoscopic phase separation in cobalt oxides
Nature Communications **5**, 5731 (2014)

Drogeler M., Volmer F., Wolter M., Terres B., Watanabe K., Taniguchi T., Guntherodt G., Stampfer C., and Beschoten B.
Nanosecond Spin Lifetimes in Single- and Few-Layer Graphene-hBN Heterostructures at Room Temperature
Nano Letters **14**, 6050 (2014)

Duchamp M., Xu Q., and Dunin-Borkowski R.
Convenient Preparation of High-Quality Specimens for Annealing Experiments in the Transmission Electron Microscope
Microscopy and Microanalysis **20**, 1638 (2014)

Duden T., Thust A., Kumpf C., and Tautz S.
Focal-Series Reconstruction in Low-Energy Electron Microscopy
Microscopy and Microanalysis **20**, 968 (2014)

Dwyer C.
Localizaton of high-energy electron scattering from atomic vibrations
Physical Review B **89**, 054103 (2014)

Eich A., Michiardi M., Bihlmayer G., Zhu X.-G., Mi J.-L., Iversen B. B., Wiesendanger R., Hofmann P., Khajetoorians A. A., and Wiebe J.
Intra- and interband electron scattering in a hybrid topological insulator: Bismuth bilayer on Bi_2Se_3
Physical Review B **90**, 155414 (2014)

El-Kareh L., Bihlmayer G., Buchter A., Bentmann H., Blügel S., Reinert F., and Bode M.
A combined experimental and theoretical study of Rashba-split surface states on the (√3×√3) Pb/Ag(111)*R*30° surface
New Journal of Physics **16**, 045017 (2014)

El-Kareh L., Mehring P., Caciuc V., Atodiresei N., Beimborn A., Blügel S., and Westphal C.
Self-assembled monolayers of methylselenolate on the Au(111) surface: A combined STM and DFT study
Surface Science **619**, 67 (2014)

Engels S., Terres B., Epping A., Khodkov T., Watanabe K., Taniguchi T., Beschoten B., and Stampfer C.
Limitations to Carrier Mobility and Phase-Coherent Transport in Bilayer Graphene
Physical Review Letters **113**, 126801 (2014)

Engels S., Terres B., Klein F., Reichardt S., Goldsche M., Kuhlen S., Watanabe K., Taniguchi T., and Stampfer C.
Impact of thermal annealing on graphene devices encapsulated in hexagonal boron nitride
Physica Status Solidi B **251**, 2545 (2014)

Fahrendorf S., Matthes F., Bürgler D., Schneider C. M., Atodiresei N., Caciuc V., Blügel S., Besson C., and Kögerler P.
Structural integrity of single bis(phthalocyaninato)-neodymium(III) molecules on metal surfaces with different reactivity
SPIN **04**, 1440007 (2014)

Faley M., Meertens D., Dunin-Borkowski R., and Poppe U.
Graphoepitaxial high-T_c SQUIDS
Journal of Physics: Conference Series **507**, 042009 (2014)

Feigl L., Yudin P., Stolichnov I., Sluka T., Shapovalov K., Mtebwa M., Sandu C. S., Wei X., Tagantsev A. K., and Setter N.
Controlled stripes of ultrafine ferroelectric domains
Nature Communications **5**, 4677 (2014)

Ferch S., Linn E., Waser R., and Menzel S.
Simulation and comparison of two sequential logic-in-memory approaches using a dynamic electrochemical metallization cell model
Microelectron Journal **45**, 1416 (2014)

Feyer V., Graus M., Nigge P., Wiessner M., Acres R. G., Wiemann C., Schneider C. M., Scholl A., and Reinert F.
Adsorption geometry and electronic structure of iron phthalocyanine on Ag surfaces: A LEED and photoelectron momentum mapping study
Surface Science **621**, 64 (2014)

Finken M., Wille A., Reuters B., Hollander B., Heuken M., Kalisch H., and Vescan A.
Growth properties and electrochemical characterization of InGaN photoanodes with different In concentrations
Physics Status Solidi C **11**, 746 (2014)

Fleck K., Bottger U., Waser R., and Menzel S.
Interrelation of Sweep and Pulse Analysis of the SET Process in $SrTiO_3$ Resistive Switching Memories
IEEE Electron Device Letters **35**, 924 (2014)

Forbes B. D., Houben L., Mayer J., Dunin-Borkowski R., and Allen L. J.
Elemental mapping in achromatic atomic-resolution energy-filtered transmission electron microscopy
Ultramicroscopy **147**, 98 (2014)

Franz C., Freimuth F., Pfleiderer C., Bauer A., Ritz R., Schnarr C., Duvinage C., Adams T., Blügel S., Rosch A., and Mokrousov Y.
Real-Space and Reciprocal-Space Berry Phases in the Hall Effect of $Mn_{1-x}Fe_xSi$
Physical Review Letters **112**, 186601 (2014)

Freimuth F., Blügel S., and Mokrousov Y.
Spin-orbit torques in Co/Pt(111) and Mn/W(001) magnetic bilayers from first principles
Physical Review B **90**, 174423 (2014)

Freimuth F., Blügel S., and Mokrousov Y.
Berry phase theory of Dzyaloshinskii–Moriya interaction and spin–orbit torques
Journal of Physics: Condensed Matter **26**, 104202 (2014)

Friese K. and Grzechnik A.
Twinning and pseudosymmetry under high pressure
Zeitschrift für Kristallographie: Crystalline Materials **229**, 158 (2014)

Fuglewicz B., Plinski E. F., Szustakowski M., Jarzab P. P., Plinska S., Cebrat M., Nowak K., Augustyn L., Walczakowski M. J., Mikulics M., and Palka N.
Selected nonapeptides in terahertz light
Optica Applicata **44**, 159 (2014)

Fukushima T., Katayama-Yoshida H., Sato K., Bihlmayer G., Mavropoulos P., Bauer D., Zeller R., and Dederichs P. H.
Hubbard U calculations for gap states in dilute magnetic semiconductors
Journal of Physics: Condensed Matter **26**, 274202 (2014)

Fukushima T., Katayama-Yoshida H., Sato K., Fujii H., Rabel E., Zeller R., Dederichs P. H., Zhang W., and Mazzarello R.
First-principles study of magnetic interactions in 3*d* transition metal-doped phase-change materials
Physical Review B **90**, 144417 (2014)

Furukawa Y., Fang X., and Kogerler P.
Spin dynamics of the giant polyoxometalate molecule $\{Mn_{40}W_{224}\}$ studied by NMR
Journal of Physics: Condensed Matter **26**, 196003 (2014)

Galanakis I., Özdoğan K., and Sasioglu E.
High-T_C fully compensated ferrimagnetic semiconductors as spin-filter materials: the case of CrV_XAl (X = Ti, Zr, Hf) Heusler compounds
Journal of Physics: Condensed Matter **26**, 086003 (2014)

Galanakis I., Özdoğan K., Şaşıoğlu E., and Blügel S.
Effect of disorder on the magnetic properties of cubic Mn_2Ru_xGa compounds: A first-principles study
Journal of Applied Physics **116**, 033903 (2014)

Galanakis I., Özdoğan K., Şaşıoğlu E., and Blügel S.
Conditions for spin-gapless semiconducting behavior in Mn_2CoAl inverse Heusler compound
Journal of Applied Physics **115**, 093908 (2014)

Galanakis I., Şaşıoğlu E., Blügel S., and Özdoğan K.
Voids-driven breakdown of the local-symmetry and Slater-Pauling rule in half-metallic Heusler compounds
Physical Review B **90**, 064408 (2014)

Gan L., Cui C., Heggen M., Dionigi F., Rudi S., and Strasser P.
Element-specific anisotropic growth of shaped platinum alloy nanocrystals
Science **346**, 1502 (2014)

Gasparyan F. and Vitusevich S.
Millimeter wave detectors developed on the basis of doped semiconductors
Modern Physics Letters B **28**, 1450001 (2014)

Gatta G. D., Vignola P., and Meven M.
On the complex H-bonding network in paravauxite, $Fe^{2+}Al_2(PO_4)_2(OH)_2{\cdot}8H_2O$: A single-crystal neutron diffraction study
Mineralogical Magazine **78**, 841 (2014)

Ghisolfi A., Monakhov K. Y., Pattacini R., Braunstein P., Lopez X., de Graaf C., Speldrich M., van Leusen J., Schilder H., and Kogerler P.
A comparative synthetic, magnetic and theoretical study of functional M_4Cl_4 cubane-type Co(II) and Ni(II) complexes
Dalton T **43**, 7847 (2014)

Gilles S., Steppert A. K., Schaal P. A., Barth M., Niewoehner L., and Simon U.
Challenging Material Patterning: Fine Lithography on Coarse Substrates
Scanning **36**, 362 (2014)

Golor M., Reckling T., Classen L., Scherer M. M., and Wessel S.
Ground-state phase diagram of the half-filled bilayer Hubbard model
Physical Review B **90**, 195131 (2014)

Golor M., Wessel S., and Schmidt M. J.
Quantum Nature of Edge Magnetism in Graphene
Physical Review Letters **112**, 046601 (2014)

Gottlob D. M., Jansen T., Hoppe M., Burgler D. E., and Schneider C. M.
Epitaxial Cu(001) films grown on a Cr/Ag/Fe/GaAs(001) buffer system
Thin Solid Films **562**, 250 (2014)

Gourdon O., Gottschlich M., Persson J., Cruz C. d. l., Petricek V., McGuire M. A., and Brückel T.
Toward a better understanding of the magnetocaloric effect: An experimental and theoretical study of $MnFe_4Si_3$
Journal of Solid State Chemistry **216**, 56 (2014)

Green M., Esat T., Wagner C., Leinen P., Grötsch A., Tautz S., and Temirov R.
Patterning a hydrogen-bonded molecular monolayer with a hand-controlled scanning probe microscope
Beilstein Journal of Nanotechnology **5**, 1926 (2014)

Grieshammer S., Grope B. O. H., Koettgen J., and Martin M.
A combined DFT plus U and Monte Carlo study on rare earth doped ceria
Phys Chem Chem Phys **16**, 9974 (2014

Grushko B. and Kapush D.
A refinement of the Al-Ni-Pt phase diagram
Journal of Alloys and Compounds **594**, 127 (2014)

Grushko B., Kapush D., Samuha S., and Meshi L.
A study of the Al-Pd-Pt alloy system
Journal of Alloys and Compounds **600**, 125 (2014)

Grutzmacher D., Wirths S., Rieger T., Buca D., Stoica T., Lepsa M. I., Zhao Q.-T., and Mantl S.,
(Keynote) Epitaxy-Based Strain-Engineering Methods for Advanced Devices
ECS Transactions **64**, 85 (2014)

Grzechnik A. and Friese K.
Reversible pressure-induced first-order phase transitions in anion-excess fluorite KY_3F_{10} studied with single-crystal X-ray diffraction
Solid State Sciences **30**, 61 (2014)

Gul O., Demarina N., Blomers C., Rieger T., Luth H., Lepsa M. I., Grutzmacher D., and Schapers T.
Flux periodic magnetoconductance oscillations in GaAs/InAs core/shell nanowires
Physical Review B **89**, 045417 (2014)

Gul O., Gunel H. Y., Luth H., Rieger T., Wenz T., Haas F., Lepsa M., Panaitov G., Grutzmacher D., and Schapers T.
Giant Magnetoconductance Oscillations in Hybrid Superconductor-Semiconductor Core/Shell Nanowire Devices
Nano Letters **14**, 6269 (2014)

Gundareva I. and Divin Y.
Optimization of electrical and structural parameters of $YBa_2Cu_3O_{7-x}$ thin-film bicrystal Josephson junctions with chemical and thermal treatments of substrates
Journal of Physics: Conference Series **507**, 042014 (2014)

Gunel H. Y., Borgwardt N., Batov I. E., Hardtdegen H., Sladek K., Panaitov G., Grutzmacher D., and Schaepers T.
Crossover from Josephson Effect to Single Interface Andreev Reflection in Asymmetric Superconductor/Nanowire Junctions
Nano Letters **14**, 4977 (2014)

Guo Y., Miyamoto K.-i., Wagner T., Schöning M. J., and Yoshinobu T.
Device simulation of the light-addressable potentiometric sensor for the investigation of the spatial resolution
Sensors and Actuators B **204**, 659 (2014)

Guo Y., Miyamoto K.-i., Wagner T., Schöning M. J., and Yoshinobu T.
Theoretical study and simulation of light-addressable potentiometric sensors
Physica Status Solidi A **211**, 1467 (2014)

Guo Y., Seki K., Miyamoto K.-i., Wagner T., Schöning M. J., and Yoshinobu T.
Novel photoexcitation method for light-addressable potentiometric sensor with higher spatial resolution
Applied Physics Express **7**, 067301 (2014)

Gushchina E. V., Dunaevskii M. S., Alekseev P. A., Ozben E. D., Makarenko I. V., and Titkov A. N.
Behavior of Charges Locally Injected into Nanothin High-k $SmScO_3$ Dielectric
Technical Physics **59**, 1540 (2014)

Haab A., Mikulics M., Sutter E., Jin J., Stoica T., Kardynal B., Rieger T., Grützmacher D., and Hardtdegen H.
Evolution and characteristics of GaN nanowires produced via maskless reactive ion etching
Nanotechnology **25**, 255301 (2014)

Hallas A. M., Cheng J. G., Wiebe C. R., Arevalo-Lopez A. M., Silverstein H. J., Su Y., Sarte P. M., Zhou H. D., Choi E. S., Attfield J. P., and Luke G. M.
Incipient Ferromagnetism in $Tb_2Ge_2O_7$: Application of Chemical Pressure to the Enigmatic Spin-Liquid Compound $Tb_2Ti_2O_7$
Physical Review Letters **113**, 267205 (2014)

Hapala P., Temirov R., Tautz F. S., and Jelinek P.
Origin of High-Resolution IETS-STM Images of Organic Molecules with Functionalized Tips
Physical Review Letters **113**, 226101 (2014)

Hapala P., Kichin G., Wagner C., Tautz F. S., Temirov R., and Jelinek P.
Mechanism of high-resolution STM/AFM imaging with functionalized tips
Physical Review B **90**, 085421 (2014)

Heedt S., Wehrmann I., Gerster T., Wenk P., Kettemann S., Sladek K., Hardtdegen H., Bringer A., Schubert J., Demarina N., Grutzmacher D., and Schapers T.
Spin injection and spin-orbit coupling in low-dimensional semiconductor nanostructures
SPIE Proceedings Spintronics VII **9167,** 916723 (2014)

Heggen M. and Feuerbacher M.
Core structure and motion of metadislocations in the orthorhombic structurally complex alloy $Al_{13}Co_4$
Materials Research Letters **2**, 146 (2014)

Heidelmann M., Barthel J., Cox G., and Weirich T.
Periodic Cation Segregation in $Cs_{0.44}[Nb_{2.54}W_{2.46}O_{14}]$ Quantified by High-Resolution Scanning Transmission Electron Microscopy
Microscopy and Microanalysis **20**, 1453 (2014)

Heidelmann M., Heggen M., and Feuerbacher M.
On the stability of metadislocations with 16 associated phason planes
Intermetallics **53**, 187 (2014)

Heittmann A. and Noll T. G.
Variability Analysis of a Hybrid CMOS/RS Nanoelectronic Calibration Circuit
IEEE International Symposium on Circuits and Systems (ISCAS), 1656 (2014)

Hell M., Wegewijs M. R., and DiVincenzo D. P.
Coherent backaction of quantum dot detectors: Qubit isospin precession
Physical Review B **89**, 195405 (2014)

Helmes J. and Wessel S.
Entanglement entropy scaling in the bilayer Heisenberg spin system
Physical Review B **89**, 245120 (2014)

Herlitschke M., Tchougréeff A. L., Soudackov A. V., Klobes B., Stork L., Dronskowski R., and Hermann R.
Magnetism and lattice dynamics of FeNCN compared to FeO
New Journal of Chemistry **38**, 4670 (2014)

Herpers A., Lenser C., Park C., Offi F., Borgatti F., Panaccione G., Menzel S., Waser R., and Dittmann R.
Spectroscopic Proof of the Correlation between Redox-State and Charge-Carrier Transport at the Interface of Resistively Switching Ti/PCMO Devices
Advanced Materials **26**, 2730 (2014)

Herpers A., O'Shea K. J., MacLaren D. A., Noyong M., Roesgen B., Simon U., and Dittmann R.
Competing strain relaxation mechanisms in epitaxially grown $Pr_{0.48}Ca_{0.52}MnO_3$ on $SrTiO_3$
APL Materials **2**, 106106 (2014)

Hiess A., Schneidewind A., Stockert O., and Fisk Z.
Signature of superconductivity in UBe_{13} as seen by neutron scattering: Superconducting and magnetic energy scales
Physical Review B **89**, 235118 (2014)

Hirschfeld J. and Lustfeld H.
Enhanced anisotropic ionic diffusion in layered electrolyte structures from density functional theory
Physical Review B **89**, 014305 (2014)

Hocking R. K., Malaeb R., Gates W. P., Patti A. F., Chang L.-Y., Devlin G., MacFarlane D. R., and Spiccia L.
Formation of a Nanoparticulate Birnessite - Like Phase in Purported Molecular Water Oxidation Catalyst Systems
ChemCatChem **6**, 2028 (2014)

Hoffmann J. M., Janssen H., Chigrin D. N., and Taubner T.
Enhanced infrared spectroscopy using small-gap antennas prepared with two-step evaporation nanosphere lithography
Optics Express **22**, 14425 (2014)

Hong H., Lim J., Choi C.-J., Shin S.-W., and Krause H.-J.
Magnetic particle imaging with a planar frequency mixing magnetic detection scanner
Review of Scientific Instruments **85**, 013705 (2014)

Hong H. B., Krause H.-J., Nam I. H., Choi C. J., and Shin S. W.
Magnetic immunoassay based on frequency mixing magnetic detection and magnetic particles of different magnetic properties
Analytical Methods **6**, 8055 (2014)

Hoppe M., Gorgoii M., Schneider C. M., and Müller M.
Wide-range Structural and Chemical Stability of the Magnetic Oxide $NiFe_2O_4$ Grown by O_2-assisted Pulsed Laser Deposition
IEEE Transactions on Magnetics **50**, 1 (2014)

Horig C. B. M., Mora C., and Schuricht D.
Transport properties of fully screened Kondo models
Physical Review B **89**, 165411 (2014)

Huck C., Poghossian A., Bäcker M., Chaudhuri S., Zander W., Schubert J., Begoyan V. K., Buniatyan V. V., Wagner P., and Schöning M. J.
Capacitively coupled electrolyte-conductivity sensor based on high-k material of barium strontium titanate
Sensors and Actuators B **198**, 102 (2014)

Huck C., Poghossian A., Schöning M. J., Kerroumi I., Schusser S., Bäcker M., Zander W., Schubert J., Buniatyan V. V., Martirosyan N. W., and Wagner P.
Multiparameter Sensor Chip with Barium Strontium Titanate as Multipurpose Material
Electroanalysis **26**, 980 (2014)

Huske M., Offenhausser A., and Wolfrum B.
Nanoporous dual-electrodes with millimetre extensions: parallelized fabrication and area effects on redox cycling
Physical Chemistry Chemical Physics **16**, 11609 (2014)

Huske M., Stockmann R., Offenhausser A., and Wolfrum B.
Redox cycling in nanoporous electrochemical devices
Nanoscale **6**, 589 (2014)

Hutanu V., Sazonov A. P., Guduru V. K., Peters L. C. J. M., Zeitler U., Romhányi J., Náfrádi B., Meven M., Roth G., Gukasov A., Murakawa H., Tokura Y., Szaller D., Bordács S., and Kézsmárki I.
Evolution of two-dimensional antiferromagnetism with temperature and magnetic field in multiferroic $Ba_2CoGe_2O_7$
Physical Review B **89**, 064403 (2014)

Hutter A., Pedrocchi F. L., Wootton J. R., and Loss D.
Effective quantum-memory Hamiltonian from local two-body interactions
Physical Review A **90**, 012321 (2014)

Ibach H.
High resolution electron energy loss spectroscopy of spin waves in ultra-thin film - The return of the adiabatic approximation?
Surface Science **630**, 301 (2014)

Imlau R., Kovács A., Kolb U., Luysberg M., Mehmedovic E., Xu P., Stewart A. A., Leidinger C., Dunin-Borkowski R., Bihlmayer G., Wiggers H., and Carius R.
Structural and electronic properties of β-$FeSi_2$ nanoparticles: The role of stacking fault domains
Physical Review B **89**, 054104 (2014)

Iqbal M., Poilblanc D., and Schuch N.
Semionic resonating valence-bond states
Physical Review B **90**, 115129 (2014)

Izarova N., Maksimovskaya R. I., Willbold S., and Kögerler P.
Tetrapalladium-Containing Polyoxotungstate $[Pd^{II}_4(\alpha\text{-}P_2W_{15}O_{56})_2]^{16-}$: A Comparative Study
Inorganic Chemistry **53**, 11778 (2014)

Jang H., Brendt J., Patro L. N., Martin M., and Yoo H. I.
Unexpected thermoelectric behavior and immiscibility of the allegedly complete solid solution $Sr(Ru_{1-x}Ti_x)O_3$
Physical Review B **89**, 144107 (2014)

Jayaraman R., Ibach H., and Schneider C. M.
Standing spin waves in ultrathin magnetic films: A method to test for layer-dependent exchange coupling
Physical Review Letters **112**, 127202 (2014)

Jeangros Q., Hansen T. W., Wagner J. B., Dunin-Borkowski R., Hébert C., Van herle J., and Hessler-Wyser A.
Measurements of local chemistry and structure in Ni(O)–YSZ composites during reduction using energy-filtered environmental TEM
Chemical Communications **50**, 1808 (2014)

Jeangros Q., Hansen T. W., Wagner J. B., Dunin-Borkowski R., Hébert C., Van herle J., and Hessler-Wyser A.
Oxidation mechanism of nickel particles studied in an environmental transmission electron microscope
Acta Materialia **67**, 362 (2014)

Jia C. L., Mi S. B., Barthel J., Wang D. W., Dunin-Borkowski R., Urban K., and Thust A.
Determination of the 3D shape of a nanoscale crystal with atomic resolution from a single image
Nature Materials **13**, 1044 (2014)

Jiang Z., Zhang R., Wang D., Sichuga D., Jia C.-L., and Bellaiche L.
Strain-induced control of domain wall morphology in ultrathin $PbTiO_3$ films
Physical Review B **89**, 214113 (2014)

Jin L., Jia C.-L., and Vrejoiu I.
Engineering 180° ferroelectric domains in epitaxial $PbTiO_3$ thin films by varying the thickness of the underlying (La,Sr)MnO_3 layer
Applied Physics Letters **105**, 132903 (2014)

Jolie W., Craes F., Petrović M., Atodiresei N., Caciuc V., Blügel S., Kralj M., Michely T., and Busse C.
Confinement of Dirac electrons in graphene quantum dots
Physical Review B **89**, 155435 (2014)

Just S., Zimmermann S., Kataev V., Buchner B., Pratzer M., and Morgenstern M.
Preferential antiferromagnetic coupling of vacancies in graphene on SiO_2: Electron spin resonance and scanning tunneling spectroscopy
Physical Review B **90**, 125449 (2014)

Kahl T., Bousack H., Schneider E. S., and Schmitz H.
Infrared receptors of pyrophilous jewel beetles as model for new infrared sensors
Sensor Review **34**, 123 (2014)

Kalikka J., Akola J., and Jones R. O.
Simulation of crystallization in $Ge_2Sb_2Te_5$: A memory effect in the canonical phase-change material
Physical Review B **90**, 184109 (2014)

Kardynal B., Xi L., Cho D.-Y., Duchamp M., Boothroyd C. B., Lek J. Y., Besmehn A., Waser R., and Lam Y. M.
Understanding the role of single molecular ZnS precursors in the synthesis of In(Zn)P/ZnS nanocrystals
ACS Applied Materials & Interfaces **6**, 18233 (2014)

Karkkanen I., Shkabko A., Heikkila M., Niinisto J., Ritala M., Leskela M., Hoffmann-Eifert S., and Waser R.
Study of atomic layer deposited ZrO_2 and ZrO_2/TiO_2 films for resistive switching application
Physica Status Solidi A **211**, 301 (2014)

Karrasch C., Kennes D. M., and Moore J. E.
Transport properties of the one-dimensional Hubbard model at finite temperature
Physical Review B **90**, 155104 (2014)

Kashid V., Schena T., Zimmermann B., Mokrousov Y., Blügel S., Shah V., and Salunke H. G.
Dzyaloshinskii-Moriya interaction and chiral magnetism in 3d − 5d zigzag chains: Tight-binding model and ab initio calculations
Physical Review B **90**, 054412 (2014)

Kätelhön E., Barnes E. O., Krause K., Wolfrum B., and Compton R. G.
Equality of diffusion-limited chronoamperometric currents to equal area spherical and cubic nanoparticles on a supporting electrode surface
Chemical Physics Letters **595-596**, 31 (2014)

Kätelhön E., Krause K., Mathwig K., Lemay S. G., and Wolfrum B.
Noise Phenomena Caused by Reversible Adsorption in Nanoscale Electrochemical Devices
ACS Nano **8**, 4924 (2014)

Kätelhön E., Krause K., Wolfrum B., and Compton R. G.
How Many Molecules are Required to Obtain a Steady Faradaic Current from Mediated Electron Transfer at a Single Nanoparticle on a Supporting Surface?
ChemPhysChem **15**, 872 (2014)

Katelhön E., Mayer D., Banzet M., Offenhausser A., and Wolfrum B.
Nanocavity crossbar arrays for parallel electrochemical sensing on a chip
Beilstein Journal of Nanotechnology **5**, 1137 (2014)

Kaulen C., Homberger M., Bourone S., Babajani N., Karthauser S., Besmehn A., and Simon U.
Differential Adsorption of Gold Nanoparticles to Gold/Palladium and Platinum Surfaces
Langmuir **30**, 574 (2014)

Kempper R. M., Mietze C., Hiller L., Stauden T., Pezoldt J., Meertens D., Luysberg M., As D. J., and Lindner J.K.N.
Cubic GaN/AIN multi-quantum wells grown on pre-patterned 3C-SiC/Si (001)
Physica Status Solidi C **11**, 265 (2014)

Kennes D. M., Klockner C., and Meden V.
Spectral Properties of One-Dimensional Fermi Systems after an Interaction Quench
Physical Review Letters **113**, 116401 (2014)

Kennes D. M., Meden V., and Vasseur R.
Universal quench dynamics of interacting quantum impurity systems
Physical Review B **90**, 115101 (2014)

Kennes D. M., Schmidt M. J., Hubscher D., and Meden V.
Renormalization group flows in one-dimensional lattice models: Impurity scaling, umklapp scattering, and the orthogonality catastrophe
Physical Review B **90**, 155129 (2014)

Khaydukova M. M., Zadorozhnaya O. A., Kirsanov D. O., Iken H., Rolka D., Schöning M., Babain V. A., Vlasov Y.G., and Legin A. V.
Multivariate processing of atomic-force microscopy images for detection of the response of plasticized polymeric membranes
Russian Journal of Applied Chemistry **87**, 307 (2014)

Kim H. S., Li W., Danylyuk S., Brocklesby W. S., Marconi M. C., and Juschkin L.
Fractional Talbot lithography with extreme ultraviolet light
Optics Letters **39**, 6969 (2014)

Kisner A., Heggen M., Mayer D., Simon U., Offenhausser A., and Mourzina Y.
Probing the effect of surface chemistry on the electrical properties of ultrathin gold nanowire sensors
Nanoscale **6**, 5146 (2014)

Klinkhammer J., Schlipf M., Craes F., Runte S., Michely T., and Busse C.
Spin-Polarized Surface State in EuO(100)
Physical Review Letters **112**, 016803 (2014)

Klobes B., Barrier N., Vertruyen B., Martin C., and Hermann R.
Quadrupole splitting and isomer shifts in Te oxides investigated using nuclear forward scattering
Hyperfine Interactions **226**, 713 (2014)

Knoch J. and Muller M. R.
Electrostatic Doping - Controlling the Properties of Carbon-Based FETs With Gates
IEEE Transactions on Nanotechnology **13**, 1044 (2014)

Knoll L., Richter S., Nichau A., Trellenkamp S., Schäfer A., Bourdelle K. K., Hartmann J. M., Zhao Q. T., and Mantl S.
Strained Si and SiGe tunnel-FETs and complementary tunnel-FET inverters with minimum gate lengths of 50nm
Solid State Electronics **97**, 76 (2014)

Knoll L., Richter S., Nichau A., Trellenkamp S., Schäfer A., Wirths S., Blaeser S., Buca D., Bourdelle K. K., Zhao Q. T., and Mantl S.
Strained silicon based complementary tunnel-FETs: Steep slope switches for energy efficient electronics
Solid-State Electronics **98**, 32 (2014)

Konschelle F.
Transport equations for superconductors in the presence of spin interaction
The European Physical Journal B **87** (2014)

Koposova E., Liu X., Kisner A., Ermolenko Y., Shumilova G., Offenhäusser A., and Mourzina Y.
Bioelectrochemical systems with oleylamine-stabilized gold nanostructures and horseradish peroxidase for hydrogen peroxide sensor
Biosensors and Bioelectronics **57**, 54 (2014)

Kováčik R., Mavropoulos P., Wortmann D., and Blügel S.
Spin-caloric transport properties of cobalt nanostructures: Spin disorder effects from first principles
Physical Review B **89**, 1 (2014)

Krause K. J., Katelhon E., Lemay S. G., Compton R. G., and Wolfrum B.
Sensing with nanopores - the influence of asymmetric blocking on electrochemical redox cycling current
Analyst **139**, 5499 (2014)

Krause K. J., Katelhon E., Offenhausser A., and Wolfrum B.
Simulation of the impact of reversible adsorption on the response time of interdigitated electrode arrays
Physica Status Solidi A **11**, 1352 (2014)

Krause K. J., Mathwig K., Wolfrum B., and Lemay S. G.
Brownian motion in electrochemical nanodevices
European Physical Journal Special Topics **223**, 3165 (2014)

Kuhlen S., Ledesch R., de Winter R., Althammer M., Gonnenwein S. T. B., Opel M., Gross R., Wassner T. A., Brandt M. S., and Beschoten B.
Unambiguous determination of spin dephasing times in ZnO by time-resolved magneto-optical pump-probe experiments
Physica Status Solidi B **251**, 1861 (2014)

Kurzke M., Melcher C., Moser R., and Spirn D.
Vortex dynamics in the presence of excess energy for the Landau-Lifshitz-Gilbert equation
Calculus of Variations and Partial Differential Equations **49**, 1019 (2014)

Laakso M. and Pletyukhov M.
Scattering of Two Photons from Two Distant Qubits: Exact Solution
Physical Review Letters **113**, 183601 (2014)

Laakso M. A., Kennes D. M., Jakobs S. G., and Meden V.
Functional renormalization group study of the Anderson–Holstein model
New Journal of Physics **16**, 023007 (2014)

Lathiotakis N. N., Helbig N., Rubio A., and Gidopoulos N. I.
Quasi-particle energy spectra in local reduced density matrix functional theory
The Journal of Chemical Physics **141**, 164120 (2014)

Lathiotakis N. N., Helbig N., Rubio A., and Gidopoulos N. I.
Local reduced-density-matrix-functional theory: Incorporating static correlation effects in Kohn-Sham equations
Physical Review A **90**, 032511 (2014)

Lazić P., Caciuc V., Atodiresei N., Callsen M., and Blügel S.
First-principles insights into the electronic and magnetic structure of hybrid organic-metal interfaces
Journal of Physics: Condensed Matter**26**, 263001 (2014)

Legut D., Tesch M. F., Mertins H. C., Gilbert M. C., Jansing C., Burgler D. E., Schneider C. M., Gaupp A., Hamrle J., and Oppeneer P. M.
Influence of the crystal structure of thin Co films on X-ray magnetic linear dichroism-Comparison of ab initio theory and reflectometry experiments
Journal of Applied Physics **115**, 17E132 (2014)

Lehman L.
Environment-induced mixing processes in quantum walks
International Journal of Quantum Information **12**, 1450021 (2014)

Leichtweiss T., Henning R. A., Koettgen J., Schmidt R. M., Hollander B., Martin M., Wuttig M., and Janek J.
Amorphous and highly nonstoichiometric titania (TiO_x) thin films close to metal-like conductivity
Journal of Material Chemistry A **2**, 6631 (2014)

Leinhos M., Schusser S., Bachmann B., Bäcker M., Poghossian A., and Schöning M. J.
Micromachined multi-parameter sensor chip for the control of polymer-degradation medium
Physica Status Solidi A **211**, 1346 (2014)

Lenser C., Kohl A., Patt M., Schneider C. M., Waser R., and Dittmann R.
Band alignment at memristive metal-oxide interfaces investigated by hard x-ray photoemission spectroscopy
Physical Review B **90**, 115312 (2014)

Lenser C., Patt M., Menzel S., Kohl A., Wiemann C., Schneider C. M., Waser R., and Dittmann R.
Insights into Nanoscale Electrochemical Reduction in a Memristive Oxide: the Role of Three-Phase Boundaries
Advanced Functional Materials **24**, 4466 (2014)

Li H. F., Wildes A., Hou B. Y., Zhang C., Schmitz B., Meuffels P., Roth G., and Bruckel T.
Magnetization, crystal structure and anisotropic thermal expansion of single-crystal $SrEr_2O_4$
RSC Advances **4**, 53602 (2014)

Li J., Pud S., Mayer D., and Vitusevich S.
Advanced fabrication of Si nanowire FET structures by means of a parallel approach
Nanotechnology **25**, 275302 (2014)

Li J., Pud S., Petrychuk M., Offenhäusser A., and Vitusevich S.
Sensitivity Enhancement of Si Nanowire Field Effect Transistor Biosensors Using Single Trap Phenomena
Nano Letters **14**, 3504 (2014)

Li M., Pietrowski M. J., De Souza R. A., Zhang H. R., Reaney I. M., Cook S. N., Kilner J. A., and Sinclair D. C.
A family of oxide ion conductors based on the ferroelectric perovskite $Na_{0.5}Bi_{0.5}TiO_3$
Nature Materials **13**, 31 (2014)

Li P. N., Wang T., Bockmann H., and Taubner T.
Graphene-Enhanced Infrared Near-Field Microscopy
Nano Letters **14**, 4400 (2014)

Libisch F., Geringer V., Subramaniam D., Burgdorfer J., and Morgenstern M.
Diffractive-wave guiding of surface electrons on Au(111) by the herringbone reconstruction potential
Physical Review B **9**, 035442 (2014)

Lichtenstein J., Maier S. A., Honerkamp C., Platt C., Thomale R., Andersen O. K., and Boeri L.
Functional renormalization group study of an eight-band model for the iron arsenides
Physical Review B **89**, 214514 (2014)

Lin T., Zhang Y., Lee Y.-H., Krause H.-J., Lin J., and Zhao J.
High-sensitivity cooled coil system for nuclear magnetic resonance in kHz range
Review of Scientific Instruments **85**, 114708 (2014)

Linn E., Siemon A., Waser R., and Menzel S.
Applicability of Well-Established Memristive Models for Simulations of Resistive Switching Devices
IEEE Transactions on Circuits and Systems I **61**, 2402 (2014)

Liu M., Zou Q., Ma C., Collins G., Mi S.-B., Jia C.-L., Guo H., Gao H., and Chen C.
Strain-Induced Anisotropic Transport Properties of $LaBaCo2O_{5.5+\delta}$ Thin Films on $NdGaO_3$ Substrates
ACS Applied Materials & Interfaces **6**, 8526 (2014)

Long N. H., Mavropoulos P., Zimmermann B., Bauer D., Blügel S., and Mokrousov Y.
Spin relaxation and spin Hall transport in 5d transition-metal ultrathin films
Physical Review B **90**, 064406 (2014)

Luckas J., Olk A., Jost P., Volker H., Alvarez J., Jaffre A., Zalden P., Piarristeguy A., Pradel A., Longeaud C., and Wuttig M.
Impact of Maxwell rigidity transitions on resistance drift phenomena in Ge_xTe_{1-x} glasses
Applied Physics Letters **105**, 092108 (2014)

Luftner D., Ules T., Reinisch E. M., Koller G., Soubatch S., Tautz F. S., Ramsey M. G., and Puschnig P.
Imaging the wave functions of adsorbed molecules
PNAS Proceedings of the National Academy of Sciences of the USA **111**, 605 (2014)

Lumeij M., Gilleßen M., Bouwmeester H., Markus T., Mayer M., Barthel J., Roitsch S., and Dronskowski R.
Influence of the Ba^{2+}/Sr^{2+} Content and Oxygen Vacancies on the Stability of Cubic $Ba_xSr_{1-x}Co_{0.75}Fe_{0.25}O_{3-\delta}$
Physical Chemistry Chemical Physics **16**, 1333 (2014)

Luong G. V., Knoll L., Suess M. J., Sigg H., Schafer A., Trellenkamp S., Bourdelle K. K., Buca D., Zhao Q. T., and Mantl S.
High On-Currents with Highly Strained Si Nanowire MOSFETs
Proceesings of the 15. International Conference on Ultimate Integration on Silicon (ULIS), 73 (2014)

Lyatti M., Gundareva I., Pavlovskii V., Poppe U., and Divin Y.
Testing of Josephson Spectrometer with Waveguide Coupling
Journal of Physics: Conference Series **507**, 042022 (2014)

Macková A., Malinský P., Sofer Z., Šimek P., Sedmidubský D., Mikulics M., and Wilhelm R. A.
A study of the structural and magnetic properties of ZnO implanted by Gd ions
Nuclear Instruments & Methods in Physics Research B **307**, 1 (2014)

Mahy J. G., Tasseroul L., Zubiaur A., Geens J., Brisbois M., Herlitschke M., Hermann R., Heinrichs B., and Lambert S. D.
Highly dispersed iron xerogel catalysts for p-nitrophenol degradation by photo-Fenton effects
Microporous and Mesoporous Materials **197**, 164 (2014)

Maier S. A., Eberlein A., and Honerkamp C.
Functional renormalization group for commensurate antiferromagnets: Beyond the mean-field picture
Physical Review B **90**, 035140 (2014)

Manassen Y., Averbukh M., and Morgenstern M.
Analyzing multiple encounter as a possible origin of electron spin resonance signals in scanning tunneling microscopy on Si(111) featuring C and O defects
Surface Science **623**, 47 (2014)

Marchewka A., Cooper D., Lenser C., Menzel S., Du H., Dittmann R., Dunin-Borkowski R., and Waser R.
Determination of the electrostatic potential distribution in Pt/Fe:$SrTiO_3$/Nb:$SrTiO_3$ thin-film structures by electron holography
Scientific Reports **4**, 6975 (2014)

Massabuau F. C.-P., Davies M. J., Dawson P., Dunin-Borkowski R., Etheridge J., Allsopp D. W. E., Oliver R. A., Oehler F., Pamenter S. K., Thrush E. J., Kappers M. J., KovACS A., Williams T., Hopkins M. A., and Humphrey C. J.
The impact of trench defects in InGaN/GaN light emitting diodes and implications for the "green gap" problem
Applied Physics Letters **105**, 112110 (2014)

Mathieu C., Conrad E. H., Wang F., Rault J. E., Feyer V., Schneider C. M., Renault O., and Barrett N.
Exploring interlayer Dirac cone coupling in commensurately rotated few-layer graphene on SiC(000-1)
Surface and Interface Analysis **46**, 1268 (2014)

Maybeck V., Edgington R., Bongrain A., Welch J. O., Scorsone E., Bergonzo P., Jackman R. B., and Offenhäusser A.
Boron-Doped Nanocrystalline Diamond Microelectrode Arrays Monitor Cardiac Action Potentials
Advanced Healthcare Materials **3**, 283 (2014)

Mehl S., Bluhm H., and DiVincenzo D.
Two-qubit couplings of singlet-triplet qubits mediated by one quantum state
Physical Review B **90**, 045404 (2014)

Mehl S. and DiVincenzo D. P.
Inverted singlet-triplet qubit coded on a two-electron double quantum dot
Physical Review B **90**, 195424 (2014)

Meier M., Paetzold U. W., Prömpers M., Merdzhanova T., Carius R., and Gordijn A.
UV nanoimprint for the replication of etched ZnO:Al textures applied in thin-film silicon solar cells
Progress in Photovoltaics **22**, 1226 (2014)

Melcher C.
Chiral skyrmions in the plane
Proceedings of the Royal Society A - Mathematical Physical and Engineering Sciences **470** (2014)

Meng T., Fritz L., Schuricht D., and Loss D.
Low-energy properties of fractional helical Luttinger liquids
Physical Review B **89**, 045111 (2014)

Mentes T. O., Zamborlini G., Sala A., and Locatelli A.
Cathode lens spectromicroscopy: methodology and applications
Beilstein Journal of Nanotechnology **5**, 1873 (2014)

Menzel S. and Waser R.
On the SET/RESET current asymmetry in electrochemical metallization memory cells
Physica Status Solidi - Rapid Research Letters **2**, 540 (2014)

Menzel S., Valov I., Waser R., Wolf B., Tappertzhofen S., and Böttger U.
Statistical modeling of electrochemical metallization memory cells
IEEE 6. International Memory Workshop (IMW), 1 (2014)

Metlenko V., Ramadan A. H. H., Gunkel F., Du H., Schraknepper H., Hoffmann-Eifert S., Dittmann R., Waser R., and De Souza R. A.
Do dislocations act as atomic autobahns for oxygen in the perovskite oxide $SrTiO_3$?
Nanoscale **6**, 12864 (2014)

Michel A. K. U., Zalden P., Chigrin D. N., Wuttig M., Lindenberg A. M., and Taubner T.
Reversible Optical Switching of Infrared Antenna Resonances with Ultrathin Phase-Change Layers Using Femtosecond Laser Pulses
ACS Photonics **1**, 833 (2014)

Michiardi M., Aguilera I., Bianchi M., de Carvalho V. E., Ladeira L. O., Teixeira N. G., Soares E. A., Friedrich C., Blügel S., and Hofmann P.
Bulk band structure of Bi_2Te_3
Physical Review B **90**, 075105 (2014)

Mikulics M., Hardtdegen H., Sobolewski R., Marso M., Adam R., Grützmacher D., Gregušová D., Novák J., Kordoš P., Sofer Z., Serafini J., and Zhang J.
Impact of thermal annealing on nonequilibrium carrier dynamics in single-crystal, freestanding GaAs mesostructures
Semiconductor Science Technology **29**, 045022 (2014)

Mikulics M., Hardtdegen H., Sofer Z., Juul L., Marso M., Arango Y., Adam R., Fox A., Grützmacher D., Gregušová D., Stanček S., Novák J., and Kordoš P.
Reduction of skin effect losses in double-level-T-gate structure
Applied Physics Letters **105**, 232102 (2014)

Mishra D., Greving D., Confalonieri G. A. B., Perlich J., Toperverg B. P., Zabel H., and Petracic O.
Growth modes of nanoparticle superlattice thin films
Nanotechnology **25**, 205602 (2014)

Misiorny M. and Barnas J.
Spin-dependent thermoelectric effects in transport through a nanoscopic junction involving a spin impurity
Physical Review B **89**, 235438 (2014)

Misiorny M. and Weymann I.
Transverse anisotropy effects on spin-resolved transport through large-spin molecules
Physical Review B **90**, 235409 (2014)

Miyamoto K.-i., Itabashi A., Wagner T., Schöning M. J., and Yoshinobu T.
High-speed chemical imaging inside a microfluidic channel
Sensors and Actuators B **194**, 521 (2014)

Modzel G., Henske M., Houben A., Klein M., Köhli M., Lennert P., Meven M., Schmidt C. J., Schmidt U., and Schweika W.
Absolute efficiency measurements with the 10B based Jalousie detector
Nuclear Instruments & Methods in Physics Research A **743**, 90 (2014)

Monakhov K. Y., Lopez X., Speldrich M., van Leusen J., Kogerler P., Braunstein P., and Poblet J. M.
Magnetochemical Complexity of Hexa- and Heptanuclear Wheel Complexes of Late-3d Ions Supported by N, O- Donor Pyridyl-Methanolate Ligands
Chemistry – A European Journal **20**, 3769 (2014)

Moseley F., Halámek J., Kramer F., Poghossian A., Schöning M. J., and Katz E.
An enzyme-based reversible CNOT logic gate realized in a flow system
The Analyst **139**, 1839 (2014)

Muller M. R., Gumprich A., Schutte F., Kallis K., Kunzelmann U., Engels S., Stampfer C., Wilck N., and Knoch J.
Buried triple-gate structures for advanced field-effect transistor devices
Microelectronic Engineering **119**, 95 (2014)

Muto S., Rusz J., Tatsumi K., Adam R., Arai S., Kocevski V., Oppeneer P. M., Bürgler D. E., and Schneider C. M.
Quantitative characterization of nanoscale polycrystalline magnets with electron magnetic circular dichroism
Nature Communications **5**, 3138 (2014)

Naboka M., Subach S., Nefedov A., Tautz S., and Wöll C.
Direct Evidence of the Temperature-Induced Molecular Reorientation in Tetracene Thin Films on AlO_x /Ni_3Al(111)
The Journal of Physical Chemistry C **118**, 22678 (2014)

Nair H., Fu Z., Voigt J., Su Y., and Brückel T.
Approaching the true ground state of frustrated A-site spinels: A combined magnetization and polarized neutron scattering study
Physical Review B **89**, 174431 (2014)

Nandi S., Jin W., Xiao Y., Su Y., Price S., Shukla D. K., Strempfer J., Jeevan H. S., Gegenwart P., and Brückel T.
Coexistence of superconductivity and ferromagnetism in P-doped $EuFe_2As_2$
Physical Review B **89**, 014512(7) (2014)

Nandi S., Jin W. T., Xiao Y., Su Y., Price S., Schmidt W., Schmalzl K., Chatterji T., Jeevan H. S., Gegenwart P., and Brückel T.
Magnetic structure of the Eu^{2+} moments in superconducting $EuFe_2(As_{1-x}P_x)_2$ with x=0.19
Physical Review B **90** (2014)

Napoli S. D., Thiess A., Blügel S., and Mokrousov Y.
Effect of magnetism and light sp-dopants on chain creation in Ir and Pt break junctions
Journal of Physics: Condensed Matter **26**, 295302 (2014)

Nghiem H. and Costi T.
Generalization of the time-dependent numerical renormalization group method to finite temperatures and general pulses
Physical Review B **89**, 075118 (2014)

Nghiem H. T. M. and Costi T. A.
Time-dependent numerical renormalization group method for multiple quenches: Application to general pulses and periodic driving
Physical Review B **90**, 035129 (2014)

Nielen L., Tappertzhofen S., Linn E., Kavehei O., Skafidas S., Valov I., and Waser R.
Live demonstration: An associative capacitive network based on nanoscale complementary resistive switches
Circuits and Systems **1**, 439 (2014)

Nielsch K., Schierning G., Hermann R., and Müller E.
Thermal transport in nanoscale semiconductors
Semiconductor Science and Technology **29**, 120301 (2014)

Nikolaev K. G., Ermakov S. S., Offenhäusser A., and Mourzina Y.
Activation of gold nanostructures with Meerwein's salt
Mendeleev Communications **24**, 145 (2014)

Nishi Y., Menzel S., Fleck K., Bottger U., and Waser R.
Origin of the SET Kinetics of the Resistive Switching in Tantalum Oxide Thin Films
IEEE Electron Device Letters **35**, 259 (2014)

Oberländer J., Kirchner P., Boyen H.-G., and Schöning M. J.
Detection of hydrogen peroxide vapor by use of manganese(IV) oxide as catalyst for calorimetric gas sensors
Physica Status Solidi A **211**, 1372 (2014)

Oehme M., Kostecki K., Arguirov T., Mussler G., Ye K. H., Gollhofer M., Schmid M., Kaschel M., Korner R. A., Kittler M., Buca D., Kasper E., and Schulze J.
GeSn Heterojunction LEDs on Si Substrates
IEEE Photonics Technology Letters **26**, 187 (2014)

Ohm C. and Hassler F.
Majorana fermions coupled to electromagnetic radiation
New Journal of Physics **16**, 015009 (2014)

Olbrich P., Golub L. E., Grützmacher D., Plucinski L., Eschbach M., Ganichev S. D., Herrmann T., Danilov S. N., Plank H., Bel'kov V. V., Mussler G., Weyrich C., Schneider C. M., and Kampmeier J.
Room-Temperature High-Frequency Transport of Dirac Fermions in Epitaxially Grown Sb_2Te_3- and Bi_2Te_3-Based Topological Insulators
Physical Review Letters **113**, 096601 (2014)

Opel M., Goennenwein S. T. B., Althammer M., Nielsen K. W., Karrer-Muller E. M., Bauer S., Senn K., Schwark C., Weier C., Guntherodt G., Beschoten B., and Gross R.
Zinc oxide - From dilute magnetic doping to spin transport
Physica Status Solidi B **251**, 1700 (2014)

Ozsoy-Keskinbora C., Boothroyd C. B., Dunin-Borkowski R., van Aken P. A., and Koch C. T.
Hybridization approach to in-line and off-axis (electron) holography for superior resolution and phase sensitivity
Scientific Reports **4**, 7020 (2014)

Panchakarla L. S., Popovitz-Biro R., Houben L., Dunin-Borkowski R., and Tenne R.
Lanthanide-Based Functional Misfit-Layered Nanotubes
Angewandte Chemie / International Edition **53**, 6920 (2014)

Panchakarla L. S., Radovsky G., Houben L., Popovitz-Biro R., Dunin-Borkowski R., and Tenne R.
Nanotubes from Misfit Layered Compounds: A New Family of Materials with Low Dimensionality
The Journal of Physical Chemistry Letters **5**, 3724 (2014)

Park D., Herpers A., Menke T., Heidelmann M., Houben L., Dittmann R., and Mayer J.
Studies of Local Structural Disortions in Strained Ultrathin $BaTiO_3$ Films sing Scanning Transmission Electron Microscopy
Microscopy and Microanalysis **20**, 740 (2014)

Parshin P. P., Alekseev P. A., Nemkovskiy K., Persson J., Chumakov A. I., and Rüffer R.
Phonons and the electronic gap in FeSi
Journal of Experimental and Theoretical Physics **118**, 242 (2014)

Patt M., Wiemann C., Weber N., Escher M., Gloskovskii A., Drube W., Merkel M., and Schneider C. M.
Bulk sensitive hard x-ray photoemission electron microscopy
Review of Scientific Instruments **85**, 113704 (2014)

Pettersen K. H., Lindén H., Tetzlaff T., and Einevoll G. T.
Power Laws from Linear Neuronal Cable Theory: Power Spectral Densities of the Soma Potential, Soma Membrane Current and Single-Neuron Contribution to the EEG
PLOS Computational Biology **10**, 1003928 (2014)

Pilch M., Molak A., and Szot K.
Thermal Treatment Effects in $PbTiO_3$ Crystals Studied by XPS and Electric Conductivity Tests
Ferroelectrics **466**, 51 (2014)

Plekan O., Feyer V., Ptasinska S., Tsud N., and Prince K. C.
Cyclic dipeptide immobilization on Au(111) and Cu(110) surfaces
Physical Chemistry Chemical Physics **16**, 6657 (2014)

Poghossian A. and Schöning M. J.
Label-Free Sensing of Biomolecules with Field-Effect Devices for Clinical Applications
Electroanalysis **26**, 1197 (2014)

Pop I. M., Geerlings K., Catelani G., Schoelkopf R. J., Glazman L. I., and Devoret M. H.
Coherent suppression of electromagnetic dissipation due to superconducting quasiparticles
Nature **508**, 369 (2014)

Pozzi G., Beleggia M., Kasama T., and Dunin-Borkowski R.
Interferometric methods for mapping static electric and magnetic fields
Comptes Rendus Physique **15**, 126 (2014)

Pradheesh R., Xiao Y., Cherian D., Elizabeth S., Hansen T., Chatterji T., Brückel T., and Nair H.
Magnetization-steps in Y_2CoMnO_6 double perovskite: The role of antisite disorder
Journal of Applied Physics **116**, 123907 (2014)

Pud S., Gasparyan F., Petrychuk M., Li J., Offenhäusser A., and Vitusevich S.
Single trap dynamics in electrolyte-gated Si-nanowire field effect transistors
Journal of Applied Physics **115**, 233705 (2014)

Pud S., Li J., Sibiliev V., Petrychuk M., Kovalenko V., Offenhäusser A., and Vitusevich S.
Liquid and Back Gate Coupling Effect: Toward Biosensing with Lowest Detection Limit
Nano Letters **14**, 578 (2014)

Puzzuoli D., Granade C., Haas H., Criger B., Magesan E., and Cory D. G.
Tractable simulation of error correction with honest approximations to realistic fault models
Physical Review A **89**, 022306 (2014)

Qureshi N., Lee C. H., Kihou K., Schmalzl K., Steffens P., and Braden M.
Anisotropy of incommensurate magnetic excitations in slightly overdoped $Ba_{0.5}K_{0.5}Fe_2As_2$ probed by polarized inelastic neutron scattering experiments
Physical Review B **90**, 100502 (2014)

Rahmanizadeh K., Wortmann D., Bihlmayer G., and Blügel S.
Charge and orbital order at head-to-head domain walls in $PbTiO_3$
Physical Review B **90**, 115104 (2014)

Rajeswari J., Michel E., Ibach H., and Schneider C. M.
Intensities of surface spin wave excitations in inelastic electron scattering
Physical Review B **89**, 075438 (2014)

Rajeswari J., Ibach H., and Schneider C. M.
Standing Spin Waves in Ultrathin Magnetic Films: A Method to Test for Layer-Dependent Exchange Coupling
Physical Review Letters **112**, 127202 (2014)

Raoux S., Xiong F., Wuttig M., and Pop E.
Phase change materials and phase change memory
MRS Bulletin **39**, 703 (2014)

Reim J. D., Rosen E., Schweika W., Meven M., Leo N. R., Meier D., Fiebig M., Schmidt M., Kuo C. Y., Pi T. W., Hu Z., and Valldor M.
Structural invariance upon antiferromagnetic ordering in geometrically frustrated swedenborgite, $CaBaCo_2Fe_2O_7$
Journal of Applied Crystallography **47**, 2038 (2014)

Reininghaus F., Pletyukhov M., and Schoeller H.
Kondo model in nonequilibrium: Interplay between voltage, temperature, and crossover from weak to strong coupling
Physical Review B **90**, 085121 (2014)

Reininghaus M., Kalupka C., Faley O., Holtum T., Finger J., and Stampfer C.
Dynamics of ultrashort pulsed laser radiation induced non-thermal ablation of graphite
Applied Physics A - Materials Science & Processing **117**, 1873 (2014)

Reiter R., Derra U., Birner S., Terres B., Libisch F., Burgdorfer J., and Stampfer C.
Negative quantum capacitance in graphene nanoribbons with lateral gates
Physical Review B **89**, 115406 (2014)

Rentrop J. F., Jakobs S. G., and Meden V.
Nonequilibrium transport through a Josephson quantum dot
Physical Review B **89**, 235110 (2014)

Reuters B., Hahn H., Pooth A., Hollander B., Breuer U., Heuken M., Kalisch H., and Vescan A.
Fabrication of p-channel heterostructure field effect transistors with polarization-induced two-dimensional hole gases at metal-polar GaN/AlInGaN interfaces
Journal of Physics D: Applied Physics **47**, 175103 (2014)

Richter S., Blaeser S., Knoll L., Trellenkamp S., Fox A., Schafer A., Hartmann J. M., Zhao Q. T., and Mantl S.
Silicon-germanium nanowire tunnel-FETs with homo- and heterostructure tunnel junctions
Solid-State Electronics **98**, 75 (2014)

Richter S., Schulte-Braucks C., Knoll L., Luong G. V., Schafer A., Trellenkamp S., Zhao Q. T., and Multl S.
Experimental Demonstration of Inverter and NAND Operation in p-TFET Logic at Ultra-low Supply Voltages down to V-DD=0.15 V
Proceedings of the 72. Annual Device Research Conference (DRC), 23 (2014)

Richter S., Trellenkamp S., Schafer A., Hartmann J. M., Bourdelle K. K., Zhao Q. T., and Mantl S.
Tunnel-FET Inverters for Ultra-low Power Logic with Supply Voltage down to V-DD=0.2 V
Proceedings of the 15. International Conference on Ultimate Integration on Silicon (ULIS), 13 (2014)

Rieger T., Jorres T., Vogel J., Biermanns A., Pietsch U., Grutzmacher D., and Lepsa M. I.
Crystallization of HfO_2 in InAs/HfO_2 core-shell nanowires
Nanotechnology **25**, 405701 (2014)

Rieger T., Schäpers T., Grützmacher D., and Lepsa M. I.
Crystal Phase Selective Growth in GaAs/InAs Core–Shell Nanowires
Crystal Growth & Design **14**, 1167 (2014)

Ringel M., Pletyukhov M., and Gritsev V.
Topologically protected strongly correlated states of photons
New Journal of Physics **16**, 113030 (2014)

Rispens G., Ziegler B., Paruch P., Zanolli Z., Íñiguez J., and Ghosez P.
Phase diagram of $BiFeO_3$/$LaFeO_3$ superlattices studied by x-ray diffraction experiments and first-principles calculations
Physical Review B **90**, 104106 (2014)

Rodenbücher C., Jauß A., Havel V., Waser R., and Szot K.
Fast mapping of inhomogeneities in the popular metallic perovskite Nb:$SrTiO_3$ by confocal Raman microscopy
Physica Status Solidi - Rapid Research Letters **08**, 781 (2014)

Rosén E., Schweika W., Reim J., Schmidt M., Meven M., Leo N. R., Meier D., Fiebig M., Kuo C.-Y., Pi T.-W., Hu Z., and Valldor M.
Structural invariance upon antiferromagnetic ordering in geometrically frustrated swedenborgite, $CaBaCo_2Fe_2O_7$
Journal of Applied Crystallography **47**, 2038 (2014)

Rossouw C. J., Dwyer C., Katz-Boon H., and Etheridge J.
Channeling contrast analysis of lattice images: Conditions for probe-insensitive STEM
Ultramicroscopy **136**, 216 (2014)

Rüffer D., Slot M., Zamani R. R., Morante J. R., Arbiol J., Fontcuberta A., Grundler D., Hubert R., Schwarze T., Heimbach F., Tütüncüoglu G., Matteini F., Russo-Averchi E., KovACS A., and Dunin-Borkowski R.
Anisotropic magnetoresistance of individual CoFeB and Ni nanotubes with values of up to 1,4% at room temperature
APL Materials **2**, 076112 (2014)

Santoro F., Dasgupta S., Schnitker J., Auth T., Neumann E., Panaitov G., Gompper G., and Offenhäusser A.
Interfacing Electrogenic Cells with 3D Nanoelectrodes: Position, Shape, and Size Matter
ACS Nano **8**, 6713 (2014)

Saptsov R. B. and Wegewijs M. R.
Time-dependent quantum transport: Causal superfermions, exact fermion-parity protected decay modes, and Pauli exclusion principle for mixed quantum states
Physical Review B **90**, 045407 (2014)

Schaab J., Krug I. P., Ramesh R., Meier D., Nickel F., Gottlob D. M., Doğanay H., Cano A., Hentschel M., Yan Z., Bourret E., and Schneider C. M.
Imaging and characterization of conducting ferroelectric domain walls by photoemission electron microscopy
Applied Physics Letters **104**, 232904 (2014)

Schäfer A., Besmehn A., Hardtdegen H., Mikulics M., Schubert J., Luysberg M., Winden A., Stoica T., Schnee M., Zander W., Niu G., Schroeder T., and Mantl S.
Hexagonal $GdScO_3$: an epitaxial high-κ dielectric for GaN
Semiconductor Science and Technology **29**, 075005 (2014)

Scherer D. D., Scherer M. M., Khaliullin G., Honerkamp C., and Rosenow B.
Unconventional pairing and electronic dimerization instabilities in the doped Kitaev-Heisenberg model
Physical Review B **90**, 045135 (2014)

Schie M., Waser R., and De Souza R. A.
A Simulation Study of Oxygen-Vacancy Behavior in Strontium Titanate: Beyond Nearest-Neighbor Interactions
Journal of Physical Chemistry C **118**, 15185 (2014)

Schmidt R. M., Ries P., Pflug A., Wuttig M., and Kubart T.
Increasing the carbon deposition rate using sputter yield amplification upon serial magnetron co-sputtering
Surface and Coatings Technology **252**, 74 (2014)

Schnedler M., Jiang Y., Wu K. H., Wang E. G., Dunin-Borkowski R., and Ebert P.
Effective mass of a two-dimensional √3×√3 Ga single atomic layer on Si(111)
Surface Science **630**, 225 (2014)

Schnedler M., Weidlich P., Portz V., Weber D., Dunin-Borkowski R., and Ebert P.
Correction of nonlinear lateral distortions of scanning probe microscopy images
Ultramicroscopy **136**, 86 (2014)

Schmidt M., Schafer A., Minamisawa R. A., Buca D., Trellenkamp S., Hartmann J. M., Zhao Q. T., and Mantl S.
Line and Point Tunneling in Scaled Si/SiGe Heterostructure TFETs
IEEE Electron Device Letters **35**, 699 (2014)

Schreiber L. R. and Bluhm H.
Quantum Computation Silicon Comes Back
Nature Nanotechnology **9**, 966 (2014)

Schulenborg J., Splettstoesser J., Governale M., and Contreras-Pulido L. D.
Detection of the relaxation rates of an interacting quantum dot by a capacitively coupled sensor dot
Physical Review B **89**, 195305 (2014)

Schulte-Braucks C., Richter S., Knoll L., Selmi L., Zhao Q. T., and Mantl S.
Experimental Demonstration of Improved Analog Device Performance in GAA-NW-TFETs
Proceedings of the 44. European Solid State Device Research Conference (ESSDERC), 178 (2014)

Schulz P., Schafer T., Zangmeister C. D., Effertz C., Meyer D., Mokros D., van Zee R. D., Mazzarello R., and Wuttig M.
A New Route to Low Resistance Contacts for Performance-Enhanced Organic Electronic Devices
Advanced Materials Interfaces **1**, 1300130 (2014)

Schwarzkopf J., Braun D., Schmidbauer M., Duk A., and Wördenweber R.
Ferroelectric domain structure of anisotropically strained $NaNbO_3$ epitaxial thin films
Journal of Applied Physics **115**, 204105 (2014)

Schweflinghaus B., dos Santos Dias M., Costa A. T., and Lounis S.
Renormalization of electron self-energies via their interaction with spin excitations: A first-principles investigation
Physical Review B **89**, 235439 (2014)

Shirazi R., KovACS A., Dan Corell D., Gritti C., Thorseth A., Dam-Hansen C., Petersen P. M., and Kardynal B.
Origin of low quantum efficiency of photoluminescence of InP/ZnS nanocrystals
Journal of Luminescence **145**, 936 (2014)

Shu M. J., Zalden P., Chen F., Weems B., Chatzakis I., Xiong F., Jeyasingh R., Hoffmann M. C., Pop E., Wong H. S. P., Wuttig M., and Lindenberg A. M.
Ultrafast terahertz-induced response of GeSbTe phase-change materials
Applied Physics Letters **104**, 251907 (2014)

Siemon A., Menzel S., Marchewka A., Nishi Y., Waser R., and Linn E.
Simulation of TaO_x-based complementary resistive switches by a physics-based memristive model
IEEE International Symposium on Circuits and Systems (ISCAS), 1420 (2014)

Šimek P., Sedmidubský D., Klímová K., Huber Š., Brázda P., Mikulics M., Jankovský O., and Sofer Z.
Synthesis of InN nanoparticles by rapid thermal ammonolysis
Journal of Nanoparticle Research **16**, 2805 (2014)

Simon R. E., Sergueev I., Kantor I., Kantor A., Persson J., and Hermann R. P.
^{121}Sb and ^{125}Te nuclear inelastic scattering in Sb_2Te_3 under high pressure
Semiconductor Science and Technology **29**, 124001 (2014)

Singh D., Yun Y., Wan W., Grushko B., Zou X. D., and Hovmöller S.
A complex pseudo-decagonal quasicrystal approximant $Al_{37}(Co,Ni)_{15.5}$ solved by the rotation electron diffraction (RED) method
Journal of Applied Crystallography **47**, 215 (2014)

Singh T., Wang S. Z., Aslam N., Zhang H. H., Hoffmann-Eifert S., and Mathur S.
Atomic Layer Deposition of Transparent VO_x Thin Films for Resistive Switching Applications
Chemical Vapor Deposition **20**, 291 (2014)

Sinmyo R., Bykova E., McCammon C., Kupenko I., Potapkin V., and Dubrovinsky L.
Crystal chemistry of Fe^{3+}-bearing (Mg, Fe)SiO_3 perovskite: a single-crystal X-ray diffraction study
Physics and Chemistry of Minerals **41**, 409 (2014)

Sinmyo R., Glazyrin K., McCammon C., Kupenko I., Kantor A., Potapkin V., Chumakov A. I., Ruffer R., and Dubrovinsky L.
The influence of solid solution on elastic wave velocity determination in (Mg,Fe)O using nuclear inelastic scattering
Physics of the Earth and Planetary Interiors **229**, 16 (2014)

Sipahi G. M., Žutić I., Atodiresei N., Kawakami R. K., and Lazić P.
Spin polarization of Co(0001)/graphene junctions from first principles
Journal of Physics: Condensed Matter **26**, 104204 (2014)

Siqueira J. R., Molinnus D., Beging S., and Schöning M. J.
Incorporating a Hybrid Urease-Carbon Nanotubes Sensitive Nanofilm on Capacitive Field-Effect Sensors for Urea Detection
Analytical Chemistry **86**, 5370 (2014)

Skoromets V., Kadlec C., Drahokoupil J., Schubert J., Hlinka J., and Kuzel P.
Systematic study of terahertz response of $SrTiO_3$ based heterostructures: Influence of strain, temperature, and electric field
Physical Review B **89**, 214116 (2014)

Slipukhina I. and Ležaić M.
Electronic and magnetic properties of the Ti_5O_9 Magnéli phase
Physical Review B **90**, 155133 (2014)

Solgun F., Abraham D. W., and DiVincenzo D. P.
Blackbox quantization of superconducting circuits using exact impedance synthesis
Physical Review B **90** (2014)

Soni R., Petraru A., Meuffels P., Vavra O., Ziegler M., Kim S. K., Jeong D. S., Pertsev N. A., and Kohlstedt H.
Giant electrode effect on tunnelling electroresistance in ferroelectric tunnel junctions
Nature Communications **5**, 5414 (2014)

Soppe W., Krc J., Leitner K., Haug F.-J., Duchamp M., Sanchez Plaza G., and Wang Q.
Silicon-Light: a European project aiming at high efficiency thin film silicon solar cells on foil
EPJ Photovoltaics **5**, 55203 (2014)

Spilla S., Hassler F., and Splettstoesser J.
Measurement and dephasing of a flux qubit due to heat currents
New Journal of Physics **16** (2014)

Stadtmüller B., Gruenewald M., Peuker J., Forker R., Fritz T., and Kumpf C.
Molecular Exchange in a Heteromolecular PTCDA/CuPc Bilayer Film on Ag(111)
The Journal of Physical Chemistry C **118**, 28592 (2014)

Stadtmüller B., Lüftner D., Willenbockel M., Reinisch E. M., Sueyoshi T., Koller G., Soubatch S., Ramsey M. G., Puschnig P., Tautz F. S., and Kumpf C.
Unexpected interplay of bonding height and energy level alignment at heteromolecular hybrid interfaces
Nature Communications **5** (2014)

Stadtmüller B., Schröder S., Tautz S., Kumpf C., Bocquet F., Henneke C., Kleimann C., Subach S., Willenbockel M., Detlefs B., Zegenhagen J., and Lee T.-L.
Adsorption height alignment at heteromolecular hybrid interfaces
Physical Review B **89**, 161407 (2014)

Starschich S., Griesche D., Schneller T., Waser R., and Böttger U.
Chemical solution deposition of ferroelectric yttrium-doped hafnium oxide films on platinum electrodes
Applied Physics Letters **104**, 202903 (2014)

Staunton J. B., Banerjee R., dos Santos Dias M., Deak A., and Szunyogh L.
Fluctuating local moments, itinerant electrons, and the magnetocaloric effect: Compositional hypersensitivity of FeRh
Physical Review B **89**, 054427 (2014)

Stefanov S., Serra C., Benedetti A., Conde J. C., Werner J., Oehme M., Schulze J., Wirths S., Buca D., and Chiussi S.
Structure and composition of Silicon-Germanium-Tin microstructures obtained through Mask Projection assisted Pulsed Laser Induced Epitaxy
Microelectronic Engineering **125**, 18 (2014)

Stella K., Franzka S., Bürstel D., Diesing D., Mayer D., and Roddatis V.
Electrochemical Oxidation as Vertical Structuring Tool for Ultrathin (d < 10 nm) Valve Metal Films
ECS Journal of Solid State Science and Technology **3**, P143 (2014)

Stepanov I., Kuhlen S., Ersfeld M., Lepsa M., and Beschoten B.
All-electrical time-resolved spin generation and spin manipulation in n-InGaAs
Applied Physics Letters **104**, 062406 (2014)

Stern M., Catelani G., Kubo Y., Grezes C., Bienfait A., Vion D., Esteve D., and Bertet P.
Flux Qubits with Long Coherence Times for Hybrid Quantum Circuits
Physical Review Letters **113**, 123601 (2014)

Sydoruk V. A., Goß K., Meyer C., Petrychuk M. V., Danilchenko B. A., Weber P., Stampfer C., Li J., and Vitusevich S. A.
Low-frequency noise in individual carbon nanotube field-effect transistors with top, side and back gate configurations: effect of gamma irradiation
Nanotechnology **25**, 035703 (2014)

Szot K., Bihlmayer G., and Speier W.
Nature of the Resistive Switching Phenomena in TiO_2 and $SrTiO_3$: Origin of the Reversible Insulator-Metal Transition
Solid State Physics **65**, 353 (2014)

Takenaga S., Herrera C., Werner C. F., Biselli M., Thönnessen V., Schnitzler T., Öhlschläger P., Almajhdi F. N., Wagner T., and Schöning M. J.
Toward multi-analyte bioarray sensors: LAPS-based on-chip determination of a Michaelis-Menten-like kinetics for cell culturing
Physica Status Solidi A **211**, 1410 (2014)

Tan H., Zhu Y., Dwyer C., and Xin H.
Energy-loss-and thickness-dependent contrast in atomic-scale electron energy-loss spectroscopy
Physical Review B **90**, 214305 (2014)

Tappertzhofen S., Linn E., Bottger U., Waser R., and Valov I.
Nanobattery Effect in RRAMs-Implications on Device Stability and Endurance
IEEE Transactions of Electron Devices L **35**, 208 (2014)

Tappertzhofen S., Waser R., and Valov I.
Impact of the Counter-Electrode Material on Redox Processes in Resistive Switching Memories
ChemElectroChem **1**, 1287 (2014)

Tarakina N. V., Schreyeck S., Molenkamp L. W., Luysberg M., Grauer S., Schumacher C., Karczewski G., Brunner K., Gould C., Buhmann H., and Dunin-Borkowski R.
Suppressing Twin Formation in Bi_2Se_3 Thin Films
Advanced Materials Interfaces **1** (5), 8 (2014)

Tashman J. W., Lee J. H., Paik H., Moyer J. A., Misra R., Mundy J. A., Spila T., Merz T. A., Schubert J., Muller D. A., Schiffer P., and Schlom D. G.
Epitaxial growth of VO_2 by periodic annealing
Applied Physics Letters **104**, 063104 (2014)

Telychko M., Mutombo P., Ondráček M., Hapala P., Bocquet F. C., Kolorenč J., Vondráček M., Jelínek P., and Švec M.
Achieving High-Quality Single-Atom Nitrogen Doping of Graphene/SiC(0001) by Ion Implantation and Subsequent Thermal Stabilization
ACS Nano **8**, 7318 (2014)

Terres B., Reichardt S., Neumann C., Watanabe K., Taniguchi T., and Stampfer C.
Raman spectroscopy on mechanically exfoliated pristine graphene ribbons
Physica Status Solidi B **251**, 2551 (2014)

Tesch M. F., Legut D., Gaupp A., Berges U., Mertins H.-C., Gilbert M. C., Jansing C., Hamrle J., Rusz J., Oppeneer P. M., Bürgler D. E., and Schneider C. M.
Magnetocrystalline anisotropy in x-ray magnetic linear dichroism at the 3*p* edges of crystalline Fe thin films
Physical Review B **89**, 140404(R) (2014)

Tessarek C., Heilmann M., Butzen E., Haab A., Hardtdegen H., Dieker C., Spiecker E., and Christiansen S.
The Role of Si during the Growth of GaN Micro- and Nanorods
Crystal Growth & Design **14**, 1486 (2014)

Theophilou I., Tassi M., and Thanos S.
Charge transfer excitations from excited state Hartree-Fock subsequent minimization scheme
The Journal of Chemical Physics **140**, 164102 (2014)

Tomka M., El Araby O., Pletyukhov M., and Gritsev V.
Exceptional and regular spectra of a generalized Rabi model
Physical Review A **90** (2014)

Tornberg L., Barzanjeh S., and DiVincenzo D.
Stochastic-master-equation analysis of optimized three-qubit nondemolition parity measurements
Physical Review A **89**, 032314 (2014)

Tran D. P., Macdonald T. J., Wolfrum B., Stockmann R., Nann T., Offenhäusser A., and Thierry B.
Photoresponsive properties of ultrathin silicon nanowires
Applied Physics Letters **105**, 231116 (2014)

Tran D. P., Wolfrum B., Stockmann R., Offenhausser A., and Thierry B.
Fabrication of locally thinned down silicon nanowires
Journal of Materials Chemistry C **2**, 5229 (2014)

Trzebiatowska-Gusowska M., Plinski E. F., Baran J., Walczakowski M. J., Jarzab P. P., Nowak K., Fuglewicz B., Mikulics M., Palka N., and Szustakowski M.
Terahertz and Raman spectra of non-centrosymmetrical organic molecular crystals
Optical Materials **37**, 28 (2014)

Tsukamoto S., Hirose K., and Blügel S.
Real-space finite-difference calculation method of generalized Bloch wave functions and complex band structures with reduced computational cost
Physical Review E **90**, 013306 (2014)

Tutsch U., Wolf B., Wessel S., Postulka L., Tsui Y., Jeschke H. O., Opahle I., Saha-Dasgupta T., Valenti R., Bruhl A., Remović-Langer K., Kretz T., Lerner H. W., Wagner M., and Lang M.
Evidence of a field-induced Berezinskii-Kosterlitz-Thouless scenario in a two-dimensional spin-dimer system
Nature Communications **5**, 5169 (2014)

Ulrich J., Adagideli I., Schuricht D., and Hassler F.
Supersymmetry in the Majorana Cooper-pair box
Physical Review B **90**, 075408 (2014)

Valov I., Tappertzhofen S., Linn E., Menzel S., van den Hurk J., and Waser R.
(Keynote) Atomic Scale and Interface Interactions in Redox-Based Resistive Switching Memories
ECS Transactions **64**, 3 (2014)

van den Hurk J., Dippel A. C., Cho D. Y., Straquadine J., Breuer U., Walter P., Waser R., and Valov I.
Physical origins and suppression of Ag dissolution in GeS_x-based ECM cells
Physical Chemistry Chemical Physics **16**, 18217 (2014)

van den Hurk J., Linn E., Zhang H. H., Waser R., and Valov I.
Volatile resistance states in electrochemical metallization cells enabling non-destructive readout of complementary resistive switches
Nanotechnology **25**, 425202 (2014)

van der Loop T. H., Ottosson N., Lotze S., Kentzinger E., Vad T., Sager W., Bakker H. J., and Woutersen S.
Structure and dynamics of water in nanoscopic spheres and tubes
The Journal of Chemical Physics **141**, 18C535 (2014)

van Heck B., Cobanera E., Ulrich J., and Hassler F.
Thermal conductance as a probe of the nonlocal order parameter for a topological superconductor with gauge fluctuations
Physical Review B **89**, 062329 (2014)

Vershynina A.
Complete criterion for convex-Gaussian-state detection
Physical Review A **90** (2014)

Viola G. and DiVincenzo D. P.
Hall Effect Gyrators and Circulators
Physical Review X **4**, 021019 (2014)

Volmer F., Drogeler M., Maynicke E., von den Driesch N., Boschen M. L., Guntherodt G., Stampfer C., and Beschoten B.
Suppression of contact-induced spin dephasing in graphene/MgO/Co spin-valve devices by successive oxygen treatments
Physical Review B **90**, 165403 (2014)

Vool U., Pop I. M., Mirrahimi M., Frunzio L., Schoelkopf R. J., Glazman L. I., Devoret M. H., Sliwa K., Abdo B., Wang C., Brecht T., Gao Y. Y., Shankar S., Hatridge M., and Catelani G.
Non-Poissonian Quantum Jumps of a Fluxonium Qubit due to Quasiparticle Excitations
Physical Review Letters **113**, 247001 (2014)

Wagner C., Fournier N., Ruiz V. G., Li C., Mullen K., Rohlfing M., Tkatchenko A., Temirov R., and Tautz F. S.
Non-additivity of molecule-surface van der Waals potentials from force measurements
Nature Communications **5**, 5568 (2014)

Wagner C., Fournier N., Tautz F. S., and Temirov R.
The role of surface corrugation and tip oscillation in single-molecule manipulation with a non-contact atomic force microscope
Beilstein Journal of Nanotechnology **5**, 202 (2014)

Wagner P. and Schöning M. J.
Engineering of Functional Interfaces
Physica Status Solidi A **211**, 1339 (2014)

Wahl T. B., Hassler S. T., Tu H. H., Cirac J. I., and Schuch N.
Symmetries and boundary theories for chiral projected entangled pair states
Physical Review B **90**, 115133 (2014)

Wang C., Gao Y. Y., Glazman L. I., Schoelkopf R. J., Pop I. M., Vool U., Axline C., Brecht T., Heeres R. W., Frunzio L., Devoret M. H., and Catelani G.
Measurement and control of quasiparticle dynamics in a superconducting qubit
Nature Communications **5**, 5836 (2014)

Wang J., de Jeu W. H., Rücker U., Ziener U., Polinskaya M. S., Ponomarenko S. A., Ruderer M. A., Herzig E. M., Müller-Buschbaum P., Moeller M., and Mourran A.
Monolayer Properties of Asymmetrically Substituted Sexithiophene
Langmuir **30**, 2752 (2014)

Wei X., Tagantsev A. K., Kvasov A., Roleder K., Jia C.-L., and Setter N.
Ferroelectric translational antiphase boundaries in nonpolar materials
Nature Communications **5**, 3031 (2014)

Weidlich P., Schnedler M., Portz V., Eisele H., Dunin-Borkowski R., and Ebert P.
Meandering of overgrown v-shaped defects in epitaxial GaN layers
Applied Physics Letters **105**, 012105 (2014)

Weis K., Wirths S., Winden A., Sladek K., Hardtdegen H., Luth H., Grutzmacher D., and Schapers T.
Quantum dots in InAs nanowires induced by surface potential fluctuations
Nanotechnology **25,** 0135203 (2014)

Wen-Jie Y., Bo Z., Chang L., Zhong-Ying X., Ming C., and Qing-Tai Z.
Mobility Enhancement and Gate-Induced-Drain-Leakage Analysis of Strained-SiGe Channel p-MOSFETs with Higher-κ $LaLuO_3$ Gate Dielectric
Chinese Physics Letters **31**, 016101 (2014)

Wenz T., Rosien M., Haas F., Rieger T., Demarina N., Lepsa M. I., Luth H., Grutzmacher D., and Schapers T.
Phase coherent transport in hollow InAs nanowires
Applied Physics Letters **105** (2014)

Wiessner M., Hauschild D., Sauer C., Feyer V., Scholl A., and Reinert F.
Complete determination of molecular orbitals by measurement of phase symmetry and electron density
Nature Communications **5**, 4156 (2014)

Wildes A., Hou B., Zhang C., Schmitz B., Meuffels P., Roth G., Brückel T., and Li H.
Magnetization, crystal structure and anisotropic thermal expansion of single-crystal $SrEr_2O_4$
RSC Advances **4**, 53602 (2014)

Wilson D., Rudolf D., Juschkin L., Weier C., Adam R., Winkler G., Frömter R., Danylyuk S., Bergmann K., Grützmacher D., and Schneider C. M.
Generation of circularly polarized radiation from a compact plasma-based extreme ultraviolet light source for tabletop X-ray magnetic circular dichroism studies
Review of Scientific Instruments **85**, 103110 (2014)

Wirths S., Buca D., Ikonic Z., Harrison P., Tiedemann A. T., Hollander B., Stoica T., Mussler G., Breuer U., Hartmann J. M., Grützmacher D., and Mantl S.
SiGeSn growth studies using reduced pressure chemical vapor deposition towards optoelectronic applications
Thin Solid Films **557**, 183 (2014)

Witzens J.
Ab initio calculation of the deformation potential and photoelastic coefficients of silicon with a non-uniform finite-difference solver based on the local density approximation
Computer Physics Communications **185**, 2221 (2014)

Wu C., Bronder T., Poghossian A., Werner C. F., Bäcker M., and Schöning M. J.
Label-free electrical detection of DNA with a multi-spot LAPS: First step towards light-addressable DNA chips
Physica Status Solidi A **211**, 1423 (2014)

Xi L. F., Cho D. Y., Duchamp M., Boothroyd C. B., Lek J. Y., Besmehn A., Waser R., Lam Y. M., and Kardynal B.
Understanding the Role of Single Molecular ZnS Precursors in the Synthesis of In(Zn)P/ZnS Nanocrystals
ACS Applied Materials & Interfaces **6**, 18233 (2014)

Xin H. L., Dwyer C., and Müller D.
Is there a Stobbs factor in atomic-resolution STEM-EELS mapping?
Ultramicroscopy **139**, 38 (2014)

Xu C., Wicklein S., Sambri A., Amoruso S., Moors M., and Dittmann R.
Impact of the interplay between nonstoichiometry and kinetic energy of the plume species on the growth mode of $SrTiO_3$ thin films
Journal of Physics D: Applied Physics **47**, 034009 (2014)

Xu D. W., Cheng X. H., Yu Y. H., Wang Z. J., Cao D., Xia C., Liu L. J., Trellenkamp S., Mantl S., and Zhao Q. T.
Improved LDMOS performance with buried multi-finger gates
Microelectronic Engineering **122**, 29 (2014)

Xu D. W., Cheng X. H., Yu Y. H., Wang Z. J., Xia C., Cao D., Zhao Q. T., Liu L. J., and Mantl S.
Multi-Gates SOI LDMOS for Improved on-state Performance
IEEE 26. International Symposium on Power Semiconductor Devices & IC's (ISPSD), 175 (2014)

Yakushenko A., Mayer D., Buitenhuis J., Offenhausser A., and Wolfrum B.
Electrochemical artifacts originating from nanoparticle contamination by Ag/AgCl quasi-reference electrodes
Lab on a Chip **14**, 602 (2014)

Yakushenko A., Schops V., Mayer D., Offenhausser A., and Wolfrum B.
On-chip fast scan cyclic voltammetry for selective detection of redox active neurotransmitters
Physics Status Solidi A **211**, 1364 (2014)

Yang Y., Gao P., Li L., Pan X., Tappertzhofen S., Choi S., Waser R., Valov I., and Lu W. D.
Electrochemical dynamics of nanoscale metallic inclusions in dielectrics
Nature Communications **5**, 4232 (2014)

Yu W., Zhang B., Liu C., Zhao Y., Wu W. R., Xue Z. Y., Chen M., Buca D., Hartmann J. M., Wang X., Zhao Q. T., and Mantl S.
Impact of Si cap, strain and temperature on the hole mobility of (s)Si/sSiGe/(s)SOI quantum-well p-MOSFETs
Microelectronic Engineering **113**, 5 (2014)

Yu W. J., Wu W. R., Zhang B., Liu C., Sun J. B., Zhai D. Y., Yu Y. H., Wang X., Shi Y., Zhao Y., and Zhao Q. T.
Experimental Investigation on Alloy Scattering in sSi/$Si_{0.5}Ge_{0.5}$/sSOI Quantum-Well p-MOSFET
IEEE Transactions of Electron Devices **61**, 950 (2014)

Zalden P., Siegert K. S., Rols S., Fischer H. E., Schlich F., Hu T., and Wuttig M.
Specific Heat of $(GeTe)_x(Sb_2Te_3)_{1-x}$ Phase-Change Materials: The Impact of Disorder and Anharmonicity
Chemistry of Materials **26**, 2307 (2014)

Zamani R. R., Ibáñez M., Arbiol J., Luysberg M., García-Castelló N., Houben L., Prades J. D., Grillo V., Dunin-Borkowski R., Morante J. R., and Cabot A.
Polarity-Driven Polytypic Branching in Cu-Based Quaternary Chalcogenide Nanostructures
ACS Nano **8**, 2290 (2014)

Zeng J., Zhang Y., Schmelz M., Mück M., Krause H.-J., Braginski A. I., Lee Y.-H., Stolz R., Kong X., Xie X., Meyer H.-G., Offenhäusser A., and Jiang M.
Analysis of a dc SQUID readout scheme with voltage feedback circuit and low-noise preamplifier
Superconductor Science and Technology **27**, 085011 (2014)

Zhang H. H., Aslam N., Reiners M., Waser R., and Hoffmann-Eifert S.
Atomic Layer Deposition of TiO_x/Al_2O_3 Bilayer Structures for Resistive Switching Memory Applications
Chemical Vapor Deposition **20**, 282 (2014)

Zhang M., Wille M., Lu J. G., Röder R., Heedt S., Huang L., Zhu Z., Geburt S., Grützmacher D., Schäpers T., and Ronning C.
Amphoteric Nature of Sn in CdS Nanowires
Nano Letters **14**, 518 (2014)

Zhang W., Jungfleisch M. B., Jiang W., Pearson J. E., Hoffmann A., Freimuth F., and Mokrousov Y.
Spin Hall Effects in Metallic Antiferromagnets
Physical Review Letters **113**, 196602 (2014)

Zhang W., Ronneberger I., Li Y., and Mazzarello R.
Ab Initio Investigation of Crystalline and Amorphous GeTe Doped with Magnetic Impurities
Science of Advanced Materials **6**, 1655 (2014)

Zhang W., Ronneberger I., Li Y., and Mazzarello R.
Ab initio investigation of amorphous Sb_2Te
Monatshefte für Chemie **145**, 97 (2014)

Zhang W., Ronneberger I., Zalden P., Xu M., Salinga M., Wuttig M., and Mazzarello R.
How fragility makes phase-change data storage robust: insights from ab initio simulations
Scientific Reports **4**, 6529 (2014)

Zhao J., Zhang Y., Lee Y.-H., and Krause H.-J.
Investigation and optimization of low-frequency noise performance in readout electronics of dc superconducting quantum interference device
Review of Scientific Instruments **85**, 054707 (2014)

Zhuang C., Schlempert C., Fuchs R., Zhang L., Huang N., Vogel M., Staedtler T., and Jiang X.
Mechanical behavior related to various bonding states in amorphous Si–C–N hard films
Surface and Coatings Technology **258**, 353 (2014)

Zhukov A. A., Volk C., Winden A., Hardtdegen H., and Schapers T.
Investigations of local electronic transport in InAs nanowires by scanning gate microscopy at liquid helium temperatures
JETP Letters **100**, 32 (2014)

Zhukov A. A., Volk C., Winden A., Hardtdegen H., and Schapers T.
The electronic transport of top subband and disordered sea in an InAs nanowire in the presence of a mobile gate
Journal of Physics - Condensed Matter **26** (2014)

Zimmermann B., Chadova K., Gradhand M., Ködderitzsch D., Blügel S., Ebert H., Fedorov D. V., Long N. H., Mavropoulos P., Mertig I., and Mokrousov Y.
Skew scattering in dilute ferromagnetic alloys
Physical Review B **90**, 220403 (2014)

Zimmermann B., Heide M., Bihlmayer G., and Blügel S.
First-principles analysis of a homochiral cycloidal magnetic structure in a monolayer Cr on W(110)
Physical Review B **90**, 115427 (2014)

Cover pictures refer to the following selected research reports (From left to right)

M. Heidelmann et al., Periodic cation segregation in Cs0.44[Nb2.54W2.46O14] quantified by HRSTEM, p. 81 | C. Rodenbücher et al., Resistive switching of a quasi-homogeneous distribution of filaments on reduced TiO2 surfaces, p. 69 | S. Just et al., Surface and Step Conductivities on Silicon, p. 99

JARA|FIT

Fundamentals of Future
Information Technology

JARA-FIT
Jülich Aachen Research Alliance
for Fundamentals of
Future Information Technology

Office
Forschungszentrum Jülich GmbH
52425 Jülich
Germany
Phone: ++49-2461-61-3107
Email: w.speier@fz-juelich.de

AN INITIATIVE OF

RWTH AACHEN UNIVERSITY

JÜLICH FORSCHUNGSZENTRUM